Title

AUGER ELECTRON SPECTROSCOPY ANALYSIS OF VANADIUM AND VANADIUM COMPOUND SURFACES

Author

Szalkowski, Frederick John.

Publication Date

1973-10-01

LBL-888
c.1

AUGER ELECTRON SPECTROSCOPY ANALYSIS OF VANADIUM AND VANADIUM COMPOUND SURFACES

Frederick John Szalkowski
(Ph.D. Thesis)

October 1973

Prepared for the U.S. Atomic Energy Commission
under Contract W-7405-ENG-48

LAWRENCE BERKELEY LABORATORY
UNIVERSITY OF CALIFORNIA • BERKELEY •

TO ALL OF THOSE PEOPLE, PLACES, AND THINGS
THAT HAVE STIRRED IN ME A SENSE OF LOVE

"I have heard the summer dust crying to be born
As much as ever flesh cried to be quiet.

. . . thence life was born,
Its nitrogen from ammonia, carbon from methane,
Water from the cloud and salts from the young seas . . .

. . . the cells of life
Bound themselves into clans, a multitude of cells
To make one being--as the molecules before
Had made of many one cell. Meanwhile they had invented
Chlorophyll and ate sunlight, cradled in peace
On the warm waves;

. . . but certain assassins among them
Discovered that it was easier to eat flesh
Than feed on lean air and sunlight; thence the animals,
Greedy mouths and guts, life robbing life,
Grew from the plants; and as the oceans ebbed and
  flowed many plants and animals
Were stranded in the great marshes along the shore,
Where many died and some lived. From these grew all
  land-life,
Plants, beasts, and men; the mountain forest and the
  mind of Aeschylus
And the mouse in the wall."

lines from Robinson Jeffers

AUGER ELECTRON SPECTROSCOPY ANALYSIS OF VANADIUM AND VANADIUM COMPOUND SURFACES

Contents

AUGER ELECTRON SPECTROSCOPY ANALYSIS OF VANADIUM AND VANADIUM COMPOUND SURFACES

Frederick John Szalkowski

Inorganic Materials Research Division, Lawrence Berkeley Laboratory and
Department of Chemistry; University of California,
Berkeley, California

ABSTRACT

An ultra-high vacuum system containing a four grid Retarding Field Energy Analyzer was constructed and its supporting electronics developed to explore the feasibility of usefully measuring chemical shifts in the energy of Auger electrons using this combination Low Energy Electron Diffraction-Auger Electron Spectroscopy (LEED-AES) type of apparatus. The availability of such chemical shift information is extremely important in determining the chemical composition of a thin surface layer since it would provide information on the state of chemical bonding of the atoms involved, this information supplementing the qualitative and semiquantitative data presently gleaned from AES and the surface structural information obtained from LEED.

Both LEED and AES studies were carried out on the (100) face of vanadium metal. It was found that the essentially clean metal surface displays a (1×1) diffraction pattern indicating a surface structure identical with the corresponding plane in the bulk, but that sulfur segregates to the surface upon heating and transforms the surface into a c(2×2) structure. Room temperature gas adsorption studies on the V(100)-(1×1) surface indicates that oxygen diffuses into the lattice

and produces a disordered structure while carbon monoxide adsorbs upon the surface in a (1×1) array. Oxygen adsorption on the V(100)-c(2×2) surface produced a complex structure in which no oxygen was observed within the probed surface layer. This structure has been interpreted in terms of additional sulfur segregating to the solid-gas interface under the influence of the altered surface conditions (i.e., oxygen adsorption) with the subsequent desorption of the oxygen as this occurs.

Characteristic Loss measurements were performed on vanadium metal and V_2O_3 for the primary beam energy range of 100 eV to 700 eV. Mechanisms which are consistant with all of the observations reported on vanadium to date have been proposed for the observed peaks. The somewhat unexpected and interesting phenomenum that a multiple interband transition loss may occur with a probability greater than that of a single interband transition loss is pointed out and is instrumental in explaining the observed data.

AES chemical shift studies were carried out on V_2O_4, V_2O_3, VO, VN, VC, V_2S_3, and VSi_2. The shifts of the totally inner shell $L_3M_{2,3}M_{2,3}$ transition and the single valence band $L_3M_{2,3}V$ transition were measured relative to their energies in metallic vanadium. The $L_3M_{2,3}M_{2,3}$ transition displayed a systematic shift which could be associated with the successive transfer of the 4s and 3d valence band electrons to the anion and the observed shifts were correlated with the Philips-Van Vechten ionicity scale. The $L_3N_{2,3}V$ transition

yields information which is useful in determining the position of the high energy edge of the valence band relative to the Fermi level. The effect of electronic relaxation on the Auger electron energy is also pointed out and discussed. Estimates of the L_3, $M_{2,3}$, and valence band widths for the compounds investigated have also been obtained from the data. Correlation of the chemical shift data and the O/V peak intensity ratio for the known vanadium oxides enables one to unambiguously determine the chemical composition of the compound formed by oxidizing vanadium metal under different temperature and pressure conditions. In addition to the "normal" vanadium oxides, the production of the V_3O_5 Magneli phase was observed during this set of experiments. The $M_{2,3}VV$ double valence band transition was also observed and its behavior upon oxidation indicates that at least one 4s electron is involved in this transition as opposed to the case of the $L_3M_{2,3}V$ transition which appears to overwhelmingly involve the 3d valence band.

I. INTRODUCTION

It is well-known that the presence of a solid surface may affect the rate of a chemical reaction that takes place in the liquid or gas phase by many orders of magnitude. As a consequence of this phenomenon, a large research effort has historically been directed toward the elucidation of the mechanisms of reactions as they occur at the solid surface and of the influence of the properties of the surface upon these mechanisms, spurred by both the desire to understand the nature of the basic interactions involved and to produce surfaces which specifically induce or inhibit the formation of a compound. The overwhelming majority of these investigations, however, were performed on ill-defined surfaces and/or using techniques which yielded information about the macroscopic parameters of the system involved (rate constants, reactant and product concentration). It has only been within the past decade that the technical advances have been made which have enabled researchers to prepare and observe surfaces which are well-defined on the atomic scale.

In short, the major impetus to the growth of surface science has been the development of ultra-high vacuum (UHV) techniques, which make the attainment of pressures below 10^{-8} Torr a routine matter. It may easily be calculated from the kinetic theory of gases that a surface which is entirely free of adsorbed species will be covered by a single layer of gas in a time[1]

$$t \approx \frac{\sqrt{MT}}{3.52\times10^{7}} \left(\frac{1}{P}\right) \qquad \text{(I-1)}$$

where t is given in seconds, M is the molecular weight of the gas, T is the temperature in degrees Kelvin, P is the gas pressure in Torr, and the assumption has been made that every gas molecule which impinges upon the surface remains there (i.e. a sticking coefficient of unity). At a typical high vacuum of 10^{-6} Torr it therefore takes only one second before a clean surface can conceivably be covered by a monolayer of gas. This is indeed not an extremely long time in which to carry out an experiment and it drastically underscores the need for UHV generation. It might also be pointed out here that the rapid growth of electronic noise-suppression and signal averaging techniques over the past twenty years has also contributed in no small way to the ability to obtain useful data within a reasonable length of time.

The two major experimental techniques that have been developed for the study of surfaces were both discovered back in the nineteen-twenties, but lay essentially dormant until the above-mentioned advances enabled them to achieve fruitation. The first of these chronologically exploited was Low Energy Electron Diffraction (LEED), the second being Auger Electron Spectroscopy (AES). These are complementary techniques and jointly possess the ultimate capability of allowing definative interpretation of surface phenomena to be carried out on an atomic scale. This requires that together they are capable of providing detailed information about the atomic surface structure and about the chemical composition of the surface. Implicit in the latter requirement is a knowledge of the elements present at the surface, the concentration of each, and the chemical binding state(s) of each species.

LEED studies (i.e. the analysis of electrons which are elastically back-scattered from a surface) using single crystal surfaces may be performed in order to determine the atomic surface structure. The analysis of 1) electrons which undergo discreet energy losses and are inelastically back-scattered from the surface (characteristic loss electrons) and 2) electrons which originate in the surface atoms and are emitted as the result of an inelastic electron scattering event can provide us with information on the chemical composition. Auger electrons are of this latter type. Auger electron peaks appear in the electron emission spectrum at absolute energies which are the property of the elements present on the surface, the intensity of each peak providing an indication of the concentration of the element associated with it. Since, as will be shown later, the Auger electron energy in a function of the energy levels in the atom from which it originates, it seems likely that the oxidation states of the atoms may be identified by the small shifts induced in these levels as the result of placing the atom in different chemical environments. It is the measurement of these so-called chemical shifts in the Auger electrons which is the main objective of this research effort.

A. Electron Energy Spectra and Surface Analysis

Instead of proceeding directly into a detailed discussion of the Auger effect, it would seem to be worthwhile to determine more fully its relationship to the other surface measurement techniques touched upon above and to the field of atomic spectroscopy in general.

A solid which is subjected to bombardment by a beam of sufficiently energetic ($>$ 50 eV) electrons or photons is known to dissipate much of the energy that is transferred to it by the incident beam through the emission of electrons with an energy distribution similar to that shown in Fig. I-1. This particular curve was obtained[2] by bombarding a graphite target with an essentially monoenergetic primary electron beam of energy $E_p = eV_p = 425$ eV. The electron energy distribution in this curve may be broken up into four main regions, the assignments hinging on the nature of the event which makes the main contribution to the structure observed in each region.

Region I is comprised of those electrons which have been elastically scattered by the target. Those which have been coherently scattered contain information about the atomic structure of the target and give rise to the diffraction phenomena observed in LEED. If the incident beam energy is sufficiently low ($<$ 500 eV), the information obtained is restricted to the contributions from the first few atomic surface layers because of the high scattering cross-sections for such low energy electrons. LEED can therefore easily perceive changes occurring in the uppermost surface monolayer and its usefulness as a surface probe is abundantly apparent.

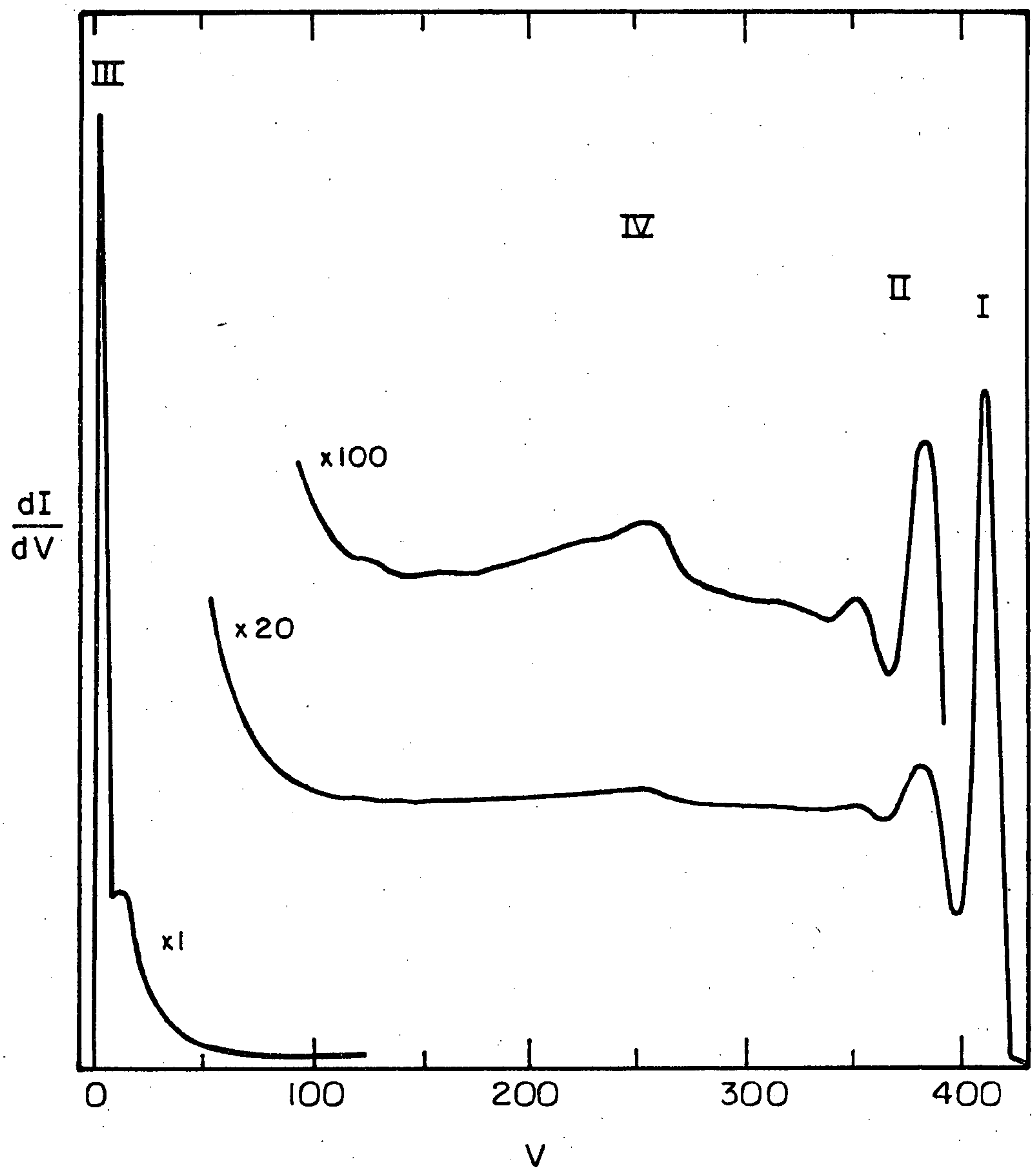

XBL733-5922

Fig. I-1. The energy distribution of electrons from graphite using an incident beam energy of 475 eV. (From Amelio and Scheibner[2])

Region II consists of electrons which have lost discreet amounts of energy in the process of being scattered by the target. These are labelled Characteristic Loss electrons since the magnitude of each energy loss is a function of the target material. The energies of the loss peaks are measured relative to the energy of the elastically scattered electrons since these peaks move concurrently with the elastic peak as the incident beam energy is varied. The mechanisms by which a Characteristic Loss may occur are 1) the excitation of a bound atomic electron to a state near the crystal Fermi level and this is called an interband transition, and 2) the excitation of a collective oscillation of the unbound electrons in the solid relative to the lattice of the ionic nuclei: a plasmon excitation.

In Region III, the large broad peak which reaches a maximum at an energy of a few electron volts is due to the emission of what are labelled true secondary electrons. The origin of this term lies in the fact that these electrons originate in bound states of the target material and are emitted from them as the result of the influence of the primary electron beam. This peak is the result of a cascade process in which secondary electrons, having been produced by collisions between the incident beam electrons and the bound-state electrons in the target, diffuse through the solid, multiplying and losing energy through more collision processes, until they either fall back into the sea of conduction electrons or reach the surface with sufficient energy to escape from the solid. The process is not unlike a successively branching chain reaction in which the momentum of the original secondary electron is diluted over all of the approximately 2^n electrons at the end of the chain (n being the number of inelastic collisions that the original electron experiences).

Region IV consists mainly of a continuous distribution of primary electrons which have undergone a large number of energy losses, and these are commonly referred to as rediffused primaries. There being no energy borderline distinction possible, this region also contains some true secondary electrons (as defined above) and blends nebulously into Region III. Superimposed upon this background, and also on the high-energy side of the cascade peak, are a number of small peaks which appear at well-defined absolute energies that are characteristic of the target material and which exhibit no energy dependence on the primary beam energy. These intensity maxima have been correlated with the atomic binding energies of the target atoms and are ascribed to an atomic reorganization process which has been described as the auto-ionization of ions, i.e. the Auger process.

Although this thesis is not a proper forum for an in-depth discussion of the theory and practice of electron scattering in general, a brief synopsis of the state-of-the-art associated with the aforementioned phenomena will be presented for the sake of completeness and since some measurements of them have been performed and will be discussed later.

1. Elastically Diffracted Electrons

In 1927 Davisson and Germer found that electrons experience diffraction by a solid in a manner similar to that demonstrated by X-rays. However, it was noted that the angular distribution of the diffracted beams could be explained by assuming that the electrons possessed a wavelength λ as given by the de Broglie relationship

$$\lambda = \frac{h}{p} = \frac{h}{\sqrt{2mE_p}} = \frac{h}{\sqrt{2m\ eV_p}} = \sqrt{\frac{150.4}{V_p}} \qquad \text{(I-2)}$$

where

h = Plank's constant

p = the momentum of the electrons

m = the electron mass

$E_p = eV_p$ = the energy of the incident electrons

e = the electronic charge

V_p = the accelerating voltage of the incident electrons

and that the scattering occurred off of the periodic lattice of the surface atoms as if it were a two-dimensional (2-D) diffraction grating.[3] The direction of the scattered beams can be determined from the kinematical (i.e. single scattering) diffraction theory as shown in Fig. I-2 for a 1-D array of identical scattering centers. Here it is seen that constructive interference occurs at angles where the electron path difference between scattering centers is an integral number of wavelengths and follows the relationship

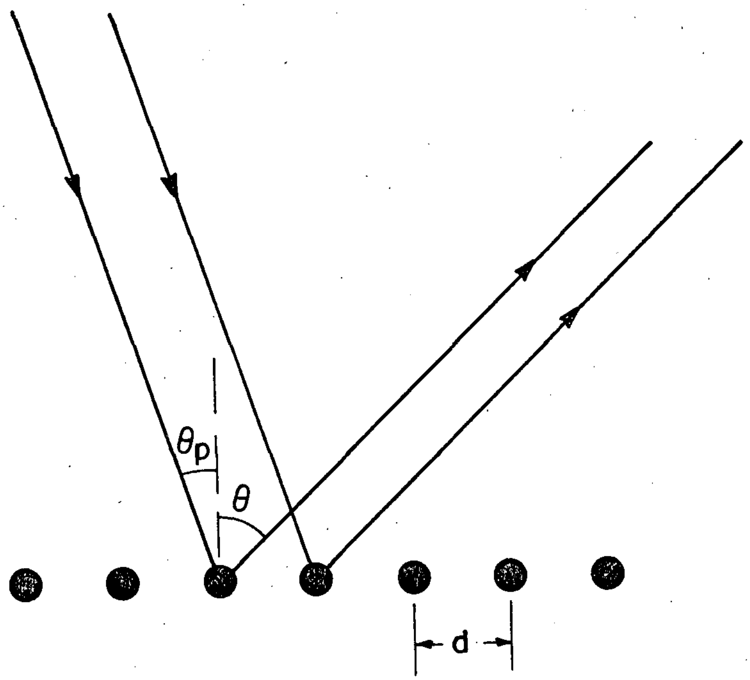

XBL733-5923

Fig. I-2. Illustration showing diffraction occurring from a one-dimensional array of scattering centers.

$$h\lambda = d(\sin\theta - \sin\theta_p) \qquad \text{(I-3)}$$

$$= d\sin\theta \quad \text{for a normally incident primary beam}$$

where

h = an integer which determines the order of diffraction
d = the distance between scattering centers
θ = the scattering angle with respect to the surface normal
θ_p = the incident beam angle with respect to the surface normal

The diffraction for the 2-D case can be similarly treated, however it is more convenient to use the Ewald sphere construction in reciprocal space. As an example, consider the (100) face of a simple cubic crystal which has the lattice parameter d. Associated with the bulk crystal is a reciprocal lattice which is also simple cubic but has a lattice parameter $d^* = 2\pi/d$. If it is imagined that the distance between (10) planes is gradually increased (while the distances between the lattice points within each layer are kept constant), the corresponding reciprocal space distances are decreased. When the (10) planes are infinitely far apart, the reciprocal lattice points have coalesced into a set of parallel rods (Fig. I-3). The primary beam may be approximated by a plane wave $\exp(i\vec{K}^\circ\cdot\vec{r})$, the propagation vector $\vec{K}^\circ$ having the magnitude $K^\circ = 2\pi/\lambda$ and being separable into its components parallel and perpendicular to the surface: $\vec{K}^{\circ}_{\parallel}$ and $\vec{K}^{\circ}_{\perp}$ respectively. The Ewald sphere is constructed so that $(1/2\pi)\vec{K}^{\circ}$ is a radius vector which terminates at the origin of the reciprocal net and the intersection of the lattice rods with the surface of the sphere determines the possible angles of diffraction. As an example, AB in Fig. I-3 is equal to $(1/2\pi)\vec{K}$, where $\vec{K}$ is the propagation vector of one of the diffracted beams. One may perceive that, in general, the relations for the conservation of energy

$$\vec{K} = \vec{K}^{\circ} \tag{I-4}$$

and conservation of parallel momentum

$$\vec{K}_{\parallel} = \vec{K}^{\circ}_{\parallel} + 2\pi\vec{\mu} \tag{I-5}$$

where

$\vec{\mu}$ = a reciprocal net vector

are satisfied.[4] For the beams shown in Fig. I-3, Eq. II-5 can be written as

$$\frac{1}{\lambda}\sin\theta = \frac{1}{\lambda}\sin\theta_p + h\frac{1}{d} , \tag{I-6}$$

which is identical to the plane grating formula of Eq. I-3.

Low energy electrons are neither scattered entirely by the first atomic layer nor do they penetrate deeply into the bulk of the crystal as do X-rays of comparable wavelength. Rather they are scattered almost completely by the first few atomic layers, as illustrated

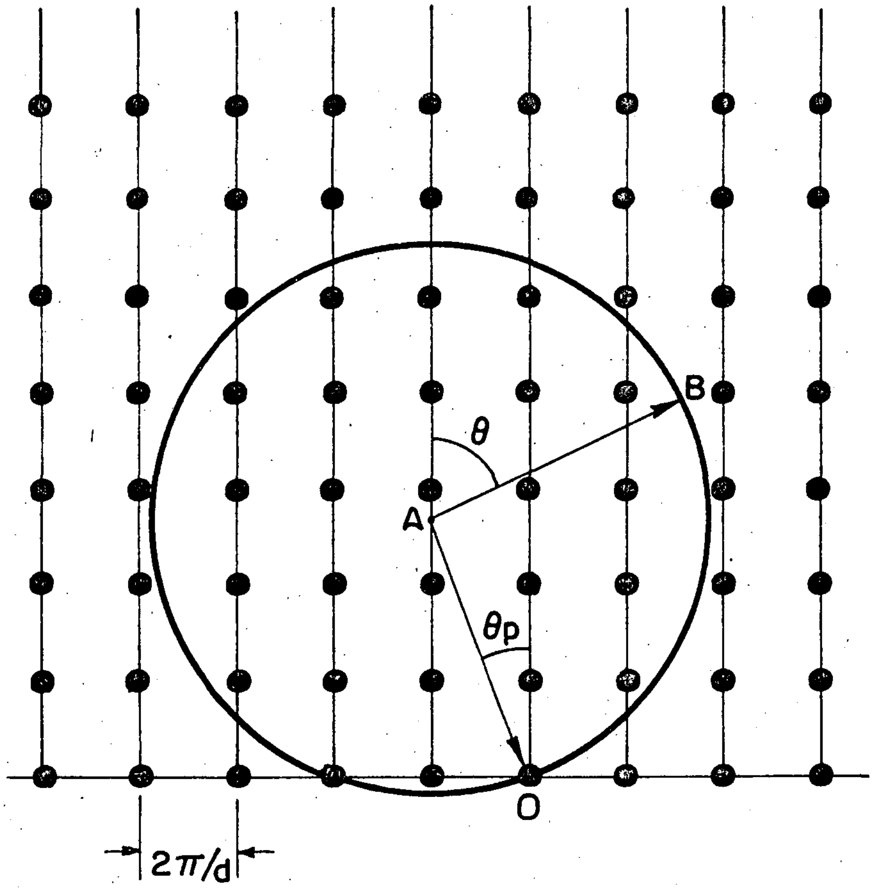

XBL 733-5924

Fig. I-3. The Ewald construction illustrating diffraction from two- and three-dimensional arrays of scattering centers.

schematically in Fig. I-4 and demonstrated by the mean free path energy dependence discussed later (section B-2-c). As the result of this intermediate scattering cross-section, multiple scattering events can occur and the kinematic theory usually fails to explain the diffracted beam intensity variations observed in LEED. Several dynamical (multiple scattering) approaches for the calculation of these diffracted intensities have been formulated, these attempting to solve the Schrödinger equation in either its differential or integral form.[5] So far these theories have proven to be inadequate, and the surface structural problem (i.e. the ability to unambiguously determine the location and nature of the different surface atoms) remains to be solved.

This by no means implies that LEED is useless since a great deal of surface-related information can be extracted from changes appearing in the diffraction pattern and from the temperature dependence of the diffracted intensities (the Debye-Waller factor). For example, LEED techniques have been used to determine that solid surfaces can undergo structural rearrangements or changes in chemical composition independently of the crystal bulk, that particular atoms and molecules can chemisorb or physisorb on surfaces in ordered arrays, and that the chemical activity of a surface can depend upon its crystallographic orientation.[4,5]

The nomenclature which has developed in LEED to depict these phenomena is as follows. In Figs. I-5, I-6, and I-7, surfaces are shown which exhibit six-fold, four-fold, and two-fold rotational

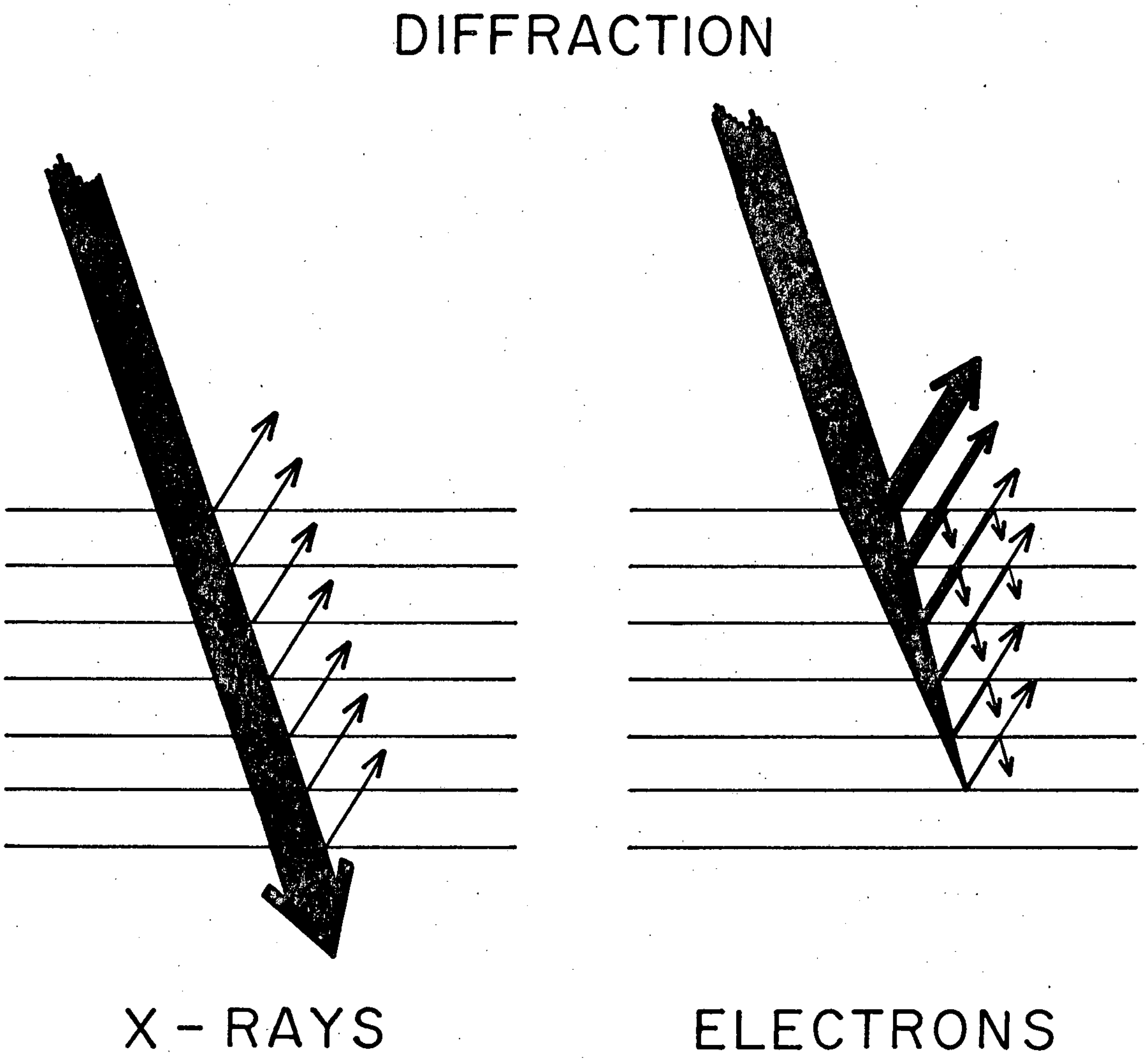

XBL 7012-7436

Fig. I-4. Schematic illustration of the scattering of X-rays and of low energy electrons by the atomic planes of a crystal. The width of the arrows show relative intensities.

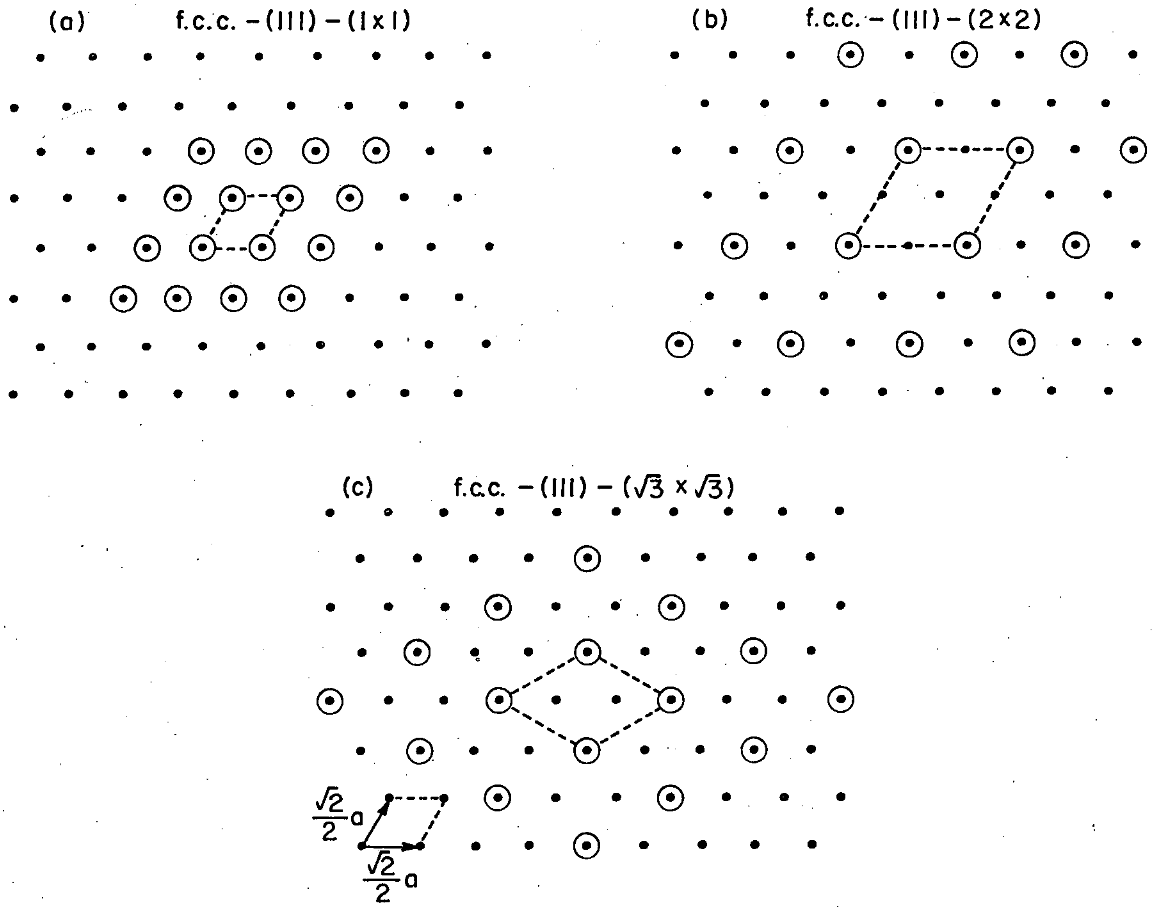

XBL 733-5925

Fig. I-5. Schematic diagrams of the most common surface structures appearing on substrates with sixfold rotational symmetry.

(a) f.c.c. - (100)-(2x2)

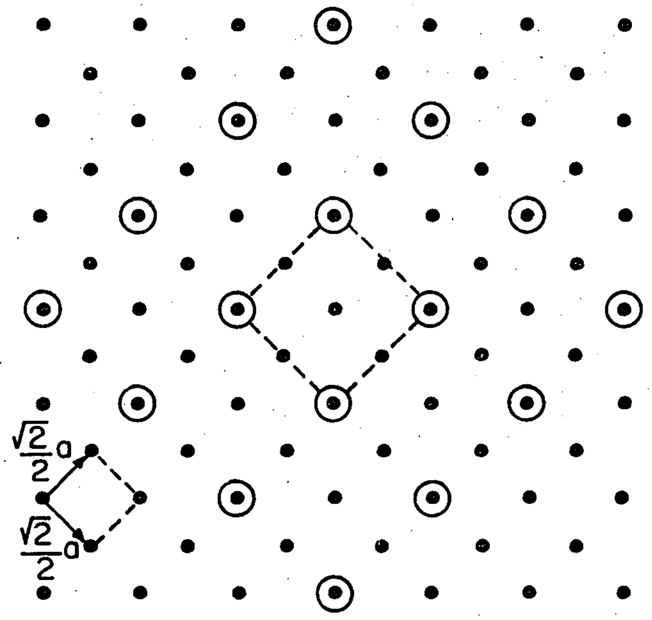

(b) f.c.c.-(100)-c(2x2)

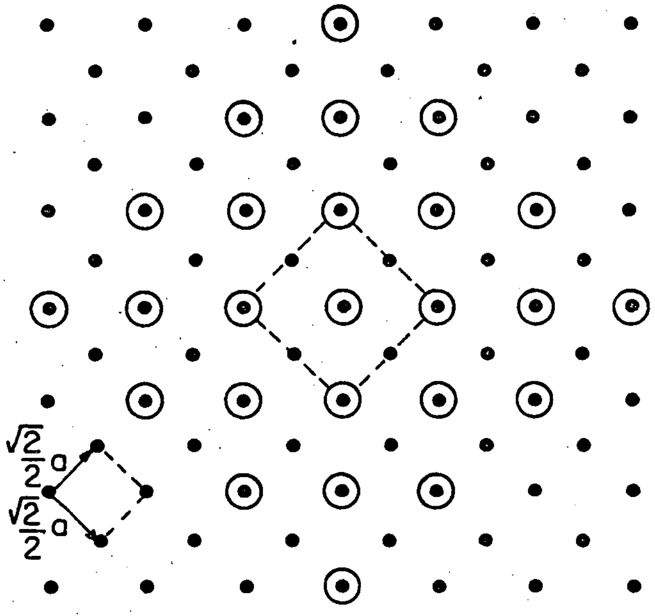

XBL 733-5927

Fig. I-6. Schematic diagrams of the most common surface structures appearing on substrates with fourfold rotational symmetry.

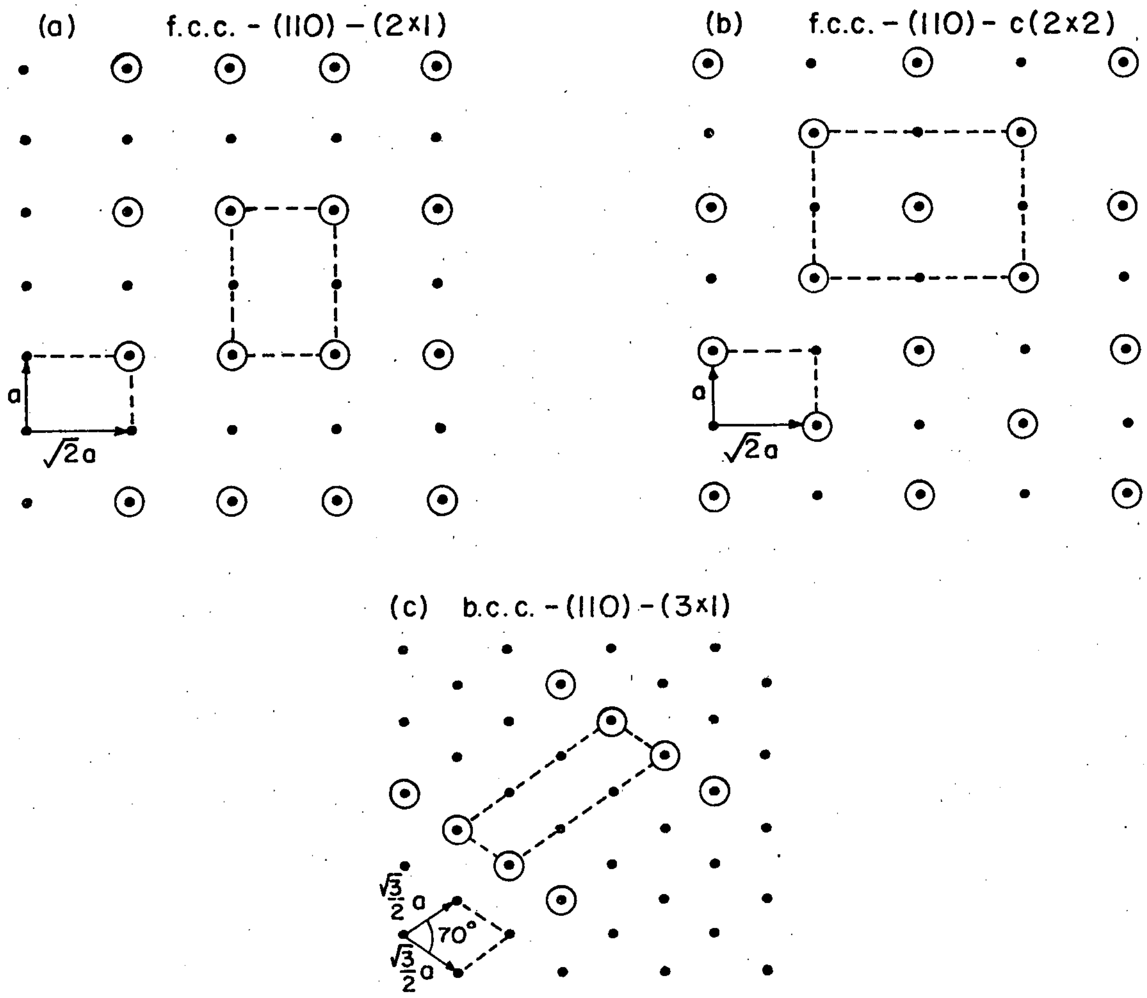

XBL733-5926

Fig. I-7. Schematic diagrams of the most common surface structures appearing on substrates with twofold rotational symmetry.

symmetries. If the surface structure which forms in the presence of an adsorbed gas is characterized by a unit cell which is identical to the primitive unit cell of the substrate, the surface structure is denoted (1×1)(Fig. I-5a). A (2×2) surface structure is formed if the unit cell dimensions of the structure are twice as large as the substrate unit cell vectors. The appearance of a diffraction pattern which is characteristic of this structure often indicates that the adsorbed atoms occupy every second lattice site on the substrate (Figs. I-5b and I-6a). If every third lattice site on a hexagonal face is distinguished from the other sites by selective adsorption, then a ($\sqrt{3} \times \sqrt{3}$) R-30° surface structure may arise (Fig. I-5c). The angle after the (n×n) notation indicates the orientation of the new unit cell relative to the substrate unit cell. If every other lattice site on a square face is unique and occupied by a chemisorbed atom, then a ($\sqrt{2} \times \sqrt{2}$) R-45° surface structure could be formed. To avoid a non-integer notation for this frequently occurring surface structure it is usually labelled as c(2×2), where the c indicates that it is a centered (2×2) structure (Fig. I-6b). Often surface structures will exist that have the dimensions of the substrate unit cell along one translation direction on the surface but a larger dimension along the other direction. These structures are frequently denoted as being (1×n), where the 1 indicates the usual bulk unit cell dimensions or substrate cell dimension along the x direction while the n indicates a dimension n times the substrate unit cell dimension along the y direction (Fig. I-7c where n=3). When both unit cell vectors of the substrate are of the same magnitude (as on the (100) face of the fcc or bcc crystals), then it is possible to have two types of domains coexisting on the surface: one set of the (1×n) and one set of the (n×1) type. In most cases the diffraction pattern arising from a surface which exhibits both (1×n) and (n×1) domains is distinguishable from a diffraction pattern arising from a (n×n) surface structure. For example, a (1×2) surface structure on a substrate with a square unit cell may contain two types of domains rotated relative to one another by 90° and giving rise to $(0,\frac{1}{2})$ and $(\frac{1}{2},0)$ spots in the diffraction (reciprocal lattice) pattern. A true (2×2) structure, however, will give rise to $(\frac{1}{2},\frac{1}{2})$ spots in addition to those which appear for the domain structures. Surface structures of the type (n×m) where $n \neq m$ are frequently formed also, especially on substrates which are characterized by unit cell vectors of unequal magnitude (e.g. fcc (110) or bcc (211) surfaces). If the surface structure is known to be associated with an adsorbed gas or condensate, it is customary to denote the adsorbate material in the description of the surface structure as (n×m)-S, where S is the chemical symbol or formula for the adsorbate.[4,5,6]

The diffraction pattern of a clean vanadium (100) surface-which displays a (1×1) surface structure - is shown in Fig. I-8a. Figure I-8b shows a typical plot of the intensity of the specularly reflected (0,0) beam vs electron energy. The energy locations of the peaks as predicted by kinematical theory are indicated by the arrows in the figure. As may be seen, the positions of the major intensity maxima

Fig. I-8. a) Picture of the (1×1) LEED surface structure pattern obtained from a clean vanadium (100) crystal face.

b) The intensity dependence upon incident beam energy of the (0,0) beam backscattered from a V(100)-(1×1) surface. The incident beam is impinging upon the crystal at an angle of 4° from the surface normal. The arrows indicate the location of the Bragg peaks following correction for the inner potential of the crystal.

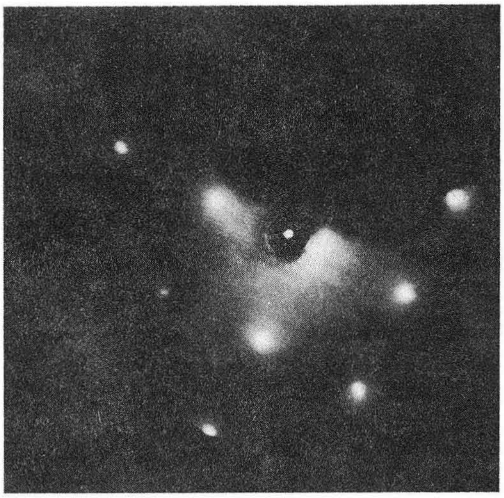

XBB 739-5489

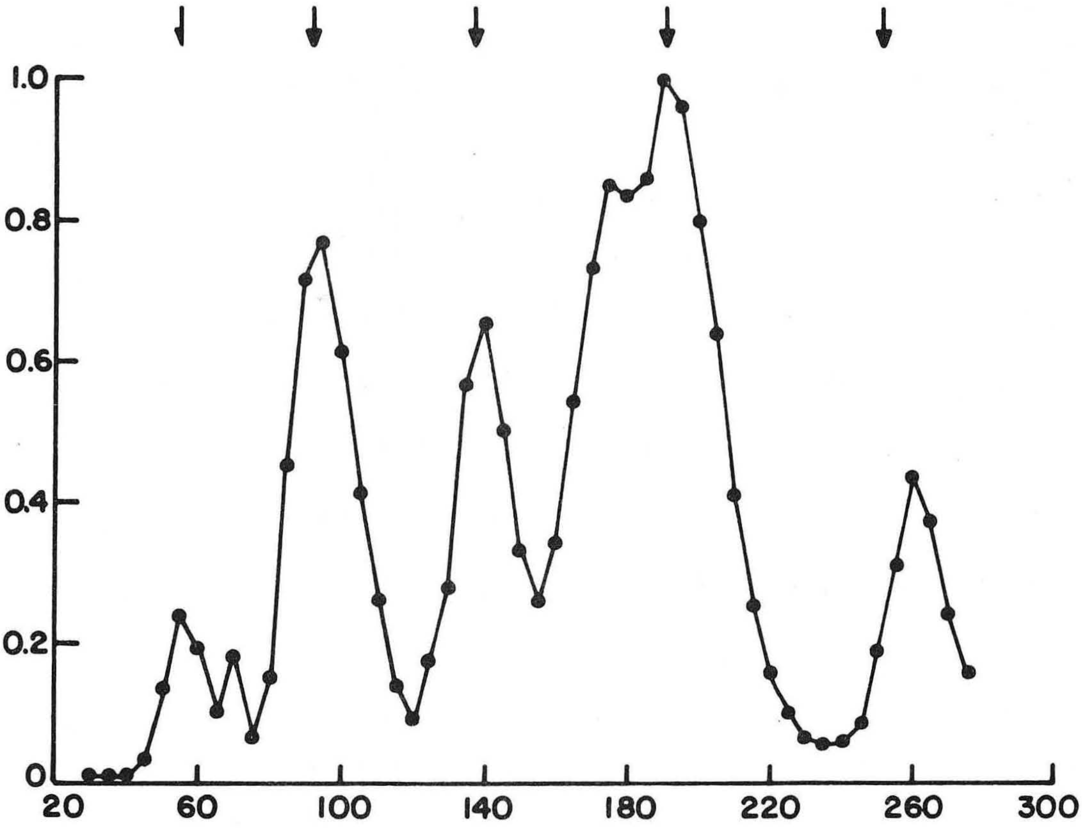

Fig. I-8.

are oftentimes fairly well predicted by this theory (with a correction applied for the inner potentials of the solid:[5] i.e. for the difference in electron energy inside the crystal vs that of the electron in free space), but the a priori prediction of all of the observed peaks and their intensity ratios lie beyond the scope of this type of treatment for the reasons touched upon above.

Finally, a word should be said about the technique of LEED. As performed here, see Fig. I-9, a nearly monoenergetic electron beam of approximately 1 mm diameter is created using an electron gun and strikes the target at normal incidence to the surface. The hemispherical grids A and C are grounded for shielding purposes and a voltage nearly equal to the gun accelerating potential is placed on grid B (which is in reality a double grid) so that only those electrons that have been elastically diffracted will possess enough energy to pass through it. These electrons are then post-accelerated by a positive 5 → 7 keV potential onto a phosphor screen where the diffraction spots may be easily observed or photographed. This display type of apparatus is extremely useful in that it enables the experimenter to continuously monitor the entire diffraction pattern as a function of electron voltage or (sometimes rapidly) changing surface conditions. For the precise measurement of intensities, an arrangement where the grid-screen system is replaced by a Faraday cage is recommended.

Thorough discussions on LEED are available in several review articles[4,5,7] in the literature and the reader is referred to them for more information on the subject.

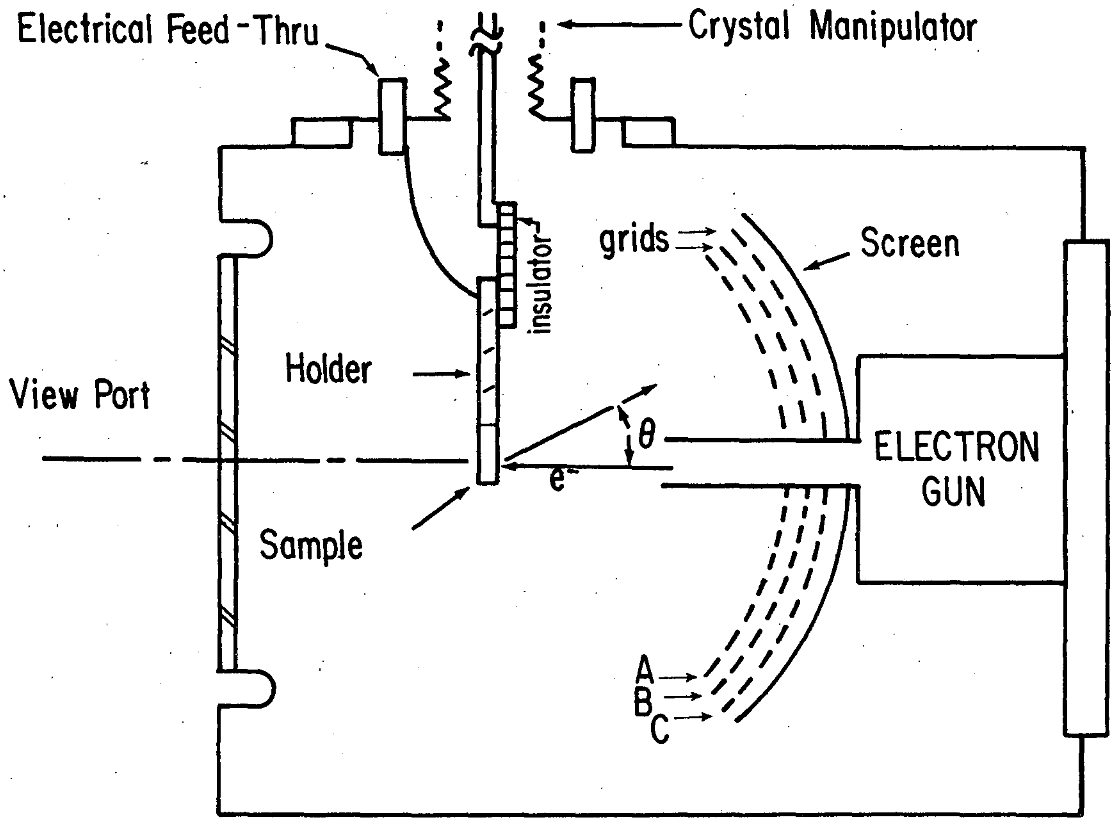

XBL 703-556

Fig. I-9. A Low Energy Electron Diffraction apparatus of the post-acceleration type such as used in this work.

2. Characteristic Loss Spectra

Although the problem of inelastic scattering of electrons from solid materials has been the subject of considerable theoretical and experimental investigations, agreement between the calculated and measured energy loss values is often not achieved. In many cases the question of which type of interaction is producing the observed energy losses has still not been resolved.

The theory that has yielded the most consistent results in the area is that dealing with the excitation of plasmons in the solid. This is probably due to the fact that present day solid-state plasma theories are capable of yielding quantitative results for those metals which can be treated in the "free electron" approximation. The identification of characteristic energy losses for metals such as occur in the transition series, however, is complicated by the contribution of interband transitions to the properties of these metals.

A plasma oscillation is defined as a collective longitudinal excitation of an electron gas. A plasmon is a quantized plasma oscillation. This type of oscillation is perhaps most simply described by considering the uniform displacement of an electron gas in a thin metallic slab, as depicted in Fig. I-10,[8] the gas being moved as a unit relative to the lattice of the positive ion cores of the parent atoms. A displacement of amplitude u produces an electric field of magnitude

$$E = 4\pi neu \tag{I-7}$$

where

n = the free electron density

e = the electronic charge

which acts as a restoring force. The resulting equation of motion of a unit volume of the electron gas is

$$nm \frac{d^2u}{dt^2} = -neE = -4\pi n^2e^2u$$

or

$$\frac{d^2u}{dt^2} + \omega_p^2u = 0 \qquad \text{(I-8)}$$

where

$$\omega_p = \left(\frac{4\pi ne^2}{m}\right)^{1/2}$$

m = the electron mass

This is exactly the equation of motion of a simple harmonic oscillator of frequency ω_p, which is called the plasma frequency. The Characteristic Loss energy is therefore[8,9]

$$\Delta E_p = \hbar\omega_p \qquad \text{(I-9)}$$

This is, of course, a simplified approach to the problem. The more rigorous treatment expresses the inelastic scattering in terms of a complex frequency-dependent dielectric constant and using this approach one can also predict the existence of a surface plasmon loss

Fig. I-10. An illustration of the phenomena surrounding the production of plasmons. In a) is shown a thin slab or film of a metal. A cross section is shown in b), with the positive ion cores indicated by + signs and the electron sea indicated by the gray background. The slab is electrically neutral. In c) the negative charge has been displaced upward uniformly by a small distance $\vec{u}$, shown exaggerated in the figure. As in d), this displacement establishes a surface charge density -neu on the upper surface of the slab and +neu on the lower surface, where n is the electron concentration. An electric field E = 4πneu is produced inside the slab. This field tends to restore the electron sea to its equilibrium position b).

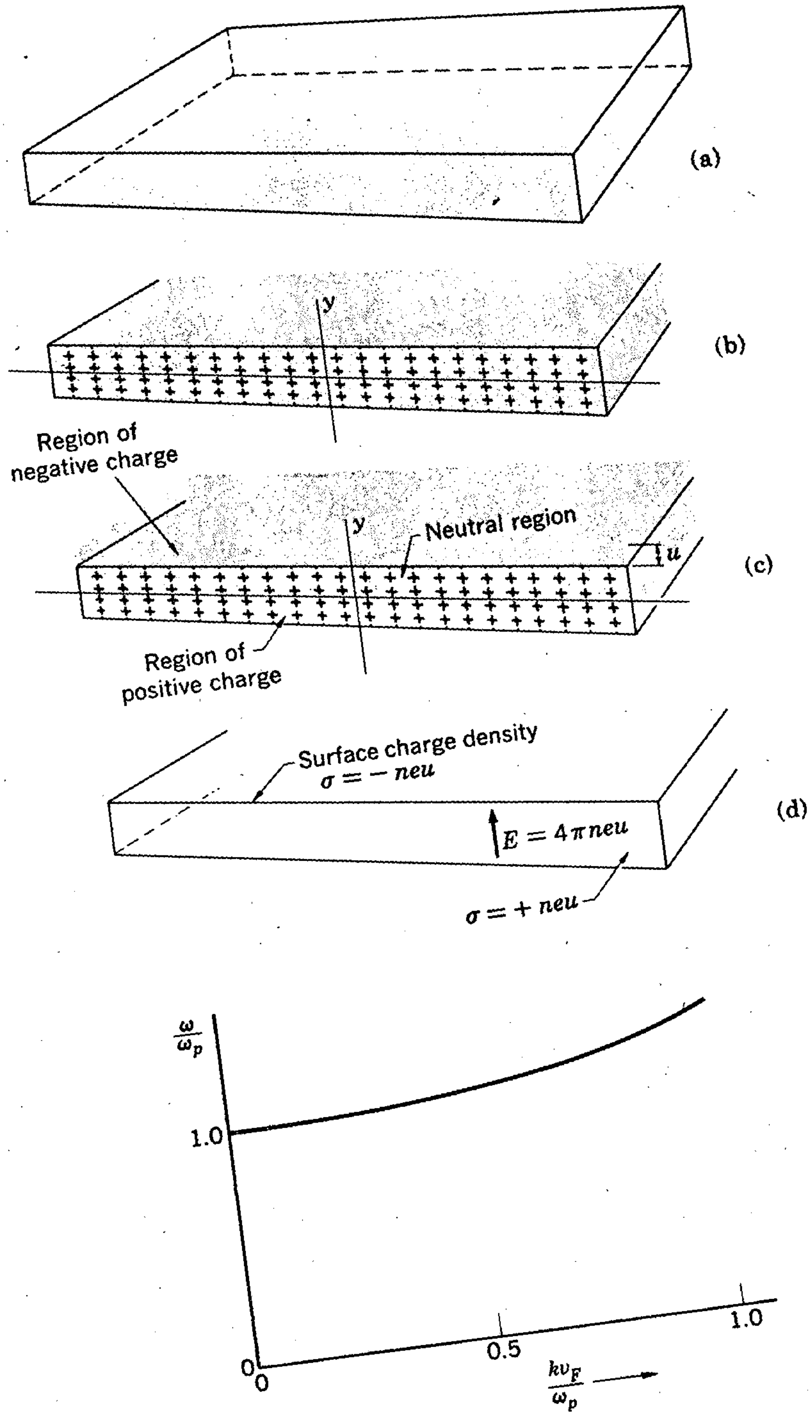

XBL 736-6370

Fig. I-10.

of magnitude[10]

$$\Delta E_s = \hbar\omega_s = \hbar\omega_p/(1+\varepsilon)^{1/2} \qquad \text{(I-10)}$$

where ε is the dielectric constant of the medium boardering upon the target surface. For a clean metal surface bounded by a vacuum $\varepsilon=1$, and Eq. I-10 reduces to[10,11]

$$\Delta E_s = \frac{\hbar\omega_p}{\sqrt{2}} \quad .$$

As electrons travel through the solid, the Coulomb field associated with an electron can couple with the electrostatic field fluctuations of the plasma oscillations. The reflected (or, if a thin film is used, transmitted) electron will show an energy loss equal to integral multiples of the plasmon energy. Electrons which have experienced combination surface-bulk losses have also been observed.

The Characteristic Losses caused by interband transitions are due to the excitation of electrons in bands and levels below the Fermi level to the Fermi level and to higher energy non-occupied levels. The theory of inelastic scattering of electrons in metals has been treated extensively by Viatskin.[12] He assumes a two-body Coulomb interaction between non-relativistic primary electrons and lattice electrons, and the problem was solved in the first Born approximation of perturbation theory using the one-electron weak-coupling approximation for the lattice electrons. The results indicate that two types of transitions occur as the result of the electron-electron interactions.

The first type of transition corresponds to the usual interaction laws for free electrons. These transitions may be both intraband and interband. The second type depends on momentum conservation involving the reciprocal lattice vector and causes the transfer of mean discreet amounts of energy (averaged over the initial states of the lattice electrons):

$$E_n \approx \frac{\hbar^2(d^*)^2}{2m^*} \qquad \text{(I-11)}$$

where

d^* = a reciprocal lattice vector

m^* = the effective mass of the lattice electron

and, for a cubic lattice

$$E_n = \frac{150}{d^2}\ n^2 \text{ (eV)}$$

where

$n^2 = n_1{}^2 + n_2{}^2 + n_3{}^2$ = an integer denoting the degree of the transition

d = the lattice constant in Angstroms

m^* = the mass of the electron (assumed).

These transitions have been shown to always be interband in nature.

In many cases the observed energy loss can be identified with either a plasmon or an interband transition by using the following criteria:

a. The magnitude of the energy loss.

b. The intensity dependence of the peak on the incident electron energy and the angle of incidence. For example, a surface plasmon peak will decrease in intensity relative to a bulk plasmon peak as the incident electron energy (and, therefore, penetration depth) is increased and as the angle of incidence approaches the surface normal.

c. The intensity dependence of the peak with respect to surface coverage by a foreign gas. A bulk plasmon or interband transition peak should be unaffected by adsorbed molecules relative to a surface plasmon peak.

d. The energy loss dependence upon a change in phase of the system. For example, a normal interband transition should be relatively unaffected by melting.

e. The angular dependence of the loss peaks.

f. The determination if photon radiation of the correct wavelength can be observed from the decay of plasmons.

From the preceeding discussion, it is obvious that the Characteristic Loss spectrum contains some qualitative and quantitative information about the constituents of a surface layer in its interband transition peaks. In addition, information concerning the chemical binding state of these elements might be obtained by observing the position of the high-energy edge of the interband transition peaks and/or the peak energy of the plasmon losses. In addition to determinations of which type of process gives rise to particular peaks, most of the work done in this area has been of the latter type in which, due to the exactness of the plasma theory, the "freeness" of the conduction electrons is deduced by comparing the experimental results with those predicted by theory. However, since most of these Characteristic Loss peaks occur within an energy band of approximately fifty electron volts and often overlap to a considerable extent, the field has been largely passed by for surface science work in favor of techniques which yield more readily useful data.

As one might surmise, one of the techniques of measuring Characteristic Loss spectra is very similar to that described previously for LEED. The only changes that need be done to the retarding field system shown in Fig. I-9 in order to measure the loss peaks in reflected electrons would be to substitute a current measuring device for the high voltage placed on the fluorescent screen and to modify the voltage source servicing the retarding grids so that their voltage may be varied independently of the electron beam accelerating voltage. As the retarding grid voltage is thus varied, the screen current at each voltage may then be measured and the resulting spectrum will show a "titration curve" type response each time a peak is encountered. Differentiation of this spectrum will yield the energy distribution peaks that are desired. This general technique is discussed in detail in the experimental section below since it is, in essence, that used to obtain Auger electron spectra. An alternative method would be to obtain the electron energy distribution directly by using a velocity analyzer (such as a 127° sector, hemispherical, or cylindrical mirror device) for a detector, this being the technique used most often when high energy transmission-type experiments are performed on thin films.

3. The Secondary Electron Cascade Effect

As mentioned previously, the true secondary electron energy distribution is dominated by a large, broad peak occurring at a low absolute energy, various subsidiary maxima being superimposed on the high energy side of it. This low energy peak was attributed to the multiple scattering of excited crystal electrons to successively lower energies resulting in a piling-up of electrons at low energies.[13]

To date most of the work done in this area of secondary electron emission has concentrated on the problem of the production of the internal secondary electrons by the interaction of the primary beam with the bound-state electrons. Since the energy distribution of the low energy peak is observed to be independent of the primary beam energy, it appears that the cascade process almost completely determines the peak shape and that the method of production of the internal secondaries is relatively unimportant. In order to solve the internal cascade problem, it is necessary to consider the elementary interactions by which electrons can lose energy within the solid. The major processes are electron-electron collisions and plasmon creation. In order to carry out a more rigorous treatment, the effect of the Auger electron distribution and amplitude, the crystal field, and electron-phonon interactions should be included. Of course the work function and the existence of surface states will also affect the observed distribution.

As the reader has no doubt perceived, the problem faced here is one of considerable magnitude and no further attempt will be made to discuss it here. Rather suffice it to say that attempts of varying degrees of sophistication have been employed to deal with the question and the interested reader is referred to the literature[14,15,16,17] for more information on the subject.

4. The Auger Effect

As mentioned above, one class of true secondary electrons is produced by the interaction of a primary electron with a bound electron within the crystal. This process obviously creates an excited-state atom which is ionized in one of its inner levels. The electron vacancy thus formed is filled by a de-excitation process in which an electron from a higher energy state falls into the vacancy, the process continuing until an electron from the conduction band is the one involved in the de-excitation. The energy released in each of these electronic transitions can be dissipated in one of two ways, depending on the magnitude of the de-excitation energy. One way is through the creation of a photon of the appropriate wavelength, the process then being known as X-ray fluorescence. The alternative method is for the de-excitation electron to transfer the energy to another electron through Coulombic interaction. If this second electron possesses a binding energy that is less than the de-excitation energy transferred to it, it will be ejected from the atom, leaving behind a now doubly-ionized species. The electron emitted as the result of this process is called an Auger electron in honor of Pierre Auger who first saw their tracks in a Wilson Cloud Chamber in 1925 and correctly explained their origin.[18]

It is obvious from the preceeding discussion that the energy of an Auger electron is primarily a function of the bound-state energy levels existing in the atom, and therefore contains qualitative analysis information about the atom from which it originated.

When atoms are brought together to form a solid, the atomic energy levels broaden into effectively continuous bands. In Fig. I-11, the Auger mechanism of de-excitation is illustrated upon a schematic diagram of the electronic band structure of a typical metallic solid of atomic number Z. The shaded areas represent the filled portions of the bands, three of which have been designated by the generalized notation W_o, X_p, and Y_q with the respective mean energies $-\bar{E}_{W_o}(Z)$, $-\bar{E}_{X_p}(Z)$, and $-\bar{E}_{Y_q}(Z)$ relative to the chosen zero of energy: the Fermi level. Θ_c is the work function of the crystal. In drawing the schematic diagram it is assumed that a single electron vacancy has already been produced in the W_o band. If an electron from the X_p band fills that vacancy, energy of the magnitude $\Delta\bar{E}_{X_p,W_o}(Z) = \{[-\bar{E}_{X_p}(Z)]-[-\bar{E}_{W_o}(Z)]\} = [\bar{E}_{W_o}(Z)-\bar{E}_{X_p}(Z)]$ is released. If this energy is transferred to an electron in the Y_q band, this electron must lose the energy $\Delta\bar{E}_{\Theta_c,Y_q}(Z') = \{\Theta_c-[-\bar{E}_{Y_q}(Z')]\} = [\bar{E}_{Y_q}(Z') + \Theta_c]$ in order to escape from the crystal; i.e. the Y_q band electron will be ejected from the atom provided that $[\bar{E}_{W_o}(Z)-\bar{E}_{X_p}(Z)] > [\bar{E}_{Y_q}(Z') + \Theta_c]$. Thus, the binding energy (relative to the vacuum level) of the electron in the Y_q energy band must be smaller than the energy transferred to it during the de-excitation process if Auger electron emission is to occur. The emitted electron appears outside the crystal with the energy

$$\bar{E}_{W_oX_pY_q}(Z) = \bar{E}_{W_o}(Z) - \bar{E}_{X_p}(Z) - \bar{E}_{Y_q}(Z') - \Theta_c \qquad \text{(I-12)}$$

relative to the crystal Fermi energy. The term $\bar{E}_{Y_q}(Z')$ has been substituted for $\bar{E}_{Y_q}(Z)$ because the latter refers to the energy level of the singly ionized atom and as the Auger electron is ejected we are simultaneously creating a doubly ionized atom. It is therefore obvious that as the Auger process occurs the diagram of Fig. I-11 becomes, strictly speaking, invalid since the energy band levels will rearrange to their most stable state under the new electrostatic conditions. It has been postulated that $\bar{E}_{Y_q}(Z')$ should be the ionization energy of an electron from the Y_q band of the Z^+ ion and so $\bar{E}_{Y_q}(Z') = \bar{E}_{Y_q}(Z+1)$. If we rewrite Eq. I-12 as

$$\bar{E}_{W_oX_pY_q}(Z) = \bar{E}_{W_o}(Z)-\bar{E}_{X_p}(Z)-\bar{E}_{Y_q}(Z+\delta)-\Theta_c \qquad \text{(I-12a)}$$

where δ is some incremental charge, in most cases the observed Auger energies have been intermediate between those calculated using Eq. (I-12a) with $\delta=0.50$ and $\delta=0.75$.[19] It perhaps seems more reasonable to use Slater's rules to determine the effective screening constant

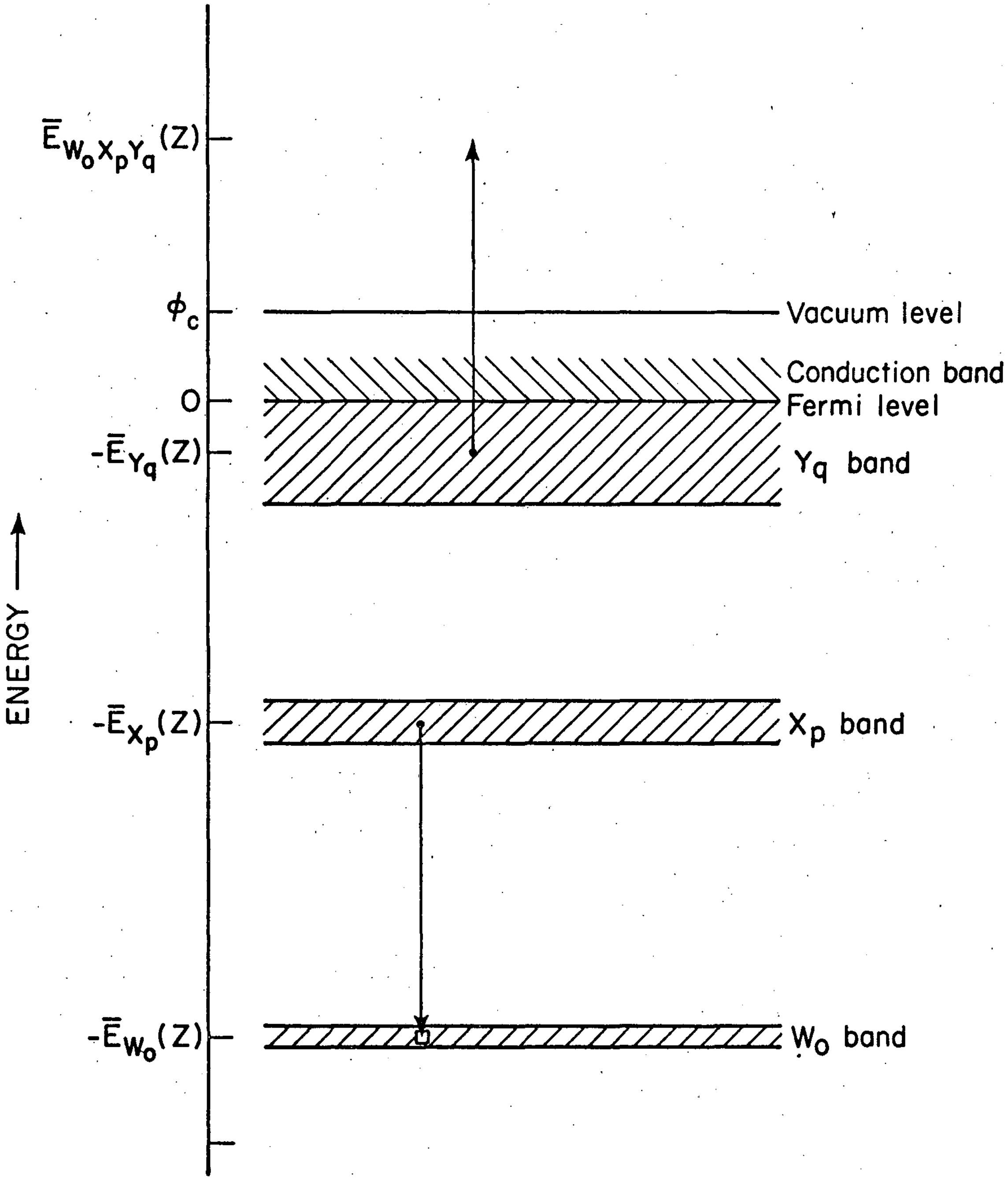

XBL 7012-7160

Fig. I-11. A schematic representation of the Auger electron emission process from a metallic solid containing an initial electron vacancy in the W_o energy band, an X_p band electron undergoing de-excitation to fill the vacancy, and a Y_q band electron being ejected from the sample.

on the Y_q electron by the X_p electron and, in this case, Eq. (I-12) becomes[20]

$$\bar{E}_{W_o X_p Y_q}(Z) = \bar{E}_{W_o}(Z)-\bar{E}_{X_p}(Z)-\{\bar{E}_{Y_q}(Z) + S[E_{Y_q}(Z+1)-\bar{E}_{Y_q}(Z)]\}-\Theta_c \qquad \text{(I-12b)}$$

where

S = Slater's formulae constant for the energy levels involved.

At any rate, the emitted Auger electron has the kinetic energy $\bar{E}_{W_o X_p Y_q}(Z)$ and is associated with what is commonly labelled as a $W_o X_p Y_q$ Auger process. Because they are energetically feasible only in parts of the periodic table, Auger transitions which result in a final vacancy in the same major shell as the initial vacancy (e.g. a $L_1 L_3 M_2$ transition) are referred to as Coster-Kronig transitions.

It is of interest to note here, and it will become quite important later on, that the Auger energy given by Eq. (I-12) is <u>not</u> the electron energy measured by the analyzer. As an electron traverses the region between the crystal and the analyzer it experiences a slight acceleration or deceleration, as shown in Fig. I-12,[21] due to the difference in work functions of the analyzer and crystal. This difference is known as the contact potential, Θ_{CP}, and its magnitude is $\Theta_{CP} = \Theta_A - \Theta_C$, where Θ_A is the analyzer work function. Equation (I-12) becomes,

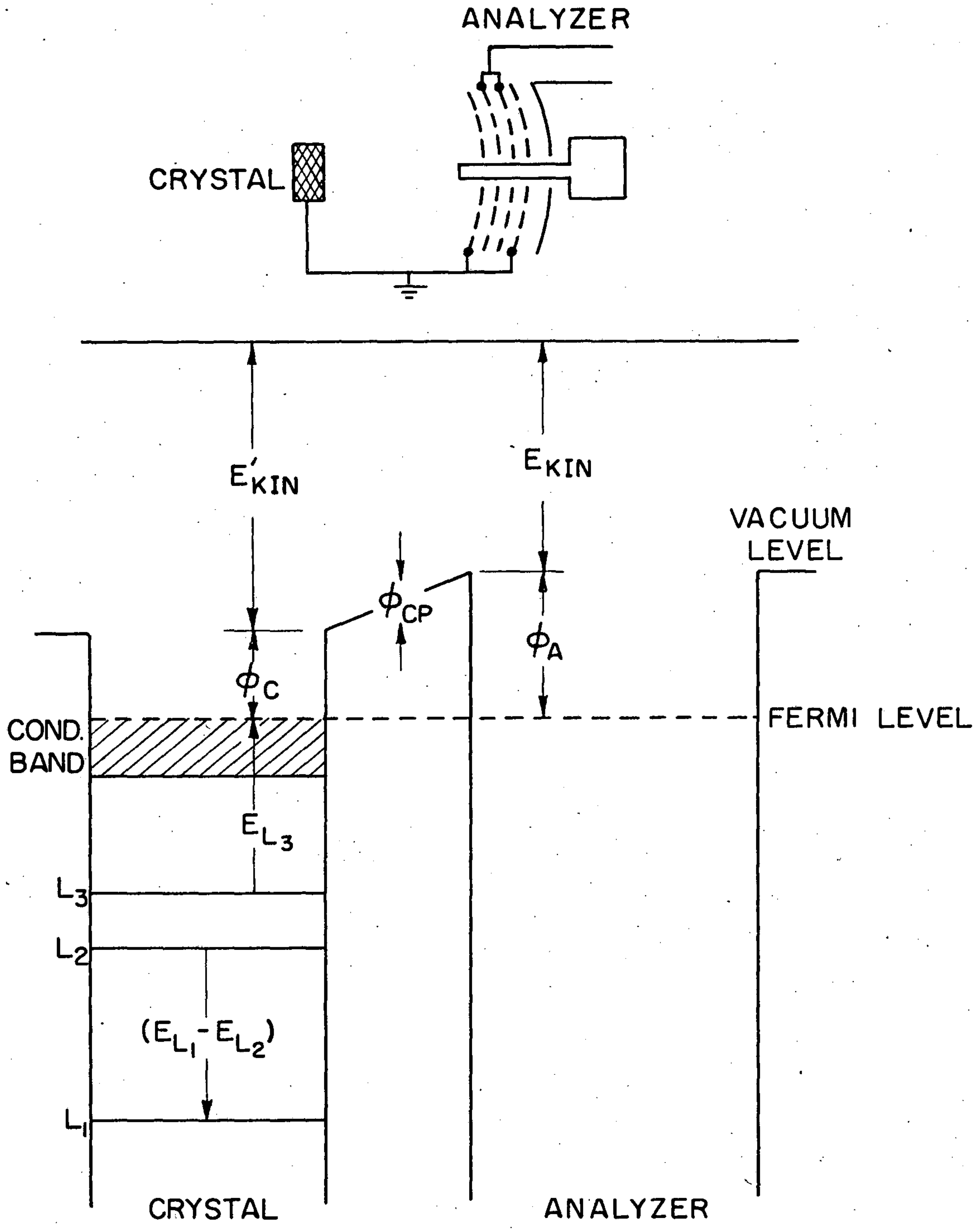

XBL 733-5928

Fig. I-12. Schematic diagram illustrating the modification of the kinetic energy of an emitted Auger electron by the sample crystal-analyzer contact potential, ϕ_{CP}.

therefore,

$$\bar{E}_{W_oX_pY_q}(Z) = \bar{E}_{W_o}(Z)-\bar{E}_{X_p}(Z)-\bar{E}_{Y_q}(Z')-\Theta_C-\Theta_{CP}$$

$$= \bar{E}_{W_o}(Z)-\bar{E}_{X_p}(Z)-\bar{E}_{Y_q}(Z')-\Theta_A \qquad \text{(I-13)}$$

In the retarding field device employed in LEED, Θ_A is the work function of the grid material.

The $W_oX_pY_q$ nomenclature that has developed is, of course, that which is commonly associated with the X-ray spectroscopic notation which is reviewed in Appendix I. As pointed out there, this notation is based on the j-j coupling scheme and is therefore valid only for atoms of high atomic number. For low atomic number elements it is the Russell-Saunders coupling scheme which is valid (Appendix I), and in the atomic number range of approximately 25 to 75 neither scheme adequately describes the atom and it is necessary to combine them into an intermediate coupling description.[22] Due to the availability of the atomic energy levels from atomic spectroscopy studies, the observed Auger transitions are usually associated with a $W_oX_pY_q$ transition regardless of the atomic number of the element involved. Although this notation is beneficial in that the Auger ejection process can be visualized in terms of the atomic X-ray levels, viewed in the light of the preceeding discussion it is misleading for the intermediate and low atomic number elements. Moreover, a description in the $W_oX_pY_q$ nomenclature does not predict the correct number of transitions.

B. Auger Electron Spectroscopy

1. Peak Energy Analysis[22]

If the simplest case is considered, i.e. the KLL transition series, the $W_oX_pY_q$ nomenclature suggests that there should be six transitions: KL_1L_1, KL_1L_2, KL_1L_3, KL_2L_2, KL_2L_3, and KL_3L_3 (since transitions involving the same two L subshells in a different order, e.g. KL_1L_2 and KL_2L_1, must be considered identical as required by energy conservation). In reality, the actual number of radiationless transitions observed from an initial K state to a final two vacancy L state is not six but nine. The fact that we assign definite values of o,p, and q means that a good quantum number is ascribed to the total angular momentum of the individual electrons in the various subshells, which is appropriate only in the j-j coupling scheme. A complete description of the Auger process can only be given in the total number of final states which result from having two electron vacancies. For the KLL case, an atom in this final state may have one of the following electron configurations in the L shell: $2s^2 2p^4$, $2s^1 2p^5$, or $2s^0 2p^6$. The qualitative splitting effects leading to the evolution of the final Auger states are schematically drawn in Fig. I-13a→d as the following (progressively restrictive) assumptions are made:

a. If the electrons move in a 1/r potential, the screening and exchange interactions are negligible, and there is no spin-orbit interaction, the three electron configurations are completely degenerate in energy.

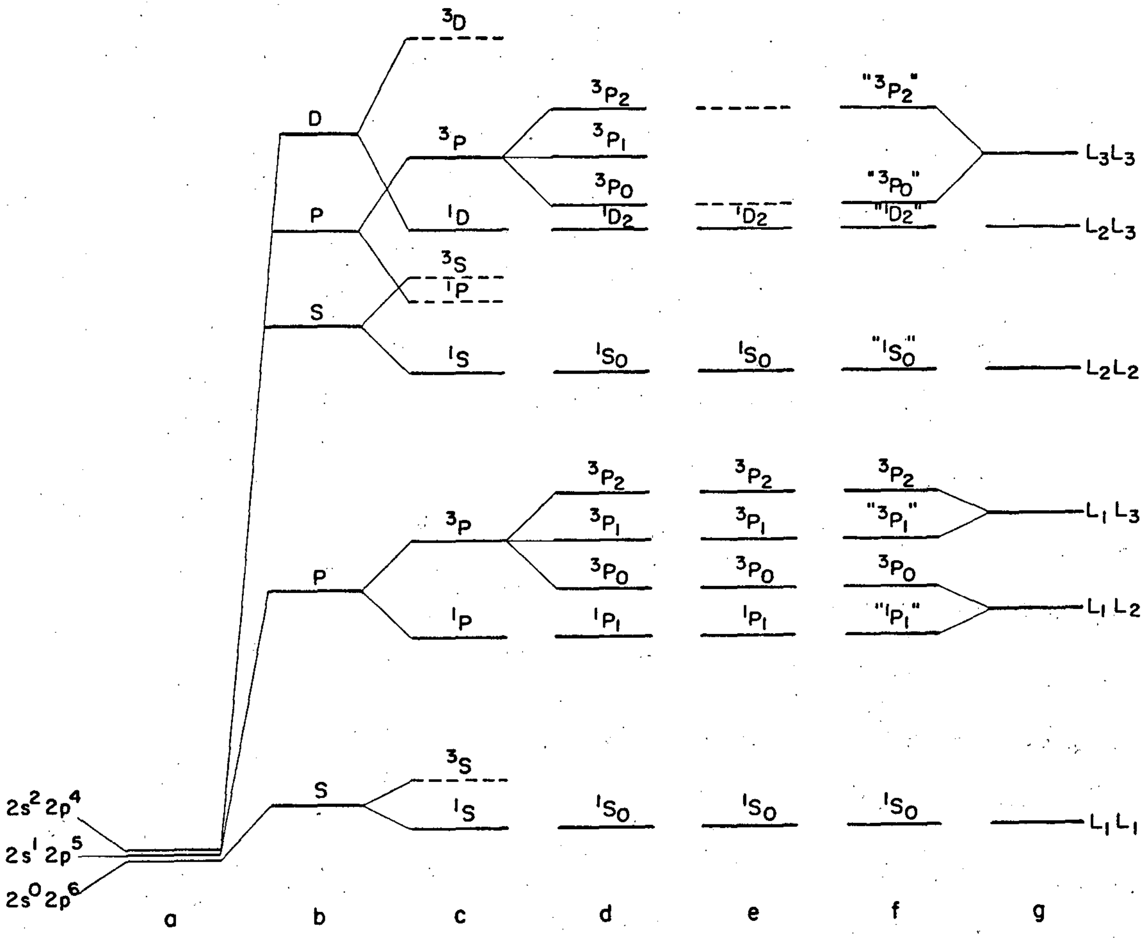

XBL733-5929

Fig. I-13. Final state of Auger transitions in the KLL group under various assumptions for the electron interaction and the type of coupling. (Level positions not to scale)

a) No election interaction, central potential of 1/r shape, completely degenerated energies.
b) Screening and Coulomb interaction between electrons generates levels of different orbital angular momentum.
c) Exchange interaction causes a splitting in singlet and triplet terms. Those excluded by the Pauli principle are indicate by broken lines.
d) Spin-orbit interaction decomposes terms into individuals levels of definite angular momentum.
e) Allowed final states (conservation of angular momentum and parity), pure LS-coupling.
f) Allowed final states, intermediate coupling, no configuration interaction. Quotation marks indicate that the states are mixed.
g) Allowed final states, pure jj-coupling.

b. If screening and Coulombic interaction among the electrons is allowed, the degeneracy is annihilated and the resulting levels possess different angular momenta.

c. Exchange interaction causes a splitting into triplet and singlet states, with some of them being forbidden by the Pauli Principle (indicated by broken lines in the figure).

d. The introduction of spin-orbit coupling causes splitting of the triplet terms as states of definite total angular momenta are produced.

In order to determine which energy levels are allowed as final states for an Auger transition, it is necessary to include consideration of the laws of conservation of angular momentum and parity. For example, a transition from the initial $^2S_{1/2}$ state of the system (i.e. from the $1s^1$ configuration) to any of the ^3P states of the $2s^22p^4$ configuration violates the law of conservation of parity and is therefore disallowed. Assuming pure L-S coupling, this reduces the number of final states to seven (Fig. I-13e). For very low atomic number elements the spin-orbit interaction is negligible and the number of allowed states is five. If, however, an intermediate coupling situation is assumed, this allows the final state eigenfunction ψ of the system to be written down as linear combinations of the Russell-Saunders eigenfunctions ψ_o which possess the same total angular momentum. The $^3P_0$ and $^3P_2$ states of the $2s^22p^4$ configuration will then be allowed since their eigenfunctions will have contributions from the allowed $^1S_0$ and $^1D_2$ states respectively and parity can therefore be conserved in transitions to these mixed states. (If configuration interaction is allowed, the $^3P_1$ term of the $2s^22p^4$ configuration will receive contributions from the $^3P_1$ and $^1P_1$ eigenfunctions of the $2s^12p^5$ configuration and a ten line KLL spectrum should be observed. Since only nine lines have been thus far experimentally measured, this effect is ignored here.) The spin-orbit interaction dominates for the heavy elements, these two electronic motions coupling together to form a total angular momentum $\vec{j}$ for each electron which now will exist in a definite $\vec{\ell},\vec{j}$ state as outlined in Appendix I. A two-electron state is described by the $\vec{\ell},\vec{j}$ values of both electrons, the j-j coupling scheme therefore predicting six final states for the KLL Auger transition series: L_1L_1, L_1L_2, L_1L_3, L_2L_2, L_2L_3, and L_3L_3. These states are shown in Fig. I-13g along with the manner in which they approach the L-S coupling states.

A more graphic presentation of this relationship is shown in Fig. I-14 where the relative energies of the experimentally observed KLL transitions (normalized to the KL_1L_1-KL_1L_3 energy interval) are plotted as a function of atomic number.[21] It is obvious that the j-j coupling notation is becoming inadequate around an atomic number of eighty, although its use in the intermediate coupling region may be justified in the cases where the finer details of the Auger spectrum can not be observed due to insufficient resolution of the analyzer or low intensity of some of the transitions. In the final analysis, however, the transitions can only be uniquely specified by using a notation in which the j-j and L-S coupling limits to which each transition tends are specified. The KLL transitions would then be

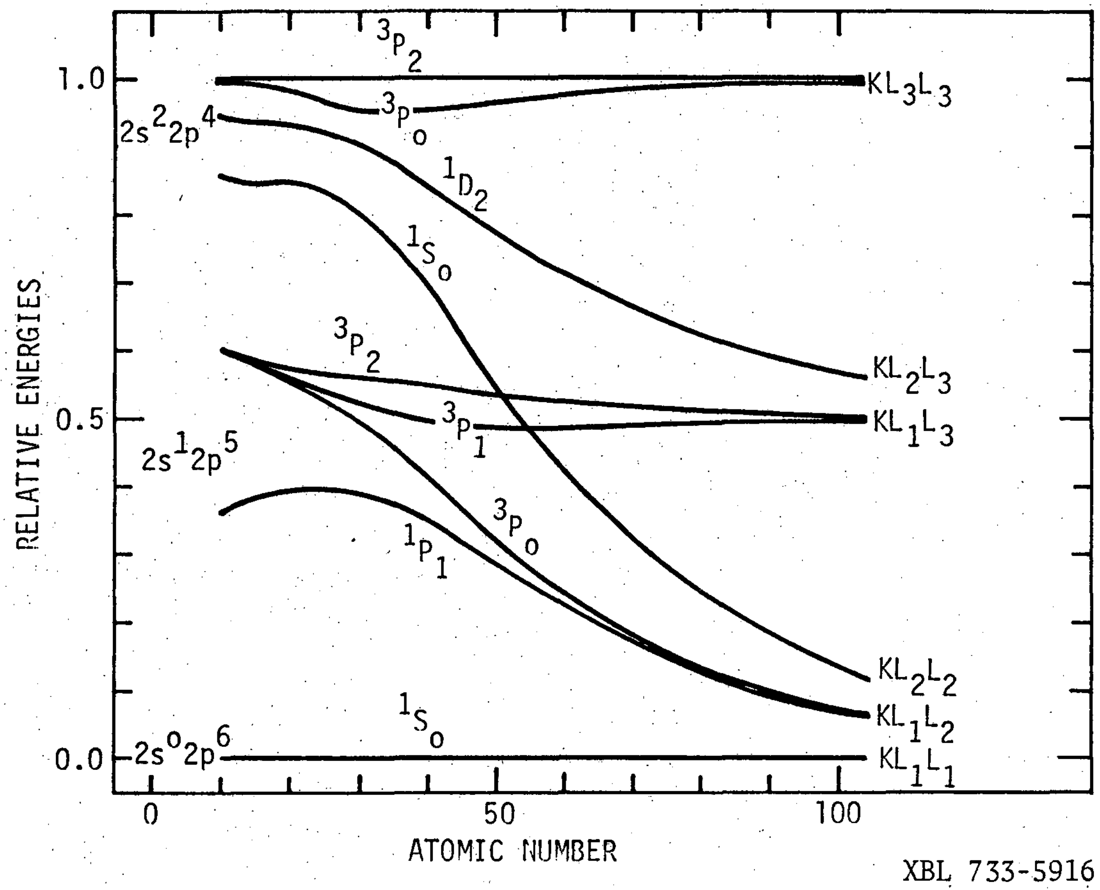

Fig. I-14. RElative line positions in the KLL Auger transition group as a function of atomic number Z. The energy difference between the lines of highest and lowest energy ranges from 55 eV at Z = 10 to 17 keV at Z = 104.

labelled as follows: $KL_1L_1(^1S_0)$, $KL_1L_2(^1P_1)$, $KL_1L_2(^3P_0)$, $KL_1L_3(^3P_1)$, $KL_1L_3(^3P_2)$, $KL_2L_2(^1S_0)$, $KL_2L_3(^1D_2)$, $KL_3L_3(^3P_0)$, and $KL_3L_3(^3P_2)$.

It must be emphasized, however, that at the present state of development of Auger spectroscopy the assignment of a $W_oX_pY_q$ process to an observed transition is tentative since it is primarily based on the agreement obtained when compared with calculated Auger transition energies. The preferred and unambiguous treatment (as alluded to above) of calculating the energy differences between the possible doubly-ionized and singly-ionized states by quantum mechanical means and comparing these values with the experimentally observed energy is difficult, if not generally impossible, at this time. As the result, researchers in the field have relied on the approximations presented above (Eqs. I-12,a,b). The assignment of an experimentally obtained peak to a particular Auger transition can nevertheless be oftentimes substantiated by applying additional experimental tests. These are:[23]

a. Varying the incident electron energy, E_p, across the threshold for ionization of the W_o subshell, $\bar{E}_{W_o}(Z)$. The appearance of Auger transitions that appear at $E_p > \bar{E}_{W_o}(Z)$ strongly suggests that the W_o subshell participates in the Auger transition. The measured Auger electron energy also assists in identifying W_o since it is necessary that $\bar{E}_{W_oX_pY_q}(Z) < \bar{E}_{W_o}(Z)$.

b. The Auger peak shape and intensity for a given transition may be expected to remain fairly constant for neighboring elements in a given row of the periodic table. Therefore, transitions should be assigned to reflect the smooth variation of energy in the atomic energy levels.

c. The peak shape and intensity could be expected to significantly change with changes in the chemical state if one or more valence band electrons are involved in the transition. Therefore marked changes in an Auger peak upon, for example, chemisorption of a gas suggests valence electron participation in the transition giving rise to that peak.

2. Intensity Analysis

The accurate calculation of the peak intensity to be expected from an Auger transition turns out to be at least as difficult as determining what its energy should be. Concisely stated, the problem reduces to the question of determining the probability of producing a particular subshell vacancy through the influence of the incident beam, what the probability of filling that vacancy by the Auger process of interest is, and what is the probability of that Auger electron escaping from the solid and being detected. These problems will be discussed separately in the following sections and then merged to provide an estimate of the magnitude of the Auger yield to be expected.

a. Ionization probability

As one may easily imagine, the distribution of primary vacancies is a function of the nature of the atomic excitation process, the ideal method being one which produces vacancies in a single atomic subshell. The techniques that have been employed to produce inner shell vacancies include orbital electron capture by the nucleus and the internal conversion of electrons in radioactive atoms, photoionization by an X-ray or low energy gamma-ray beam, and excitation by charged particle (electron or proton) impact.

Since electron impact excitation was used in this investigation, this discussion will be limited to that method of ionization. In the range of intermediate beam energies (1-10 keV) such as used here, little work has been done on the determination of the energy dependence of the ionization cross-section for a given atomic energy level. Most of the theoretical work has used variations of the Bethe expression[24]

$$Q_{W_o} = \frac{2\pi e^4}{E_p E_{W_o}} \, b \, \ell n(4E_p/B)$$

where

Q_{W_o} = the cross-section for ionization of the W_o subshell
e = the electronic charge
E_p = the primary electron beam energy
E_{W_o} = the binding energy of the W_o subshell
b,B = empirical constants

which is valid for higher energy collisions. However, the most accurate values for these cross-sections seem to be based on the classical calculations done by Gryzinski[25] for inelastic atomic collisions. These computations were based on the relations for binary collisions (i.e. the independent pair interactions of the individual elements of the colliding systems) as well as for the Coulomb collisions derived in the laboratory system of coordinates. For the process of single ionization by electron impact, Gryzinski's equation for the ionization cross-section assumes the simple form

$$Q_{W_o} = \left[\frac{\sigma_0}{(E_{W_o})^2}\right] g_{W_o}(U) \qquad \text{(I-14)}$$

$$g_{W_o}(U) = \frac{1}{U}\left(\frac{U-1}{U+1}\right)^{3/2} \{1 + \frac{2}{3}(1-\frac{1}{2U})\ \ell n[2.7+(U-1)^{1/2}]\}$$

where

$\sigma_0 = \pi e^4 Z_p{}^2 = 6.5\times10^{-14}\ Z_p{}^2\ (\mathrm{eV}^2\mathrm{cm}^2)$

Z_p = the charge of the bombarding particle in units of the elementary charge

$U = E_p/E_{W_o}$

A graph of the ionization function $g_{W_o}(U)$ plotted against U is shown in Fig. I-15. From this graph it is obvious that the energy of the primary beam should be adjusted to a value between three and five times that of the binding energy of the W_o subshell if one wishes to maximize the ionization rate of that subshell. Using this theoretical approach, if it is desired to calculate the total ionization cross-section Q for an atom it is merely necessary to sum over the contributions from each of the subshells:

$$Q = \sum_{W_o} n_{W_o} Q_{W_o} \qquad \text{(I-15)}$$

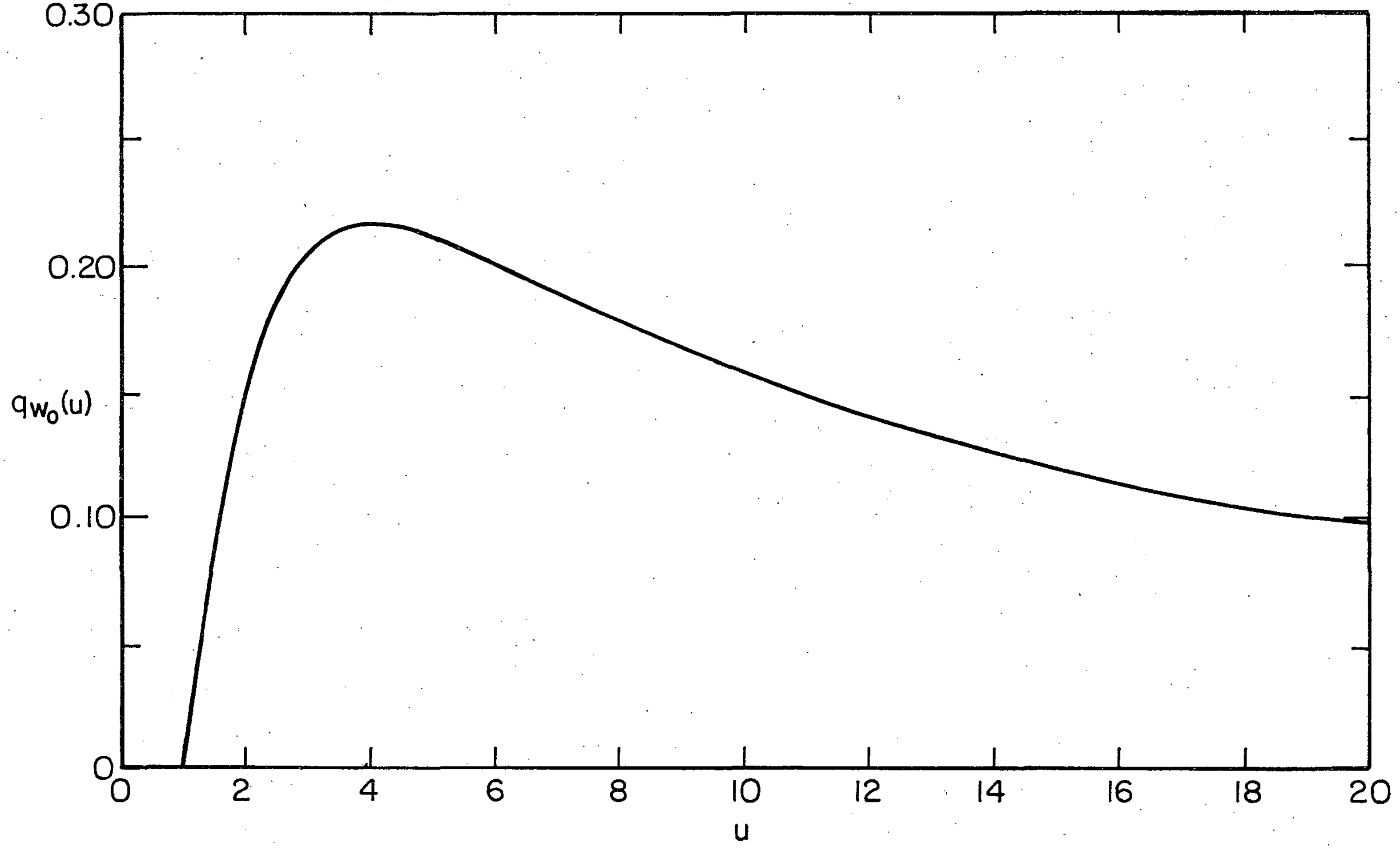

XBL 733-5930

Fig. I-15. The variation with U of the ionization function $g_{W_o}(U)$ for the W_o subshell when ionization is caused by electron impact.

where n_{W_o} is the number of electrons in the W_o subshell.

Since there exist scattered electrons with energies between E_{W_o} and E_p travelling through the crystal, an additional contribution to the total W_o subshell ionization will ensue from this source. Of course it will be desirable to estimate the number of W_o vacancies produced by this electron distribution and include it in our intensity calculations. To this end, the average value of the Gryzinski ionization function for these electrons was calculated using the formula

$$\bar{g}_{W_o}(U) = \frac{\int_1^U g_{W_o}(U)\, dU}{U-1}$$

and $\bar{g}_{W_o}(U)$ is plotted vs U in Fig. I-16.

b. Transition probability[26]

The rate of a particular Auger process is determined by the energy transfer probability between electrons in the various energy levels. As mentioned previously, the interaction between the electrons that participate in the Auger process is essentially electrostatic in nature and theoretical Auger transition probability calculations therefore require the evaluation of transition matrix elements of the form[27]

$$D = \iint \psi_f^*(r_1)\, \psi_f(r_2)\, \frac{e^2}{|r_1 - r_2|}\, \psi_i(r_1)\, \psi_i(r_2)\, dr_1\, dr_2 \qquad \text{(I-16)}$$

where $\psi_i(r_1)$ and $\psi_f(r_1)$ are the initial and final state wave functions respectively of one electron, $\psi_i(r_2)$ and $\psi_f(r_2)$ are the equivalent

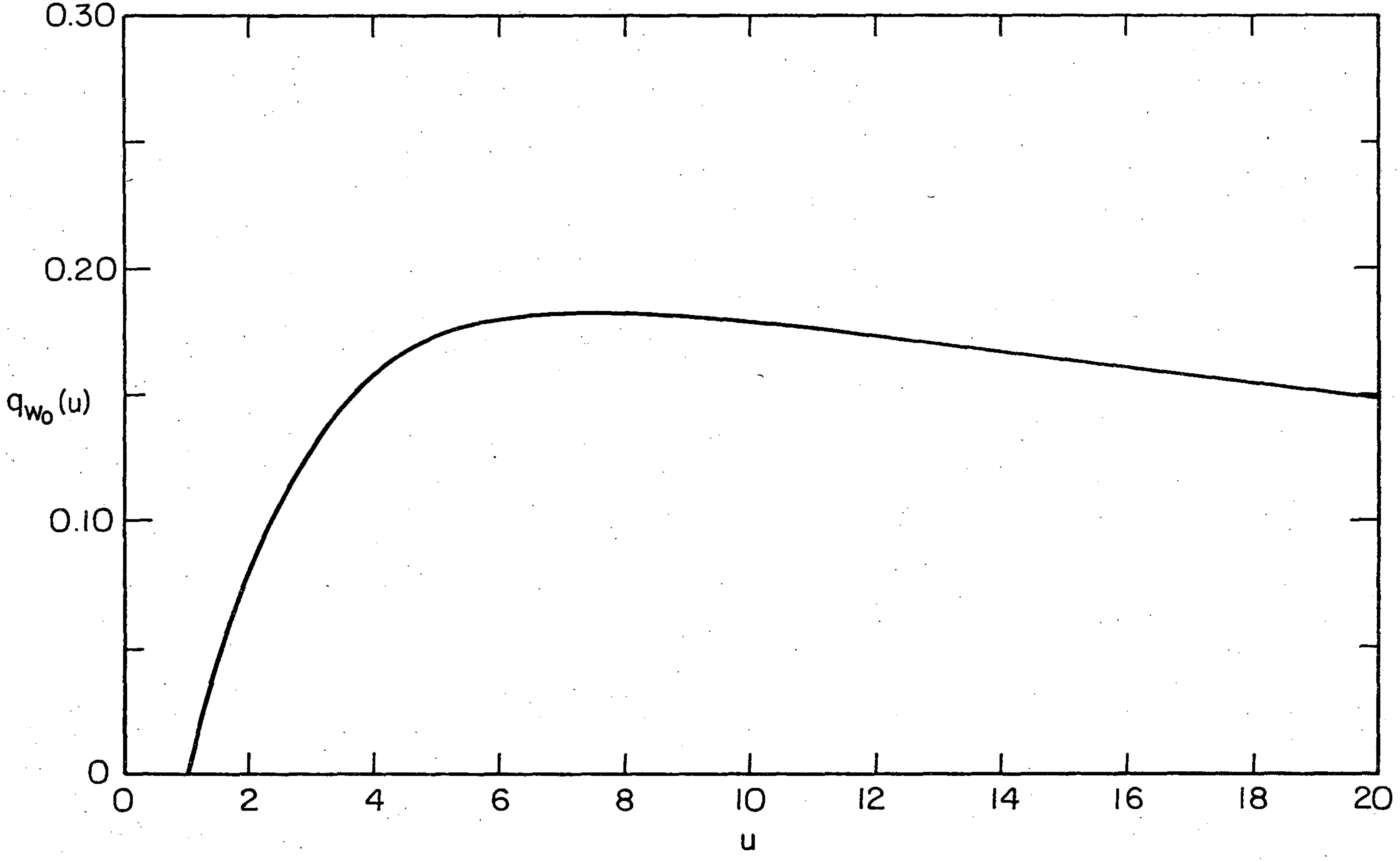

XBL 733-5931

Fig. I-16. The variation with U of the averaged ionization function $\bar{g}_{W_o}(U)$ for the W_o subshell when ionization is caused by electron impact.

wave functions of the second electron, and r_1 and r_2 are the respective spacial co-ordinates of the two electrons. $\psi_f^*(r_2)$ is, of course, a continuum wave function whereas the others are bound-state wave functions. The exchange matrix elements are therefore

$$E = \iint \psi_f^*(r_2)\ \psi_f(r_1)\ \frac{e^2}{|r_1-r_2|}\ \psi_i(r_1)\ \psi_i(r_2)\ dr_1\ dr_2 \tag{I-17}$$

and the transition probability per unit time may be shown to be

$$w_{fi} = (\hbar)^{-2}\ |D-E|^2\ . \tag{I-18}$$

The total transition rate is the properly weighted sum of the probabilities for the individual transitions.

It might be pointed out here that the angular momenta coupling schemes previously invoked effectively describe the Auger transition process (even though magnetic interactions do not constitute the driving force) because the relative electronic positions of Eqs. I-16 and I-17 which determine the interaction are quantized according to the magnetic fields produced by the electronic spin and orbital angular momenta.

The various models that have been used to carry out the aforementioned calculations have run the gamut from non-relativistic unscreened hydrogenic bound-state/unscreened Coulomb continuum wave functions to relativistic Hartree-Fock-Slater numerical methods incorporating intermediate coupling and configuration interaction.

A discussion of the work carried out in this field is beyond the scope of this thesis, and the interested reader is invited to peruse the excellent review by Bambynek et al. for information concerning the existing state-of the art in theoretical techniques.

The development of a precise theory has been hampered in no small way by the complexity of the problem and the consequent paucity of reliable experimental information. The experimental problem essentially reduces to a determination of the atomic vacancy distributions produced by a given inner shell ionization. The radiative emission (X-ray fluorescence) process merely moves the existing vacancy to a different energy level, however non-radiative processes complicate the situation by causing a multiplication of vacancies: the Auger process leaves the atom in a doubly-ionized state.

The probability that a vacancy in an atomic subshell is filled through a radiative transition is defined as the fluorescence yield of that subshell. An atom possessing an electron vacancy is in an excited state and that state has a definite lifetime $\tau(W_o)$. By means of the Heisenberg Uncertainty Principle, a total energy width $\Gamma(W_o)$ may be associated with that state where

$$\Gamma(W_o)\,\tau(W_o) = \hbar \qquad \text{(I-19)}$$

The decay probability per unit time of the state is therefore

$$\frac{1}{\tau(W_o)} = \frac{\Gamma(W_o)}{\hbar} \quad . \qquad \text{(I-20)}$$

If the radiative decay probability is denoted by $\Gamma_R(W_o)/\hbar$, the radiationless (Auger) decay probability by $\Gamma_A(W_o)/\hbar$, and the Coster-Kronig decay probability by $\Gamma_{CK}(W_o)/\hbar$, it follows that the total width of the state is

$$\Gamma(W_o) = \Gamma_R(W_o) + \Gamma_A(W_o) + \Gamma_{CK}(W_o) \qquad \text{(I-21)}$$

Directly from the preceeding definition, the fluorescence yield of the state is

$$\omega_{W_o} = \frac{\Gamma_R(W_o)}{\Gamma(W_o)} = \frac{\Gamma_R(W_o)}{\Gamma_R(W_o) + \Gamma_A(W_o) + \Gamma_{CK}(W_o)} \qquad \text{(I-22)}$$

and, for a sample containing a large number of atoms, is equal to the number of photons emitted when vacancies in the subshell are filled divided by the total number of primary vacancies in the subshell. That is

$$\omega_{W_o} = I_{W_o}/v_{W_o} \qquad \text{(I-23)}$$

where

I_{W_o} = the total number of characteristic W_o X-ray photons emitted from the sample

v_{W_o} = the number of primary W_o subshell vacancies

For shells above the K level the definition becomes increasingly more complicated due to the existence of more than one subshell and due to the possibility of Coster-Kronig transitions, which enable a primary vacancy created in one subshell to shift to a higher subshell before the vacancy is filled by another transition. The mean yield for the W shell can be defined as

$$\bar{\omega}_W = \sum_{W_o} V_{W_o} \omega_{W_o} \tag{I-24}$$

where V_{W_o} is the relative number of primary vacancies in the subshell o of shell W:

$$V_{W_o} = v_{W_o} / \sum_{W_o} v_{W_o} \; ; \; \sum_{W_o} V_{W_o} = 1 \tag{I-25}$$

and the summations in Eqs. (I-24 and I-25) extend over all the subshells of W. In order to determine ω_{W_o} for each of the k_W subshells of W, it is necessary to perform k_W experiments, each giving rise to a different known ratio of primary vacancies among the subshells, and solve the resulting set of simultaneous equations.

For the definition of $\bar{\omega}_W$ given in Eq. (I-24) to be applicable, it is necessary that the primary vacancy distribution remain unaltered until the vacancies are filled by transitions involving higher shells; i.e. Coster-Kronig transitions must be absent. In order to compensate for the occurrance of these transitions, Eq. (I-24) may be rewritten as

$$\bar{\omega}_W = \sum C_{W_o} \omega_{W_o} \tag{I-26}$$

where the coefficients C_{W_o} denote the relative number of vacancies in the W_o subshells including vacancies shifted to each subshell by Coster-Kronig transitions. In this case, the relation

$$\sum_{W_o} C_{W_o} > 1$$

is obeyed because some of the vacancies created in subshells below W_o must be counted more than once as Coster-Kronig transitions shift them into W_o. The Coster-Kronig probability for shifting a vacancy from a subshell W_o to a higher subshell W_p is denoted by $f_{W_{op}}$, and the coefficients C_{W_o} may be written in terms of the relative numbers of primary vacancies, V_{W_o}, as follows:

$$C_{W_1} = V_{W_1}$$

$$C_{W_2} = V_{W_2} + f_{W_{12}} V_{W_1}$$

$$C_{W_3} = V_{W_3} + f_{W_{23}} V_{W_2} + (f_{W_{12}} + f_{W_{12}} f_{W_{23}})V_{W_1}$$

$$\vdots$$

$$C_{W_k} = V_{W_k} + f_{W_{k-1,k}} V_{W_{k-1}} + (f_{W_{k-2,k-1}} f_{W_{k-1,k}})V_{W_{k-2}} + \ldots$$

$$+ (f_{W_{1k}} + f_{W_{12}} f_{W_{2k}} + f_{W_{12}} f_{W_{23}} f_{W_{3k}} + \ldots)V_{W_1}$$

From the preceeding equations, it is quite evident that the deduction of the individual subshell fluorescence yields from experimental measurements can be quite complicated, requiring a knowledge of the appropriate Coster-Kronig transition probabilities in addition to performing a sufficient number of measurements of $\bar{\omega}_W$ with different vacancy distributions.

In a manner similar to that above, the Auger yield a_{W_o} is defined as the probability that a vacancy in the W_o subshell is filled through a non-radiative transition by an electron from a higher shell. This definition specifically excludes Coster-Kronig transitions since the de-excitation electron originates in the subshell W_p which is in the same major shell as W_o. From these definitions, it is obvious that the following relationships must hold between the fluorescence yield, the Auger yield, and the Coster-Kronig yield of a given subshell:

$$\omega_{W_o} + a_{W_o} + \sum_{W_p > W_o} f_{W_{op}} = 1 \ . \qquad \text{(I-27)}$$

By analogy with Eq. I-26, the mean Auger yield $\bar{a}_W$ is defined as

$$\bar{a}_W = \sum_{W_o}^{i} C_{W_o} a_{W_o} \ , \qquad \text{(I-28)}$$

the C_{W_o} being the same altered vacancy numbers discussed previously. It follows, therefore, that the sum of the mean fluorescence yield and the mean Auger yield of a shell for the same initial vacancy distribution is equal to unity:

$$\bar{\omega}_W + \bar{a}_W = 1 \ . \qquad \text{(I-29)}$$

The variation with atomic number of the K shell fluorescence yield is shown in Fig. I-17. Several attempts have been made to fit this curve to semiempirical formulae, the basis for the early attempts being the theoretically deduced result of Wentzel[28] which showed that the radiative transition probability (being of the electric dipole

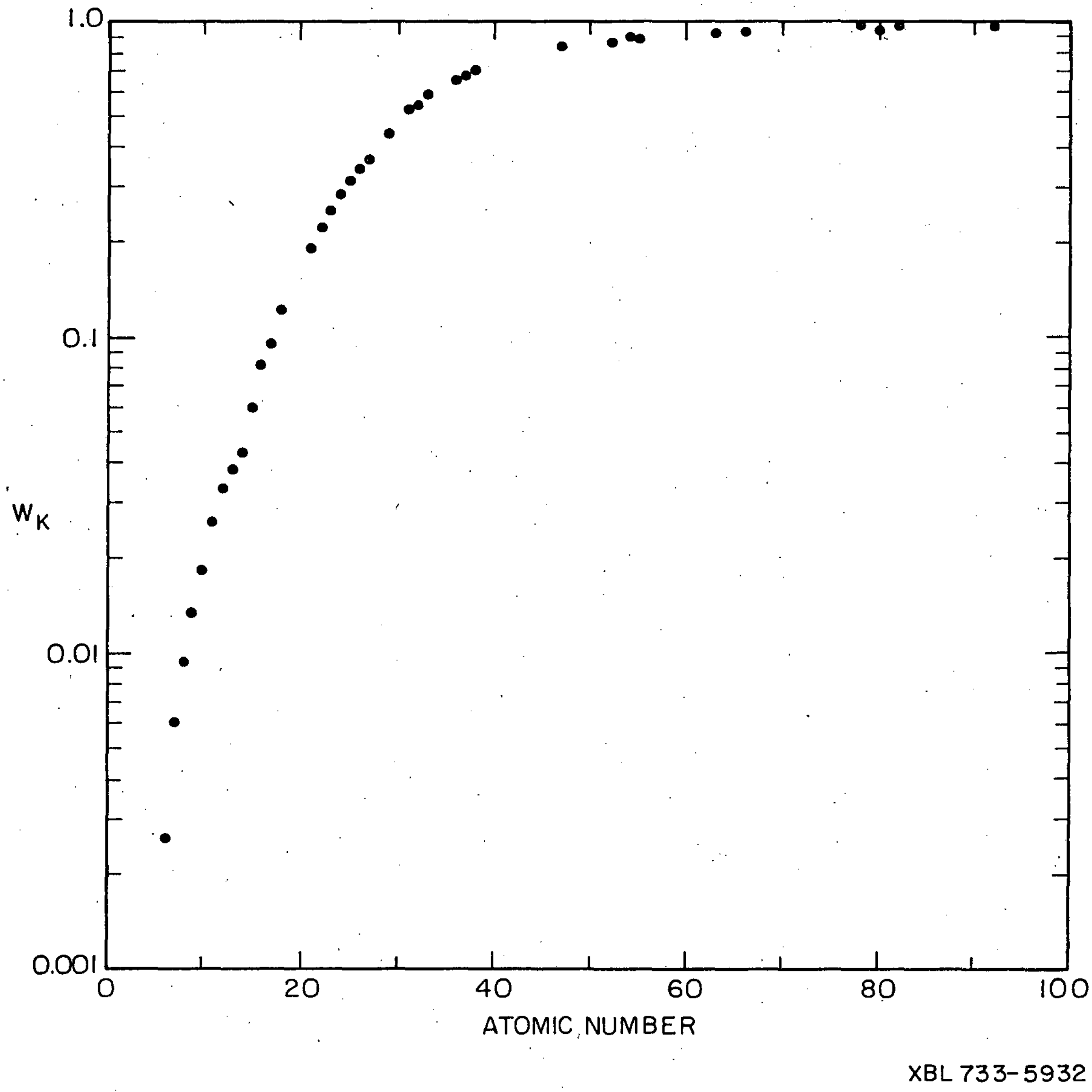

Fig. I-17. The variation of the K-shell fluorescence yield with atomic number Z.

type) is proportional to the fourth power of the atomic number and the radiationless transition probability is constant:

$$\frac{\Gamma_R(K)}{\hbar} = aZ^4 \quad \text{and} \quad \frac{\Gamma_A(K)}{\hbar} = b \ .$$

Therefore

$$\omega_K = \frac{aZ^4}{aZ^4+b} = (1 + \alpha Z^{-4})^{-1} \qquad \text{(I-30)}$$

where

$$\alpha = b/a = O(10^6)$$

This relationship is only a first approximation since Wentzel used unscreening hydrogenic wave functions in deriving his result. Of the modifications made to this formula, that proposed by Bishop[29] to allow for screening and relativistic effects

$$[\omega_K/(1-\omega_K)]^{1/4} = A + BZ + CZ^3 \qquad \text{(I-31)}$$

where

$$A,\ B,\ C = \text{constants}$$

is better than most and many authors have fitted their data to this equation. For example, Hagedoorm and Wapstra[30] have determined that the constants $A = 6.4\times10^{-2}$, $B = 3.40\times10^{-2}$, and $C = 1.03\times10^{-6}$ predict ω_K with an accuracy of 0.005, independent of Z. Recently it has become possible to calculate K shell fluorescence yields from first principles with an accuracy consistantly better than 0.01, except for high Z elements since relativistic effects have not been generally included in the calculations. This has been made possible by

a. Advances in developing more realistic wave functions, both by improved screening of hydrogenic functions and the development of better SCF numerical functions.

b. The availability of more accurate binding energies, radiationless transition probabilities being quite sensitive to the continuum electron energy.

c. The ability to include all of the transitions contributing to the Auger width through the use of high speed computers.

d. The comprehensive and more accurate calculation of radiative transition probabilities.

In order to illustrate the relative lack of work which has been performed on the higher energy levels, presented in Fig. I-18 are the presently available experimental data for the average L- and M-shell fluorescence yields respectively. Data is even more lacking for the individual subshell yields.

In conclusion, it may easily be seen that for the cases considered here (i.e. $E_{W_o X_p Y_q} < 1000$ eV) the probability of fluorescence is negligible and it may be assumed that a vacancy is filled by a radiationless transition with unit probability. Unfortunately, however, it is not yet possible to predict the probability distribution among the possible transitions and the question of peak intensities is still an open question.

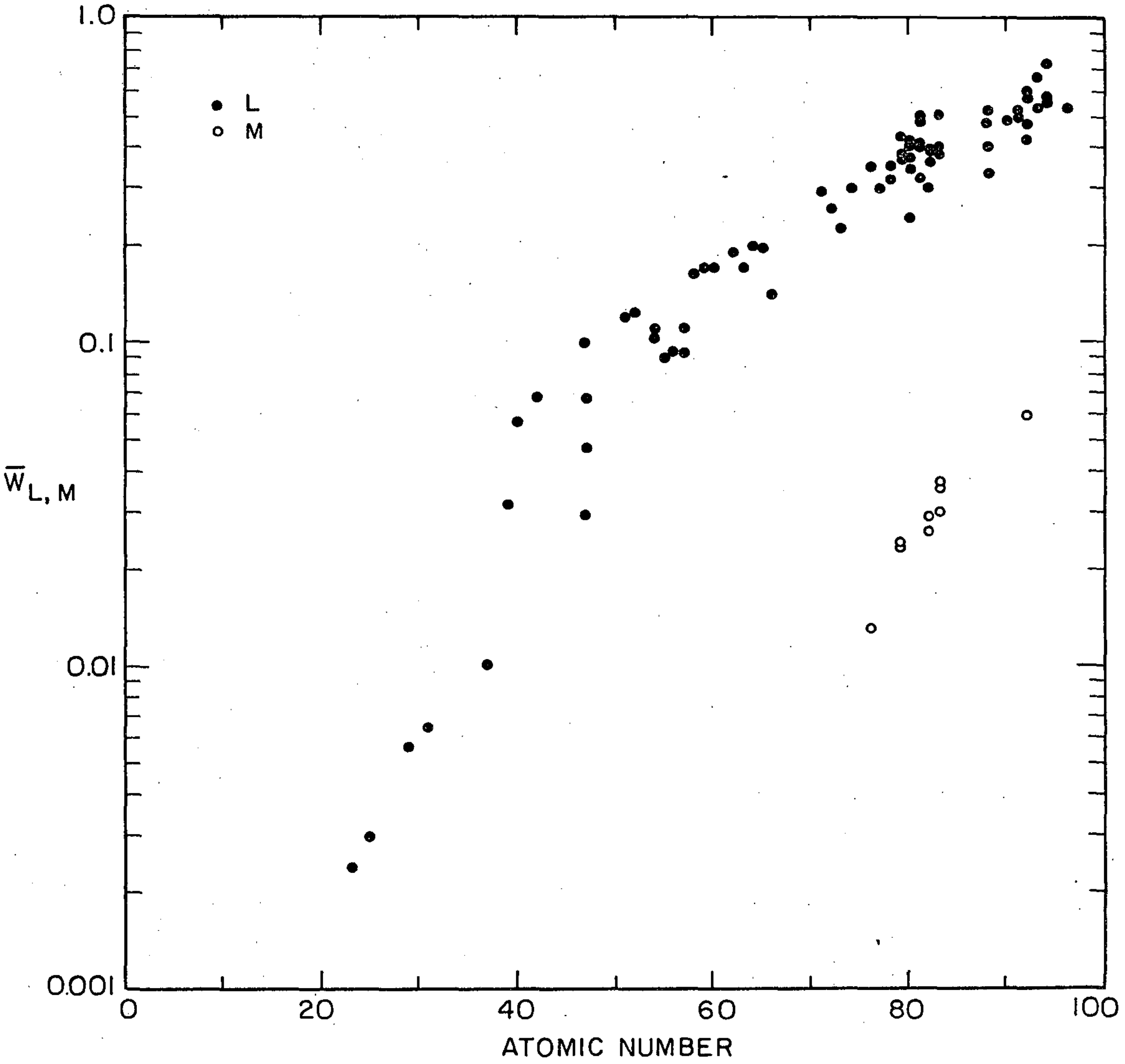

XBL 733-5933

Fig. I-18. The variation of the average L- and M-shell fluorescence yields with atomic number Z.

c. The detected volume

It is necessary to have an understanding of the concept of the detected volume in order to correctly interpret AES data. The detected volume is simply defined as the total crystal volume that is analyzed under the particular experimental conditions used. Although this definition appears straightforward enough, it is difficult to apply in practice since two of the major factors which contribute to the signal strength are not well known.

The probability of escape of a particular electron from a solid is primarily determined by the distance of the electron below the surface of the solid and by the mean free path of the electron in the material. The mean free path, or escape depth, is in turn dependent upon the energy of the electron. Until recently, few studies of the energy dependence of the escape depth have been carried out. Indeed, most of the work that has been done in this area has used Auger electrons, an overlayer of some material being epitaxity deposited upon a substrate and the rate of increase and decrease respectively of the signal from each species is monitored as the overlayer thickness is increased.

If the deposited material condenses upon the surface in a monolayer by monolayer fashion, then an estimate of the escape depth may be secured. Assuming that the rate of peak intensity growth or decrease varies in an exponential manner, the overlayer and substrate intensities may be respectively written as:[31]

$$I_o = I_o^o\ [1-\exp(-z/\lambda_o)] \qquad \text{(I-32)}$$

and

$$I_s = I_s^o\ \exp(-z/\lambda_s) \qquad \text{(I-33)}$$

where

I_o^o = the intensity of the overlayer peak for an infinitely large film thickness

I_s^o = the intensity of the pure substrate peak

λ_o, λ_s = the mean free path of the overlayer and substrate peak electrons respectively.

z = the depth of the overlayer

In order to measure the mean free path for the energy of the substrate Auger electrons, it is necessary to note the overlayer thickness when $I_s = I_s^o/e = I_s^o/2.718$ since $\lambda_s = z$ at this point. Similarly for the overlayer, $\lambda_o = z$ when $I_o = I_o^o(1-e^{-1}) = 0.632\ I_o^o$. If the overlayer material congregates into "islands" upon the surface instead of being evenly deposited (i.e. when the surface free energy of the substrate is lower than that of the deposited material), it is obvious that this simple model will break down. Indeed, this island formation may be identified using the experimental data since the sum of the normalized substrate and overlayer intensities should remain essentially constant. This situation exists for gold deposited upon silver, the results of Palmberg and Rhodin[32] being shown in Fig. I-19. It should be possible

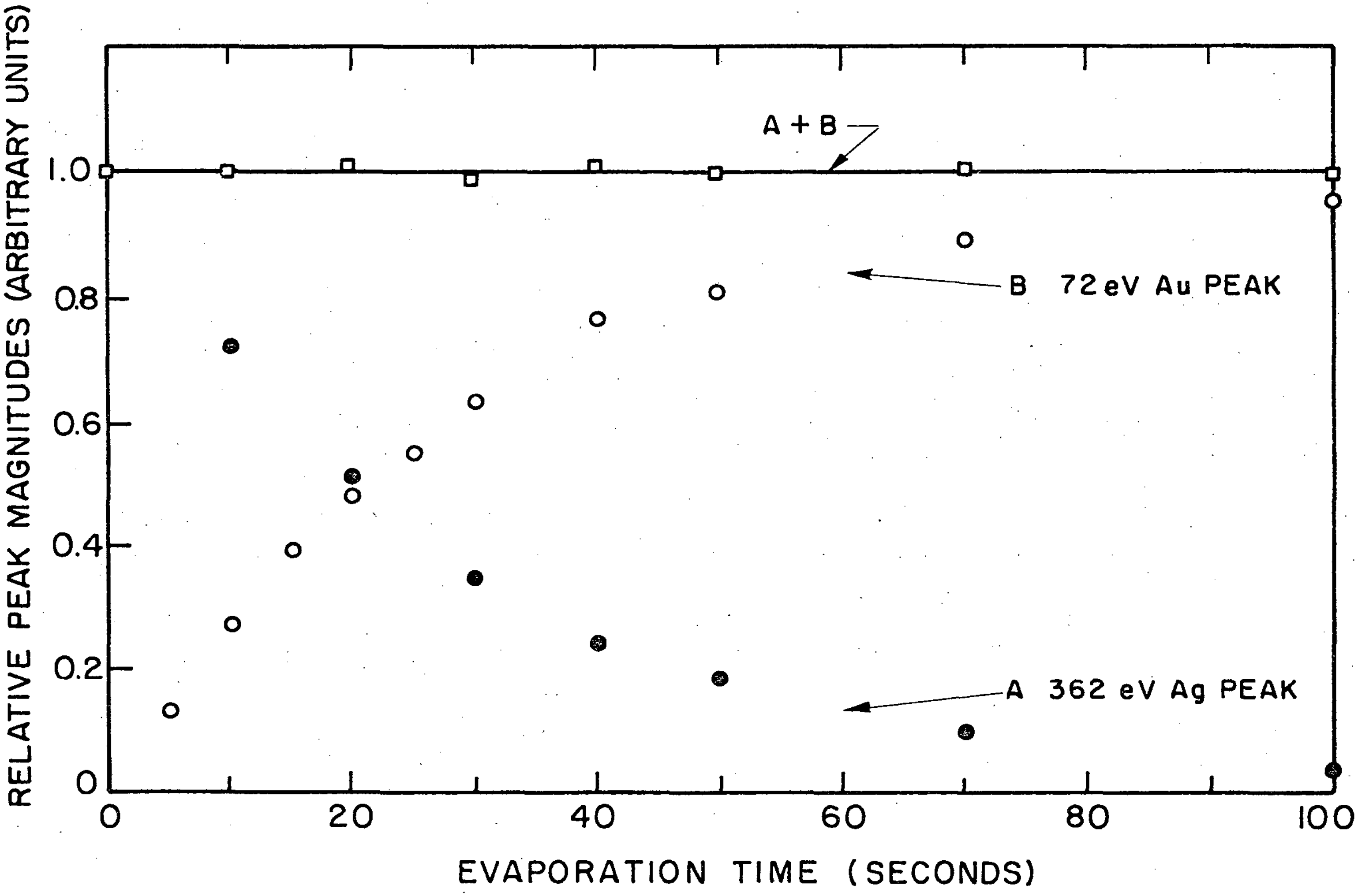

XBL733-5934

Fig. I-19. The relative magnitude of the Ag 362 eV and Au 72 eV Auger peaks vs. an evaporation time. (From Palmberg and Rhodin[32]) to determine the mean free paths from such data if the amount of surface coverage by the islands is independently measured.

The energy dependence of the mean free paths of electrons through a variety of materials is shown in Fig. I-20.[31-45] The increase at higher energies is due to the reduced scattering cross-section for electrons under these conditions. The increase for low energy electrons, however, is attributable to the reduced number of bound-state crystal electrons which are available for interaction with free electrons in this energy range.

Since we are working with overlayers of a few monolayers and less in thickness, the main uncertainty in the measurements lies in the determination of the depth of the deposited material. Perhaps the best technique developed for this purpose is the simultaneous deposition of the overlayer upon a quartz crystal oscillator,[31] the frequency of the oscillator being a function of the mass of the deposited material. The main other methods that have been employed in determining the amount of deposited material are LEED,[34] ellipsometry,[46] radioactive tracer techniques,[47] and work function measurements.[48]

It might be noted here that the detected volume is essentially independent of the incident beam energy (Eq. I-12), depending only upon the attenuation suffered as it penetrates into the crystal. For the general optimal situation suggested by Fig. I-15, i.e. $E_p \approx 4E_{W_o}$, the primary beam intensity may be seen to be reduced by a factor $\approx e^{-1/2} \approx 0.6$ by the time that it reaches the maximum escape depth

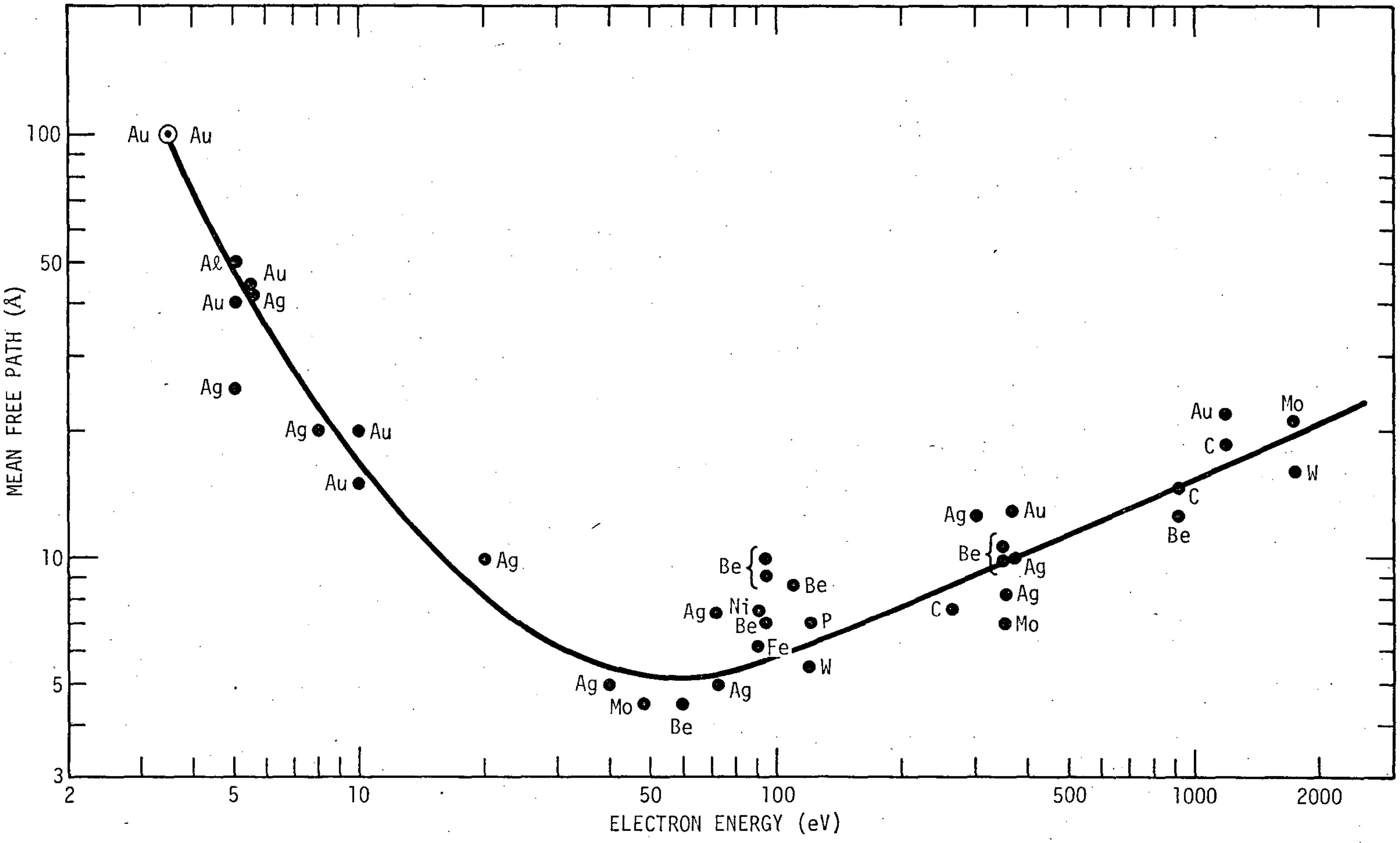

XBL 733-5917

Fig. I-20. The variation of the electron mean free path as a function of the electron energy in various solid materials.

of the Auger electron. If desired, the Auger peak intensity can be increased by directing the ionizing beam upon the target at a grazing angle of incidence with respect to the surface plane. This increase varies approximately as $\cos^{-1} \Theta_p$ (where Θ_p is the angle of the incident beam with respect to the surface normal) and results from the fact that a glancing incidence angle gives a larger effective number of bombarded atoms per unit area. Although the problem of maximizing the intensity through the choice of an optimum angle of incidence is somewhat involved, this angle generally lies between 10° and 30° from the surface tangent and depends mainly upon the degree of surface roughness.[49]

The other factor contributing to the Auger intensity is the distribution of all the atomic species present within the detected volume. It is obvious that those atoms laying closer to the surface will contribute more electrons to their respective Auger peaks than those further into the bulk. Harris[50] has demonstrated that surface atoms may sometimes be distinguished from bulk atoms by the angular distribution of the electrons emitted from each. An indication of this distribution with depth may also be obtained by sputtering away the surface in monolayer by monolayer fashion using the technique of noble gas ion bombardment and monitoring the changes in Auger peak intensity as the process progresses into the bulk.

In order to carry out a quantitative analysis on a material both the mean free path and initial depth distribution of the Auger electrons must be precisely known. Since both quantities are inexactly known, one solution to the problem is to specify surface concentrations using a two-dimensional nomenclature, i.e. n atoms per cm^2 with n proportional to the peak intensity, and then to evaluate the significance of n in terms of what is indicated to be the approximate detected volume and depth distribution. If no sputter profiling is performed, then the analysis must be carried out in terms of what might reasonably expected to be the depth distribution. This entire technique has the advantage that n can always be obtained from the data and has direct significance for up to a monolayer of adsorbate. The disadvantage is that n can be dangerously misleading if the details of the detected volume are ignored.[51]

d. Calculation of the total Auger yield

The factors discussed in the preceeding three sections will be combined here to produce an order of magnitude estimate of the Auger electron yield to be expected in the course of a typical experiment. As alluded to earlier, the initial inner shell ionization process realizes two contributions: one from the primary electron beam and the other from the electron current which results from back-scattering and secondary electron emission from the target atoms. The calculation will also require factors which reflect 1) the probability of an Auger process resulting from an inner shell ionization event, and 2) the probability of detection of these electrons.

The Auger electron current from a W_o subshell vacancy is then given by[46,54,55]

$$I_{W_o} \doteq m\, N_o \left[\frac{Q_{W_o}(U)}{\cos\,\Theta_p} + r \left(\frac{E_p - E_{W_o}}{E_p} \right) \overline{Q_{W_o}}(U) \right] I_p \, (1-\omega_{W_o})\, T$$

where

m = the number of atomic monolayers laying within the Auger electron escape depth.

N_o = the number of atoms per cm^2 in a monolayer

$Q_{W_o}(U)$ = the cross-section for ionization of the W_o subshell by primary electrons of energy $E_p = UE_{W_o}$ (U being a real number greater than unity).

Θ_p = the angle of incidence of the primary electron beam with respect to the surface normal

r = the inelastic back-scattering coefficient

$\overline{Q_{W_o}}(U)$ = the average cross-section for W_o subshell ionization by electrons in the energy range E_{W_o} to UE_{W_o}.

I_p = the primary beam current

ω_{W_o} = the total fluorescence yield for the W_o subshell

T = the transmission factor for the analyzer used

The simple model which gives rise to the preceeding equation makes the following assumptions: 1) the primary beam suffers no attenuation as it traverses the escape depth of the Auger electrons, 2) all of the Auger electrons generated within the escape depth which are travelling in the direction of the analyzer escape from the target, 3) the distribution of the secondary electrons within the target is isotropic, 4) the secondary electron current is constant over the energy range 0 to E_p (and therefore only that fraction between E_{W_o} and E_p are available to ionize the W_o subshell), 5) the inelastic back-scattering coefficient is independent of the incident beam angle, and 6) there is no contribution to the detected current from secondary emission within the analyzer.

We will consider the simple case of monolayer adsorption, i.e. m=1, of oxygen gas upon a surface. It will be assumed that the primary beam is normally incident upon the surface (cos 90° = 1) and its energy has been optimized to obtain the greatest amount of primary beam ionization of the W_o subshell by setting $E_p \approx 4\ E_{W_o}$. Since the probability $(1-\omega_{W_o})$ that an Auger process occurs after an energy level up to 600 eV below the Fermi level is ionized is 99-100%, this probability has been taken as unity in the calculation. The inelastic back-scattering coefficient is typically about 0.3 and the transmission of the four grid RFEA is 0.2.[53] Introducing these quantities into the preceeding equation, we obtain $I_K = (2.1\times10^{-5})\ I_p$. That is, the probability of observing an Auger transition in this case is about 2×10^{-5}; alternatively stated, for an initial current of 10 microamperes, the Auger electron current will be about 2×10^{-10} amps.

3. Chemical Effects

Auger Electron Spectroscopy has the capability of providing two kinds of information concerning the chemical bonding state of atoms, the type obtained from a particular peak depending on whether the transition that produced it involves the valence band or not. The first type of information is contained in the "chemical shift" in the energy of the peak, and this reflects the changes occurring in the binding energy of the inner shell electrons induced by the charge transfer occurring in the valence shell. The second type of information is contained in the "valence spectra" peaks which directly reflect the charge transfer taking place as the atom changes its chemical state. The distinction between chemical shifts and valence spectra is made because the valence spectra changes are not shifts in energy of the Auger peak with little change in peak shape, but rather are drastic changes in the electron energy distribution within the peak incurred upon the formation of a new chemical bond.

a. Chemical shifts

A simple model, attributable to Siegbahn et al.,[21] may be invoked to demonstrate that the change in valence shell charge distribution which occurs when an atom changes its valence state is relayed to all of the inner shell electrons and modifies the binding energy of each. First of all, it may be argued that the atomic valence electron orbitals essentially define a spherical "valence shell" of electric charge and the inner shell electrons reside within this charged shell. If electrons are added to or removed from this valence shell, using purely classical considerations the electric potential inside the shell is changed. Adopting the convention of defining zero potential energy of a system when the particles that comprise the system are separated by an infinite distance, the Coulombic potential energy existing in a system of two charges of magnitude q_1 and q_2 which are separated by a distance r_{12} is given by

$$E = \frac{1}{4\pi\varepsilon_o} \frac{q_1 q_2}{r_{12}} \qquad \text{(I-35)}$$

$$= \frac{q_1 q_2}{r_{12}} \text{ atomic units (a.u.)}$$

where ε_o is the permittivity constant. For the case where one of the particles is an electron, Eq. (I-35) becomes

$$E = \frac{-q_2}{r_{12}} \text{ a.u.}$$

Consider now an atom which is isolated in space. The potential energy of an electron in this atom will be denoted by E_B. If the atomic potential acting upon the outermost electron of the atom is considered to be that corresponding to an effective nuclear charge of one (i.e. Z_{eff} = Z protons - (Z-1) electrons), if a charge of magnitude q_e is removed from the valence shell of radius r to infinity the potential energy of the inner shell electron will become

$$E_{FI} = E_B + \left[\frac{(-q_e)(1)}{\infty} - \frac{(-q_e)(1)}{r}\right]$$

$$= E_B + \frac{q_e}{r} \quad .$$

The change in binding energy of this inner electron is therefore

$$\begin{aligned} \Delta E_{FI} &= E_{FI} - E_B \\ &= q_e/r \end{aligned} \qquad \text{(I-36)}$$

Since r is typically on the order of 1 Ångstrom (2 a.u.), it follows that for the "free ion" model described above $\Delta E_{FI} \approx 14$ eV if one electron is completely removed from the atom.

If it is now taken into account that an electron is not removed to infinity when an ionic bond is formed but rather transferred from the valence shell of atom A to the valence shell of atom B, the inner shell electron energy becomes

$$\begin{aligned} E_{AB} &= E_B + \left[\frac{(-q_e)(1)}{R} - \frac{(-q_e)(1)}{r}\right] \\ &= E_B + q_e\left[\frac{1}{r} - \frac{1}{R}\right] \end{aligned}$$

where R is the internuclear distance of the AB molecule. The energy shift is therefore

$$\begin{aligned} \Delta E_{AB} &= E_{AB} - E_B \\ &= q_e\left[\frac{1}{r} - \frac{1}{R}\right] \end{aligned} \qquad \text{(I-37)}$$

and has the opposite sign for the $A^{q_e^+}$ and $B^{q_e^-}$ atoms. When these ions are arranged in a lattice to form a crystal, one must consider the Coulombic interaction of a core electron in one ion with all of the ions in the lattice. This is essentially the same problem that one faces in calculating the lattice energy of ionic crystals and Eq. (I-37) is modified by the Madelung constant α to become

$$\Delta E = q_e \left[\frac{1}{r} - \frac{\alpha}{R}\right] \quad . \tag{I-38}$$

Since α has been calculated to be approximately 1.7 for diatomic crystals when based on unit charges and referred to the nearest-neighbor distance ($R \approx 5$ a.u.), it follows that

$$\Delta E \approx 1 \left[\frac{1}{2} - \frac{1.7}{5}\right] \text{ a.u.}$$

$$\approx 4 \text{ eV}$$

It should be noted that electronic relaxation has been neglected in Eq. (I-38). This term should be independent of q_e. Also, it has been assumed that there is no valence electron penetration into the atomic core region. For this situation a constant chemical shift should be experienced by all of the inner shell electrons. If significant penetration occurs then different chemical shifts will be experienced by the electrons in different energy levels.

Theoretically, chemical shifts in Auger spectra are not trivial to analyze since they will be determined by the following equation[56]

$$\Delta E_{W_oX_pY_q}(Z) = \{[E_{W_o}(Z) + \Delta_{W_o}(Z)] - [E_{X_p}(Z) + \Delta_{X_p}(Z)] - [E_{Y_q}(Z') + \Delta_{Y_q}(Z')] - \Theta_A\}$$

$$- [E_{W_o}(Z) - E_{X_p}(Z) - E_{Y_q}(Z') - \Theta_A]$$

$$= \Delta_{W_o}(Z) - \Delta_{X_p}(Z) - \Delta_{Y_q}(Z') \qquad \text{(I-39)}$$

where $\Delta_{W_o}(Z)$, $\Delta_{X_p}(Z)$, and $\Delta_{Y_q}(Z')$ are the chemical shifts in the finding energies of the W_o, X_p, and Y_q energy levels respectively. Since all three Δ's must be known while $\Delta E_{W_oX_pY_q}(Z)$ is the only experimentally determined quantity, the analysis might certainly prove to be difficult. However, data obtained from X-ray Photoelectron Spectroscopy[21] indicates that the Δ's are essentially equal in magnitude for all of the inner shells. Therefore, the chemical shifts of inner shell Auger transition electrons would be expected to be of the same magnitude as the shifts in binding energy of the individual inner shells for the same chemical system.

b. Valence spectra

Due to the large width of the valence shell relative to the inner shells, it is obvious that the peaks resulting from Auger transitions of the types W_oX_pV and W_oVV (where V denotes the valence band) will depend heavily upon the characteristics of the valence band. In fact, for the former case the observed spectrum should mimic the variations in structure of the valence band. For the second case the situation is more complicated. Referring to Fig. I-21,[2] it is obvious that the

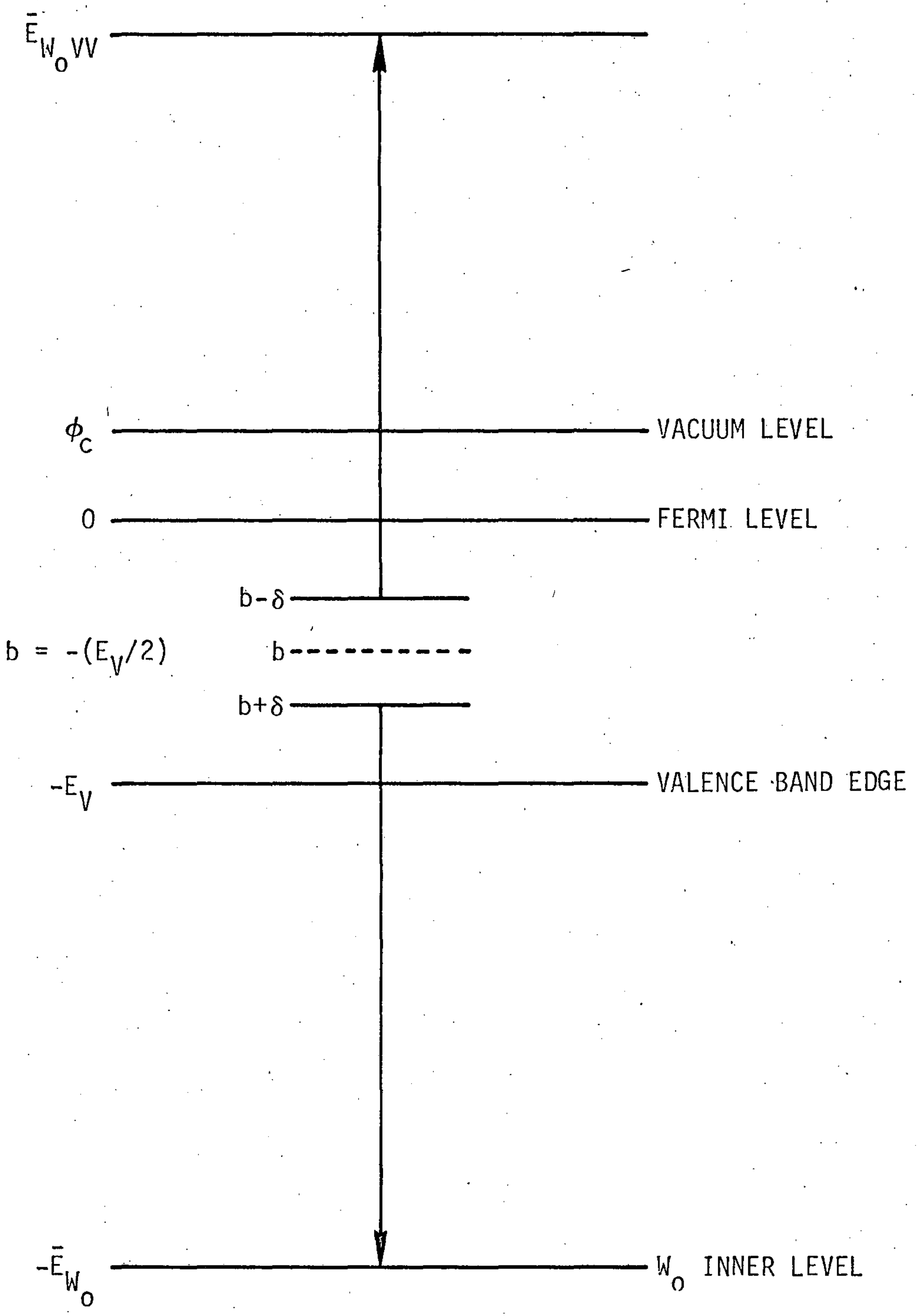

XBL 733-5918

Fig. I-21. The energy level diagram for a double valence band Auger transition.

band variable b is related to the Auger energy E_{W_oVV} by the conservation relation

$$E_{W_oVV} = E_{W_o} - 2b - \Theta_c \qquad \text{(I-40)}$$

Here it is necessary to note that:

a) Since E_{W_o} and Θ_c are assumed to be constant there is a unique correspondence existing between E_{W_o} and b. It follows that a representation of the transition in either one of these terms is equivalent.

b) Equation (I-40) is independent of δ, which is defined as one-half of the initial state separation. Therefore, in order to determine the total contribution from the valence band to the Auger spectrum it is necessary to integrate over δ.

In terms of b, the Auger distribution is

$$f(b) = \int g(b+\delta)\ g(b-\delta)\ d\delta \qquad \text{(I-41)}$$

where the integration is over all δ such that the initial and final states are within the allowed band and g(b) is the transition density, which is essentially a product of the transition matrix elements and the density of occupied states. It might be noted that the internal Auger distribution f(b) is related to the experimentally observed distribution by an escape probability function which can be assumed constant for energies above 50 eV.

The transition density g(b) can be obtained by inverting Eq. (I-41). Because of the dependence of the integration limits on b, the resulting problem is most easily handled by dividing f(b) into two parts:

$$f(b) \begin{cases} F_1(b) = \int_o^b g(b+\delta)\ g(b-\delta)\ d\delta \quad \text{for} \quad 0 \leqslant b \leqslant (E_V/2) \\ \\ F_2(b) = \int_o^{E_V-b} g(b+\delta)\ g(b-\delta)\ d\delta \quad \text{for} \quad (E_V/2) \leqslant b \leqslant E_V \end{cases} \tag{I-42}$$

Either of the above equations may be inverted to find the transition density. If $F_1(b)$ is considered, a change of variables may be made to $y = b+\delta$ and another may be made to $x = b-\delta$. If the two results are added together, the resulting equation may be developed into a form compatible with the Convolution Theorem of Laplace Transforms. Applying this theorem, one obtains the expression

$$\begin{aligned} g(y) &= L^{-1}\left\{\sqrt{L[2F_1(y/2)]}\right\} \\ &= 2\ L^{-1}\left\{\sqrt{\Gamma(s)}\right\} \end{aligned} \tag{I-43}$$

where $\Gamma(s)$ is the Laplace transform of the Auger distribution $F_1(y)$. An alternative approach is outlined in Ref. 57.

Another type of chemical information obtainable from valence spectra is due to "molecular orbital energy spectra." This name derives itself from the fact that the energy levels in valence spectra can be compared with the corresponding levels in compounds where the molecular orbitals are known. Although there is no way at present of associating an energy level with a particular molecular orbital, it may be possible to guess at the molecular orbital involved in a given chemical reaction by observing the changes in the valence spectra or by comparison with spectra from known compounds. Once the molecular orbital is identified, the symmetry of its component wave functions is known and this information may be used to infer the point group symmetry of an atom in a crystal thereby uniquely locating the atom within the unit cell.[51]

II. EXPERIMENTAL

A. Apparatus

Figure II-1 is a photograph of the vacuum apparatus and its supporting electronic equipment which were used in these experiments. A schematic diagram of the vacuum apparatus is shown in Fig. II-2. Although composed mainly of commercially available components, this apparatus was designed and built at the Lawrence Berkeley Laboratory especially for the experiments described in this thesis. Except for the viewing ports, the system is completely constructed of stainless steel with copper sealing gaskets used at the mating flanges. This provides one with a system which is bakeable to 475°K and capable of achieving an ultra-high vacuum (UHV) of better than 10^{-9} Torr.

The vacuum chamber is a standard cylindrical type manufactured by Varian Associates, and it is pumped by a 50 liter/sec ion pump and a titanium sublimation pump (TSP) which are attached to the chamber at right angles by means of a "Tee" arrangement. The TSP was included in the system specifically to assist in pumping carbon monoxide, which is one of the principal residual gases present in ion pumped systems. In addition to its geometrical arrangement with respect to the experimental chamber, a metal shield was in corporated into the TSP in order to prevent any sublimed titanium from reaching the chamber; also, the pump walls were cooled with water to prevent outgassing due to heating by the deposited titanium. The TSP has a calculated pumping speed for CO of approximately 400 liters/sec in its conductance limited mode, and Fig. II-3 shows its effect on the ambient CO

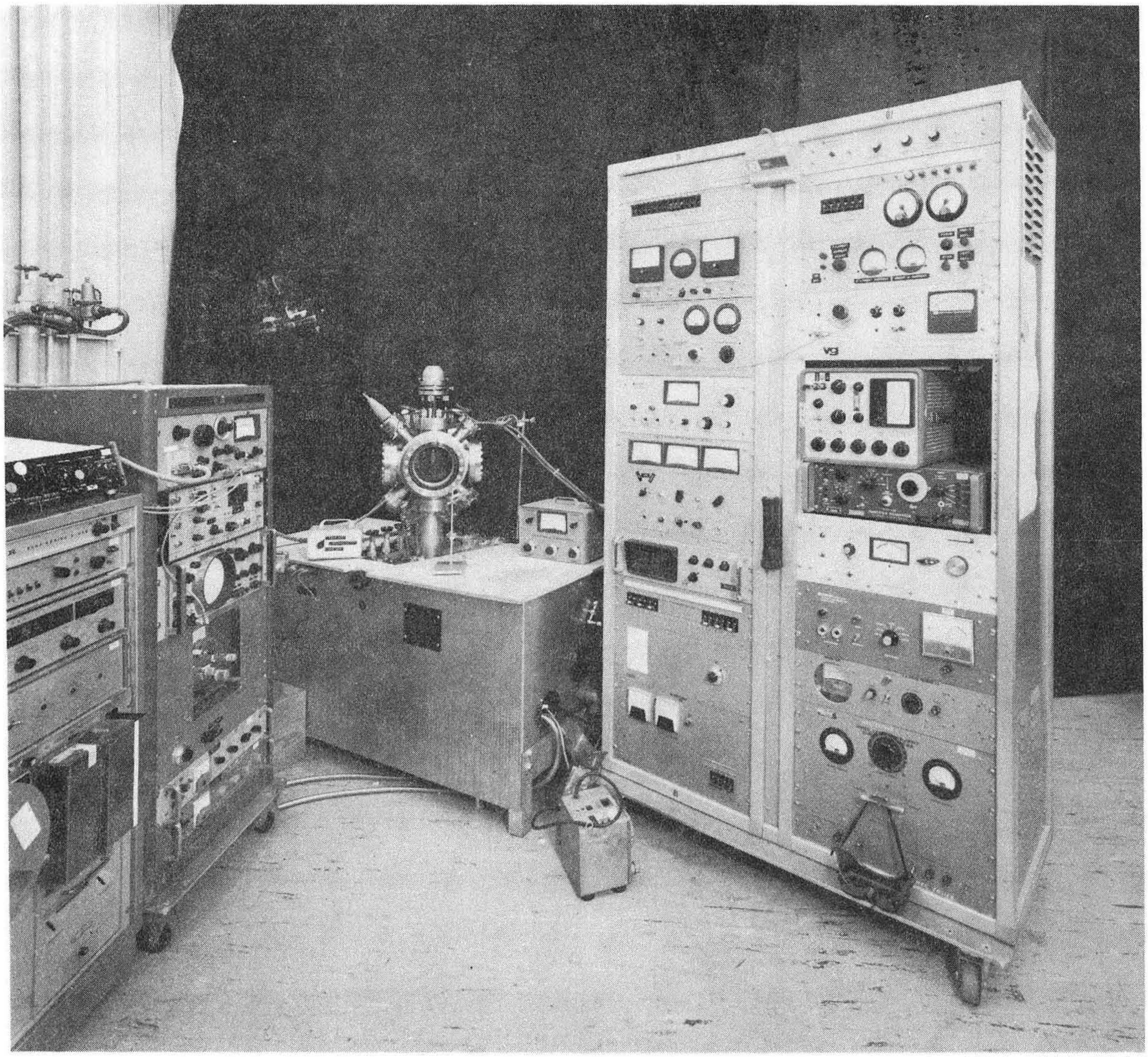

XBB 727-3845

Fig. II-1. Photograph of the vacuum apparatus and its supporting electronics used in this investigation.

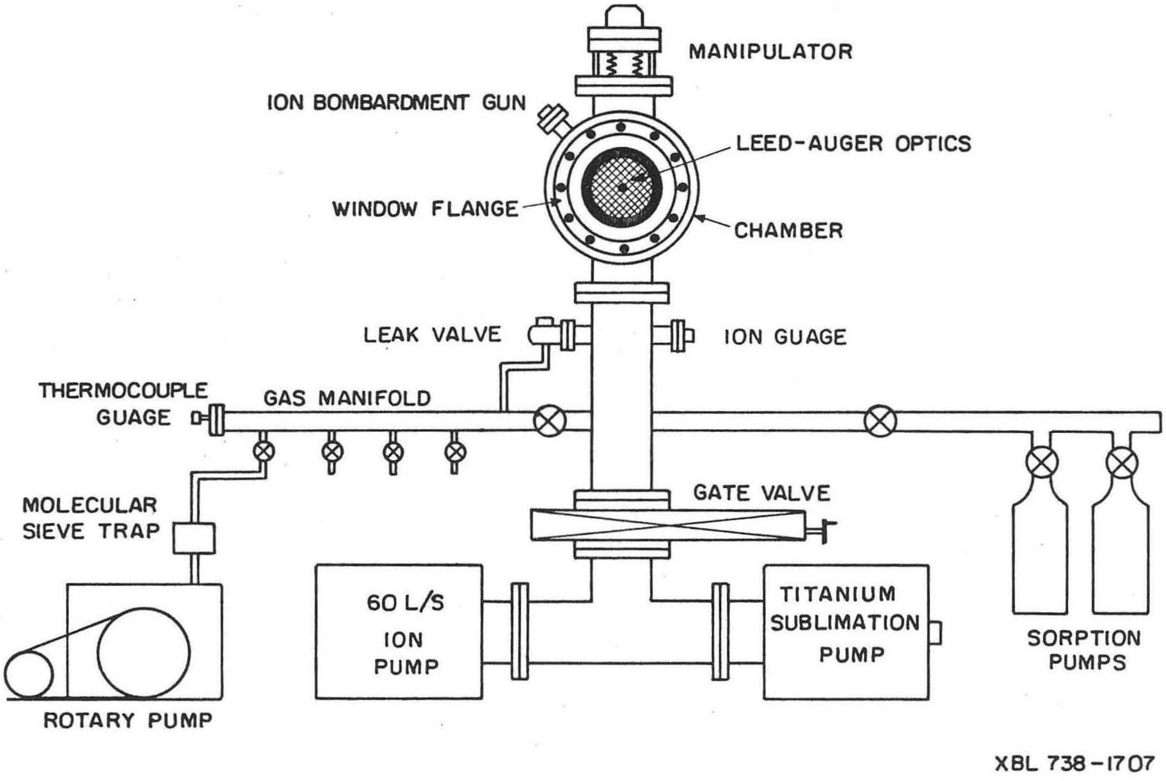

Fig. II-2. Schematic diagram of the vacuum apparatus used in this investigation.

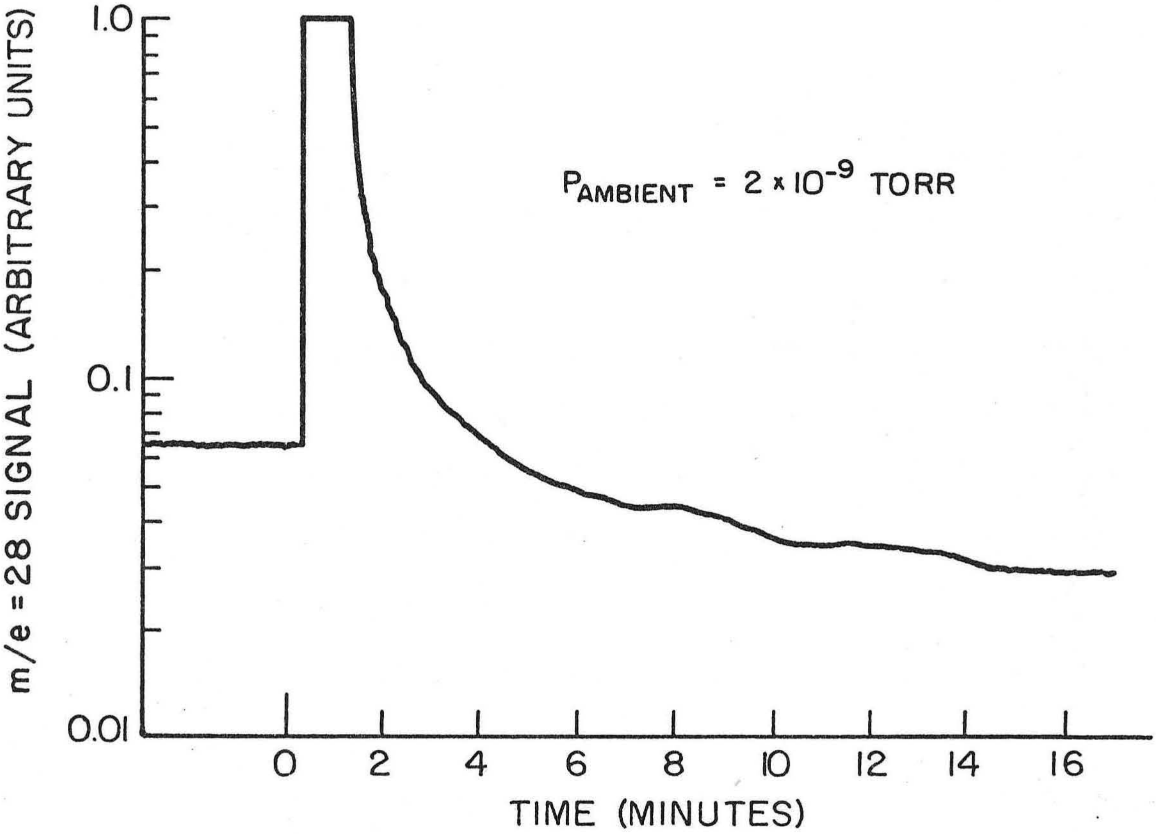

XBL733-5935

Fig. II-3. Effect of sublimed titanium from the TSP on the ambient CO concentration.

concentration.[58] Here the TSP was fired for 1 minute starting at t=0, and the 28 a.m.u. peak was monitored using a quadrupole mass spectrometer. The initial pressure burst is attributable to outgassing of the titanium filament as it is being heated. However, within 15 minutes after firing the CO pressure has improved by a factor of two over the prefiring reading and is still falling. Under normal UHV conditions, it was found quite adequate to fire the TSP once a day in order to assist the ion pump in maintaining a low ambient pressure. This approach also conserves titanium since it allows the newly evaporated film to reach some degree of saturation before a new layer is evaporated. Since the TSP also removes other chemically active gases (such as H_2, N_2, O_2, CO_2, and H_2O) from the ambient, it was normally used after adsorption studies during which such gases were controllably leaked into the vacuum chamber. It also served well during the initial pumpdown following the exposure of the chamber to atmospheric pressure and during the subsequent 24 hour bakeout period (a 1 minute firing being automatically actuated every 30 minutes).

The two pumps are able to be isolated from the vacuum chamber by a gate valve which is capable of assuring the integrity of the UHV within the pumps when the chamber has been brought to atmospheric pressure. Whenever any part of the system was brought up to atmospheric pressure, it was protected against contamination by backfilling it with a positive pressure of dry nitrogen.

Since ion pumps are inoperable above a pressure of approximately 10 microns, two sorption pumps (containing liquid nitrogen cooled molecular sieve) were sequentially employed to evacuate the chamber to a pressure below 1 micron. The use of this type of roughing pump eliminates any fear of contamination of the apparatus such as would occur with a mechanical pump due to backstreaming of the pump oil. At this point, the sorption pumps are valved off from the system, the TSP is switched on, and the gate valve is opened. This type of chamber pumpdown, with the ion pump and TSP operating in an UHV environment behind the gate valve, is referred to as a "hot start" in contrast to the situation where the entire system has been up to atomospheric pressure and, consequently, the pumps have been completely shut down. The advantages of the hot start vs the cold start are:

1) the ion pump is already at operating temperature and one does not therefore outgas the pump elements and walls at a time when one is striving to achieve a low enough system pressure for the pump to operate efficiently. The same arguement holds for the TSP also.
2) the pressure achieved by the sorption pumps within the chamber area is lowered by a factor of two as the gate valve is flung open. This usually assures, assuming reasonable sorption pump performance, that the system pressure will be low enough for the ion pump-TSP combination to pump efficiently.
3) if the roughing system is unable to evacuate the chamber to a pressure which is low enough to permit the normal pumpdown procedure to be effective, one may still achieve a high vacuum condition by using the ion pump-TSP combination to

complete the rough pumping. This may be done by only slightly opening the gate valve so that a significant pressure difference may be maintained across the valve by the pumping system, which will still be operating at a low enough internal pressure to pump efficiently. Slowly the pressure in the chamber area will be reduced, and eventually the point will be reached where the gate valve may be completely opened and the normal pumpdown procedure initiated.

Provision for introducing pure gases into the chamber for the purpose of carrying out adsorption studies and/or cleaning of the sample by chemical means was made by incorporating a gas manifold and a Varian leak valve in the system. A molecular sieve trapping arrangement was included in order to protect the manifold from the possibility of oil contamination from the mechanical rotary pump which services it. This configuration was chosen because of the potentially large gas loads that a manifold pump must endure, especially since the manifold was routinely flushed twice with the gas that it was to contain before it was isolated from its pump and filled for the experiment.

Because of its physical proximetry to the chamber, the gas manifold fits within the bakeout oven and is routinely baked to 400°K along with the UHV system proper. For this reason and because the manifold is capable of UHV operation, it was decided to treat the chamber and the manifold as a single entity during pumpdown and bakeout. This mode of operation has the advantage that the Hasting's DV-3M thermocouple (TC) gauge which normally serves as the pressure indicator for the manifold may also be used to monitor the chamber pressure during the rough pumping cycle. Therefore the necessity of placing a TC gauge (which is capable of, but not specifically designed for, holding an UHV) on the chamber is eliminated. Also, since the bellows valve between the chamber and the manifold is open during bakeout, a viton O-ring seal is quite adequate and the expense of a metal seal valve is eliminated.

When operating under UHV, the chamber pressure is measured by means of a nude ion gauge which is capable of accurately reading pressures down in the low 10^{-10} Torr range.

The sample was attacked to a manipulator which enabled one to modify the sample position and orientation after it had been sealed inside the chamber. This manipulator had the following capabilities:

1) a linear displacement of 4.7 cm along the centerline of the device.

2) a lateral displacement of 0.5 cm in any direction perpendicular to the centerline.

3) continuous rotation through 360 degrees of arc.

4) a tilt of 5 degrees in any direction from the axis centerline.

In addition, the manipulator contained six electrical feedthroughs rated at 1000 volts and 100 amperes each. The degrees of freedom described above virtually assure that the sample can be positioned for the experiment at the center of curvature of the electron optics as well as moved so that any preparative procedure deemed necessary may be carried out on it.

Provision was made for heating the sample by electron bombardment and/or resistance heating, depending upon the type of sample holder being employed for the particular experiment. The electron bombardment device was a 20 mil tungsten wire mounted between tantalum rods which were attached to a pair of the manipulator feedthroughs. When ohmatic heating was used, copped braid heating leads were attached to another pair of the manipulator feedthroughs.

The sample was able to be purged of impurities which preferentially segregated to the surface or were deposited there by the ambient through the use of an ion bombardment gun. This device works by sputtering the surface atoms off of the sample as the consequence of bombardment with gaseous ions, usually those from the noble gas atoms. The geometry was such that the ion beam impinged on the surface at an angle of 45 degrees from normal incidence, since this configuration has been shown to result in more efficient sputtering than a normally incident beam. An ion current of 1 microampere at energies ranging up to 300 eV was able to be delivered to a 0.40 cm^2 sample when the chamber was backfilled to a pressure of 5×10^{-5} Torr of argon. Under these circumstances and assuming that each argon ion dislodges a single surface atom, it may be calculated that a monolayer of the surface material is sputtered away every 64 seconds.

The last major component of the vacuum system is the standard Varian spherical-grid display type Low Energy Electron Diffraction electron optics assembly. This assembly consists of an electron gun, a four grid energy selection system, and a collector plate coated with fluorescent material. The electron gun contains a bariated nickel cathode which is indirectly heated by an alumina-coated tungsten filament. It is capable of producing a 10 microampere beam of electrons with an upper energy limit of at least 1500 electron volts. Beam focusing is achieved electrostatically, and the beam diameter at the target is less than 1 mm. The fluorescent screen has a radius of 70 mm and an acceptance angle of 97 degrees. The four energy selection grids are isocentric with the fluorescent screen, and the electron gun protudes down the centerline of the grid-screen system. The grids are constructed of 100-mesh, nickel-plated tungsten, and each grid has a transparency factor of 0.80. The operating characteristics of the grid system will be discussed in detail in the following sections.

The vacuum chamber also contains two viewing ports. A 16.5 cm diameter window allows one to view the fluorescent screen for LEED work. Together with a 3.7 cm window which is at right angles to the large window, one is able to accurately monitor the positioning of the target at the center of curvature of the electron optics assembly.

B. Technique

1. General Considerations

A schematic diagram of the Auger Electron Spectroscopy apparatus used in this investigation is shown in Fig. II-4. Figure II-5a is a photograph of the supporting electronics. The right-hand rack contains: 1) the Princeton Applied Research HR-8 lock-in amplifier, 2) an extensively modified Varian Model 981-0538 Auger Analyzer which contained

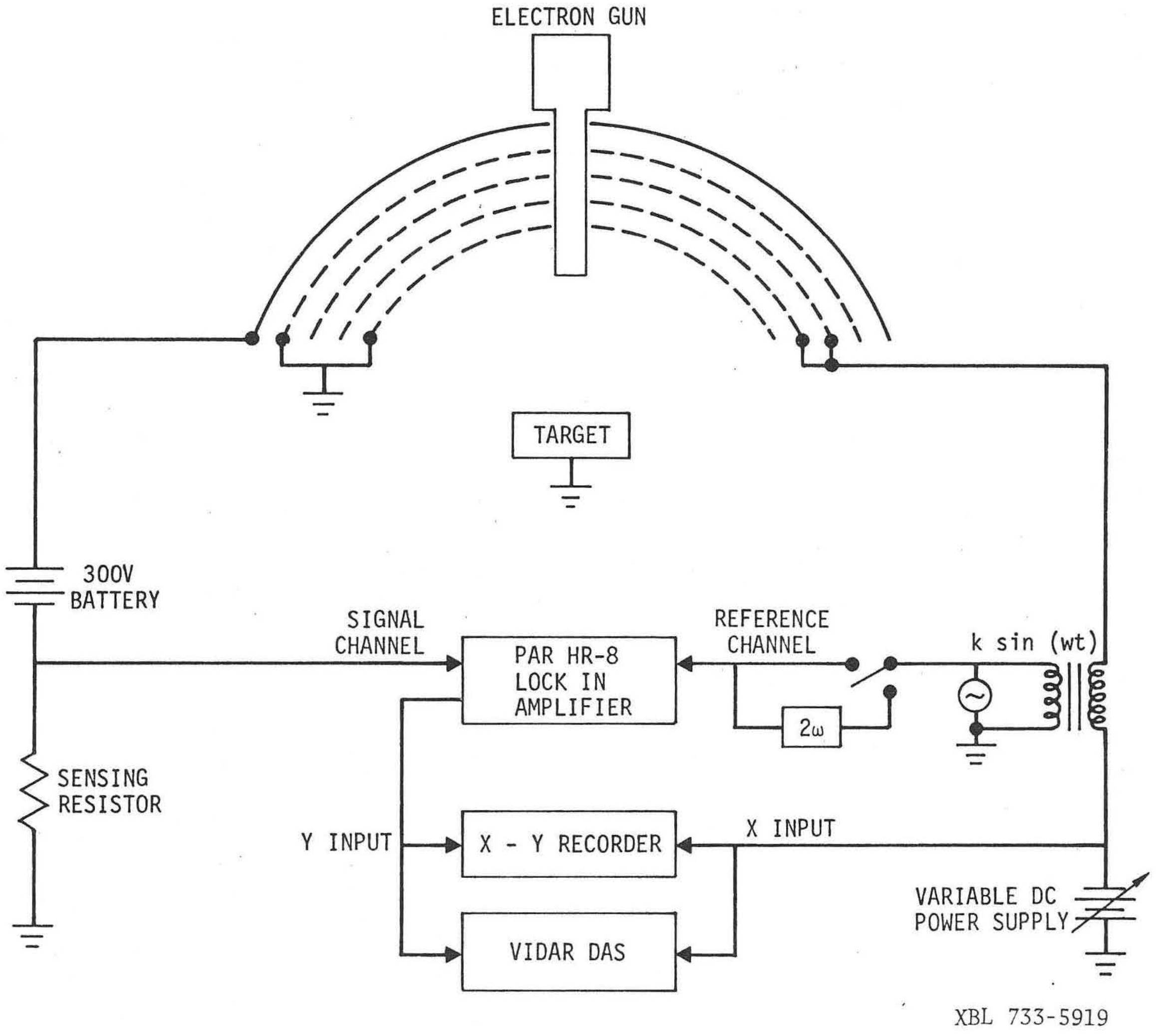

Fig. II-4. Schematic diagram of the Retarding Field Energy Analyzer and its supporting electronics when used for Auger Electron Spectroscopy.

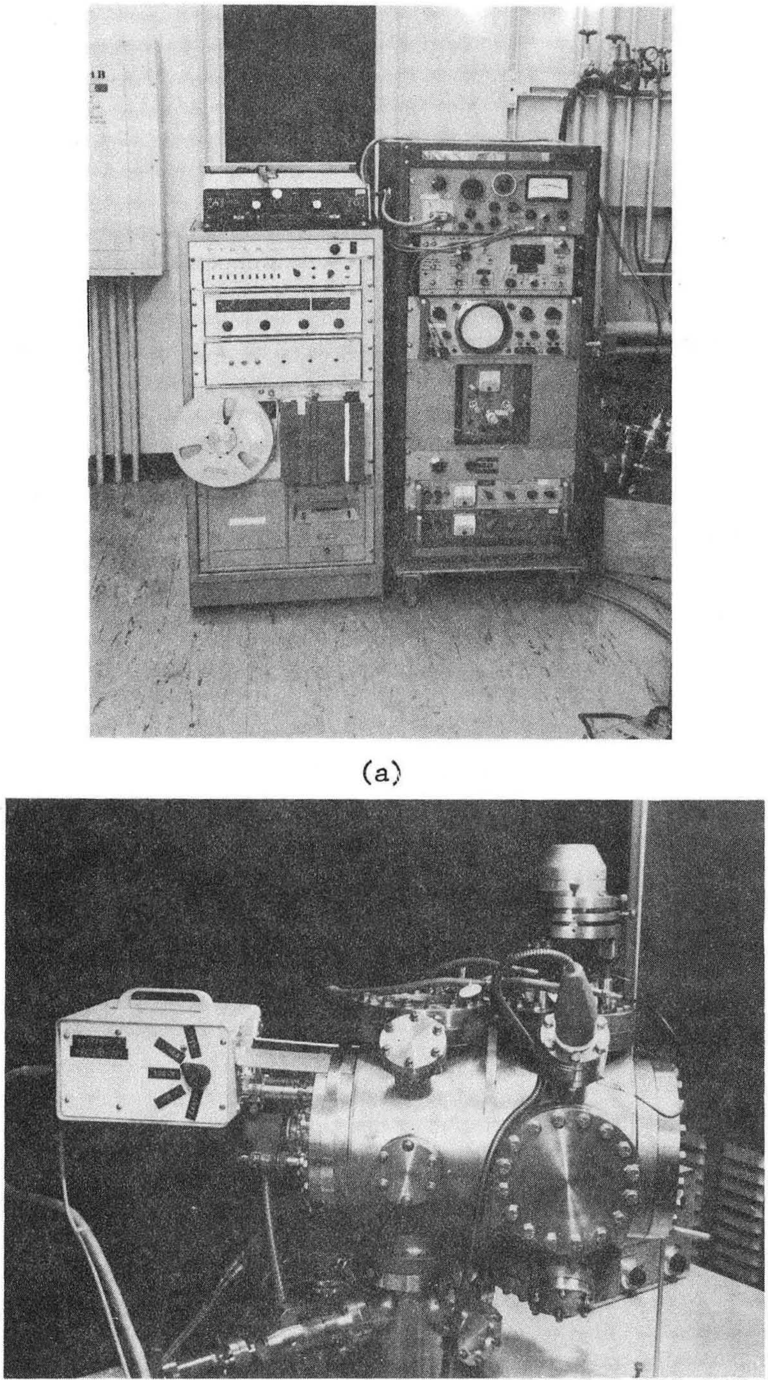

(a)

(b)

XBB 734-2397

Fig. II-5. a) Photograph of the AES electronics (right and the Vidar DAS (left) used in this investigation. b) Close-up photograph of the vacuum chamber showing the attachment of the remote preamplifier to the collector feedthrough on the RFEA flange. Also visible are the crystal manipulator, the ion bombardment gun, the leak valve, and the ion guage.

the dc ramp voltage generator and a proportional output for driving the X-axis of the recorder, a Burr-Brown 4023/25 precision oscillator, and a three-winding transformer for coupling the ac modulation voltage to the ramp and which provided the input to the variable amplitude-variable phase network used in neutralizing the ac capacitive pick-up between the collector and the modulated grids, 3) a monitoring oscilloscope, and 4) well-regulated dc power supplies to heat the electron gun filament and to provide high voltage to the gun components. The small box hanging on the right-hand side of this rack is a frequency doubler of the same design as PAR has incorporated into their later-model amplifiers. The left-hand rack contains the data recording devices. These include: 1) an X-Y recorder, and a Vidar Data Acquisition System which converted the analog output from the PAR into a digital record which could be 2) punched out on a Tally paper tape unit for processing by a computer, or 3) printed out on a Hewlett-Packard digital recorder. The photograph in Fig. II-5b shows the connection between the collector feedthrough and the remote amplifier box which contained the 300 volt battery, three sensing resistors, and the Type C pre-amplifier for the HR-8. Operation in this configuration, rather than transmitting the signal to the electronics rack before amplification, resulted in an increase in the signal-to-noise ratio by at least a factor of two.

The inner shell vacancies necessary to initiate the Auger reorganization in the target atoms, as implied by the schematic diagram, are produced by electron beam excitation. It should be noted that although an electron gun was used for this purpose, the incident beam does not have to be monoenergetic since its energy does not enter into either calculations of the Auger electron energy or of the Auger peak widths.

The electrons emanating from the grounded target traverse an essentially field-free region to the grounded first grid of the energy analyzer, undergoing a small (but, as we have seen, important) acceleration or deceleration due to the contact potential existing between them. Any magnetic fields in this region of space are effectively nulled out through the use of a small trimming magnet. This is accomplished by observing the normally diffracted LEED beam and adjusting the trimming magnet so that the pattern does not drift as the beam energy is varied below 20 eV. This assures that the magnetic field is reduced below 0.1 Gauss and, consequently, that the maximum uncertainty in energy is below 0.05 eV.

The second and third grids are strapped together and are used for energy selection by imposing a negative dc voltage upon them. We therefore have a Retarding Field Energy Analyzer (RFEA), since only those electrons with an energy greater than that corresponding to the grid potential will pass through these grids. These electrons will be collected at the fluorescent screen by virtue of the positive potential placed upon it. The fourth grid is grounded and serves as a shield for the energy selection grids from the screen potential, thereby improving the system resolution by eliminating field penetration effects from this source.

If the analyzer of Fig. II-4 is considered to be a dc device (i.e. ω is zero), as the retarding voltage is swept using the ramp generator the plot of the analyzer current vs electron energy obtained is an integral curve of the energy distribution of the electrons entering the apparatus. That is, the response function of a dc RFEA of spherical geometry is:[59]

$$I(V_0) = e \int_{eV_0}^{\infty} N(E)\,dE \qquad \text{(II-1)}$$

where

$I(V_0)$ = the current reaching the collector when the energy selection grids are at a potential V_0

$N(E)$ = the energy distribution of the current entering the analyzer

where any effect due to space charging or due to interception and secondary emission of electrons at the analyzer components has been ignored.

In our application, however, it is the electron energy distribution, N(E), which is the desired quantity. This distribution may be extracted from the dc data by differentiating it either graphically or through digital techniques. A superior alternative to this course of action is available, though, and it is centered on an analog method of performing the required differentiation during the course of the experiment. This method is based on the fact that if a small ac nodulation is superimposed on the retarding potential then the signal current contains an ac component of the same frequency and its amplitude is proportional to N(E). The process is graphically illustrated in Fig. II-6[60] where:

V_0 = the instantaneous value of the dc retarding voltage
$\Delta V = k \sin \omega t$ = the ac modulating voltage
k = the modulation amplitude
ω = the angular frequency of modulation
t = time
$I(V_0)$ = the dc current obtained at the retarding voltage V_0
$\Delta I(V_0)$ = the ac current (of frequency ω) obtained at the retarding voltage V_0 due to the ac modulation ΔV

As V_0 is changed with ΔV being kept constant, the magnitude of $\Delta I(V_0)$ will produce a difference curve corresponding to the integral curve such as is shown in Fig. II-7a and b. Obviously as the magnitude of ΔV is decreased, this difference curve will approach a true differential curve.

The great advantage that ensues from using this method of differentiation rests in the fact that the system has been modified to enable the use of ac signal recovery techniques (i.e. lock-in amplifier detection) thereby greatly mitigating the voltage level and stability problems that are inherent in a dc detection scheme.

The current that is collected at the fluorescent screen is converted into a voltage across the sensing resistor, amplified, and transmitted to the lock-in amplifier. The lock-in amplifier is a synchronous phase-sensitive detector, which means that it can be

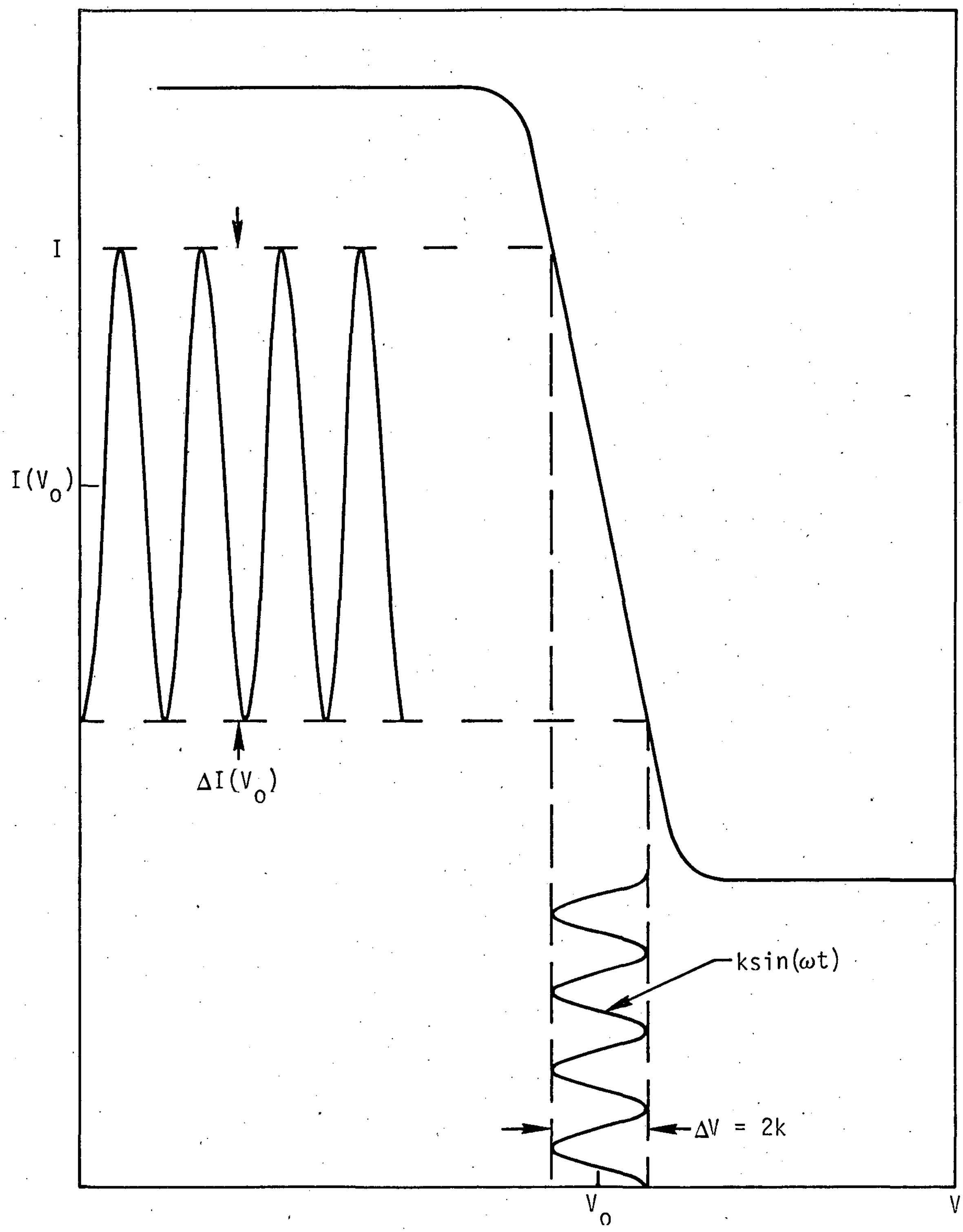

XBL 733-5920

Fig. II-6. The integral curve of current vs. the retarding voltage showing the ac output current, $\Delta I(V_o)$, which results from the ac modulating voltage ΔV superimposed on the retarding potential V_o.

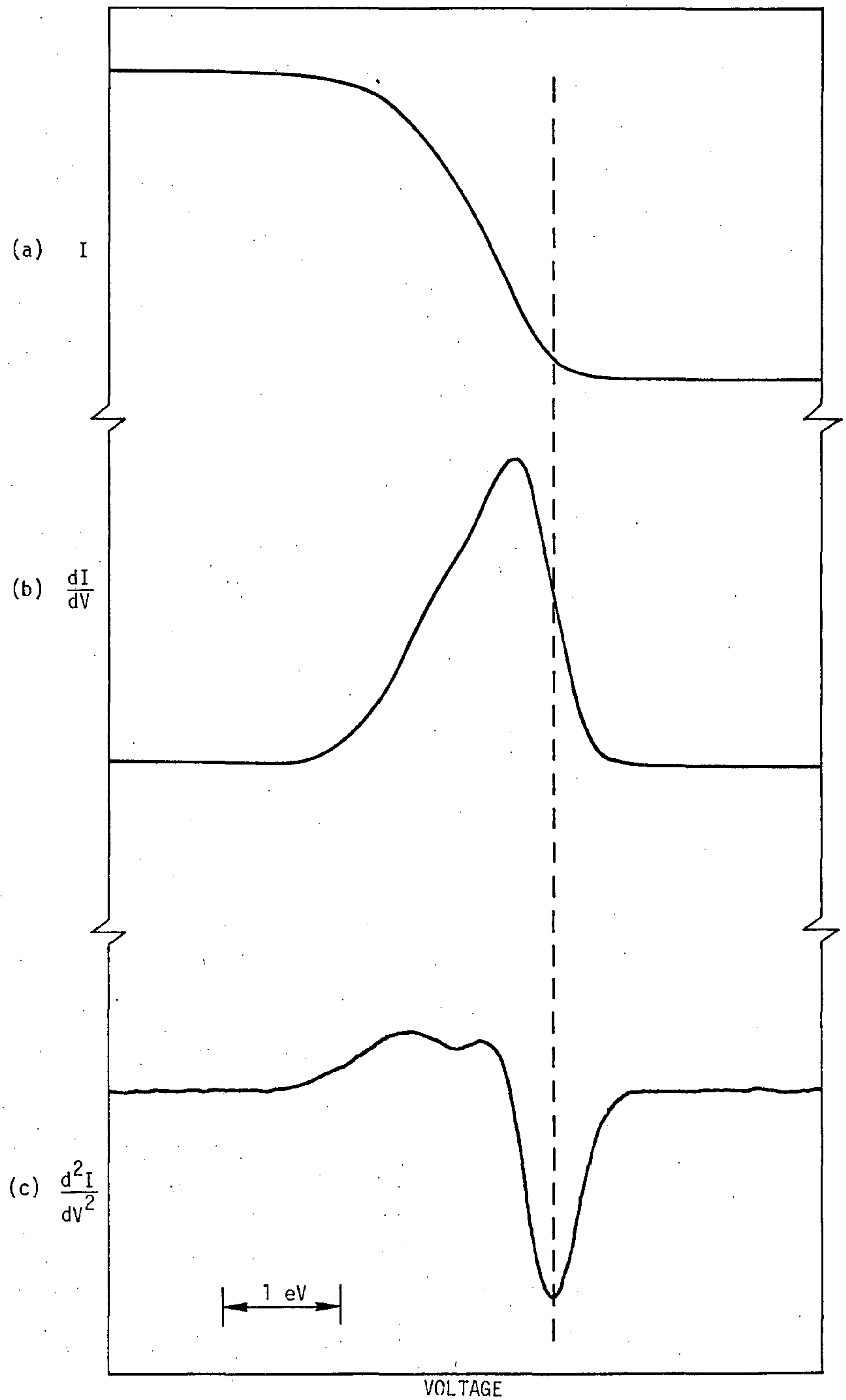

Fig. II-7. Graphs of the collected, I, and its derivatives dI/dV and D^2I/dV^2, as a function of the RFEA retarding voltage. These plots were obtained for the 100 eV elastically diffracted peak from a V(100) surface using a 0.1 volt p-t-p modulation magnitude.

tuned to discriminate against all signals except those which occur at the frequency of, and with the proper phase relation to, the reference signal supplied to it. The detector response is, of course, proportional to the intensity of the desired input signal. This response is correlated with the instantaneous value of the retarding sweep voltage and is stored in a permanent manner. The methods used for data storage in these experiments were:

1 - hard copy analog readout on an X-Y recorder

2 - conversion to a digital format by the Vidar DAS with the data being punched out on a paper tape. This method was used exclusively for the measurement of chemical shift effects since it lends itself to a higher resolution experiment (i.e. enables the use of a smaller modulating voltage) by allowing the use of run-averaging techniques to enhance the signal to noise ratio. After scanning across a peak several (≈ 20) times, the tape was read into a CDC 6600 computer for data reduction. The functioning of the Vidar DAS and the computer program used for the data analysis are discussed in detail in Appendix II.

Since Auger peaks induced by electron bombardment are oftentimes superimposed on a steeply sloping background (due to rediffused primary and/or secondary electrons), it may be advantageous to null out this background contribution to the signal, particularly when attempting to detect small peaks.[61] If the slope of the background is linear in the vicinity of a given peak (usually an excellent first approximation), it is clear that the background will assume a constant value if the derivative of the energy distribution curve is taken. Although it is not abundantly obvious intuitively, this differentiation may also be easily performed electronically merely by detecting the signal occurring at the second harmonic of the frequency at which the retarding grid is being modulated, i.e. by tuning the lock-in amplifier to 2ω. The only modification necessary to the existing circuitry is to install a frequency doubler between the oscillator and the reference channel input to the lock-in amplifier.

As will be shown below, the peak intensity in this derivative of the energy distribution mode of operation is typically an order of magnitude less than the intensity of an energy distribution peak using the same modulating voltage. Due to the reduction in the signal-to-background ratio, however, this intensity difference can usually be more than offset by the ability to increase the amplifier gain far beyond that conveniently possible in the latter case. Also, the rapid variations of the energy distribution derivative mode-an inflection point becoming a peak-make its use desirable from the standpoint of sensitivity. The drawbacks to its use are that: 1) it is more intractable conceptually than is an energy distribution curve, and 2) its signal-to-noise ratio is an order of magnitude less than that of the energy distribution mode for equivalent resolution parameters. In short, the derivative of the energy distribution mode of operation merely offers the ability to scan over large energy ranges without re-adjusting the detector response variables. If the experimental system is able to be chosen or the parameters varied so that the background slope does not overwhelm the peaks being measured, it is advantageous to operate in the energy distribution mode for the two reasons cited above.

Returning to Fig. II-7, the results of each of the above-mentioned techniques is illustrated by plotting in:

a - the current, $I(V) = I$

b - the first derivative of the current with respect to voltage (i.e. the energy distribution of the electrons),

$$\frac{dI(V)}{dV} \equiv \frac{dI}{dV} = I^{i} = N(E)$$

c - the second derivative of the current with respect to voltage (i.e. the derivative of the energy distribution),

$$\frac{d^{2}I(V)}{dV^{2}} \equiv \frac{d^{2}I}{dV^{2}} = I^{ii} = N^{i}(E)$$

vs the retarding grid voltage. The results shown are for an elastically diffracted peak at an energy of 100 eV from a vanadium (100) surface, and the modulation amplitude for the first and second derivative curves was 0.1 volts peak-to-peak. The amplitudes are arbitrary, but the signal-to-noise ratio may be seen to decrease upon successive differentiation.

2. Intensity Relationships

The relationship between the fundamental and second harmonic signals to the energy distribution and its derivative may be quantified by performing a Taylor series expansion of the current vs voltage.

The mathematics is presented in Appendix III, and it is clearly seen there that the signal current has components at the frequency of modulation and at its harmonics in addition to a dc contribution. Since the amplitudes of the fundamental and second harmonic frequencies are:

$$A_1 = [kI^{i} + \frac{k^3}{8} I^{iii} + \frac{k^5}{192} I^{v} + \ .\ .\ .] \qquad \text{(II-2)}$$

and

$$A_2 = [\frac{k^2}{4} I^{ii} + \frac{k^4}{48} I^{iv} + \frac{k^6}{1536} I^{vi} + \ .\ .\ .] \qquad \text{(II-3)}$$

respectively, it is obvious that the proportionality between A_1 and I^{i} and between A_2 and I^{ii} is dependent upon the modulation amplitude, k, being sufficiently small so that the error terms in Eqs. (II-2) and (II-3)(i.e. those terms after the first on the right-hand side of the equations) are negligible. In order to evaluate the contribution of these error terms to the amplitude, some form of the energy distribution function must be assumed. Results are presented here for both the Gaussian and Lorentzian distributions, whose respective definitions are:

$$I_G{}^{i}(V) = i \left(\frac{1}{\sqrt{2\pi}\ \sigma}\right) \exp\left(\frac{-V^2}{2\sigma^2}\right) \qquad \text{(II-4)}$$

and

$$I_L{}^{i}(V) = i(\frac{1}{\pi}) \left(\frac{(\Gamma/2)}{V^2+(\Gamma/2)^2}\right) = i(\frac{1}{\pi}) \left(\frac{(\sigma/c)}{V^2+(\sigma/c)^2}\right) \qquad \text{(II-5)}$$

where

i = the total current in the peak

σ = the point of maximum slope (PMS) of each distribution

V = the deviation from the mean voltage of each peak

$(\Gamma/2)$ = the half-width at half height (HWHH) of the Lorentzian peak

c = 0.5775

The successive five derivatives of these distributions are listed in Appendix IV.

It should perhaps be noted here that in the "true" definition of the Gaussian distribution σ is the standard deviation of the peak. However, in this case σ coincides with the PMS (as may be proven by setting $I_G^{iii} = 0$ and solving for V) and this is precisely the point at which it was found convenient to measure the peak energy on the d^2I/dV^2 curves! Also, the Lorentzian distribution is actually defined in terms of the HWHH, $(\Gamma/2)$. Since the PMS is the quantity of interest here, though, σ has been calculated and is seen to occur at 0.5775 $(\Gamma/2)$ - see Appendix IV.

The deviations of the dI/dV and d^2I/dV^2 peak amplitudes from proportionality to the fundamental and second harmonic frequencies respectively are defined as:

$$\Delta A_1 = \frac{A_1 - kI^i}{kI^i} \qquad \text{(II-6)}$$

and

$$\Delta A_2 = \frac{A_2 - (-k^2 I^{ii}/4)}{(-k^2 I^{ii}/4)} \qquad \text{(II-7)}$$

These quantities have been calculated at the peak maximum (V=0) and at the point of maximum slope (V=σ) for the assumed Gaussian and Lorentzian distributions and, expressed as percentages, are plotted as a function of k/σ in Fig. II-8a and b respectively. The algebraic calculations are outlined in Appendix IV.

It is apparent from the graphs in Fig. II-8 that the signal amplitudes, for both the Gaussian and Lorentzian cases, are given by

$$A_1(V) = kI^i(V) \qquad \text{(II-8)}$$

and

$$A_2(V) = \frac{k^2}{4} I^{ii}(V) \qquad \text{(II-9)}$$

with errors at the peaks of the amplitudes of less than 5% when $k < \sigma/2$. Assuming these conditions of proportionality, an estimate may be made of the peak amplitudes relative to the total current in the Auger peak. For the Gaussian distribution, the maximum current in the peak is

$$\begin{aligned} A_{1,G}(0) = kI^i_G(0) &= ki\left(\frac{1}{\sqrt{2\pi}\,\sigma}\right) \exp(0) \\ &= 0.3992 \left(\frac{k}{\sigma}\right) i \qquad \text{(II-8a)} \\ &= 0.1996\, i \quad \text{at } k=\sigma/2 \end{aligned}$$

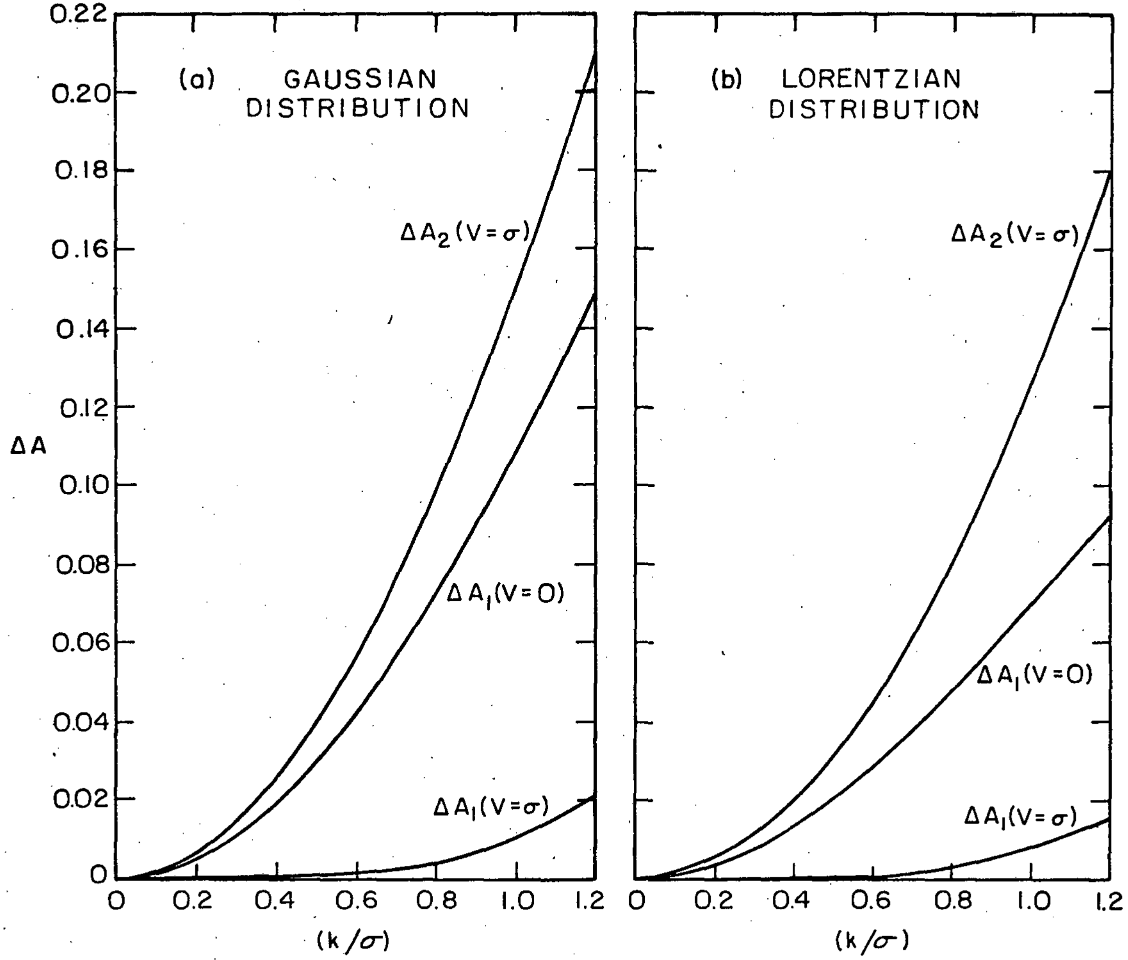

XBL 733-5936

Fig. II-8. Peak amplitude errors as a function of modulation magnitude for Gaussian- and Lorentzian-type peaks. $\Delta A_1(0)$ and $\Delta A_1(\sigma)$ show the percentage deviation below proportionality for the fundamental signal as a function of the modulation amplitude at the peak maximum and at the point of maximum slope respectively. $\Delta A_2(0)$ and $\Delta A_2(\sigma)$ provide the equivalent information for the second harmonic signal.

and the maximum current in the peak derivative is

$$A_{2,G}(\sigma) = \left(\frac{k^2}{4}\right) I_G^{ii}(\sigma) = \left(\frac{k^2}{4}\right)\left(\frac{-\sigma}{\sigma^2}\right) i \left(\frac{1}{\sqrt{2\pi}\,\sigma}\right) \exp(-1/2)$$

$$= -\,0.06053\,\left(\frac{k}{\sigma}\right)^2\, i \qquad \text{(II-8b)}$$

$$= -\,0.01513\, i \quad \text{at } k=\sigma/2$$

Similarly, for the Lorentzian distribution, we have:

$$A_{1,L}(0) = 0.1838\,\left(\frac{k}{\sigma}\right)\, i \qquad \text{(II-9a)}$$

$$= 0.09190\, i \quad \text{at } k=\sigma/2$$

$$A_{2,L}(\sigma) = -0.01723\,\left(\frac{k}{\sigma}\right)^2\, i \qquad \text{(II-9b)}$$

$$= -0.004308\, i \quad \text{at } k=\sigma/2$$

The preceeding equations may, of course, be reversed and the current in a peak determined. From this the relative or absolute transition probability, depending on the amount of addition information available, of a process may be calculated. On the other hand, since the mere ability to detect a peak (or establish an upper limit as to its presence) may be of importance, the limitations of the method are of interest. As k/σ becomes large, the small perturbation conditions which led to the validity of the Taylor expansion approximation no longer hold. The only available calculation[52] shows that, at least for a Gaussian-type peak, $A_2(\sigma)$ approaches 0.32 i when $k/\sigma \gg 1$.

3. Resolution Considerations

Since this investigation is not merely concerned with the detection of peaks but also with the ability to perceive shifts in the peak energy, it is of interest to investigate the resolution attainable in the RFEA instrument.

If a monoenergetic beam of electrons of energy E=eV is injected into the analyzer, a peak of full width at half-height (FWHH), ΔE, is recorded due to various instrumental limitations. The quantity ΔE is referred to as the half-width of the line. The ratio $E/\Delta E$ defines the resolution of the instrument while its reciprocal expressed as a percentage, $100\times\Delta E/E$, is labelled the instrumental linewidth (ILW). The factors which limit the instrumental resolution may be generally grouped into those which are independent of the electron energy (i.e. ΔE = constant) and those which are proportional to the electron energy ($\Delta E/E$ = constant).

1. Independent of electron energy
   - a. The ac modulation on the retarding grid. It is obvious that the base width energy spread of a monoenergetic beam entering the analyzer will contain a component which is equal to the peak-to-peak modulation amplitude impressed upon the retarding potential. That is, $\Delta E = 2k$.
   - b. The variation of the work function over the surface of the retarding grid. The energy base width will reflect the total energy spread of the grid work function. The shape of the intensity distribution of the monoenergetic beam

throughout this spread will reflect the fraction of the grid surface at each value of the work function. Measurements indicate that the contribution to ΔE from this source is less than 0.2 eV.[53]

c. Magnetic field effects. Calculations of the maximum base width due to angular deviations caused by a transverse dc magnetic field predict a $\Delta E = 0.15$ eV for a field strength of 0.6 Gauss (i.e. the magnitude of the earth's field). Field cancellation by means of a small trimming magnet can reduce these values to 0.1 Gauss and $\Delta E < 0.05$ eV. Ac fields will produce similar results and should be guarded against. Elimination of the problem by spacial isolation of the current source and/or mu-metal shielding is trivially accomplished.

2. Proportional to electron energy

a. The effect of potential variations in the vicinity of the retarding grid. The spherical surface defined by the grid is not an equipotential surface since a potential variation exists across the space between the grid wires. Calculations based on the work of Liebmann[62] and of Huchital and Rigden[63] indicate that for a single 100 mesh 0.025 mm wire grid at potential V placed between and separated by 3.18 mm (0.125 inch) from each of two similar grounded grids a potential difference ΔV exists between the center of the grid aperture and the grid wires such that $\frac{\Delta E}{E} = \frac{\Delta V}{V} \approx 2\%$.

Improvements in this ILW can be achieved by increasing the grid spacing, (thereby reducing field penetration effects), using finer mesh grids, and increasing the depth of the retarding grid mesh. An effective way of accomplishing the latter is to add another grid to the analyzer and forming a double retarding grid system by coupling the middle two together.[49] This approach results in an basic ILW < 0.46 eV as measured on the analyzer used in this investigation. (See the next section)

b. Abberations caused by the potential distribution about the retarding grid. If, in the approximation of a plane retarder, electrons of energy $E = eV$ are considered to impinge upon a pair of grids which have retarding electric field of magnitude $E_r = V_r/d$ (where d is the intergrid spacing) between them, it may be seen that the cells of the mesh of grid 1 act as divergent leases where focal length is determined by[64]

$$\frac{1}{f_1} = \frac{V_r/d}{4V}$$

Similarly, grid 2 is seen to consist of an array of convergent lenses with a focal length given by

$$\frac{1}{f_2} = \frac{V_r}{4d(V-V_r)}$$

It is obvious that the lens effects of grid 2 are much stronger than those of grid 1, especially in the near-cutoff condition when $V_r \approx V$. If Θ is the angle of divergence from the grid normal of an electron travelling through the retarding field region, simple energy considerations require that the potential needed to stop this electron be ΔV less than that needed for a normally incident electron where

$$\frac{\Delta V}{V} = \sin^2 \Theta \qquad \text{(II-10)}$$

In the cutoff condition, the focal length of grid 1 is seen to be 4d, and therefore electrons will traverse the inter-grid field at an angle

$$\Theta = \tan^{-1} \left(\frac{r}{4d}\right) \qquad \text{(II-11)}$$

where r is the radius of the grid aperture. Substituting the geometrical values previously presented, it is found that

$$\frac{\Delta E}{E} = 0.008\%$$

As alluded to above, the effect of the convergent lens of grid 2 at cutoff is not so easily perceived. However, Huchital and Rigden have performed computer predictions of electron trajectories at the 2nd grid in order to determine the magnitude of this effect, and from their results one may calculate that

$$\frac{\Delta E}{E} = 0.8\%$$

for our geometrical situation.

c. The effects of beam size and improper sample positioning. Any electron originating at a point other than the center of curvature of the analyzer will enter the retarding field region in an off-normal fashion and the instrumental resolution is, once again, degraded as predicted by Eq. (II-10). Since the electron beam diameter is less than 1 mm and since the sample may be easily placed to within ± 1 mm of the center of curvature, geometrical considerations (assuming a mean radius of 60 mm for the double retarding grid) show a

$$\frac{\Delta E}{E} \leqslant 0.063\%$$

contribution to the ILW from this source.

d. Deviations of grids from ideal spherical symmetry. Such deviations (ragged edges, wrinkles, etc.) result in local non-radial fields between grids and, therefore, non-radial electron trajectories. Cutoff of these electrons occurs at a reduced retarding grid voltage as predicted by Eq. (II-10).

4. Experimental Determination of Resolution

An experimental investigation of the resolution of our four grid RFEA was carried out using elastically diffracted electrons from a vanadium (100) surface as a source of a "monoenergetic" beam. The results which are presented in Fig. II-9a and b show the variation with incident beam energy of the full width at half height (FWHH) and of the half width at half height (HWHH) of the electron energy distribution peak. The HWHH is measured between the peak maximum and the half-maximum point on the high energy side of the peak. A least squares fit was done to each of these curves, and the resulting equations were FWHH = 0.72 + 0.00461 V and HWHH = 0.32 + 0.00124 V.

Since the elastic peak was used in this analysis, a correction for the energy spread inherent in the source must be carried out. The smallest energy width possible in the incident beam is that given by a Maxwellian distribution at a temperature corresponding to that of the electron gun cathode. In actuality, the magnitude of the energy spread has been found to depend on the current flux, and the Maxwellian value must be considered a minimum.[65] At the filament currents used here, the predicted Maxwellian FWHH is 0.24 eV and the high energy HWHH is 0.16.[66] Correction of the curve fit for this effect and that of the modulating voltage used in the analysis (0.02 v p-t-p) results in the equations

$$\text{FWHH} = 0.46\text{ eV} + 0.00461\, E_p \qquad \text{(II-12)}$$

$$\text{HWHH } (\times 2) = 0.30\text{ eV} + 0.00248\, E_p \qquad \text{(II-13)}$$

Fig. II-9 a. The FWHH variation of the elastically diffracted electron peak with incident beam energy; the modulation magnitude is 0.02 v p-t-p.

b. The variation in the HWHH, measured from the peak maximum to the high energy edge of the peak, of the elastically diffracted electron peak as a function of incident beam energy; the modulation magnitude is 0.02 v p-t-p.

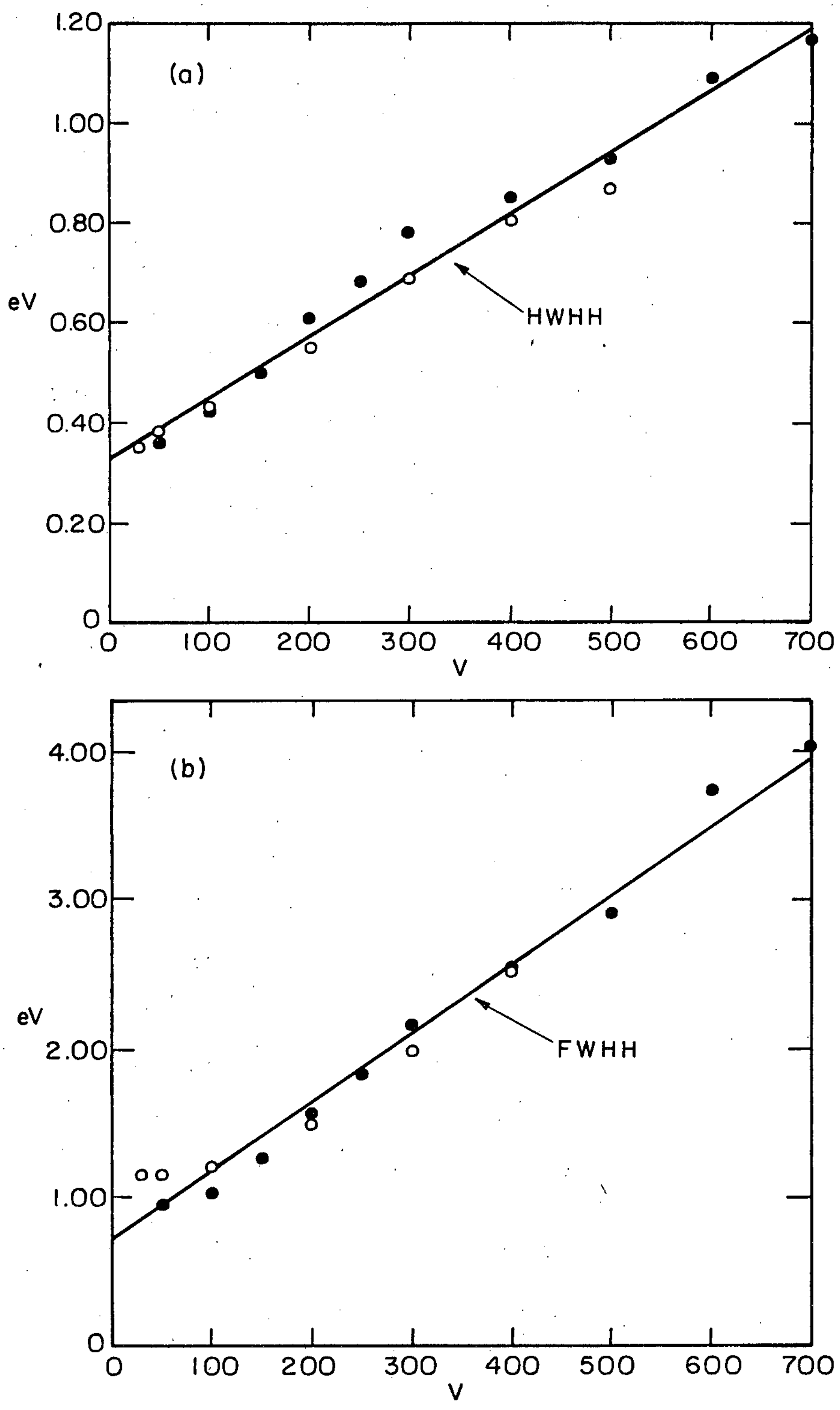

XBL733-5937

Fig. II-9.

The latter equation agrees well with the predicted magnitude of the ΔE = constant term. The additional magnitude evident in the FWHH equation is most likely due to the inelastic scattering of electrons out of the peak.

The value obtained above for the $\Delta E/E$ = constant factor suggests that the contributions to this term have been overestimated. To resolve this minor dilemma, refer again to Fig. II-7b and note the structure which appears on the low energy side of the peak. The position of this shoulder relative to the peak maximum is observed to vary monotonically with the incident beam energy, the peak separation being 0.7 to 0.8 eV for the 100 eV elastic peak shown in the figure. These facts strongly suggest that this subsidiary peak is the consequence of the convergent focusing of the electrons at the retarding grid. The magnitude of this effect relative to the broadening of the main peak occasioned by the other factors discussed above rapidly moves this subsidiary peak beyond the half height point of the main peak and therefore its effect does not demonstrate itself in Eqs. (II-12 and II-13).

The FWHH equation also undoubtedly contains a $\Delta E/E$ = constant term due to the increased inelastic scattering of electrons out of the elastic peak as its energy (and, therefore, penetration depth) is increased. The magnitude of this effect being unknown, it can only be said that the "proportional to electron energy" ILW lies somewhere between the limits set in Eqs. (II-12) and (II-13).

It is also of interest to note that the FWHH and the HWHH were observed to remain constant until the modulating voltage was increased past the point $k/\sigma = 0.7$.

5. Signal-to-Noise Ratio[53]

In the final analysis of any detection system, it is the ability to obtain a useful signal at a reasonable time rate that is of importance. This ability, of course, depends on the amount of noise present in the system relative to the desired signal. Since noise is present throughout the entire frequency spectrum, using the phase-sensitive synchronous-detection principle raises the question of how narrow a detection bandwidth, B, can be tolerated to reduce noise. By reducing B, the amplitude of the noise is reduced but the rate at which data can be taken is also reduced. In order to determine the resolution-sensitivity-time tradeoff capabilities of the RFEA system, the effect of the main noise sources present in the system shall be probed. These are:

1. The noise associated with the fluctuations of the current leaving the sample and reaching the detector, i.e. shot noise. The mean square of the fluctuation current (in amperes) is

$$I^2 = 2e\, I_0 B \qquad \text{(II-14)}$$

where

I = the fluctuation current

e = the electronic charge

I_0 = the sample current reaching the detector

B = the bandwidth (in Hertz)

The rms voltage developed across a resistance R is then

$$e_{rms} = IR = (2e)^{1/2} (I_0B)^{1/2}R = (5.66\times10^{-10})(I_0B)^{1/2}R \ . \quad \text{(II-15)}$$

For $I_0 = 10^{-5}$ amperes, B = 0.125 Hz (i.e. a time constant of 1 second at a 12 db/octave rolloff) and R = 1 megohm, $e_{rms} = 6.35\times10^{-7}$ volts.

2. The thermal (Johnson) noise in the sensing resistor. At room temperature, the rms noise associated with a bandwidth B and developed across a resistor of R ohms is

$$e_{rms} = (1.26\times10^{-10})(RB)^{1/2}$$

This corresponds to a rms voltage of 4.5×10^{-8} volts for a 1 megohm resistor and a bandwidth of 0.125 Hz.

3. The gain modulation (flicker effect) noise associated with the transistor amplifying circuitry. This noise spectrum varies inversely with the detection frequency and can be made negligible by operating at frequencies above 1 kHz.

Since, under the typical experimental conditions specified above, the shot noise is the noise limiting factor, its relationship to the signal contained in an Auger peak will be explored. The subsequent calculations will consider peaks which are assumed to be Gaussian and Lorentzian in nature, the $k/\sigma = 0.5$, and the detected peak current is related to the primary beam current by

$$i = yTI_p \quad \text{(II-16)}$$

where

i = the detected current in the Auger peak.

y = the Auger yield, i.e. the ratio between the total current in the Auger peak under consideration and the primary beam current.

T = the analyzer transmission factor, i.e. the fraction of the total Auger current which is entering the analyzer. This factor also takes into account interception at the grids.

I_p = the primary beam current.

For a Gaussian distribution peak, the rms signal voltage induced across the sensing resistor at the maxima of the dI/dV and d^2I/dV^2 peaks are

$$v_{1,G} = \frac{1}{\sqrt{2}} A_1 R = 0.2823 \left(\frac{k}{\sigma}\right) i R = 0.2823 \frac{k}{\sigma} y_{1,G} T I_p R \qquad \text{(II-17a)}$$

and

$$v_{2,G} = \frac{1}{\sqrt{2}} A_2 R = 0.04280 \left(\frac{k}{\sigma}\right)^2 i R = 0.04280 \left(\frac{k}{\sigma}\right)^2 y_{2,G} T I_p R \qquad \text{(II-17b)}$$

respectively. The equivalent voltages for a Lorentzian distribution are

$$v_{1,L} = 0.1300 \left(\frac{k}{\sigma}\right) y_{1,L} T I_p R \qquad \text{(II-18a)}$$

and

$$v_{2,L} = 0.01219 \left(\frac{k}{\sigma}\right)^2 y_{2,L} T I_p R \quad . \qquad \text{(II-18b)}$$

Referring back to Fig. I-1, it will be further assumed that the peak of interest is of energy $E_{W_o X_p Y_q}$ and lies in region III of that curve. Since the elastic backscattering coefficient is typically around 1% for primary beam energies above 100 eV and since the cascade effect does not start asserting itself until an energy on the order of 50 eV, for our purposes an adequate approximation to the electron distribution will be obtained by considering region III to extend from E=0 to $E=E_p$ and that it contains a uniform distribution of current whose integrated magnitude is rI_p, r being the inelastic backscattering coefficient.

Using the retarding field method to measure the peak occurring at $E_{W_o X_p Y_q}$, that fraction of electrons with energies greater than this energy will pass through the retarding field and reach the collector. If the effect from secondary emission at the grids is ignored, then it is these electrons which are responsible for the shot noise in the analyzer. The dc current reaching the collector is therefore

$$I_0 = T\left(\frac{E_p - E_{W_o X_p Y_q}}{E_p}\right) rI_p = qI_p \tag{II-19}$$

where q is defined in the equation.

Since the rms shot noise voltage is

$$v_n = (5.66\times10^{-10})(q\ I_p\ B)^{1/2}\ R\ ,$$

the signal-to-noise ratios (S/N) for the dI/dV and d^2I/dV^2 peaks of a Gaussian distribution are

$$\frac{v_{1,G}}{v_n} = \frac{0.2823}{5.66\times10^{-10}} \cdot \frac{(k/\sigma)\; yTI_p\; R}{(q\; I_p\; B)^{1/2} R} = (5.00\times10^{8})\left(\frac{k}{\sigma}\right)\left(\frac{I_p}{qB}\right)^{1/2} Ty_{1,G}\;. \tag{II-20a}$$

and

$$\frac{v_{2,G}}{v_n} = \frac{0.04280}{5.66\times10^{-10}} \; \frac{(k/\sigma)^2\; y\; TI_p\; R}{(q\; I_p\; B)^{1/2}\; R} = (7.56\times10^{7}) \left(\frac{k}{\sigma}\right)^2 \left(\frac{I_p}{qB}\right)^{1/2} Ty_{2,G} \tag{II-20b}$$

For a Lorentzian distribution, these quantities are:

$$\frac{v_{1,L}}{v_n} = (2.30\times10^{8}) \left(\frac{k}{\sigma}\right) \left(\frac{I_p}{q\; B}\right)^{1/2} Ty_{1,L} \tag{II-21a}$$

and

$$\frac{v_{2,L}}{v_n} = (2.15\times10^{7}) \left(\frac{k}{\sigma}\right)^2 \left(\frac{I_p}{q\; B}\right)^{1/2} Ty_{2,L}\;. \tag{II-21b}$$

Equations (II-20) and (II-21) may be inverted to determine the minimum detectable Auger yield for each case under the conditions of the experiment. These quantities are plotted in Fig. II-10a and b as a function of the detection bandwidth B, of the ratio q/I_p, and for the vlaues $k/\sigma = 0.5$ and $v_{1,2}/v_n = 1$ (this signal to noise ratio being arbitrarily selected as the limit of detectability of a peak). The inelastic backscattering coefficient is a function of the incident beam energy, the angle of incidence, and the composition of the target. A typical value for r is 0.3 and the transmission factor for the

Fig. II-10 a. The dependence of the minimum detectable Auger yields for the dI/dV and d^2I/dV^2 peaks of a Gaussian distribution, $y_{1,G}$ and $y_{2,G}$ respectively, on the detection bandwidth B for various values of q/I_p.

b. y_{1L} and y_{2L} provide similar information as that outlined above but for a Lorentzian distribution.

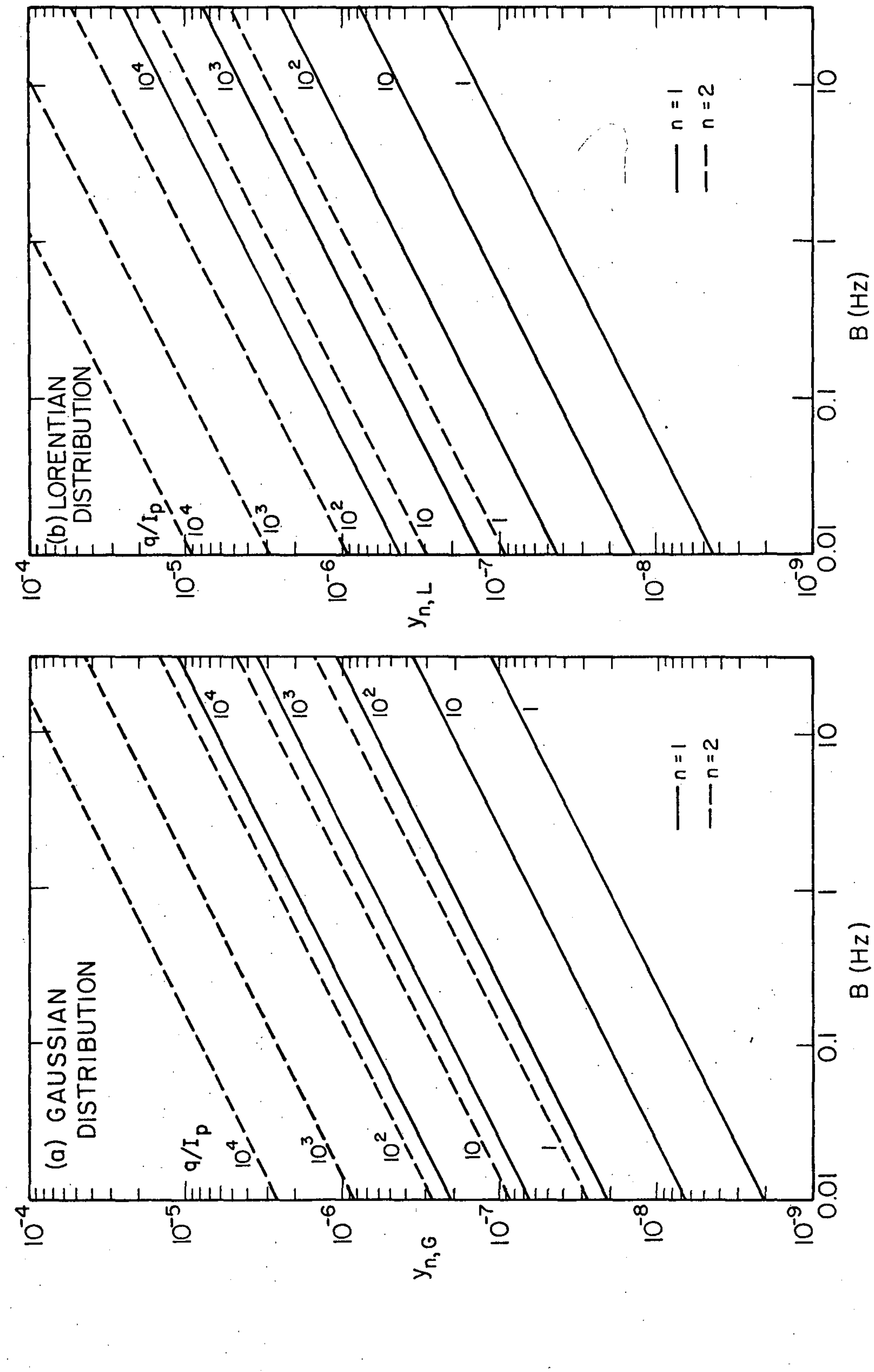

XBL 733-5938

Fig. II-10.

LEED-Auger device is about 0.2, these values therefore resulting in a $q = 0.06\ [(E_p - E_{W_oX_pY_q})/E_p]$. As an example of the use of these graphs, assume that the incident beam energy has been adjusted so that it is four times as large as the energy of the Auger peak of interest, i.e. $E_p = 4\ E_{W_oX_pY_q}$. The quantity q is then equal to 0.03, and the $q/I_p = 10^3$ line will predict the variation with bandwidth of the minimum detectable Auger yield for an incident beam current of $I_p = (0.03/10^3)$ amperes = 30 μamperes.

From Eqs. (II-20) and (II-21), it is obvious that the detection capability of the RFEA system may be enhanced for a given Auger peak in the following ways:

a. Decreasing the detection bandwidth B.

b. Increasing k/σ. It must be remembered, however, that the resolution suffers when large modulation amplitudes are employed and, when signal strengths allow, there are definite advantages in operating at $k/\sigma \leqslant 0.5$ since the resultant peak amplitudes may then be used in a more quantitative manner.

c. Increasing the incident beam current I_p. At high currents (≈ 500 μamps), however, space charging effects at the retarding grid begin to degrade the detection capability of the low energy (< 100 eV) peaks. Localized sample heating may also become a problem at these currents. Therefore, these factors must be considered and an I_p chosen which is consistant with the information desired from a particular experiment.

d. Optimizing the incident beam energy E_p so that it does not result in an unnecessarily increased value of q while the ionization cross-section of $E_{W_o X_p Y_q}$ (as suggested by Fig. I-15) is maximized. Since increasing E_p usually results in a larger beam current, the effects discussed immediately above in c. also factor into this problem.

C. Crystal Preparation

The vanadium metal single crystals used in this investigation were obtained from a 0.25 inch diameter rod purchased from the Materials Research Corporation. This single crystal rod was grown by electron beam zone refining techniques and had a specified purity of 99.94%, the impurity analysis of the bulk material being shown in Table II-1. The rod was oriented to ± 1° of the desired crystal plane through the use of back-reflection Laue X-ray techniques, and 1 mm thick samples were removed by means of a spark cutter. Using standard metallographic procedures, a sample was polished on 1) successively finer grades of emery paper, 2) one micron diamond paste, and 3) 0.05 micron alumina paste. The crystal was then etched in a 1:1 solution of HF and HNO_3 for 3-5 minutes at room temperature in order to remove the mechanical damage and surface contamination introduced during the final polishing, washed with distilled water, and finally rinsed in reagent grade methanol.

Table II-1. Mass spectrometric analysis of 99.94% purity vanadium single crystal.

Impurity	Content (ppm)	Impurity	Content (ppm)
H (a)	2	Mn	< 0.3
B	6	Fe	50
C (a)	150	Co	1
N (a)	2	Ni	20
O (a)	40	Cu	1
F	10	Zn	< 1
Na	2	Ga	< 0.2
Mg	1	As	1
Al	30	Zr	4
Si	200	Nb	30
P	10	Mo	20
S	10	Ru	< 0.5
Cl (b)	⩽ 100	Pd	< 0.2
K	0.3	Sn	< 0.3
Ca	0.4	Sb	< 0.2
Sc	< 0.3	Ta	20
Ti	10	W	3
Cr	⩽ 10	Ag	< 0.5

(a) Contamination due to vacuum fusion methods
(b) Probable etch contamination

Single crystals of non-stoichiometric VO and of V_2O_3 were obtained from and characterized by the Lincoln Laboratory and Semi-Elements Corp. respectively. These were polished with 0.05 micron alumina paste, etched with a dilute HNO_3 solution, and sequentially rinsed with water and methanol.

Powders of VO_2, V_2O_3, V_2S_3, VN, VC, and VSi_2 were obtained from the Research Organic/Research Inorganic Corp. and were hydrostatically pressed (at 50,000-60,000 p.s.i.) into 1 mm thick wafers in a stainless steel jig. The jig was thoroughly scrubbed with water and rinsed with methanol before the sample pressing of each compound took place, and, in addition, the first two samples made from each compound were discarded. This procedure was apparently sufficient to produce clean surfaces since the initial experiments with VO_2 and V_2O_3 revealed no discerible AES difference between pressed powder samples which underwent no further treatment (except for a methanol rinse) and samples which were mildly etched with a HNO_3 solution (followed by water and methanol treatments). Thereafter, all samples were merely rinsed in methanol.

An experiment was also carried out on sintered plates of VN and VC which were purchased from the Materials Research Corp. These sintered samples were subjected only to a methanol rinse.

Three types of holders were employed at various times in this investigation to support the samples upon the manipulator within the vacuum chamber. The one used for the chemical shift work entailed the fabrication of a polycrystalline vanadium slab of the dimensions 4" × $\frac{1}{4}$ " × $\frac{1}{8}$ ". Two holes were tapped at one end and the slab was bolted to the alumina insulator on the manipulator coupling, a lead wire being provided to an electrical feedthrough for grounding purposes. The back of the vanadium metal reference crystal was directly spot welded to this support rod. The compounds were wrapped in 10 mil thick vanadium foil, leaving exposed a much larger area than that probed by the electron beam, and this foil was spot welded to the holder. In this configuration, sample heating was accomplished either by direct electron bombardment of the sample face or indirectly by bombarding the opposite side of the holder. This method of sample heating is clearly undesirable when an active gas is simultaneously present in the chamber. Therefore the vanadium single crystal oxidation experiments were carried out with the sample spot welded between two electrically isolated vanadium support rods. Provision was made so that a current could be passed through this system and thereby resistively heat the sample. A number of individually heatable metal samples were able to be serially studied without breaking the vacuum by using a third type of holder. An alumina slab (6" × 1" × $\frac{1}{8}$") was made with two sets of through holes drilled near each edge along its entire length. A few hundred Ångstroms thick layer of vanadium metal was evaporated onto the slab to prevent surface charging. Vanadium foil tabs were bolted down on one side of the holder and bent around the edge to the opposite side, each sample being spot welded across two of these tabs. Individual heating leads were provided to each tab on one side of the holder, and a common lead was connected to the tabs on the opposite side.

When a multiple crystal holder is employed, it is only necessary to use the linear translation function of the crystal manipulator to bring each sample into the measurement position. Therefore the manipulator (with the support slab attached) could be pre-aligned in a jig so that the slab was parallel to the direction of translation and that each sample-except for minor variations in thickness-would be at the focal point of the hemispherical grid system when under analysis. This alignment procedure was deemed adequate when an experiment performed on the $L_3 M_{2,3} M_{2,3}$ Auger peak of a vanadium single crystal revealed that the peak position did not vary by more than 0.03 eV when the sample was moved 1-2 mm nearer the analyzer. This value is within the uncertainty of the experiment itself.

After placement within the vacuum chamber and bakeout at 150°C, the samples were typically cleaned _in situ_ by bombardment with 300 eV Argon ions at a current density of 5-10 microamperes/cm^2 for periods of 30-60 minutes. This treatment was followed by heating to temperatures ranging from 300-1200°C for 0.1 to 15 minutes depending on the crystal and the purpose of the heat treatment (i.e. to remove adsorbed or occluded gases or, in the case of single crystals, to anneal out the surface damage caused by the ion bombardment). The sample temperatures were measured with the aid of optical and infrared pyrometers.

III. RESULTS AND DISCUSSION

A. Low Energy Electron Diffraction

1. Vanadium Metal Structures

As a prelude to its use as reference crystal in the studies of the AES chemical shifts which occur in the vanadium compounds, an investigation was launched to determine the surface characteristics and behavior of metallic vanadium. To this end both LEED and AES techniques were employed. The (100) crystal face was eventually chosen for use as the reference since it was the most homogeneous and easily understood surface of those which were observed. The clean (100) surface displays the (1×1) diffraction pattern that would be predicted from the projection of the bulk unit cell onto this plane. The LEED patterns from the vanadium (110) and (111) surfaces were also observed, both being discarded for use as a reference because the former surface rearranged into a one-dimensional superlattice structure and the latter produced an unrecognizable LEED pattern due to the faceting which occurred most likely as the result of the open atomic structure of that face. No vanadium surface was ever obtained completely free from sulfur, which preferentially segregated to the surface (as demonstrated by AES), but the (100) surface was the only one on which a (1×1) surface unit mesh was obtained.

Since vanadium is a body-centered cubic material, the atomic arrangement of its (100) surface is characterized by a square unit mesh with, ideally, the bulk lattice parameter of 3.03 Ångstroms.[8]

The LEED pattern characteristic of this atomic arrangement could be obtained by cleaning the surface using the technique of noble gas ion bombardment followed by a gentle heating in order to anneal out the resultant surface damage and to remove adsorbed and/or occluded gases. Various other cleaning procedures had been unsuccessfully tried in the attempt to deplete the amount of sulfur present at the surface. These included: 1) heating in oxygen, 2) heating in hydrogen, and 3) annealing near the melting point.[67] None of these treatments appeared to reduce the amount of sulfur segregating to the surface; only when alternate ion bombardment-annealing cycles were employed was any progress made. The point of diminishing returns was reached after about 25 of these cycles and further improvement was evident only after months of experimentation.

If enough sulfur was present in the surface layer, a c(2×2) diffraction pattern was formed. Annealing the crystal for 5-10 minutes at 1000°C was initially sufficient to enable the sulfur to migrate to the surface in quantities large enough to form this pattern. Since this surface structure implies that a 0.5 monolayer coverage by the impurity exists,[5] one might make an estimate of the amount of sulfur present on the "clean" (1×1) vanadium surface by using the amount observed concurrant with the c(2×2) structure as a calibration. This procedure is quite possibly unsatisfactory, however, since it is based on the assumption that all of the detected sulfur exists as an overlayer. The existence of a concentration gradient normal to the surface may be deduced using some of the data which was obtained for the compound V_2S_3. The observed sulfur 150 eV peak to vanadium 474 eV peak intensity ratio, S/V, for this compound was 27.3/1. The average value of this ratio observed simultaneously with a well-developed c(2×2) pattern was about 3.7/1. If the V_2S_3 value is corrected for the atom ratio (× 2/3), the effect of different escape depths (× 10.5/6.5), and the number of atoms within each escape depth assuming that 0.5 monolayer of sulfur resides at the surface to produce the c(2×2) structure (× 0.5/6.5), the predicted S/V ratio for the c(2×2) structure is 2.3/1. Since this value is only about 60% of that actually observed, it is evident that all of the sulfur atoms are not present in the overlayer. It is of interest to note, however, that the first traces of the c(2×2) structure begin to appear at a S/V ratio of 2.3 → 2.5/1. The typical amount of sulfur found in the detected volume of the cleaned crystal was 0.3 of a monolayer. Also, it should probably be re-emphasized at this point that these intensity ratios are misleading in terms of absolute numbers since the effective ionizing current, the probability of ionization, the transition rate, and the detected volume all vary for the sulfur and vanadium transitions involved.

Pictures of the (1×1) and c(2×2) LEED patterns are shown in Fig. III-1. The (0,0) diffraction beam is being back-reflected down the electron gun and is therefore not visible. The (0,1) beam spots are located approximately horizontally and vertically relative to the electron gun. These particular (1×1) pictures show streaks appearing along the (0,1) directions and may assist the reader in orienting

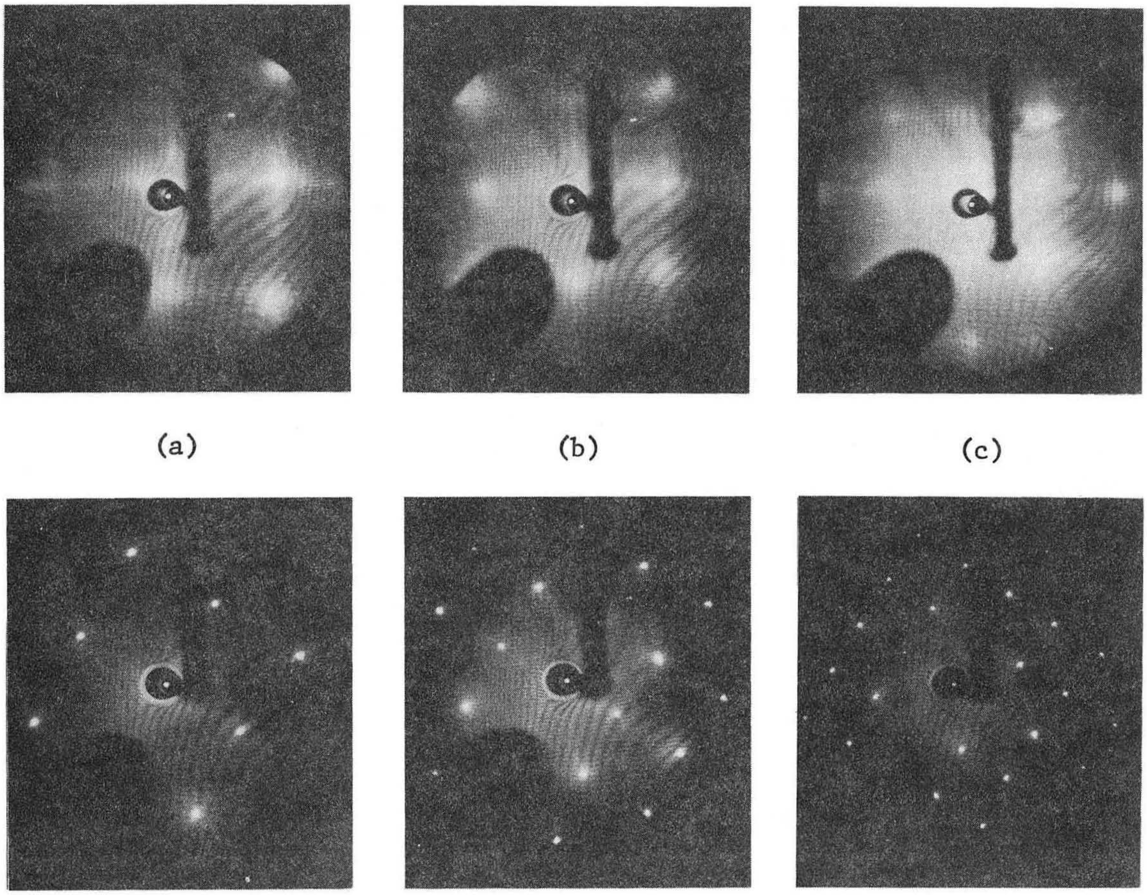

(a) (b) (c)

(d) (e) (f)

XBB 739-5589

Fig. III-1. The (1×1) LEED pattern fo the V(100) surface at incident beam energies of (a) 64 eV, (b) 96 eV, and (c) 148 eV. The c(2×2) LEED pattern of the V(100) sufface at incident beam energies of (d) 45 eV, (e) 79 eV, and (f) 147 eV.

himself; this streaking phenomena is indicative of one-dimensional disorder[5] and appeared only on crystals that had been subjected to long periods of heating in the presence of oxygen. In the case of the c(2×2) structure, the extra (1/2, 1/2) spots are readily perceived. The observed variations of diffraction beam intensity with incident beam energy are shown in Fig. III-2a, b, c, d, e for a variety of diffraction beams from these two surface structures. All of these graphs have been normalized to the most intense peak occurring within each scan and the factor by which each graph must be multiplied in order to relate it to the (0,0) beam intensity of the (1×1) structure is shown to the right of each curve. All of the intensities were measured with a Gamma Scientific Co. spot photometer using an acceptance angle of 6 minutes. All of the intensities were recorded with the incident beam impinging normally on the crystal face except those for the (0,0) beam where an angle of incidence 4° from the normal was used.

Using the technique developed by Kaplan,[68] values for both the lattice parameter at the surface and for the inner potential experienced by an electron when it is inside the crystal may be extracted from this data. Kaplan has shown that, in the limit of kinematical scattering, the observed intensity maxima should occur at the voltages

$$V'_{max} = V_o + \left(\frac{37.6}{d^2}\right) F \qquad \text{(III-1)}$$

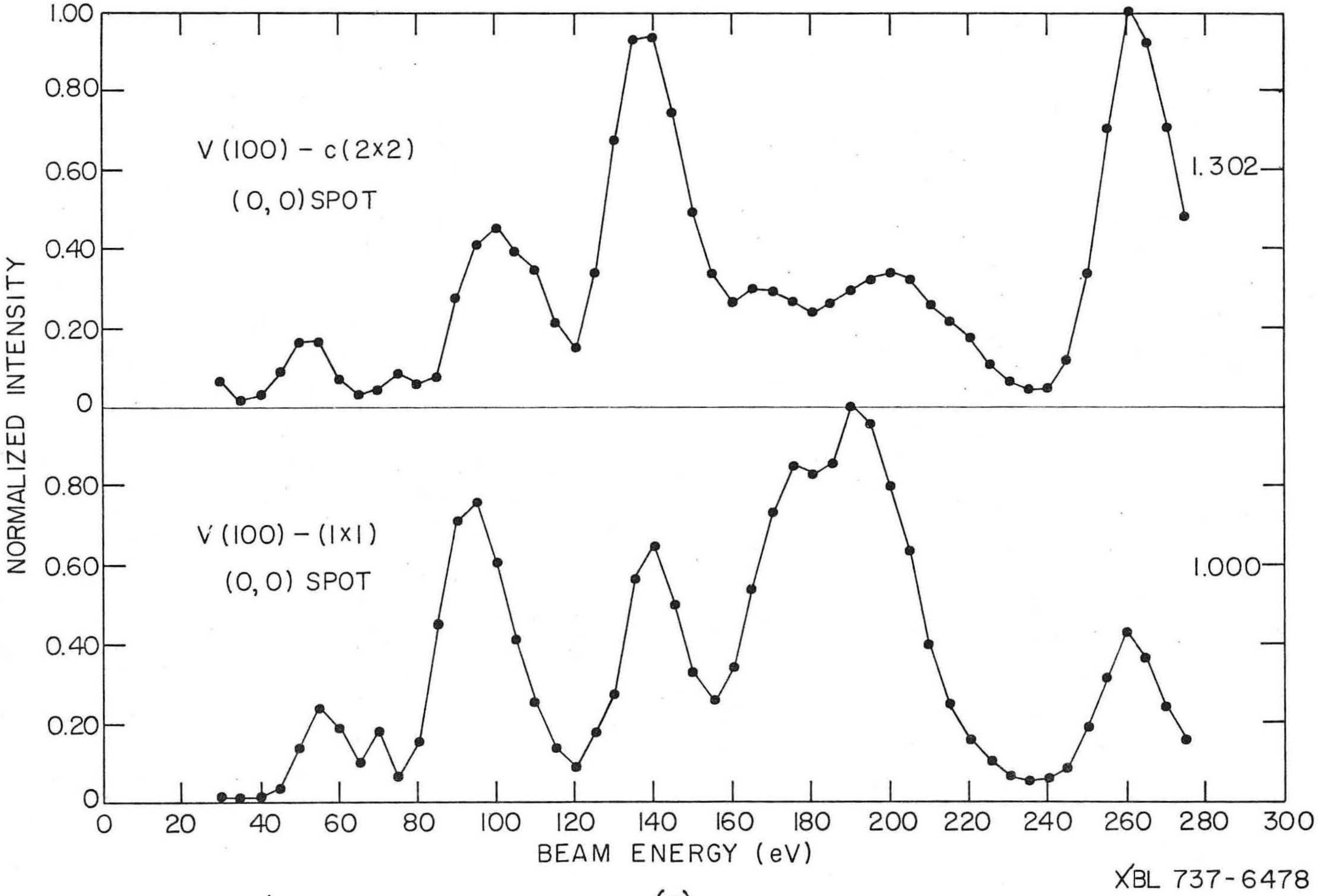

(a)

Fig. III-2. The I vs eV curves for the (1×1) and c(2×2) structures of the V(100) surface for the a) (0,0) diffraction beam, b) the (0,1) beam, c) the (1,1) beam, and d) the (0,2) beam. The (1/2,1/2) beam I vs eV curve from the c(2×2) structure is shown in e).

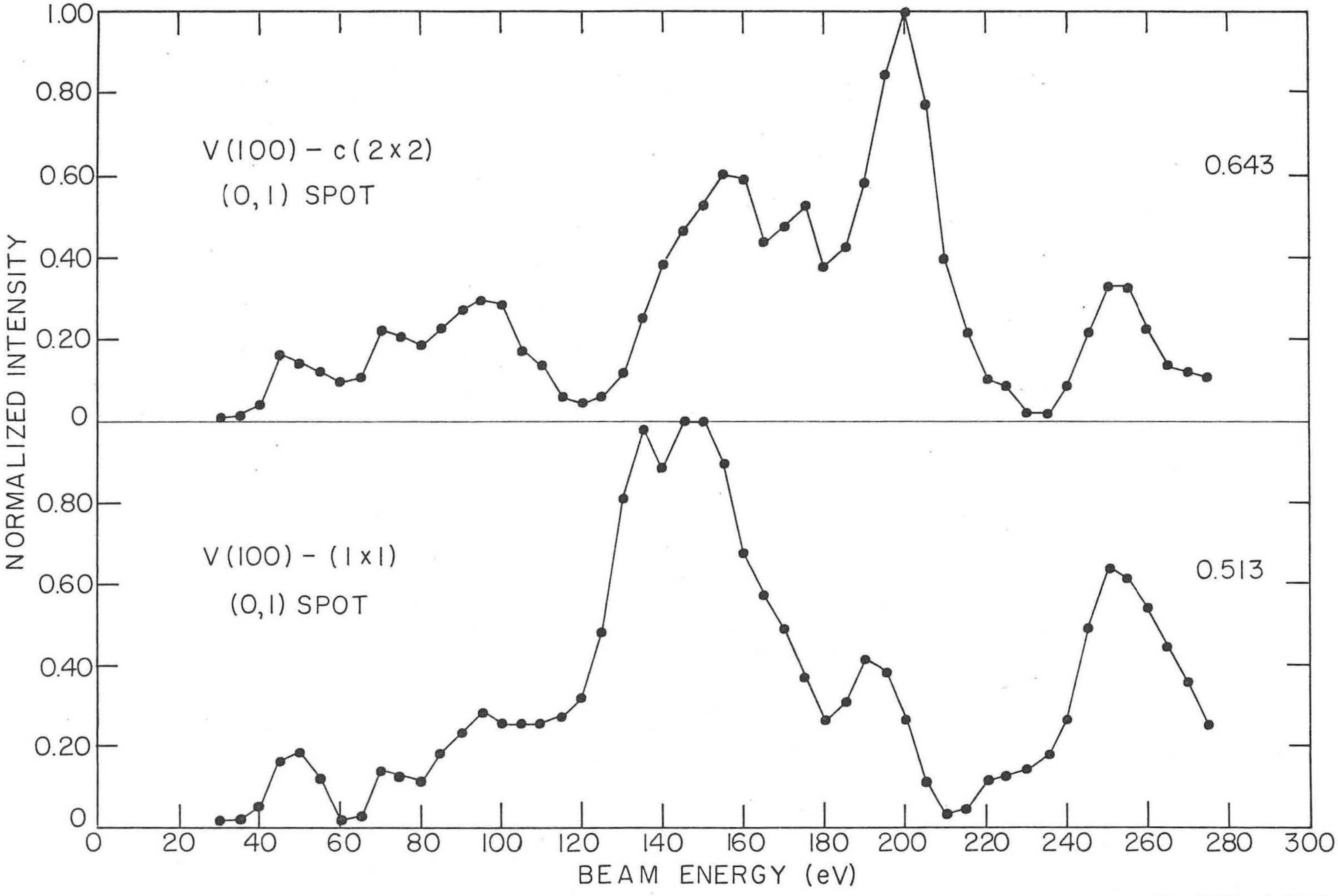

XBL 737-6479

(b)

Fig. III-2 (Cont.)

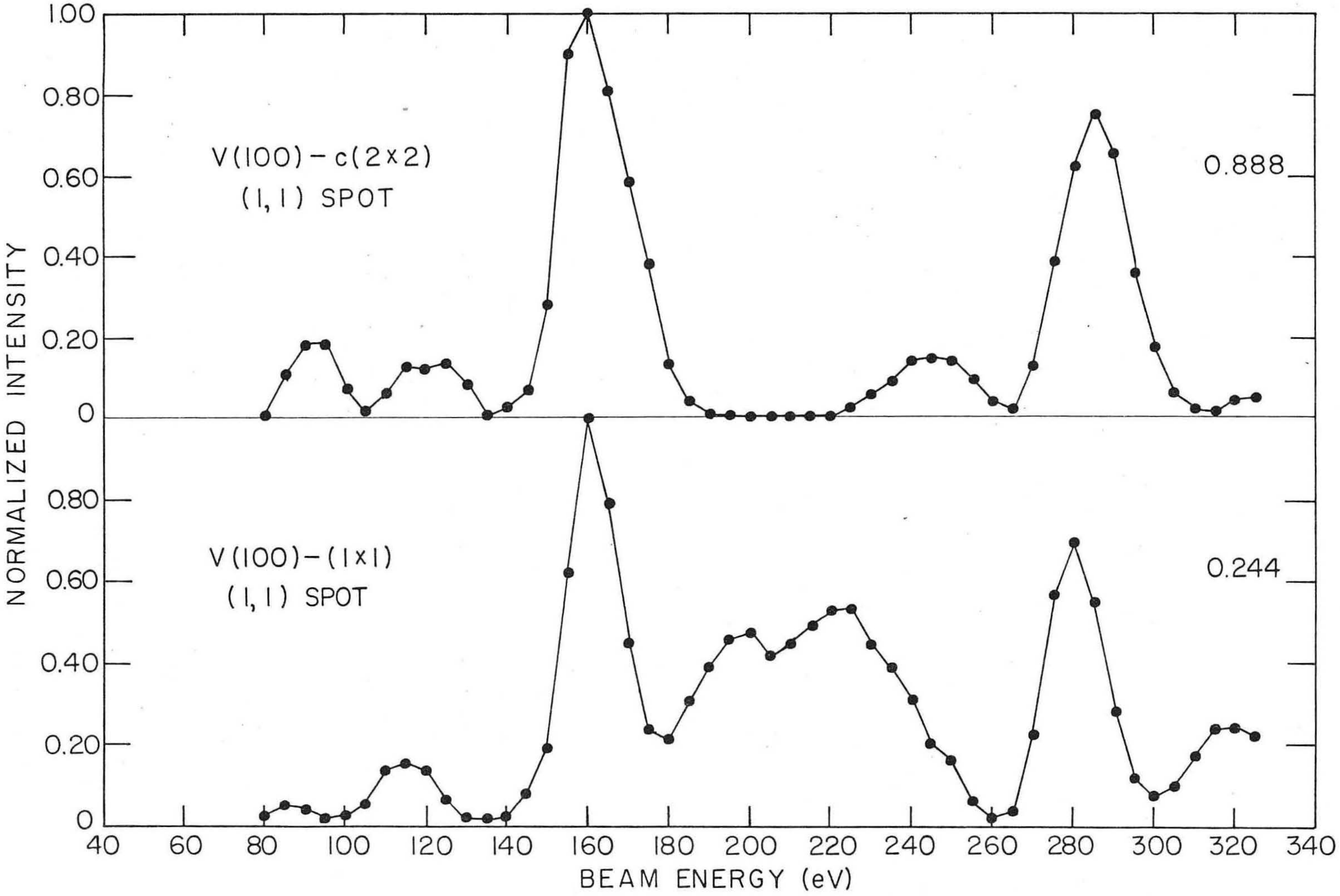

(c)

XBL 737-6480

Fig. III-2 (Cont.)

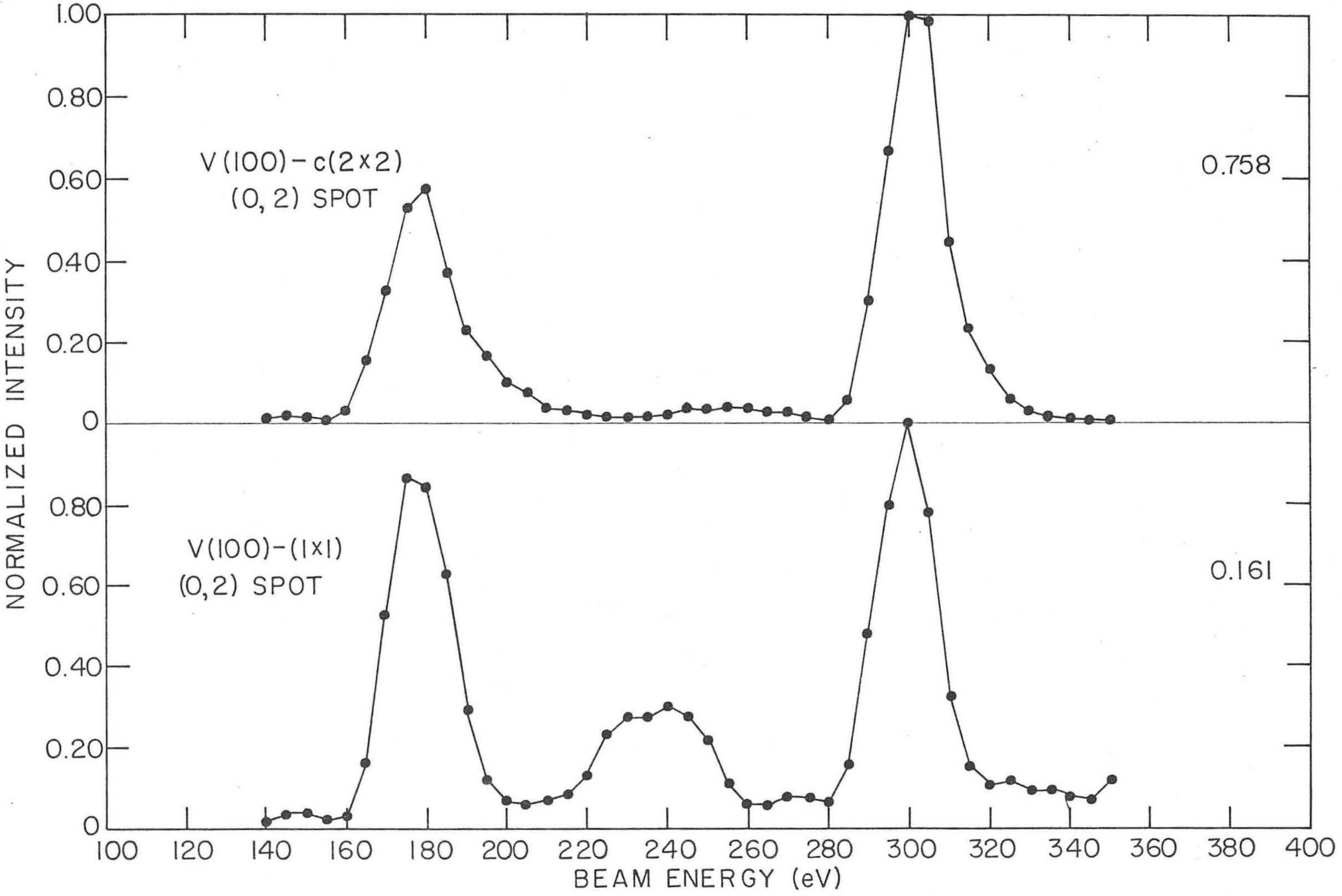

XBL 737-6481

(d)

Fig. III-2 (Cont.)

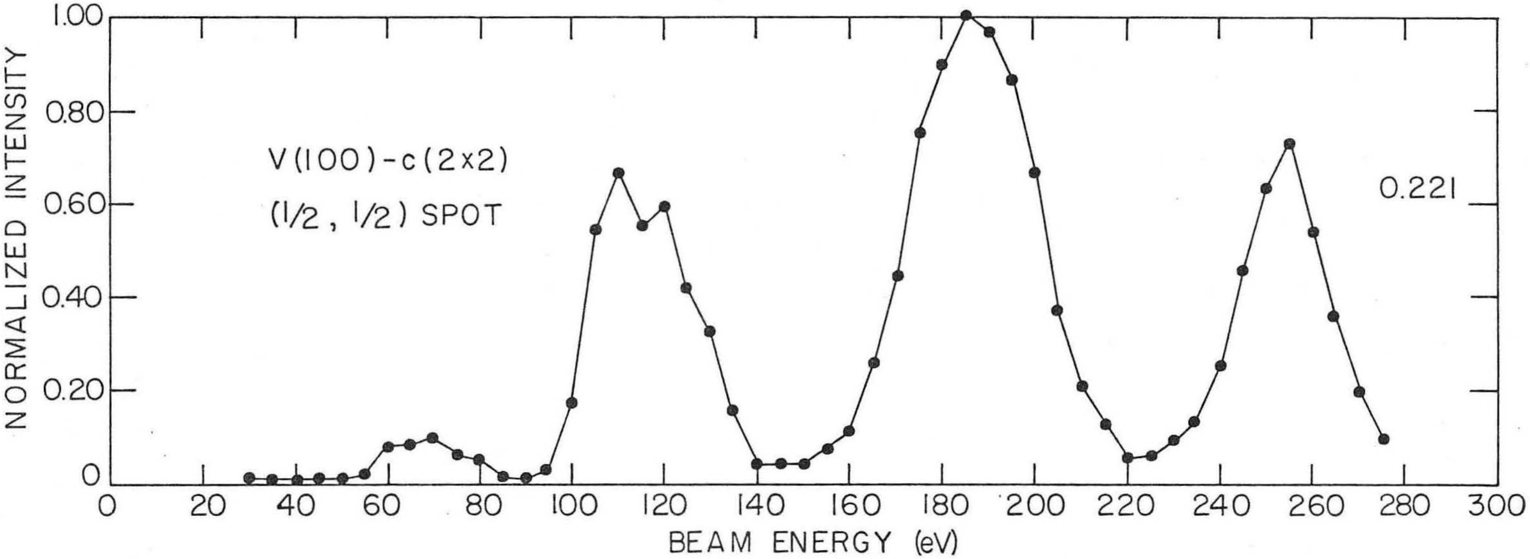

(e)

XBL737-6482

Fig. III-2 (Cont.)

where

V_o = the inner potential

d = the lattice parameter associated with the X-ray unit cell

$$F = d^2 \left\{ \frac{|\vec{G}|^2}{|\vec{G}_\perp|^2} \right\}^2$$

$\vec{G}$, $\vec{G}_\perp$ = the total reciprocal lattice vector and its component perpendicular to the surface normal respectively.

As it is formulated above, the function F is independent of d since the quantity in the brackets contains the factor $1/d^2$. In this form F is the same for all crystals having a given structure and surface. For the (100) surface plane of a b.c.c. crystal,

$$F = \frac{1}{4} \left\{ \frac{(n_1+n_2)^2 + 2(n_1-n_2)^2 + (n_1-n_2+2n_3)^2}{(n_1-n_2+2n_3)} \right\}^2$$

where the n's are running indices indicating the diffraction beam (n_1 and n_2) and the order of diffraction (n_3). If the indexing of the intensity maxima is correct and if the kinematical model is appropriate, all of the data points will lie on a single straight line. From the form of Eq. (III-1) it is evident that the intercept of this line at F=0 and its slope determine V_o and d respectively. Such an analysis was performed for the vanadium (1×1) surface structure and the graph of the results is shown in Fig. III-3. The inner potential is -9.9 eV (the negative sign indicates that the potential

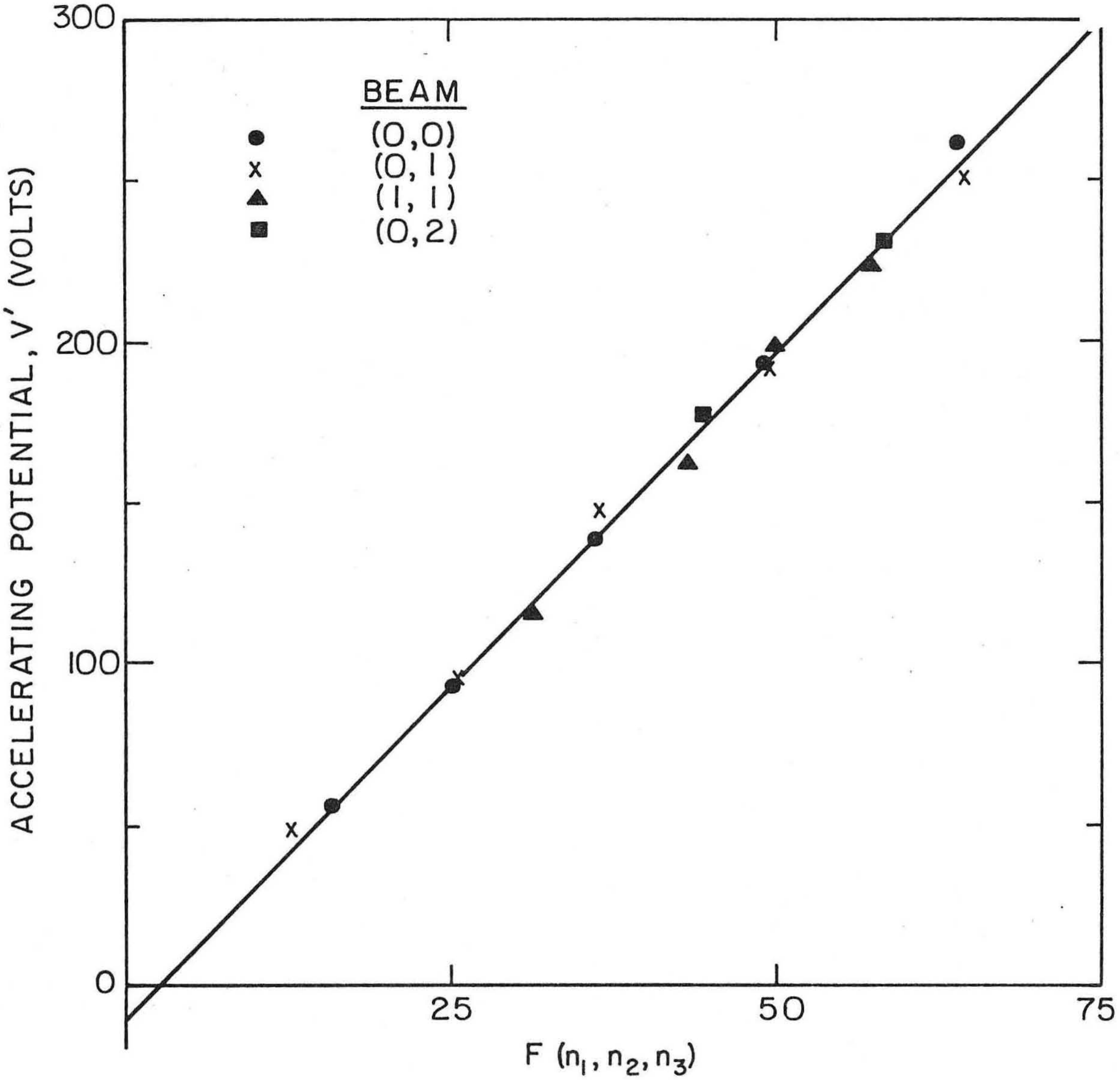

XBL737-6489

Fig. III-3. Values of the accelerating potential at which intensity maxima were observed for the indicated diffraction beams of the V(100)-(1×1) structure plotted vs the corresponding F values.

is attractive) and the surface parameter is 3.02 Å (i.e. equal to the bulk value within the experimental error). Such an analysis proved to be unsuitable for the c(2×2) structure-the reason for this presumably lies in the predominence of multiple scattering events.

Because, as noted previously, a structural analysis is not currently able to be performed using LEED data, the exact position of the sulfur atoms in the c(2×2) structure is not able to be uniquely determined. The most probable sites for these atoms are: 1) directly above the appropriate vanadium atoms in what would be a singly co-ordinated position, 2) astride two neighboring vanadium atoms (a doubly co-ordinated position), and 3) within the "well" in the square formed by four vanadium atoms (a quadruply co-ordinated position). Since vanadium monosulfide crystallizes in the NiAs structure,[69] it is most probable that the latter of the three possibilities is the appropriate one. The spacial directionality of the vanadium 3d orbitals also argues in favor of this co-ordination position.

2. Adsorption Structures

The exposure of the (1×1) surface structure to oxygen and to carbon monoxide did not result in the formation of an ordered superlattice structure in either instance but the AES results indicated that adsorption did indeed occur. In the oxygen case a general increase in the background intensity was exhibited and the (1×1) pattern eventually disappeared, indicating that a totally disordered surface resulted. The CO adsorption, on the other hand, did not appear to alter the pattern (except for a slight increase in the background intensity) and this suggests that it is adsorbed in the (1×1) configuration.

The exposure of the c(2×2) surface structure to oxygen produced the structure shown in Fig. III-4. This unusual structure can not be readily indexed using the simple LEED notation that has been previously outlined; instead recourse must be made to the more elegant matrix notation developed by Park and Madden[70] to describe complex structures. This structure is interpreted as being composed of two domains perpendicular to each other and the matrix for this structure is $\begin{pmatrix} 1 & 1 \\ 2 & -1 \end{pmatrix}$. It might be noted here that the matrices which describe the c(2×2) and (1×1) structures are $\begin{pmatrix} 1 & 1 \\ 1 & -1 \end{pmatrix}$ and $\begin{pmatrix} 1 & 0 \\ 0 & 1 \end{pmatrix}$ respectively. This complex structure is extremely interesting in that the AES results indicate that the amount of sulfur present appears to be about 40% greater than that which occurs in the c(2×2) structure and that <u>no</u> oxygen is present. The only explanations that can be offered to rationalize this phenomena is that either 1) the adsorption of oxygen induces the sulfur atoms laying below the surface to migrate to the surface and thereby forcing the oxygen to desorb, or 2) the oxygen diffuses into the bulk and drives more sulfur to the surface in the process. Since this same structure was also observed after a long term exposure to the ambient gases of the vacuum system, CO and CO_2 being the major gases present which are likely to adsorb upon the surface, the former explanation must be considered the most likely one. The surface structure proposed to explain these results is shown

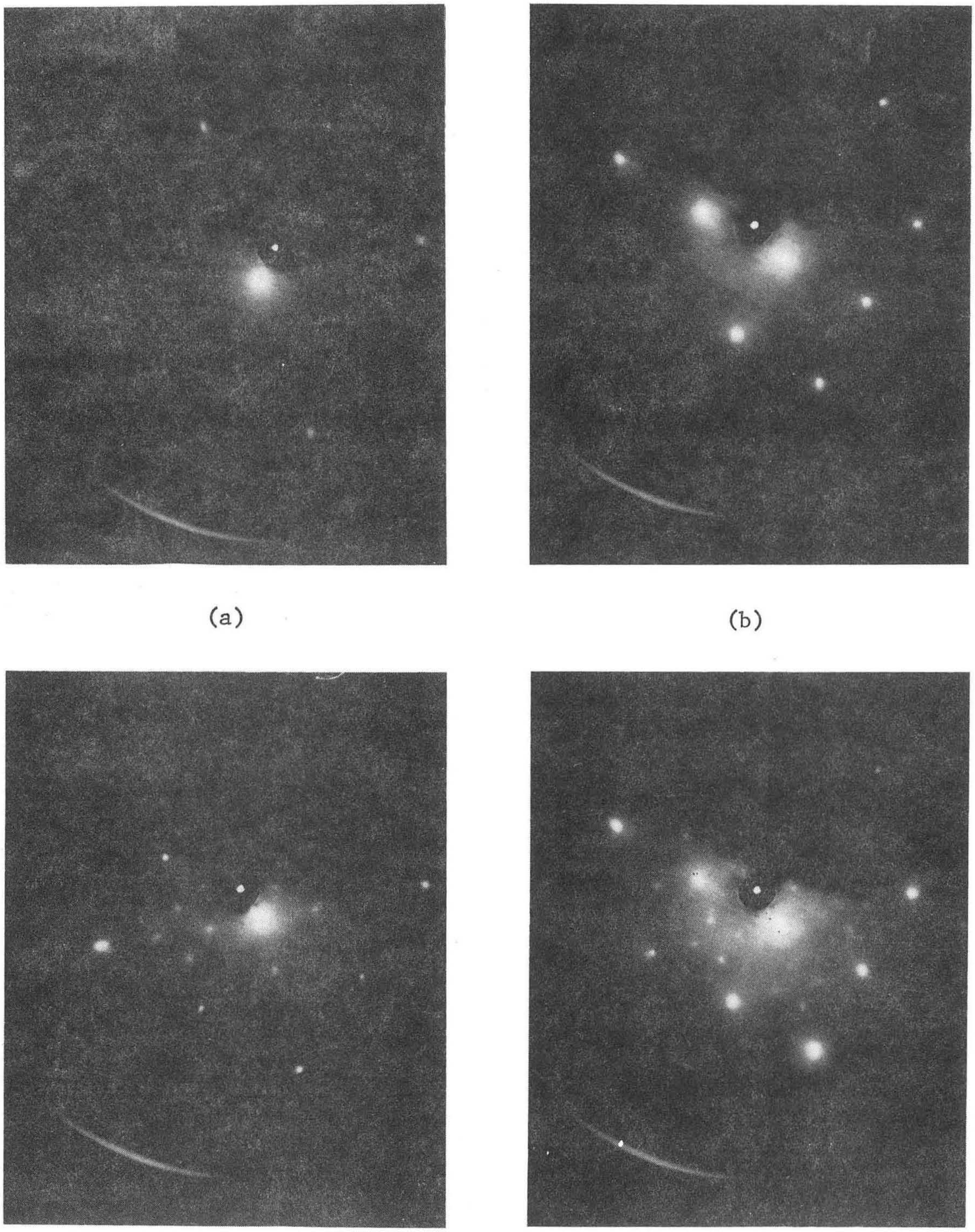

(a) (b)

(c) (d)

XBB 739-5588

Fig. III-4. The V(100)-(1×1) LEED pattern at incident beam energies of (a) 100 eV and (b) 150 eV. The oxygen-modified c(2×2) structure of the V(100) surface at incident beam energies of (c) 100 eV and (d) 150 eV.

in Fig. III-5. In the figure the points of intersection of the square array represent the positions of the vanadium atoms in the (100) surface and the circles represent the sulfur atoms in the overlayer. It has been assumed that these sulfur atoms are situated in the four-fold co-ordinated sites of the (100) lattice. The unit cell vectors for the overlayer are shown in the upper left hand corner of the figure. This structure contains 0.67 of a monolayer of sulfur and additional credence is lent to its acceptance over any other structure by the observation that hexagonal S_6 rings (see the outline in the lower left hand corner of the figure) are known to exist in the free state.[71]

3. Comparison with Other LEED Experiments

The results presented here are in accordance with those of Fiermans and Vennik[72] who have also noted the existence of a (1×1) structure on the vanadium (100) face and its transformation into a c(2×2) structure simultaneously with the segregation of sulfur to the surface. Although they also investigated the same crystal face, Vijai and Packman[73] have not reported the formation of the c(2×2) structure upon heating but rather only noted an increase in the background intensity of their LEED pattern. Since these investigators did not supplement their data with AES information, one can only surmise that they had initially obtained a sufficiently sulfur-free crystal or had initially cleaned it so well that the amount of sulfur which was able to surface segregate during heating was inadequate to form the c(2×2) structure. Our own experience showed that the amount

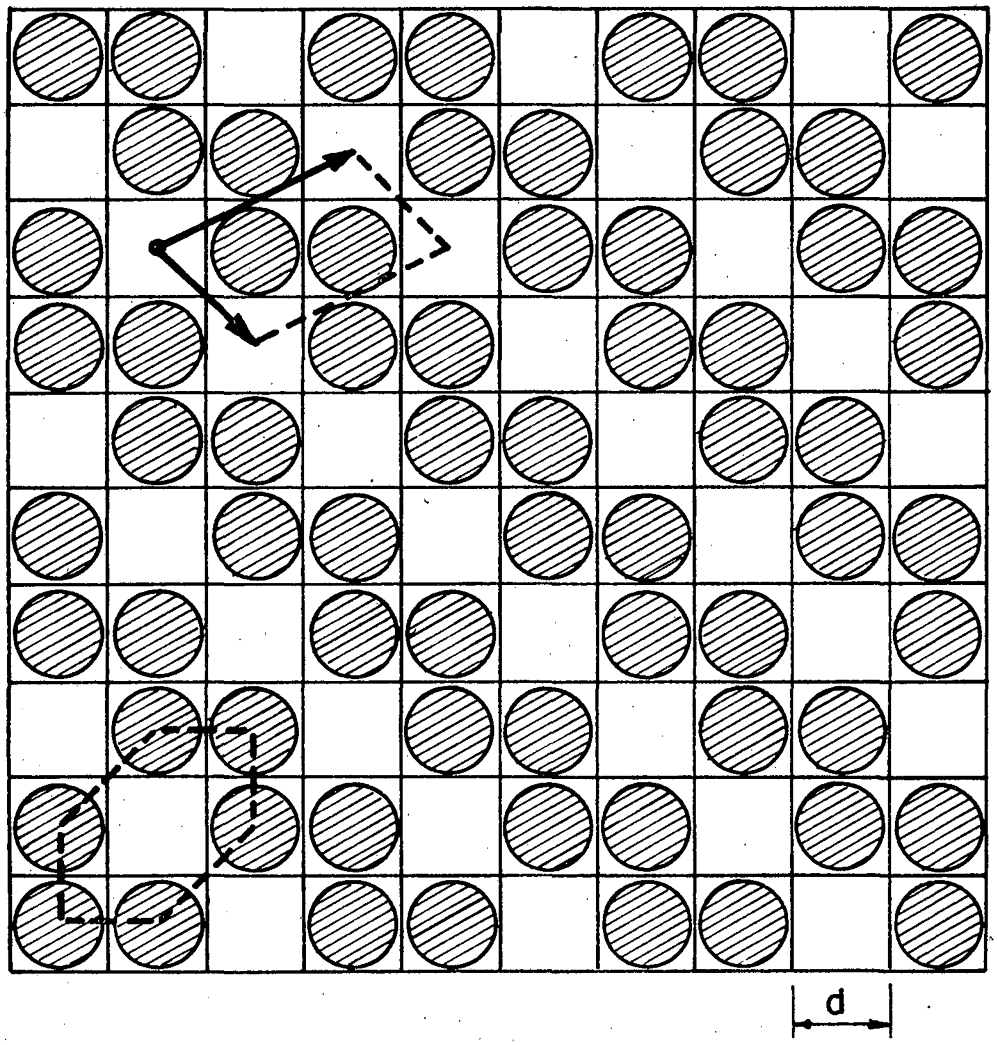

XBL 737-6488

Fig. III-5. The proposed surface structure for the sulfur atoms on the oxygen-modified V(100)-c(2×2) structure. The surface unit cell is shown in the upper left-hand corner and the pseudo-hexagonal S_6 ring structure is shown in the lower left-hand corner.

of annealing necessary to produce this structure gradually increased with the number of cleanings to which the crystal was subjected. Eventually an 60 minute anneal at 1200°C proved insufficient to produce the c(2×2) structure.

The data of these same authors on the energies of the maxima occurring in the (0,0) beam intensity curve for the clean (100) surface agree well with that shown above except for the conspicuous and unexplained absence of the seventh order (≈ 190 eV) diffraction maxima from their data. The relative intensities of their diffraction maxima are quite different from ours but this discrepancy is partially due to the fact that they made no attempt to normalize their curves to a constant emission current from the LEED gun (the current realized from the electron gun increases monotonically with the accelerating voltage). The fact that they used a different angle of incidence from ours (the intensities of the (0,0) beam maxima have been shown to exhibit a strong dependence on this parameter) and integrated over the entire LEED spot also assist in making the results difficult to compare.

These authors also reported the formation of a (2×2) structure as the results of annealing their oxygen-exposed surfaces, which had retained the (1×1) structure. The heating of our totally disordered oxygen-exposed surfaces to temperatures comparable with theirs (1100-1200°C) resulted in the return of the (1×1) structure and the absence of oxygen was demonstrated using AES. The (2×2) structure that they observed transformed back to a (1×1) structure upon heating to 1400°C. These results are not inconsistant with each other since, under the temperature and pressure conditions of their experiments, they obviously adsorbed a smaller amount of oxygen upon the surface than we did; this is evidenced by the fact that they never observed the total extinction of the LEED pattern. One could not expect the ordered and disordered surfaces to behave similarly as a function of temperature. Their observation of a lower coverage structure upon heating, the (1×1) structure corresponds to a full monolayer coverage while the (2×2) indicates a 0.25 monolayer coverage, is a well documented phenomena; the total expulsion of oxygen that we observed upon heating might well be expected from a structural viewpoint as the oxide compound which we formed reverts from its lattice structure back to the b.c.c. lattice of vanadium.

B. Characteristic Loss Spectra

1. Results and General Remarks

In an additional attempt to better understand the vanadium system, Characteristic Loss spectra of metallic vanadium and of V_2O_3 (in the form of a pressed powder) were also measured. The losses up to 70 eV below the incident beam energy have been measured and the variation of the loss intensities as a function of the beam energy are shown in Fig. III-6a & b. The spectra appearing here were taken using a 1.0 volt p-t-p modulation voltage, a 0.4 volt/second sweep rate, and a system time constant of 1 second. More accurate data was obtained for these samples at incident beam energies of 300 and 400 eV for V and V_2O_3 respectively (where it was concluded from the above data that intensity and resolution considerations would make the determination

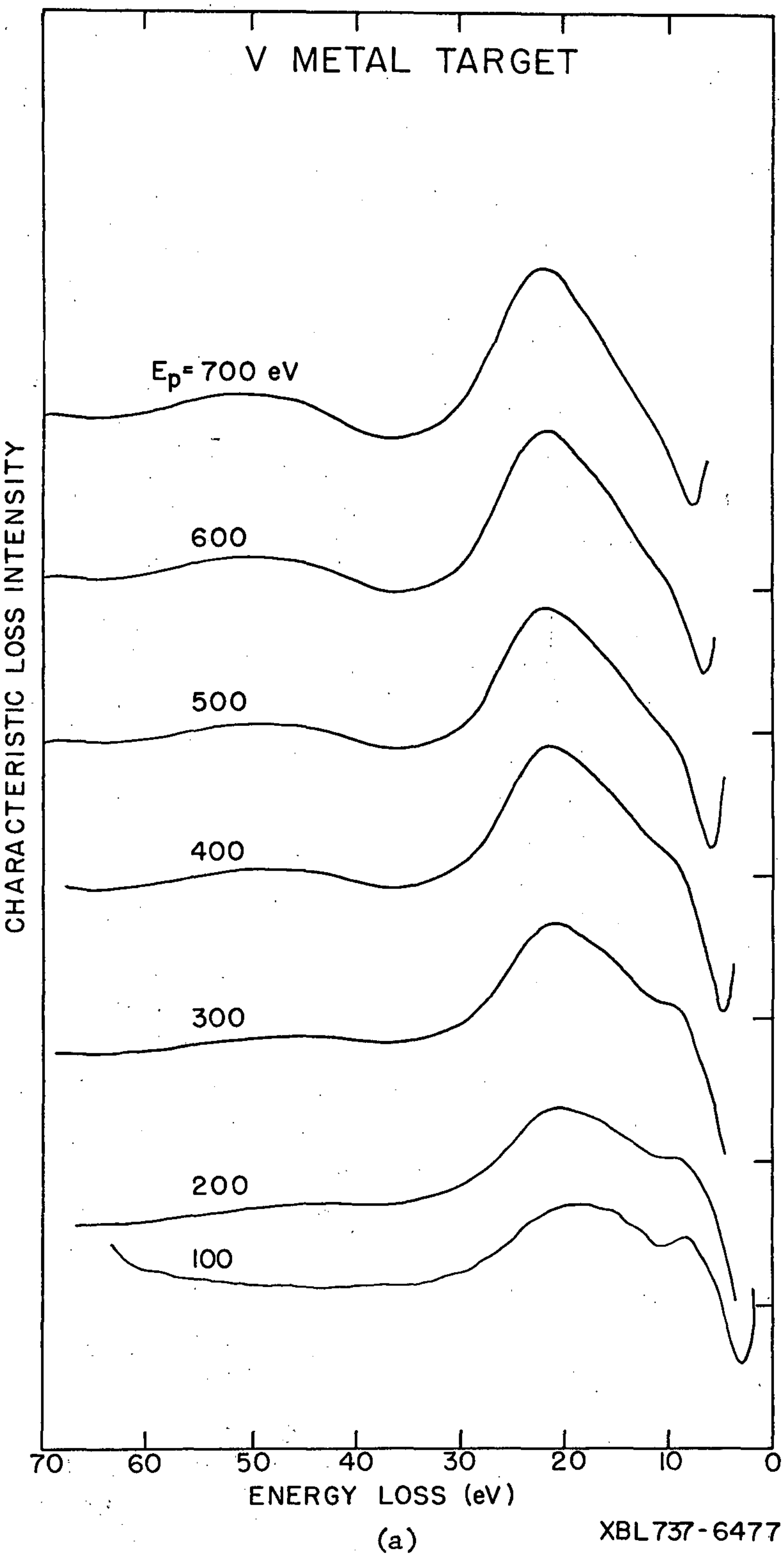

Fig. III-6. The a) vanadium metal and b) V_2O_3 characteristic loss spectra for incident beam energies in the 100 eV to 700 eV range.

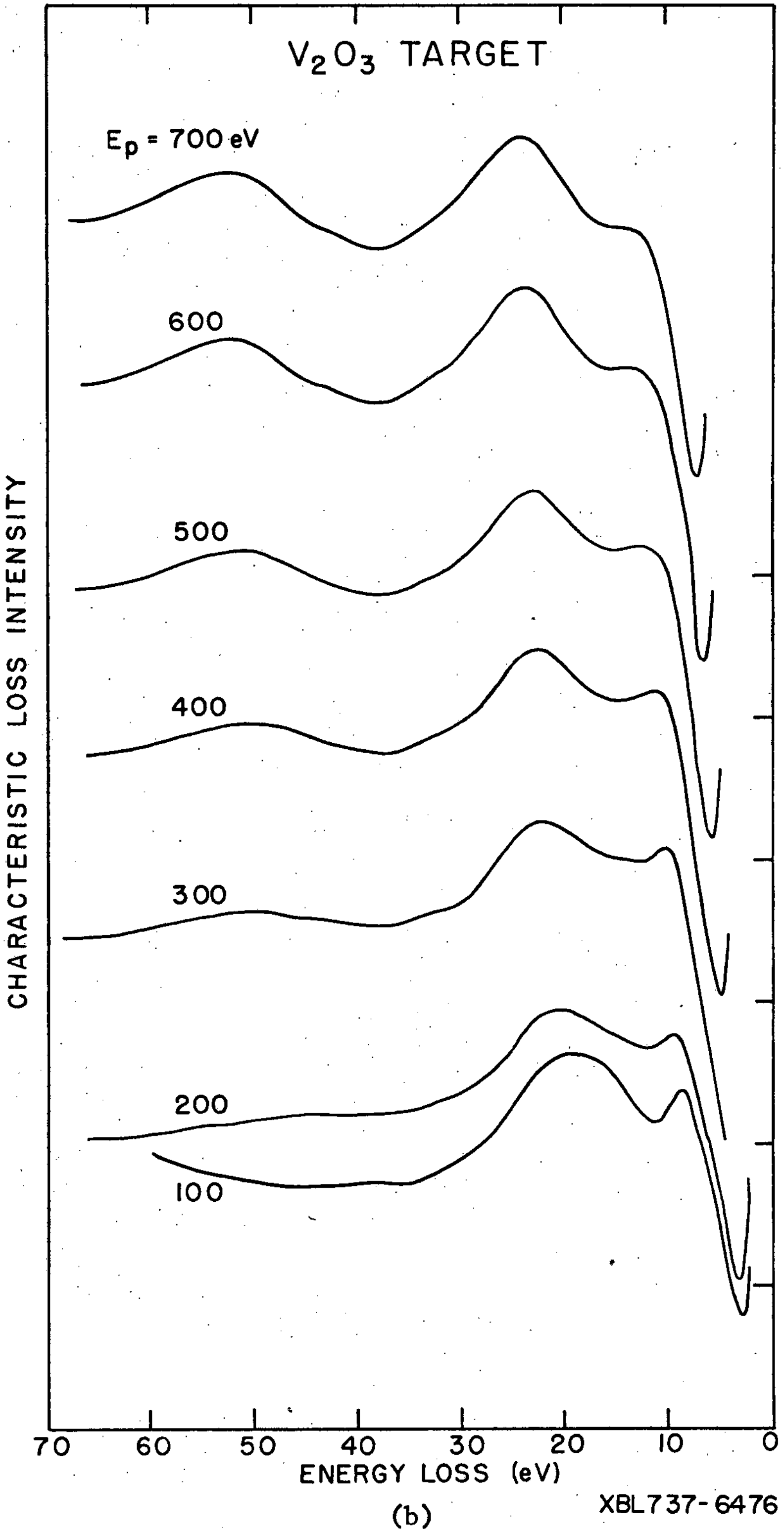

(b)

XBL737-6476

Fig. III-6 (Cont.)

of the loss energies most convenient) by using a 0.4 volt modulation voltage and averaging over four scans with the assistance of the Vidar DAS method outlined earlier. These results are presented in Table III-1 where they are compared with the results obtained by other investigators.[74-78] Our results have been corrected for a factor which appears to be related to the resolution of the analyzer. If the spectra appearing in Fig. III-6a & b are carefully scrutinized, it will be obvious that the Characteristic Loss energies appear to increase as the incident beam energy is increased; this increase in the loss energy has been measured to be 0.00467 eV per unit incident beam energy. This number is in excellent agreement with that presented in Eq. (II-12) which was determined using the increase in linewidth of the elastically diffracted peak. If the published energy dependence curves of Simmons and Scheibner are inspected, a $\Delta E/E \approx 0.006$ may also be observed for their 3 grid R.F.E.A. system. Although this effect is not entirely understood, our results have been corrected to those which would be theoretically observed at an incident beam energy of 0 eV.

From the results listed in the table, it is seen that a general concensus seems to be developing that there exist at least seven loss peaks in the 0-70 eV range in metallic vanadium. It should be pointed out that Simmons and Scheibner did not concern themselves with any other peaks than the four which they reported; they investigated a 30 eV energy range and a deconvolution of the spectra yielded the results shown. Although we did not perform such an elegant processing of our data, it is quite evident that the peak which they report at

Table III-1

Characteristic Losses of Vanadium

	$(M_{4,5}+N_1)$	$2(M_{4,5}+N_1)$	SP	VP	$VP+2(M_{4,5}+N_1)$	$M_{2,3}$	E_{111}	M_1
Szalkowski	5.1±0.5	10.3±0.5	14.3±0.5	20.0±0.1	30.0±0.5	37.8±0.5	47.6±0.2	66.6±0.2
Simmons and Scheibner[74]	5.1	10.5	16.5	24.0	RNI	RNI	RNI	RNI
Fiermans and Vennik[75]	3.5 5.5 7	10.5	15	20 22.5	27 34	37.5 41.5	47.5 56.5	62 67.5
Robins and Swan[76]	5.4	O/NR	O/NR	21.6	NO	41.9	51.6	67.4
Robins[77]	7.1	11.3	18.1	25.5	NO	41.2	52.4	69.5

Characteristic Losses in the V-O System

	$L_{2,3}$	SP	-	VP & L_1	VP + SP	$M_{2,3}$	E_{111}	M_1
Szalkowski (V_2O_3)	5.5±1.0	10.4±0.1	NO	22.1±0.1	32.3±0.2	40.2±0.5	49.8±0.1	68.5±0.5
Simmons Scheibner (VO)	NO	10.5	NO	24.0	RNI	RNI	RNI	RNI
Fiermans and Vennik (V_6O_{13})	6	8 9 11.5	13 15 18	21 23 26	31 34	42	53	72
Best[78] (V_2O_3)	NO	10.2	18.7	24.4	O/NR	NO	47.2	NO

RNI = region not included in observations
O/NR = peak observeable but no value reported
NO = peak not observed

16.5 eV also exists in our data. Our 100 eV incident beam energy data may also be seen to exhibit a low energy peak corresponding to the one that they report at 5.1 eV. These two peaks are also observable in the published data of Swan but are not reported. Some degree of liberty has been assumed in listing the observations of Fiermans and Vennik due to the fact that their work, except for one reported spectrum, was carried out in the d^2I/dV^2 mode and shows a great deal more structure than that observed in the energy distribution spectra; they have since stated that their recent dI/dV low energy loss spectra agree well with that of Simmons and Scheibner.[79]

A few other remarks concerning Table III-1 should also be made. The vanadium spectrum attributed to Robins was measured on what was described as "altered" vanadium. It appears that this sample contains both oxidized and elemental vanadium within the detected volume of the experiment (see Ref. 80 and Section III.B.2.c.). Although it has been grouped with the other vanadium metal results because it appears to agree with them most closely, it should be kept in mind that it actually falls in a category between the two general types of results reported. Also because of the different oxide compounds on which they were measured, it is not clear to what extent the non-ionization losses in these samples can be compared; the results indicate, however, that the Characteristic Loss spectra are remarkably similar to each other and to metallic vanadium. Finally a word on the various experimental techniques used: we used a 4 grid R.F.E.A. and a normal incidence beam between the energies of 100 and 700 eV, Simmons and Scheibner used a 3 grid R.F.E.A. and a normal incidence 100 eV beam, Fiermans and Vennik used a 3 grid R.F.E.A. and a 100-700 eV normal incidence beam, Robins and Swan and Robins alone used a 127° sector analyzer with a 1200 eV beam at a 45° incident angle and a take-off angle perpendicular to the incident beam, Best used the same system described directly above but with an incident beam energy of 800 eV.

2. Characteristic Loss Peak Assignments for Vanadium Metal

In keeping with the spirit of Characteristic Loss spectra, there has been little agreement among the authors listed in Table III-1 as to the origin of the observed peaks. We believe that this was basically due to 1) the lack of intensity vs. beam energy data such as the type presented in Fig. III-6, and 2) the non-realization of the large double to single interband transition probability ratio for loosely bound energy levels. In fact this latter effect provides the key to the interpretation of the vanadium spectrum (and, it appears, other transition metal spectra) and we believe that this is the first time that such an effect has been promulgated to explain any Characteristic Loss spectra. We might add that the peak assignments listed below are the only ones which explain all of the observations on metallic vanadium.

The major peak in the spectra of Fig. III-62 is due to a volume plasmon excitation. Although this peak is reported to be at 20.0 eV, this energy loss value is probably too low since it was merely measured at the intensity maximum and no attempt was made to compensate for the effect of the background which was due to the overlap of the lower energy loss peaks. The energy of this same peak is probably overestimated by Simmons and Scheibner since, when they carried out their deconvolution of the spectrum, they assumed that it was fixed at the same energy that it appeared at in their oxidized sample. A more reasonable value of the peak energy is that of Robins and Swan (21.6 eV) which is close to the average value of all the reported data; the 21.8 eV measurement of this loss performed by Soviet workers[80] also supports this viewpoint. The assignment of this peak to a volume plasmon loss process is based on the observations that 1) it is in good agreement with the energy loss predicted by theory (22.15 eV according to Bakulin et.al., 21.0 eV when polarizability effects are accounted for, and compensation for dispersion effects will increase these values),[80] 2) volume plasmons have typically been observed to be the most prominent loss processes in the incident electron energy range of concern here,[81] and 3) this loss is observed to increase in intensity at the greatest rate when the incident beam energy is increased. The fact that 4) it is the peak which we have labelled as due to the creation of a surface plasmon that is most enhanced in intensity when the incident beam angle is moved from normal incidence to a 45° incident angle[75] is also strong evidence for this major peak being correlated with the volume plasmon excitation.

The assignment of a surface plasmon excitation loss to the peak which lies between 14 and 16 eV stems from 1) its energy relationship to the volume plasmon loss peak (i.e., it appears at a factor of $\sqrt{2}$ lower energy as theory predicts), 2) the fact that its intensity increases at a slower rate than the volume plasmon peak as the incident beam energy is raised (the fact that it does increase somewhat in absolute intensity hinges on the fact that the incident beam current was increasing as a function of its energy), and 3) the angular dependence of its intensity as noted above.

The loss peaks occurring near the energies of 5, 38, and 67 eV can be ascribed to the excitation of interband transitions from the vanadium $M_{4,5}$, $M_{2,3}$, and M_1 subshells respectively. The energies of these peaks correlate well with the subshell binding energies of 2, 38, and 66 eV determined by XPS and related techniques. In actuality the 5 eV loss peak is about 3 eV too large to be associated with the $M_{4,5}$ transition. However since it is of the proper amplitude when compared to the other interband transitions and since no other low energy peak has been observed, the assignment is a logical one. Also a high density of states appears to exist about 3 eV above the Fermi level,[82] at the point where the bottom of the 4p band joins the top of the 4s band, and it is possible that these low energy transitions are preferentially coupling to this final state whereas the higher energy transitions are exciting electrons only to the Fermi level. As far as is able to be determined, all of these interband transition peaks appear to remain essentially constant in amplitude in the incident beam energy region investigated-a relationship to be expected given the opposite variations in ionization cross-section and beam current with the incident beam energy.

The 10 eV peak is ascribed to the excitation of a double interband transition of the valence band levels occurring in the vicinity of a single atom. It would prove to be difficult to rationalize this peak as being due to two successive interactions occurring in different atoms since the 10 eV peak is of greater intensity than the 5 eV and no other large multiple energy loss events were observed throughout the incident energy range studied. Instead the authors are proposing that this peak is due to a double "ionization" event caused by a single electron and with the two interactions occurring within an atomic radius of each other. Gryziński[25] has developed an expression for the cross-section of such an event and the ratio of this cross-section to that of a single ionization event may be written as

$$\frac{Q_{2W_o}}{Q_{W_o} - Q_{2W_o}} = \frac{g_{2W_o}(U_2)}{\left[\frac{4\pi\bar{r}^2 E_{W_o}^{\;2}}{(n-1)\sigma_o}\, g_{W_o}(U)\right] - g_{2W_o}(U_2)} \qquad \text{(III-2)}$$

where

n = the number of electrons in the subshell(s) being ionized

$\bar{r}$ = the mean distance between electrons in the atom $\approx \bar{R}n^{-1/3}$

$\bar{R}$ = the mean radius of the doubly ionized atom

$g_{2W_o}(U_2)$ = the ionization function for double ionization by a single electron

$U_2 = E_p/2E_{W_o}$

and the other terms have been defined earlier (see Section I.2.a). This ratio was calculated for the case of a 100 eV beam of electrons incident upon a vanadium metal target and using the values $\bar{R} = 1.34$ Å and $E_{W_o} = 5$ eV. For n equal to 5 and 3, the ratio is 120/1 and 0.55/1 respectively. Since the areas under the appropriate peaks in the deconvoluted spectrum of Simmons and Scheibner is 4.8/1, it appears that both the $M_{4,5}$ and N_1 subshells of vanadium participate to some extent in these transitions. The cross-section ratio of Eq. (III-2) is about a factor of 100 lower for the $M_{2,3}$ vanadium subshell, the $1/E_{W_o}^{\ 2}$ term obviously making the intensity ratio quite sensitive to the energy of the transition, and this explains why multiple loss peaks are not observed for the $M_{2,3}$ and M_1 interband transitions. By comparing Gryziński's curves for $g_{2W_o}(U_2)$ and $g_{W_o}(U)$ it is evident that the maximum ratio of double to single ionization events will occur around $U_2 = 3$. For the case where $E_{W_o} = 5$ eV and n = 5, this maximum ratio will occur around an incident beam energy of 30 eV and its value at this point should be about 82/1. At incident beam energies which are large compared to this 30 eV number the cross-section ratio becomes essentially constant and the variation in intensity with incident beam energy of this double ionization loss peak will be identical to that exhibited by the single ionization loss peaks.

The existence of the peak that we have reported at 30 eV is open to question. Its existence was postulated after observing that the high energy loss side of the volume plasmon loss peak deviated from the Gaussian-type symmetry that would be expected. Some additional support is lent to the possibility of its existence by noting that 1) the two loss mechanisms which would give rise to it yield the two most intense peaks in the low energy loss region of the spectrum, and that 2) a similar multiple event loss peak is present in the V_2O_3 spectrum where it is clearly due to the most intense low energy peaks occurring therein.

The remaining peak in the spectrum occurs at an energy of 47-48 eV. No previous author has forwarded an explanation as to the type of process giving rise to it. The presence of this peak is particularly disturbing because it is a quite prominent feature of the loss spectrum, especially at the higher incident beam energies since the rate of increase in its intensity rivals that of the volume plasmon loss peak. It would appear that there is the possibility that this peak is due to a momentum conservation interband transition loss of the type described by Viatskin.[12] The first loss predicted for this type of event would occur at $n_1 = n_2 = n_3 = 1$ and this results in a predicted loss of 49.0 eV for the case of free electrons in vanadium. This value is remarkably close to the observed energy loss and such an assignment seems quite convincing on the basis of its energy value alone since there is no other known type of transition which predicts a loss energy near the observed value. Also one would expect the intensity of such an interband transition to be roughly proportional to the penetration depth of the incident electron beam (as is the volume plasmon loss intensity) because more lattice unit cells are traversed, thereby accounting for the observed energy dependence of this peak's intensity.

3. Characteristic Loss Peak Assignments for V_2O_3

Similar arguments to those propounded for the vanadium metal sample can be made regarding the origin of the 22 eV volume plasmon loss peak, the 40 eV $M_{2,3}$ and 68.5 eV M_1 interband transition peaks, and the 50 eV momentum conservation interband transition peak. In addition a low energy (5-6 eV) peak is seen to be observed at low incident beam energies and is attributed to an interband transition from the oxygen $L_{2,3}$ levels.[83,84]

The 10-11 eV loss appears to be predominently of a different origin in the case of the oxide than it is in the metal. Although there must undoubtedly be an intensity contribution from the type of double ionization event previously discussed, it is observed that this peak increases in amplitude as the incident beam energy is raised but that this increase is not as rapid as that of the 22 eV volume plasmon peak. This suggests that a surface plasmon loss is also contributing to the intensity of this peak. This assignment is made more plausible by noting that the $1/\sqrt{2}$ energy relationship of the surface plasmon to the volume plasmon peak does not hold for non-metallic surfaces.

The 32 eV peak also appears to increase in amplitude as a function of the incident beam energy and it may be ascribed to the combination of a volume plasmon and a surface plasmon loss. Besides having an appropriate absolute intensity and the correct intensity variation with beam energy, the exactness of the loss energy as the sum of these two events argues strongly for this multiple loss interpretation.

The E_{111} peak is assigned almost exclusively on the basis of its similarity to the corresponding peak in the metal. It might be noted that the unit cells of the vanadium oxides are not very different in size from that of vanadium metal. In concluding, it might be pointed out that although this peak appears to be increasing at a significantly greater rate than the corresponding one in the metal (see Fig. III-6a & b), this is not true on an absolute scale since the ordinate in the vanadium metal graphs is a factor of 2.5 larger than that in the V_2O_3 graphs. Part of this all-around lower intensity in V_2O_3 is undoubtedly due to scattering from the roughness of the pressed powder surface but it is probably safe to say that this does not account for all of the discrepancy. Assuming that the E_{111} intensities are equal to those in the metal and that the vanadium interband transitions are 40% as large as those in the metal (the higher resolution data shows that these two conditions are simultaneously satisfied after the background is subtracted out), it appears that the probability of volume plasmon excitation is a factor of three lower in V_2O_3 than it is in metallic vanadium.

C. Auger Electron Spectroscopy

1. Vanadium Metal

As mentioned previously, the standard to which the shifts in energy of the Auger transitions in the vanadium compounds were measured is, quite naturally, the energy of these transition in metallic vanadium. The electron configuration of the neutral vanadium atom is [Ar] $4s^2$ $3d^3$, and the energy level scheme for the metal is shown in Fig. III-7. The energies of the inner shell levels has been determined using X-ray Photoelectron Spectroscopy (XPS)[21,72] and they are on the order of 0.5 eV in width.[85] The valence band consists of a mixture of the 4s and 3d states, it has been calculated to be 6.8 eV in width,[82] and it contains high optical densities of states of approximately equal magnitude at 0.6 and 1.6 eV below the Fermi level;[86] the combined FWHH of these two ODS is about 2.9 eV.

Typical dI/dV and d^2I/dV^2 AES spectra obtained for vanadium metal are shown in Fig. III-8, the excitation of only those transitions below 1000 eV being attainable in these experiments. Our results are in agreement with the previously published spectra of vanadium[72,87,88,89] and the transitions to which the peaks have been assigned are shown in the figure. The splitting of the peaks labelled $L_3M_1M_{2,3}$, $L_3M_{2,3}M_{2,3}$, and $L_3M_{2,3}V$ has been ascribed to the spin-exchange splitting caused by the interaction of the two electron vacancies in the final state;[89] such a splitting in the $L_3M_1M_1$ transition is not possible because the M_1 shell is empty in the final state and therefore the observed doublet must be due to another process. The transitions that were monitored in the vanadium compound chemical shift studies were the major $L_3M_{2,3}M_{2,3}$ and $L_3M_{2,3}V$ ones. These transitions were chosen because they 1) are characteristic of two different types of Auger transitions: the former being a transition in which all of the participating energy levels are inner shells while the latter transition involves the valence band, and 2) give the most intense peaks in this part of the high energy region of the Auger spectrum.

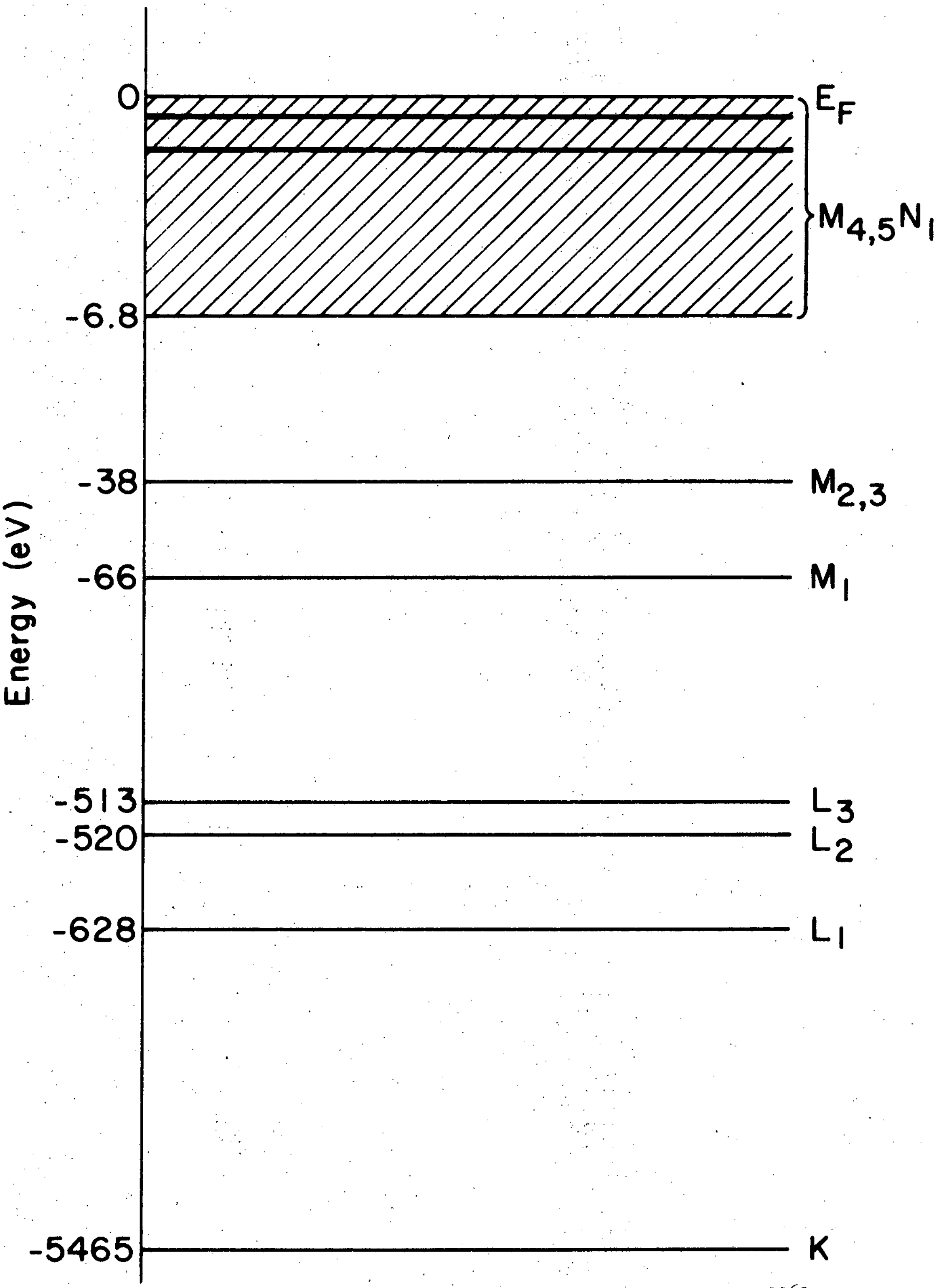

XBL 7112 - 2260

Fig. III-7. A schematic representation of the energy level scheme of vanadium metal.

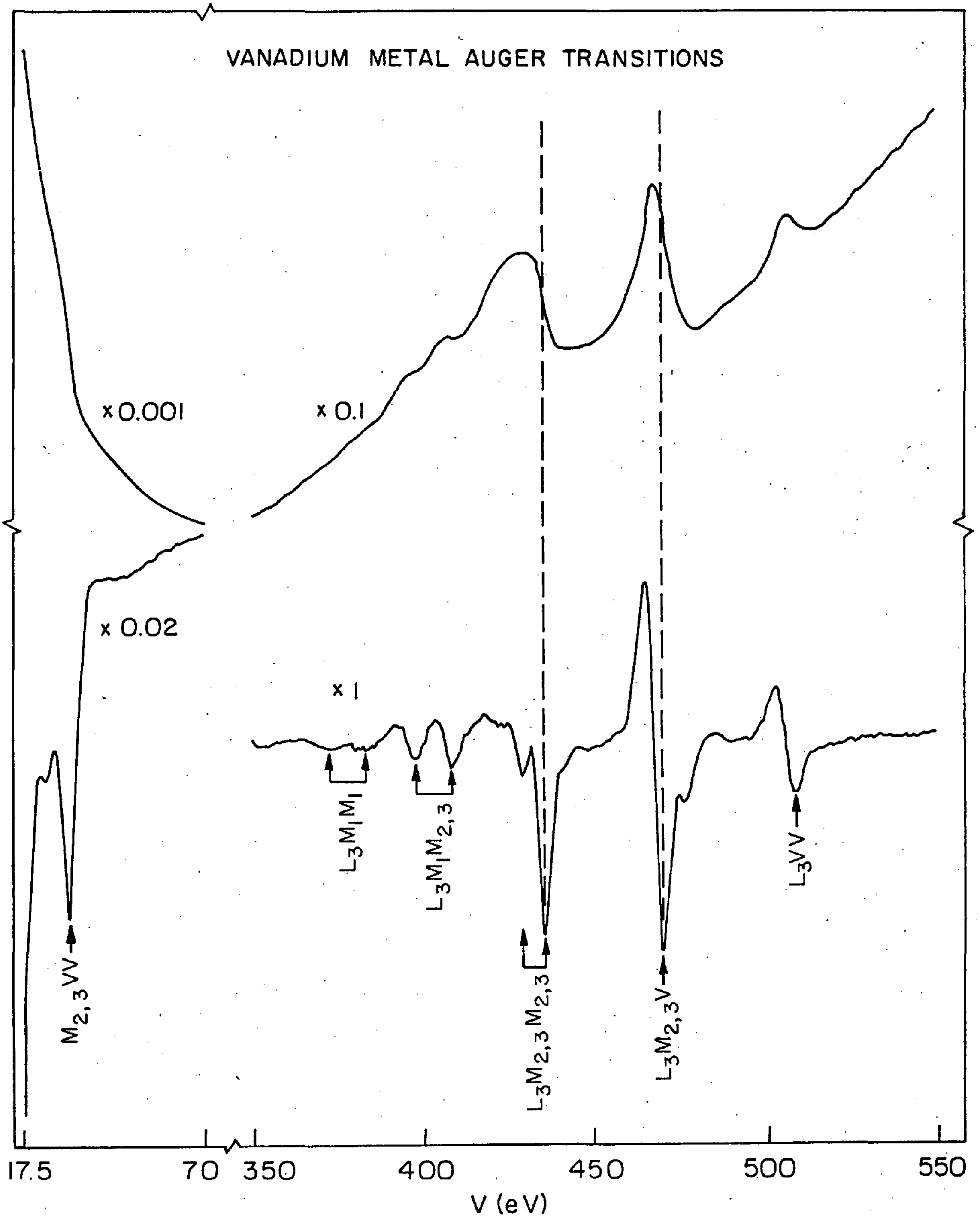

XBL7112-2259A

Fig. III-8. The dI/dV and d^2I/dV^2 Auger spectra of a vanadium metal (100) surface. The incident beam energy is 1000 eV and the p-t-p modulation is 3.0 volts.

As discussed earlier in connection with the LEED results, the reference crystal was always covered with a partial overlayer of sulfur which typically amounted to 0.3 of a monolayer. Of course the presence of this impurity would be expected to modify the state of the reference crystal and thereby affect the magnitude of the observed shifts. This is indisputable. However upon further reflection it rapidly become apparent that the perturbation of this small amount of sulfur upon the state of the entire detected volume of the reference crystal is indeed small. Since mean free path considerations suggest that approximately seven atomic layers of vanadium atoms are being probed, even if the sulfur atoms were assumed to affect two of these layers to the same extent that a one-to-one sulfur to vanadium atomic ratio would, it can be shown that the measured high energy minimum (of the d^2I/dV^2 curve) of the $L_3M_{2,3}M_{2,3}$ reference peak would move downward in kinetic energy by only 0.03 eV. The maximum of the electron energy distribution (i.e. the dI/dV) peak would be affected to a larger extent, moving downward in energy by about 0.11 eV. These values were obtained by mathematically superimposing two Gaussian peaks of equal standard deviation, one peak being 2/5 as large as the other and shifted downward in energy by 0.20 of a standard deviation. This latter value was obtained from the experimental results to be presented where, as we shall see, the measured standard deviation for the vanadium $L_3M_{2,3}M_{2,3}$ Auger transition peak is 2.0 eV and the energy shift of this peak in VS could not possibly exceed 0.4 eV. Minimum estimates of the impurity shift to be expected in this reference peak, i.e. 1/14 of the vanadium atoms shifted by 0.24 eV, yield values of 0.04 and 0.02 eV for the d^2I/dV^2 and dI/dV peak positions respectively. Similarly, the $L_3M_{2,3}V$ reference peak would not be affected by more than 0.01 eV in any of these cases.

2. Chemical Shifts of the Vanadium Compounds

a. The $L_3M_{2,3}M_{2,3}$ transition. Table III-2 summarizes the chemical shift data which was obtained for the vanadium $L_3M_{2,3}M_{2,3}$ and $L_3M_{2,3}V$ Auger transition peaks. All data are reported in terms of the observed kinetic energy of the vanadium compound peaks relative to the energy of the appropriate vanadium metal peaks. Although the shifts are reported to the nearest 0.01 eV this is the result of averaging over the number of experimental runs (shown in parentheses) performed on each species; the uncertainty in the determination of the shifts is about ± 0.1 eV. Because of the proximetry of the peak on the low energy side of the main $L_3M_{2,3}M_{2,3}$ transition peak, the two maxima being separated by 5.3 eV in metallic vanadium, and the peak tailing evident in the compounds no acceptable data was obtainable for the shift in the maximum of the energy distribution peak for this transition.

The compounds which were investigated are separated into two groups. The first four results were obtained using the conventional d^2I/dV^2 method of AES, recorded on graph paper, and analyzed by hand; the modulation magnitude was 6.0 volts p-t-p and 5-10 scans across the high energy minimum of each peak was made during each experiment.

TABLE III-2

AES Chemical Shifts of Vanadium in Various Compounds

		$L_3M_{2,3}M_{2,3}$ Transition[a]	$L_3M_{2,3}V$ Transition[a]	
		$\Delta(d^2I/dV^2)$	$\Delta(d^2I/dV^2)$	$\Delta(dI/dV)$
1.	V_2O_4	- 2.29 (4)	- 0.74 (4)	NA
2.	V_2O_3	- 1.46 (4)	0.00 (4)	NA
3.	$VO_{0.92}$	- 0.65 (2)	0.00 (1)	NA
4.	$VO_{0.83}$	- 0.93 (3)	- 0.01 (1)	NA
5.	V_2O_4	- 1.59 (7)	- 0.06 (4)	- 0.04 (6)
6.	V_2O_3	- 1.38 (4)	- 0.05 (3)	- 0.03 (3)
7.	$VO_{0.83}$	- 1.07 (3)	0.00 (1)	+ 0.05 (1)
8.	VN	- 0.98 (4)	+ 0.02 (3)	+ 0.05 (3)
9.	VC	- 0.86 (5)	+ 0.40 (5)	NA
10.	V_2S_3	$\begin{Bmatrix} -0.53 \\ -0.24 \end{Bmatrix}$ (4) (5)	+ 0.05 (2)	- 0.03 (2)
11.	VSi_2	- 0.53 (6)	- 0.17 (3)	- 0.43 (3)
12.	$VO_{1.11}$	- 1.40 (1)	+ 0.45 (1)	- 0.35 (1)
13.	VN(sintered)	- 1.33 (2)	+ 0.10 (1)	+ 0.15 (1)
14.	VC(sintered)	- 1.37 (3)	0.00 (1)	- 0.10 (1)

NA = not available

a) reference state is the energy for the same Auger transition in the vanadium metal.

The second group of results was acquired in the energy distribution mode, digitized and recorded on paper tape by the Vidar DAS, and computer averaged with the derivative also being mathematically calculated; the modulation was 2.0 volts p-t-p and 15-25 scans were typically averaged. When the latter set of experiments was initiated it was observed that the magnitudes of the observed shifts were not consistant with the previous results. Since the only real difference in the experiments was the amplitude of the modulation voltage, a study of the effect of its amplitude upon the magnitude of the chemical shift was launched. It was determined by computer analysis and by experiment that the magnitude of the observed $L_3M_{2,3}M_{2,3}$ transition shift was 0.28 eV larger for the 6.0 volt than it was for the 2.0 volt modulation magnitude in the case of the vanadium oxides; the discrepancy in the observed shift magnitude was similarly determined to be 0.35 in the $L_3M_{2,3}V$ transition experiments. From the computer analysis of this problem it was apparent that about 80% of the magnitude of this shift arose from the variation in the measured position of the vanadium reference crystal peaks. The cause of this type of modulation amplitude induced shift was touched upon in Section II.B.1 where the analyzer response function was discussed. As the modulation amplitude is increased, the output signal approximates a true derivative curve less and less as progressively greater non-linear portions of the peak are sampled. Due to the greater amount of peak tailing in the compounds relative to metallic vanadium, this variation from linearity is quenched in the compounds and therefore is not affected to such a large degree by changes in the modulation amplitude. For the instrumental peak widths encountered here, the data shows that virtually no variation is encountered for modulation magnitudes below 3.0 volts p-t-p and therefore the second series of results reported here should reflect the true values of the chemical shifts. The values obtained for the first four compounds have been corrected from their 6.0 volt p-t-p values so that they also reflect the true shift in their energy levels.

In Table III-3 the amplitudes of the anion and impurity peaks are listed relative to the amplitude of the vanadium $L_3M_{2,3}V$ transition peak. In each case the amplitude of the largest non-vanadium transition peak was measured. These are the KL_2L_2 peak in oxygen, nitrogen, and carbon, and the $L_3M_{2,3}M_{2,3}$ peak in sulfur and silicon. The presented data was internally standardized by using a 6.0 volt p-t-p modulation magnitude and a 1000 eV incident beam energy throughout. As demonstrated earlier, the intensity of a Gaussian or Lorentzian peak is proportional to the peak-to-peak amplitude of its derivative trace. Since, as noted previously, the low energy sides of the Auger peaks were often distorted due to tailing and/or overlapping, the peak amplitudes were measured from the trace centerline to the high energy minimum portion of the peak.

It will be noted again that these ratios should not be taken literally since the effective ionizing current, the ionization cross-section, the Auger transition probability, and the detected volume vary for each transition cited. The transition probability variation

Table III-3

AES Peak Intensity Ratios in Various Vanadium Compounds

		O/V	N/V	C/V	S/V	Si/V	Ca/V
1.	V_2O_4	2.25					
2.	V_2O_3	1.58					
3.	$VO_{0.92}$	1.03		NA	NA		
4.	$VO_{0.83}$	0.84		0.18	4		
5.	V_2O_4	1.82			0.23		
6.	V_2O_3	1.72			0.23		
7.	$VO_{0.83}$	0.82		0.26	4		
8.	VN	0.44	0.99				0.59
9.	VC			3.07			
10.	V_2S_3	0.66		$\left\{\begin{matrix}0.67\\0.38\end{matrix}\right\}$	27.3		
11.	VSi_2	0.12		0.16		44.6	
12.	$VO_{1.11}$	1.24		2.78	3.79		
13.	VN(sintered)	1.63	1.81	0.48	4		0.85
14.	VC(sintered)	1.29		1.66	4		

BLANK = element not detected

NA = not available

is perhaps the most important since the number of possible Auger transitions increases dramatically as one progresses down the rows of the Periodic Table and as the Auger current resulting from the ionization of a given energy level is spread more and more thinly among the various transitions. The effect of the effective ionizing current also becomes an important factor when the inner shell ionization energy lies within the limits of the secondary electron cascade peak; this influence is reflected in the sulfur and silicon compound ratios. Despite the limitations, the peak intensity information is an important supplement to the chemical shift data and is invaluable in correctly interpreting it. Most of the listed ratios are average values and the standard deviation is typically less than 0.10 units. Because of the sensitively of the low energy sulfur and silicon peak magnitudes to surface contamination, the maximum observed ratios are reported for the compounds containing these elemments. Finally it should be noted that all of the O/V intensity ratios were reduced by 0.20 units, this value being the calculated contribution of the nearby vanadium L_3VV transition to the oxygen peak intensity.

In order to begin to understand the data contained in Tables III-2 and III-3, the following observations will be made:

1. The magnitude of the observed chemical shifts (ignoring the last three compounds) generally increase with an increasing difference in electronegativity of the compounding elements.
2. The samples of V_2O_4, V_2O_3, VC, and VSi_2 are, for all practical purposes, free from contamination.

3. The anomalously small chemical shift associated with the V_2S_3 compound suggests that the $VO_{0.83}$ and $VO_{0.92}$ samples (assuming that the impurity levels in the $VO_{0.92}$ are similar to those in the $VO_{0.83}$ sample) are also relatively free from impurities that may affect the magnitude of their observed chemical shifts.

4. If the O/V ratio for the set of V_2O_4 samples in row #1 is accepted as a standard (this compound possesses the most exact stoichiometry of the vanadium oxides), it is seen below that then is a remarkable agreement between the experimentally observed ratios and the calculated ones. Listing all of the theoretical predictions in the manner VO_x, we have

Table III-4.

Comparison of Theoretical and Experimental O/V Peak Intensity Ratios in the Vanadium Oxides

Row	Compound	Calculated*	Experimental
1.	V_2O_4	2.00	2.00
2.	V_2O_3	1.50	1.40
3.	$VO_{0.92}$	0.92	0.92
4.	$VO_{0.83}$	0.83	0.75
5.	V_2O_4	2.00	1.62
6.	V_2O_3	1.50	1.53
7.	$VO_{0.83}$	0.83	0.75
12.	$VO_{1.11}$	1.11	1.10

*Theoretical or determined by crystal grower.

> These results indicate that the vanadium oxides retain their composition throughout the detected volume of the samples and that the acceptance of the row #1 V_2O_4 sample as a standard is justified.

From these observations it may be concluded that the chemical shift values obtained for all of the "clean" compounds mentioned above might fairly accurately reflect the oxidation state of the vanadium atoms in each compound. It is obvious from the combined chemical shift and O/V ratio data that the row #5 samples, which were originally believed to be of the composition V_2O_4, have undergone reduction. Although these samples had been made from the same batch of powder that the original experiments were performed on, this powder obviously was exposed to reducing conditions during the time interval between these two sets of experiments if one is to rationalize its observed surface composition during the latter measurements.

The source of the 294 eV calcium peak in the VN is not known but it must have originated in the manufacturing process since it was also present in the sintered VN which was obtained from a different supplier. An X-ray fluorescence analysis of these samples revealed that no more than 0.02% of the bulk sample was calcium.[90] This indicates that it is concentrated at the surface, most likely as the compound CaO. The fact that the VN chemical shift is of the expected magnitude suggests that this CaO impurity is located primarily as a surface overlayer covering the VN. Such an interpretation is also consistant with the observed magnitude of the N/V intensity ratio.

From the interpolation of the anion/V ratios in the oxide and the carbide, the N/V ratio would be expected to be about 2.1/1. However if the CaO is present as an overlayer then since the detected volume associated with the nitrogen peak is less than that of the vanadium peak, the magnitude of the nitrogen peak will be more severely attenuated than that of the vanadium and this is what is observed. Although the intensity ratios indicate that a small amount of vanadium oxide my also be present, the VN chemical shift data will be regarded as being representative of the pure nitride.

Two chemical shift values have been reported for V_2S_3. The larger value is the one that should be associated with this compound. The smaller value is, I believe, representative of the compound VS. It is well known that V_2S_3 undergoes the decomposition reaction

$$V_2S_3 \rightarrow 2VS + S$$

when it is heated above 950°C.[91] This heat treatment was performed inside the vacuum system and resulted in the magnitude of the observed shift changing from -0.53 to -0.24 eV. Since the S/V peak intensity ratio essentially remained constant throughout these experiments, it appears that the free sulfur remained evenly distributed throughout the sample. It is not felt that the small amount of carbon present is appreciably affecting the magnitude of the shift results since although some of the V_2S_3 samples contained almost twice as much of this impurity as others there was no difference observed in the shifts. Upon heating the amount of carbon was generally reduced, strongly suggesting that this impurity is not bound to the vanadium atoms (VC being a highly refractory material) but may have been deposited on the surface during the manufacture of the compound (V_2S_3 may be prepared by the reaction of CS_2 with V_2O_5). The reason for the anomalously small chemical shifts exhibited by these sulfides is not entirely understood. Since sulfur is the only one of the anions studied which has its unfilled 3d levels low enough in energy to impart some appreciable portion of their character to the chemical bonds formed, it is likely that this fact underlies the peculiar behavior of these compounds. This phenomena may be viewed as a form of back-donation of electrons to the cation through the medium of these d-orbitals. Hartree-Fock-Slater calculations have been carried out for sulfur and their results have shown that even a small amount of d-orbital character in a bond will significantly alter the change in binding energy of the inner shells.[21] Unfortunately the amount of d-orbital participation in the bonding is unknown and is therefore unable to be compensated for. For this reason, the sulfide data will not be included in the discussion regarding the dependence of the chemical shift upon bond ionicity.

The last three entries in Tables III-2 and III-3 were not extensively investigated since it was apparent that they were too complex in their make-up to readily glean useful information from them. Due to the obvious influence of impurities upon the observed shifts and the lack of information concerning their distribution throughout the surface layer, there is simply not enough information available in these results to untangle the problem. Although one could conjecture as to the state of each impurity and rationalize the observed data, this will not be done. These results are therefore presented only so that the interested reader may peruse them and will appreciate the difficulties involved in working with these more complicated systems and recognize the practical limitations of the technique.

The real question at hand is, of course, what sort of correlation can be made between the sign and magnitude of the observed shifts and the strength of the chemical bond in the observed compounds. This question will first be directed at the $L_3M_{2,3}M_{2,3}$ transition results. The fact that all of the transition energies decrease in absolute magnitude would be expected a priori. As previously pointed out, the more electropositive element in a binary compound will tend to transfer some fraction of its valence electronic charge to the more electronegative element, thereby resulting in a greater effective nuclear charge on its remaining electrons and increasing their binding energy. If the magnitude of the binding energy increase is similar for each energy level, a supposition which is confirmed by XPS results,[21] reference to Eq. (I-13) shows that the observed Auger inner shell transition energy change will be toward a smaller kinetic energy of the ejected electron.

In order to glean any information about the nature of the charge transfer associated with the observed chemical shift, it is necessary to compare the results with a standard: a scale of bond ionicity.

At the present time there exist four basic theories which deal with the problem of creating such a yardstick. These are listed in Table III-5 along with the experimental origins of the parameters which appear in each theory. Discussion of the merits of each approach is beyond the scope of this thesis and will not be presented here, especially since a fairly detailed comparison is made in the literature. The dispersion theory of Philips and Van Vechten (henceforth referred to as PV) is the most suitable for our purposes. This statement stems from the fact that it was specifically designed to account for solid state effects, it treats the covalent and ionic contributions to the ionicity on equal terms (unlike the Thermochemical approach which ignores the effect of the covalent bond or the VB-MO

Table III-5

Bond Ionicity Theories

Type of Bond Theory	Covalent	Ionic
Thermochemical	Heats of formation of elements	Extra-ionic or heteropolar energy
Valence bond-M.O.	Heats of formation of homopolar IV crystals	Atomic spectra
Pseudopotential	Three parameters fitted to interband energies	Three parameters fitted to interband energies
Dispersion Theory	Dielectric constants of homopolar IV crystals	Dielectric constants of heteropolar crystals

approach which includes it only as a second order term), and it is not affected by the requirement of subjectively weighting the various parts of the experimental spectrum in fitting the theory to it (as in the Pseudopotential case).

Detailed discussions of the PV Dispersion Theory and its modifications are presented in various papers[92-96] and therefore only a short sketch of it will be given here. The theory originally grew out of an attempt to develop a simple model to explain the observed dielectric properties of solid compounds. The usually complicated crystalline band structure is instead represented by the isotropic bands associated with the nearly free electron model of the band structure. The total (average) energy band gap, E_g, which is associated with this model is shown to be decomposable into homopolar and heteropolar parts, designated as E_h and C respectively, and the relationship which exists among them is

$$E_g^{\,2} = E_h^{\,2} + C^2 \quad . \qquad \text{(III-3)}$$

The fraction of ionic and covalent character of the bond may then be defined by the expressions

$$f_i = C^2/E_g^{\,2} \quad \text{and} \quad f_c = E_h^{\,2}/E_g^{\,2} \quad . \qquad \text{(III-4a,b)}$$

The average homopolar energy gap is taken to be a function of the nearest-neighbor distance only, and an expression for it may be derived by observing the dispersion of the dielectric constant in the Group IV elements of the Periodic Table (i.e. C, Si, Ge, and Sn). The expression developed for this gap is

$$E_h = \frac{39.74}{d^s} \text{ (eV)} \qquad \text{(III-5)}$$

where

d = the bond length expressed in Ångströms

s = 2.48

An analytic formula for the heteropolar gap was then constructed to describe the variation of the observed values of the total band gap for different compounds. This expression, which has been extended to accomodate compounds of the A_mB_n type which may contain cationic d-electrons,[96] is

$$C = 14.39 \; b \left[\frac{1+\Gamma}{1-(\Gamma f_c/f_i)}\right]^{1/2} e^{-k_s r_o} \left[\frac{\sigma Z_A-(n/m)Z_B}{r_o}\right] \text{ (eV)} \qquad \text{(III-6)}$$

where

$b = 0.089\ (\bar{N}_c)^2$

$\bar{N}_c$ = the average co-ordination number of the crystal =

$$\left[\left(\frac{m}{m+n}\right) N_c(A) + \left(\frac{n}{m+n}\right) N_c(B)\right]$$

Γ = the fraction of empty d-levels = the number of d-shell holes per formula unit/the total number of valence electrons

$e^{-k_s r_o}$ = the Thomas-Fermi screening factor

k_s = $2.729\ n^{1/6}$

n = the number of s and p electrons per A_mB_n/the molecular volume of A_mB_n in Å^3

r_o = d/2

σ = the bond length of the Group IV element in the same row of the Periodic Table as B/the bond length of the Group IV element in the same row as A

Z_A, Z_B = formal valencies of A and B respectively

In determining C for a compound containing d-electrons, it is obvious that a self-consistant calculation must be performed since the right-hand side of Eq. (III-6) contains the term C^2 within the f_c/f_i ratio appearing therein.

Using this PV theory, the calculated ionicity values of the compounds which have been studied are

Table III-6

Calculated PV Ionicities for Vanadium Compounds

Compound	f_i
V_2O_4	0.95
V_2O_3	0.94
VO	0.93
VN	0.87
VC	0.70
V_2S_3	0.90
VSi_2	0.52[97]

The observed chemical shifts of the clean compounds listed in Table III-2, with the exception of V_2S_3, have been plotted vs. these ionicity values and the results are shown in Fig. III-9. As expected the graph varies in a fairly linear manner from an ionicity value of zero to that ionicity region near the compound VO. Such behavior is quite easily rationalized since the two most loosely bound electrons in vanadium are in the 4s subshell. These electrons have relatively little core penetration[98] and therefore their "removal" from the vanadium atom could reasonably result in the system following the dictates of the previously expounded valence shell model of the inner shell shifts. The next set of electrons that would be affected are in the 3d subshell. These electrons have a significant amount of core penetration and any increase in their mean distance from the nucleus would be expected to result in a significantly larger increase in the effective nuclear charge upon the remaining electrons than that which results from the donation of the 4s electrons to another atom. Consequently it is very attractive to associate the "knee" in Fig. III-9 with such a 3d electron loss effect. Although this interpretation may be generally valid, it may well be suspected that the situation is indeed more complicated than this simple model suggests. There are a number of effects which modify the energy of the emitted Auger electron and most of these are to some degree dependent upon the oxidation state of the atom. These effects will be brought to light in the following discussion of results which are related to ours.

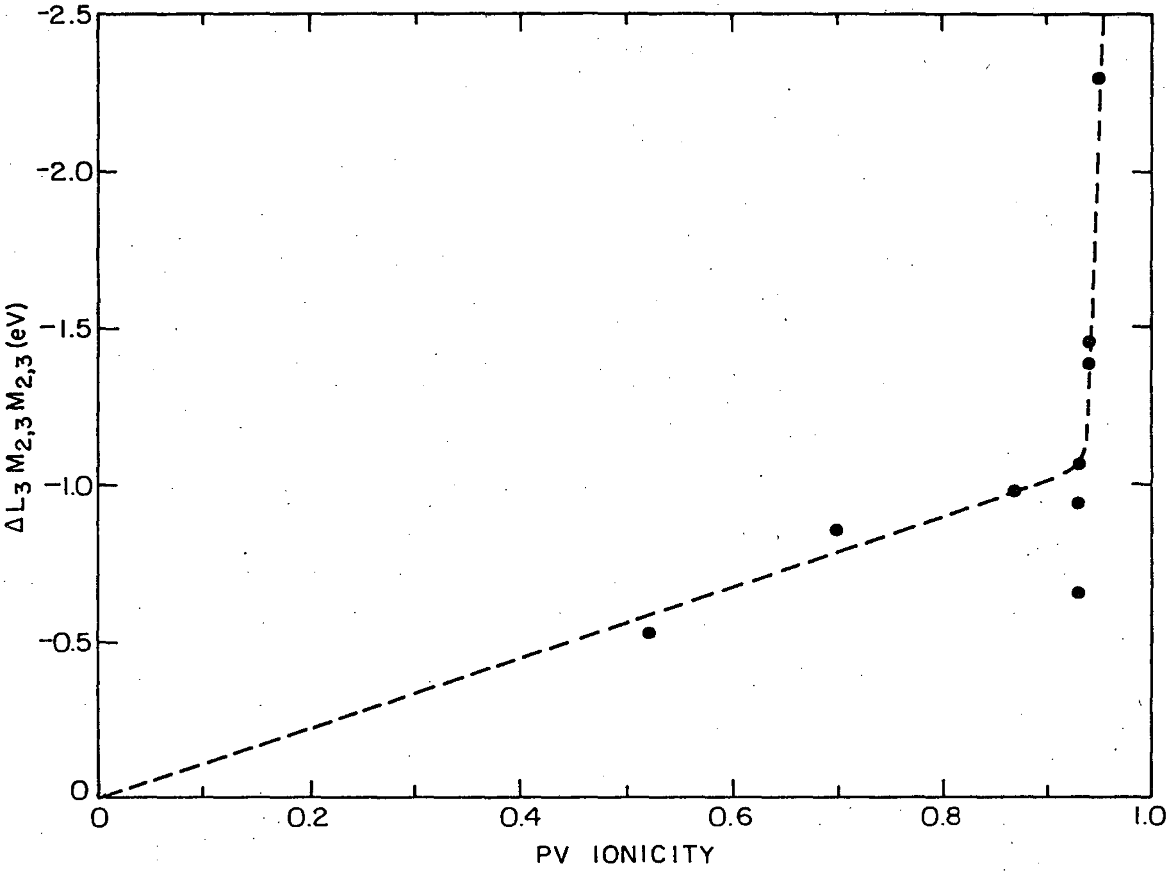

XBL 737-6485

Fig. III-9. The magnitude of chemical shift of the vanadium $L_3M_{2,3}M_{2,3}$ Auger transition in the vanadium compounds relative to vanadium metal plotted vs the calculated Phillips-Van Vechten ionicity values for the compounds.

Two papers have appeared in the literature which directly bear upon our results. The first of these was a series of XPS and AES chemical shift experiments carried out on TiC, TiN, TiO, TiO_2, and VC by Ramqvist et.al.[99] on the Uppsala instrument. The second contains similar experiments on V_2O_5 done by Fiermans and Vennik;[79] their XPS data was obtained using a HP 4950A XPS machine and the AES experiments were carried out in a R.F.E.A. system identical to ours. All of these authors measured their shifts at the maximum in the energy distribution curve and their combined results are listed in Table III-7.

It will be noted that the magnitude of the XPS shift for a given energy level increases as the oxidation state of the cation is increased; the fact that TiO appears to be an exception to this trend is probably due incomplete oxidation since the Ti-O system also possesses a solid solution range around the monoxide. It will also be noticed that the shifts for TiO_2 and V_2O_5 are much larger than would be anticipated if the trend of the lower oxidation states were to be linearly extrapolated out to these compounds. This effect is a logical one since, as previously mentioned, the removal of the core-penetrating 3d electrons would be expected to have a greater effect than that of the 4s electrons. All of these results are in accordance with our observations. The sequence of shifts in the V_2O_5 L and M subshells can also be rationalized using core penetration effects. Although it might be expected that the complete removal of a 3d electron from the cation would affect the M electrons to a greater extent than the L electrons (see, for example, the electronic probability density distributions

Table III-7

Supplementary XPS and AES Data[79,99]

	ΔK	ΔL_2	ΔL_3	ΔM_1	$\Delta M_{2,3}$
TiC	-1.0±0.4		-1.3±0.1		
TiN	-1.2±0.4		-1.5±0.2		
TiO	-1.0±0.4		-1.0±0.2		
TiO_2	-4.3±0.4		-4.9±0.2		
VC	-1.5±0.4		-1.8±0.3		
V_2O_5		-5.3	-5.3	-4.2	-4.7

	$\Delta(KL_2L_3)$	$\Delta(L_3M_1M_1)$	$\Delta(L_3M_1M_{2,3})$	$\Delta(L_3M_{2,3}M_{2,3})$	$\Delta(L_3M_{2,3}V)$
TiC	-1.5±0.4				
TiN	-1.9±0.4				
TiO	-1.6±0.5				
TiO_2	-5.8±0.4				
VC	-2.4±0.4				
V_6O_{13}		-2	-2.5	-2.1	-1.2

in Fig. 20 of Ref. 98), it will also be perceived that since the true effect is rather a slight outward redistribution of these electrons from the nucleus the amount of change in the 3d-L overlap may be of a similar magnitude as the change in the 3d-M overlap. Combined with the fact that the L subshells tend to shield the outer subshells from the effective increase in the nuclear charge, the observed larger shifts for the L shell energy levels can be rationalized. The observation that the $M_{2,3}$ subshell shift is of a greater magnitude than that of the M_1 subshell may be ascribed to a geometrical effect: the 3d orbitals overlapping the directional $M_{2,3}$ levels to a greater extent than the symmetrical M_1 level.

The fact that Ramqvist et.al. found the difference between subshell shifts to decrease in the order TiC, TiN, TiO is more difficult to explain. Those authors concluded that this indicated that 3d electrons are to some extent transferred to the anion and that the amount of this transfer increases in the order TiO, TiN, TiC. This effect was rationalized by arguing that although the non-metal bonding levels will be more localized in going from the carbide to the oxide, the additional electrons in TiN and TiO partially enter the nearly higher energy levels which are antibonding in nature and are primarily localized around the cation. The position of Ramqvist et.al. is supported by some observations on the variation of the vanadium $L_3M_{2,3}V/L_3M_{2,3}M_{2,3}$ peak intensity ratio. This data is presented in Table III-8. Although the numerical results are tenative since they are typically based on four individual observations of this ratio in the compounds, a trend is definately indicated. As pointed out in the next section, the available evidence suggests that it is the 3d electrons which make the overwhelming contribution to the intensity of the $L_3M_{2,3}V$ transition peak. From the table it will be noted that the intensity ratio declines in the order VO, VN, VC, thereby indicating that more of the 3d electron density is being transferred to the anion in the carbide than in the oxide. XPS measurement of the shifts in the subshells outside of the L_3 subshell would prove useful in further clarifying this question. This data also indicates that the amount of this spacial transfer of electron density is relatively small with respect to the metal atom radius since the amount of overlap of the electronic densities of the $M_{2,3}$ and $M_{4,5}$

Table III-8

Vanadium Single Valence Band to Inner Shell Transition Peak Intensity Ratios for Various Compounds

Compound	$L_3M_{2,3}V/L_3M_{2,3}M_{2,3}$ Intensity Ratio
V	1.13
V_2O_4	0.73
V_2O_3	0.84
VO	0.93
VN	0.89
VC	0.85
V_2S_3	0.96
VSi_2	0.96

shells is seen to remain surprisingly constant, a fact which would also seem to warrent further experimental investigation. It is not clear to what degree this d-electron donation interpretation is valid since the effect of orbital relaxation also enters into the picture. There are two relaxation effects which modify the energy of a photoemitted (or Auger) electron. The first is due to what has been termed dynamic relaxation[100,101] and is the result of the occupied outer shell orbitals undergoing a collapse toward the newly created vacancy thereby accelerating the outgoing electron and resulting in an apparent decrease in its binding energy. Since this atomic relaxation energy is dependent upon the number of electrons outside the ionized shell, one would expect the (negative) shift in the relaxation energy upon the removal of electrons during compound formation to be greater for the outer shell electrons than for the inner shell ones. Calculations suggest that this shift would be on the order of magnitude of 0.1-1 eV. The size of the change between the L_3 and K shifts would however be expected to increase from the carbide to the oxide, in contradiction to the observed ($\Delta L_3-\Delta K$) difference. There also exists an energy contribution due to extra-atomic relaxation.[101] This effect has been observed for atoms which are placed in a solid-state environment and is attributed to the relaxation of electrons from the neighboring atoms. This relaxation effect would be expected to be of the same magnitude as and vary in a manner similar to that discussed for atomic relaxation. Therefore it is concluded that the d-electron donation effect in the carbide, nitride, oxide series is real and, if anything, larger than that indicated by the XPS results.

Turning our attention to the AES results in Table III-7, it will be noted that 1) the AES shifts of Ramqvist et.al. are generally slightly larger than those predicted by their XPS data, and 2) the AES shifts predicted by the XPS data of Fiermans and Vennik are substantially larger than those observed and the magnitude of the shifts varies anomalously for the $L_3M_1M_1$, $L_3M_1M_{2,3}$, and $L_3M_{2,3}M_{2,3}$ transitions.

Although experimental uncertainty may account for the trend noted in the first observation, another explanation is also possible. Shirley[102] has recently pointed out the discrepancy between the observed absolute energies of inner shell Auger transitions and those calculated using Eq. (I-13). He noted that two corrections should be made to that equation. The first of these was first proposed by Asaad and Burhop[103] who realized that the binding energy of the Auger electron will be increased by the amount of the two-electron interaction for the energy levels in which the final state vacancies are located. Shirley[102] noted that the use of empirical XPS binding energies in the calculation would automatically compensate for the dynamic relaxation processes occurring during an Auger event, but that a so-called static relaxation effect also exists. He reasoned that the relaxation of the outer orbitals during the de-excitation of the X_p electron would create a more repulsive environment for the Y_q electron, thereby raising its orbital energy by an amount R. The Auger energy should therefore be given by the expression

$$\bar{E}_{W_o X_p Y_q}(Z) = \bar{E}_{W_o}(Z) - \bar{E}_{X_p}(Z) - E_{Y_q}(Z) - \phi_A - F_o(X_p, Y_q) + R \qquad \text{(III-7)}$$

where

$F_o(X_p,Y_q)$ = the Slater integral for the X_p-Y_q interaction

R = the static relaxation energy (See Ref. 102 for its form)

To a degree sufficiently accurate for our purposes, the electron interaction correction for inner shells should not vary upon chemical bond formation. However, the amount of relaxation should decrease for a compounded atom relative to an atom in a metal. This would increase the magnitude of the AES shift and this is what is observed for the results of Ramqvist et.al. Since the magnitude of the change in the static relaxation energy would be expected to be on the order of 0.1-1 eV, it is suggested that this effect may be being observed here.

As to the results of Fiermans and Vennik, it should be first pointed out that those authors have used LEED and AES techniques to establish that V_2O_5 undergoes a decomposition to V_6O_{13} upon interacting with an electron beam.[104] This fact is recognized in the table and accounts for some part of the discrepancy between the observed AES shift magnitudes and those calculated from the X-ray data for V_2O_5. Difficulties in the determination of the work function of the AES spectrometer might also contribute to the discrepancy. One other piece of information suggests, however, that a fairly large discrepancy does exist. If the absolute values for the L_2, L_3, M_1, and $M_{2,3}$ energy bands for V_2O_3 (by Honig et.al.[84]) and for V (Fiermans and Vennik[79]) are compared, the values obtained for the shifts of these levels are -4.3, -4.5, -3.1, and -4.1 eV respectively. (This procedure is not quite as risky as it appears since both XPS experiments were carried out at the Hewlett-Packard laboratories, on the same machine, and with H-P personnal. The energy calibration was therefore, in all probability, carried out in the same manner.) These calculated XPS shifts for V_2O_3 are quite consistant with those observed for V_2O_5 and TiO_2 and the predicted AES shifts calculated from them are again too large when compared with our AES data. The source of this difficulty may again lie in the question of relaxation. Although the conclusions presented above for the KL_2L_3 titanium compound shifts are quite valid since the equations dealing with the relaxation phenomena have been proven to work well with the tightly bound inner shells, it is not clear to what extent they may apply, if at all, to the loosely bound inner shells. Although the author can only surmise that this is indeed the cause of the observed discrepancy, it does seem to be the only valid arguement available to rationalize the observations. More work is obviously called for in this area. When this effect is better understood perhaps it will also explain the observed variation in energy of the $L_3M_1M_1$, $L_3M_1M_{2,3}$, and $L_3M_{2,3}M_{2,3}$ transition shifts. It is also possible that due to the small magnitude of the first two transitions relative to the latter one, the uncertainty in peak positions is large for these transitions (Fiermans and Vennik do not specify any confidence limits) or that their position was altered by the method of background subtraction employed. It might also be noted that the observed $L_3M_{2,3}M_{2,3}$ shift for V_6O_{13} appears to be a bit too low when compared to our results but this may be due to the aforementioned difficulty of measuring the position of the energy distribution maximum for this transition peak in the compounds.

Despite all of the difficulties mentioned above it is quite clear from the data which was accumulated on the vanadium $L_3M_{2,3}M_{2,3}$ Auger transition that the chemical shift associated with this (loosely bound) inner shell transition varies in a reasonable and understandable manner upon compound formation. This has been the first in-depth study[79,105,106] of the chemical shift effect for inner shells using electron-excited AES techniques and one can readily grasp its potential in supplementing LEED and regular (i.e. qualitative and quantitative) AES data in elucidating the chemical composition of a thin surface layer.

b. The $L_3M_{2,3}V$ transition. That the situation existing for the single valence shell $L_3M_{2,3}V$ transition is somewhat different is evident by observing the shift variation for this process in Table III-2. Before proceeding to a discussion of this transition, however, an additional piece of information that can be gleaned from the AES information will be presented: the variation in the width of the valence band. As previously pointed out, the width of the inner shell transition peaks in the compounds is not expected to (or appear to) vary from that observed for vanadium metal. The observed standard deviation of the $L_3M_{2,3}M_{2,3}$ transition was measured at 1.99 eV. This number is based upon the assumption that the peak is Gaussian in nature since the value was calculated from the difference in energy between the maximum of the dI/dV curve and the high energy minimum of its derivative. When this value is corrected for the amplitude of the modulation voltage and for the ILW of the analyzer (see Appendix V), the corrected standard deviation, σ_c, is 0.92 eV and the $FWHH_c = 2.15$ eV. Using X-ray absorption techniques, Fischer[85] has determined that the width of the L_3 peak is 0.5 eV. This value is the width between the 0.25 and 0.75 amplitude points of the absorption curve and it is not clear whether this value should be considered the FWHH of the peak as suggested by Beeman and Friedman[107] or whether this value is equal to 1.35 σ, assuming a Gaussian peak distribution. In the latter case, the FWHH would prove to be 0.9 eV. Assuming equal widths for the L_3 and $M_{2,3}$ energy levels and recognizing that the maximum possible Auger peak width is the sum of the individual level widths, our data would imply a minimum FWHH of 0.7 eV for each of these levels-a value in good agreement with Fischer's observations.

The observed standard deviations of the $L_3M_{2,3}V$ peaks, the corrected standard deviation, and the corrected FWHH of each are listed in Table III-9. The last column gives the calculated width of the valence band alone after subtracting out the assumed contribution (2/3 of 2.15 eV) of the inner levels. Our valence band FWHH of 2.7 eV for vanadium metal compares well with the ≈ 2.9 eV width of the 3d levels as measured by Eastman.[86] From these results it is strongly indicated that the main contribution to the $L_3M_{2,3}V$ transition width

Table III-9

Valence Band Widths for the Vanadium Compounds

	σ(eV)	σ_c	$FWHH_c$	$FWHH_{VB}$
V	2.86	1.75	4.12	2.69
V_2O_4*	2.81	1.70	4.00	2.57
V_2O_3	2.82	1.71	4.02	2.59
$VO_{0.83}$	2.85	1.74	4.10	2.67
VN	3.07	1.96	4.61	3.18
VC	4.60	3.49	8.21	6.78
V_2S_3	2.98	1.87	4.40	2.97
VSi_2	3.17	2.06	4.85	3.42

*The actual composition of this reduced V_2O_4 is V_3O_5

from the valence band in metallic vanadium comes from the 3d levels, a not unexpected result considering the high density of states occurring in this level and its large overlap with the core levels relative to that of the 4s electrons.

The most notable features of these results are the slightly larger valence band widths of VN and VSi_2 and the very large width of VC. Although no other data on VSi_2 could be found, Fischer[85] has reported X-ray emission spectra of VN and VC. Although his data suggests that the VN $M_{4,5} \rightarrow L_3$ emission peak is 10-20% wider than that observed for the metal, this also appears to be true for his V_2O_3 spectrum peak and the observed adsorption peak widening may be due to the uncertainties in separating out the various components of the spectrum. The situation existing for VC is less confusing. The emission spectrum from this compound shows the peaks from the vanadium $M_{4,5} \rightarrow L_3$ transition and the carbon $L_{1,2} \rightarrow$ vanadium L_3 cross-transition to overlap to a large extent. The combined width of the resulting peak is 2 to 2.5 times as large as the vanadium $M_{4,5} \rightarrow L_3$ transition peak width. Since it has been pointed out that a strong admixture of the carbon 2s and 2p levels with the vanadium 3d levels is likely,[107] it would appear that the valence band contribution to the $L_3M_{2,3}V$ Auger transition is reflecting this interatomic interaction.

Returning to the topic of chemical shifts, upon a bit of reflection it will soon become obvious that when one is concerned with the measurement of the d^2I/dV^2 high energy minimum of a single valence band Auger transition it is the position of the high energy edge of the valence band that will enter into the calculations and not the position of the peak maximum. This is true because the highest kinetic energy Auger electrons will be emitted from this edge and the high energy minimum of the d^2I/dV^2 trace should mimic its movement. The filled 3d density of states drops off precipitously at the Fermi level and therefore our reference is well defined. In fact all of the compounds studied, with the exception of V_2O_4, are conductors at room temperature. It will therefore be assumed that the steepest portion of the high energy valence band edge (henceforth referred to as the HEVBE) occurs at the Fermi level for V_2O_3, VO, VN, VC, V_2S_3 (and VS), and VSi_2. It is unfortunate that, except for V_2O_3, no valence band XPS spectra have been published for these compounds so that this assumption may be verified. It is desirable to have a check on this seemingly valid assumption because a high density of states edge may be present at some energy below the Fermi level with only a low density of states intersecting the Fermi level to provide the properties of conduction.

The coincidence of the X-ray emission peak and absorption edge in V, V_2O_3, VN, and VC argues that the preceeding assumption is a good one for these compounds. The V_2O_3 valence band spectrum by Honig et.al.[84] clearly shows the large drop-off of the occupied states at the Fermi level and provides direct confirmation of the assumption for this compound. From the trend noted above, one would expect the situation to be similar for the vanadium monoxides and the vanadium sulfides of interest here. If there is little or no net d-electron transfer in $VO_{0.92}$, $VO_{0.83}$, V_2S_3, and VS, a supposition supported by the $L_3M_{2,3}M_{2,3}$ shift data and the ensuing discussion, then the L_3-$M_{2,3}$ shift difference in these compounds relative to the metal would be expected to be zero. Since the position of the HEVBE is also unaltered, the $L_3M_{2,3}V$ shift would be expected to be zero if static relaxation effects are ignored. For the conditions stated above, no shift would be expected for VN either, and the $L_3M_{2,3}V$ shift result might then be considered as evidence that little or no d-electron transfer occurs in this compound. It seems likely that such transfer does occur in VC, however. If the ΔL_3-$\Delta M_{2,3}$ shift is the same for VC as that measured for V_2O_3 and V_6O_{13} and calculated for V_2O_4, noting that the shift difference appears to remain constant throughout this range of d-electron removal and may therefore be a geometrical effect, valid for any significant amount of d-electron transfer, then a $L_3M_{2,3}V$ shift of + 0.4 eV would be expected. This value is of the correct sign and magnitude as that observed for VC. Applying the same logic as above, the V_2O_3 shift should also be + 0.4 eV and this value is larger than the observed. Proceeding on to V_2O_4 and noting that Goodenough places the HEVBE 0.4 eV below the Fermi level, the anticipated shift would be 0.0 eV which is at least in the right direction relative to V_2O_3 and VC. It might be pointed out that the V_2O_4 band gap is 0.7-0.8 eV wide, which means that if the V_2O_4 Fermi level is positioned at the top of the band gap then the experimentally observed difference in the V_2O_3 and V_2O_4 $L_3M_{2,3}V$ transition shifts would be predicted. More likely, however, is the possibility that a localized static relaxation energy is affecting the observed Auger electron energy. Since the magnitude of such a relaxation would be dependent upon the number of valence electrons available to move toward the vanadium atom, one can argue that the relaxation energy should increase in the order V_2O_4, V_2O_3, VO, VN, VC, V. If this relaxation energy remains essentially unchanged until true d-electron bond formation occurs and is on the order of 0.3-0.4 eV for V_2O_3 and V_2O_4, then the observed results will be reproduced by the calculations.

From the above discussion it is clear that the type of chemical bonding information that is desired for elucidating surface chemical compositions is not readily obtainable from the observed Auger single valence band transitions. However it also is apparent that when the appropriate XPS information on inner shell shifts and the valence band density of states becomes available, observations on this type of transition may provide valuable information about the variation in electronic screening which occurs in the valence band upon chemical combination.

3. The Oxidation of Vanadium

After it was determined that the shift of the $L_3M_{2,3}M_{2,3}$ transition was useful in distinguishing between the various oxidation states of vanadium, a number of oxidation runs were carried out upon a vanadium metal single crystal in an attempt to further probe the chemistry and homogeneity of the V-O system in the thin surface layer sampled by AES.

A (100) crystal face was oxidized by various temperature-pressure combinations in the ranges 25-1200°C and 10^{-7} - 10^{-2} Torr respectively. The exposures varied from 10^2 - 10^7 L (1L = 10^{-6} Torr-sec). The O/V intensity ratio was monitored after each gas exposure as was the position of the $L_3M_{2,3}M_{2,3}$ peak. A graph illustrating the results obtained from one of the (room temperature) oxidation runs is shown in Fig. III-10. This graph is useful since it shows all of the spectrum changes that have and will be discussed. These are

1. The quite noticeable downward shift in energy of the $L_3M_{2,3}M_{2,3}$ transition peak.
2. The virtually unaffected position of the $L_3M_{2,3}V$ transition peak.
3. The changes in the intensity ratio of the $L_3\,{}_{2,3}V$ and $L_3M_{2,3}M_{2,3}$ transition peaks.
4. The overlapping of the vanadium L_3VV and the oxygen KVV transition peak (near 510 eV).
5. The changes which occur in the low energy part of the spectrum.

After measuring the effects of the oxidation run, the position of the reference (i.e. vanadium metal) peak was established by resistively heating the crystal above 1000°C in vacuum for 2 minutes, this heat treatment being sufficient to restore the AES trace which is characteristic of the unoxidized surface. Using this procedure one eliminates any error due to a work function change of the energy analyzer resulting from the adsorption of oxygen upon its surface. In these experiments

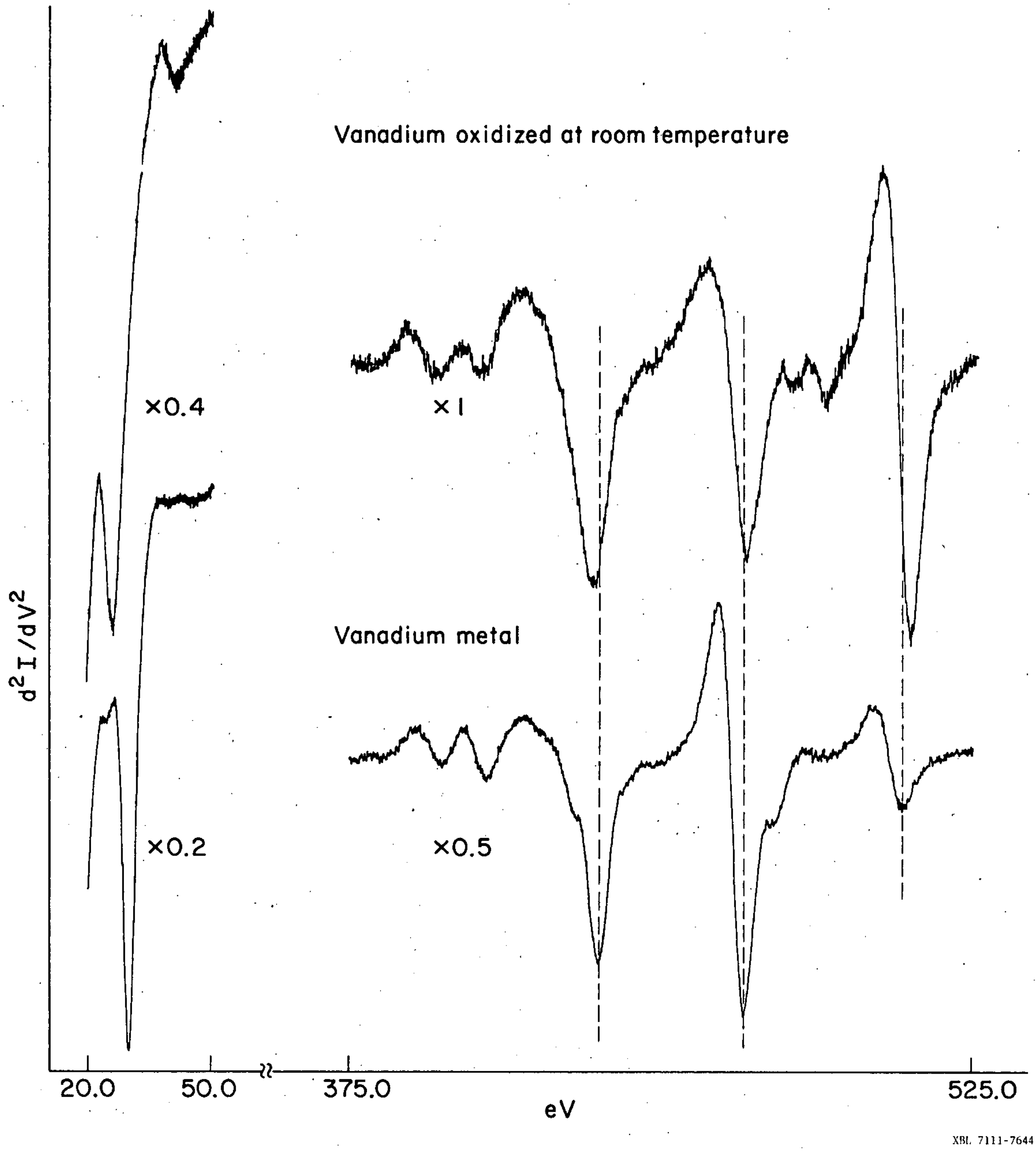

Fig. III-10. The d^2I/dV^2 AES spectra of vanadium metal and of room temperature oxidized vanadium (approximate compositions: $VO_{0.8}$) showing the peak intensity changes and chemical shifts occurring as the result of oxidation.

the vanadium reference peak was typically monitored both before and after the oxygen exposure and the detected change in the analyzer work function never exceeded 0.05 eV. This is within the error of the experiment and, in fact, one would expect little or no change in the analyzer work function for a simple gas like oxygen since the analyzer is already covered with the adsorbed ambient gases and therefore the sticking coefficient for the surface would be essentially zero.

The results that were obtained are shown in Fig. III-11, which is a plot of the observed chemical shifts vs. the observed O/V peak intensity ratios obtained from the oxidation runs. The data for the "known" vanadium oxides are also included to serve as reference points. These experiments had been carried out as part of the program run at 6 volts p-t-p modulation magnitude in the d^2I/dV^2 mode and are corrected, as explained previously, to the 2 volt p-t-p values. The data points clustered below the $VO_{0.92}$ reference point are the results of runs carried out at 25°C, in the pressure range of 10^{-7} - 5×10^{-4} Torr., and at exposures varying from 90 - 5×10^{6} L. These results indicate that the product formed is in the oxygen-deficient region of the VO solid solution range and has an approximate composition of $VO_{0.8}$. The single point occurring at the approximate composition of $VO_{1.2}$ was obtained after oxidation near a temperature of 75°C, a pressure of 3×10^{-4} Torr, and $\approx 3\times10^{6}$L exposure; it indicates the ability to form an oxygen-rich solid solution at this slightly elevated temperature. Those points clustered between the V_2O_3 and V_2O_4 reference points

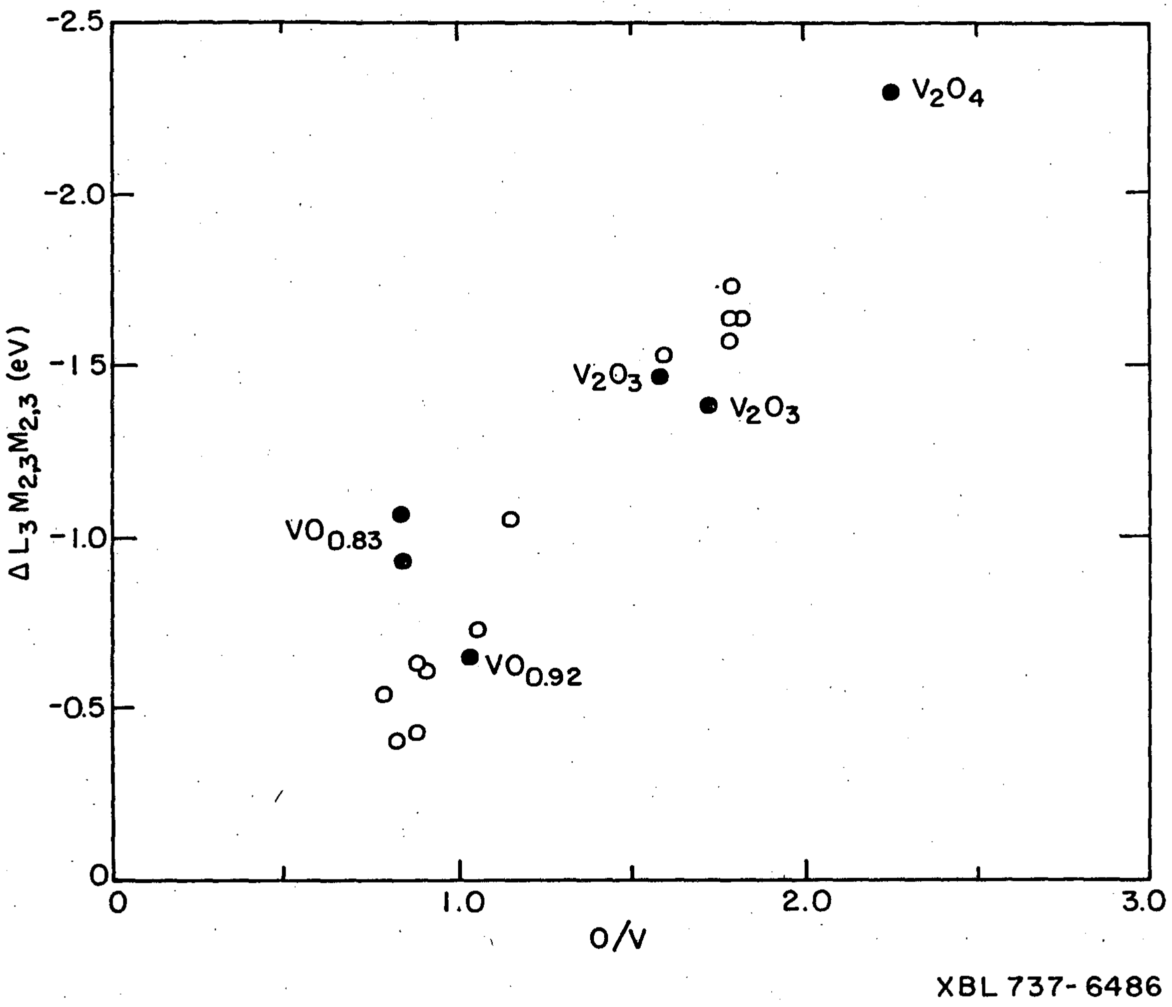

Fig. III-11. The chemical shift of the vanadium $L_3M_{2,3}M_{2,3}$ Auger transition plotted as a function of the oxygen KVV/vanadium $L_3M_{2,3}V$ half-peak height ratio for the vanadium metal oxidation runs. The "known" vanadium oxides are included for use as reference points.

resulted from runs in the temperature range 400-1200°C, pressures in the 5×10^{-4}-5×10^{-3} Torr range, and exposures from 2×10^{5} - 8×10^{6} L. They suggest the formation of an oxide with a chemical composition corresponding to $VO_{1.6-1.7}$. Since these peaks did not appear to be broadened with respect to those obtained from the known oxides, it seems unlikely that these data points are the result of the formation of a mixture of V_2O_3 and V_2O_4. The point occurring near the V_2O_3 reference points was obtained after a 150°C oxidation run at a pressure of 2×10^{-4} Torr and an exposure of 1.5×10^{6} L.

Because of the linearity of the results, it may be concluded that the oxygen diffuses into the vanadium lattice and a seemingly homogeneous surface layer of the oxide at least 10 Ångströms thick is being formed at the oxygen exposures used. It should be noted that the structural rearrangement of the b.c.c. vanadium metal to accommodate the oxygen atoms in the VO crystal lattice should not prove difficult since VO has the f.c.c. (NaCl) structure.[69] The higher vanadium oxides, however, have more complex crystal structures and the results indicate that the energy available at 25°C is not sufficient to form these structures, at least at a fast enough rate to be detected by these experiments. In all of the experiments no surface structure due to the formation of the V-O compound was observed. Monitoring of the surface using LEED merely showed a dimming of the vanadium diffraction pattern and its subsequent blending into the background, indicating that a completely disordered surface has resulted.

It is perhaps initially surprising that the high temperature oxidation of the metal did not produce VO_2, the V^{4+} species being the most stable of the vanadium oxidation states. However an investigation of the phase equilibria in the V_2O_3 - VO_2 system by Katsura and Hasegawa[109] has demonstrated that a number of Magneli phases are formed when the system is heated to high temperatures, the particular phase depending upon the oxygen partial pressure in the system. They determined that the V_3O_5 phase was formed in the pressure range 3.3×10^{-4} to 9.6×10^{-3} Torr, this being the range in which most of our high temperature oxidation runs were carried out. Since these experiments yielded a composition on the order of $VO_{1.6-1.7}$ (i.e. $V_3O_{4.8-5.1}$), it appears likely that we were observing the formation of this Magneli phase. The lack of broadening of the $L_3M_{2,3}M_{2,3}$ transition peak also indicates the presence of a surface layer in which all of the vanadium atoms are in the same oxidation state, as they are in this defect structure of VO_2.[110] In the case of the formation of an oxide mixture (V_2O_3 and VO_2), a broadening of this transition peak would be expected due to the overlap of the peaks from each oxidation state. Furthermore, we observed the formation of a compound with the composition of V_2O_3 when the oxidation was performed at an oxygen pressure in the range (below 3.3×10^{-4} Torr) where Katsura and Hasegawa prepared V_2O_3 in bulk quantities. Our results therefore support their data on the presure dependence of the formation of V_2O_3 and V_3O_5 and, in addition, indicate that no compositional anomalies occur within the surface region.

4. The Low Energy Auger Transitions

a. Transition assignments. The low energy Auger spectrum of vanadium was also monitored during the oxidation of the metal. Figure III-12 shows typical spectra obtained in the 0-75 eV region both before and after room temperature oxidation runs. As shown previously, the oxide formed is of the approximate composition $VO_{0.8}$. The energies of the observed d^2I/dV^2 high energy minima are listed in Table III-10. For the most part the origins of the peaks occurring in this part of the spectrum are uncertain. The reasons underlying this are well-known among workers in the field of UV photoemission.[111] The main problems which arise are due to 1) the variations which exist in the unfilled density of states for a region extending several tens of eV above the Fermi and 2) the complex and

Table III-10

Low Energy AES Peaks in the Spectra of V and VO

V	$VO_{0.8}$
3.7	6.0
9.8	
12.4	13.6
24.8±0.2	25.7±0.3
30.5	
40.0	41.3±0.3
45.6±0.3	

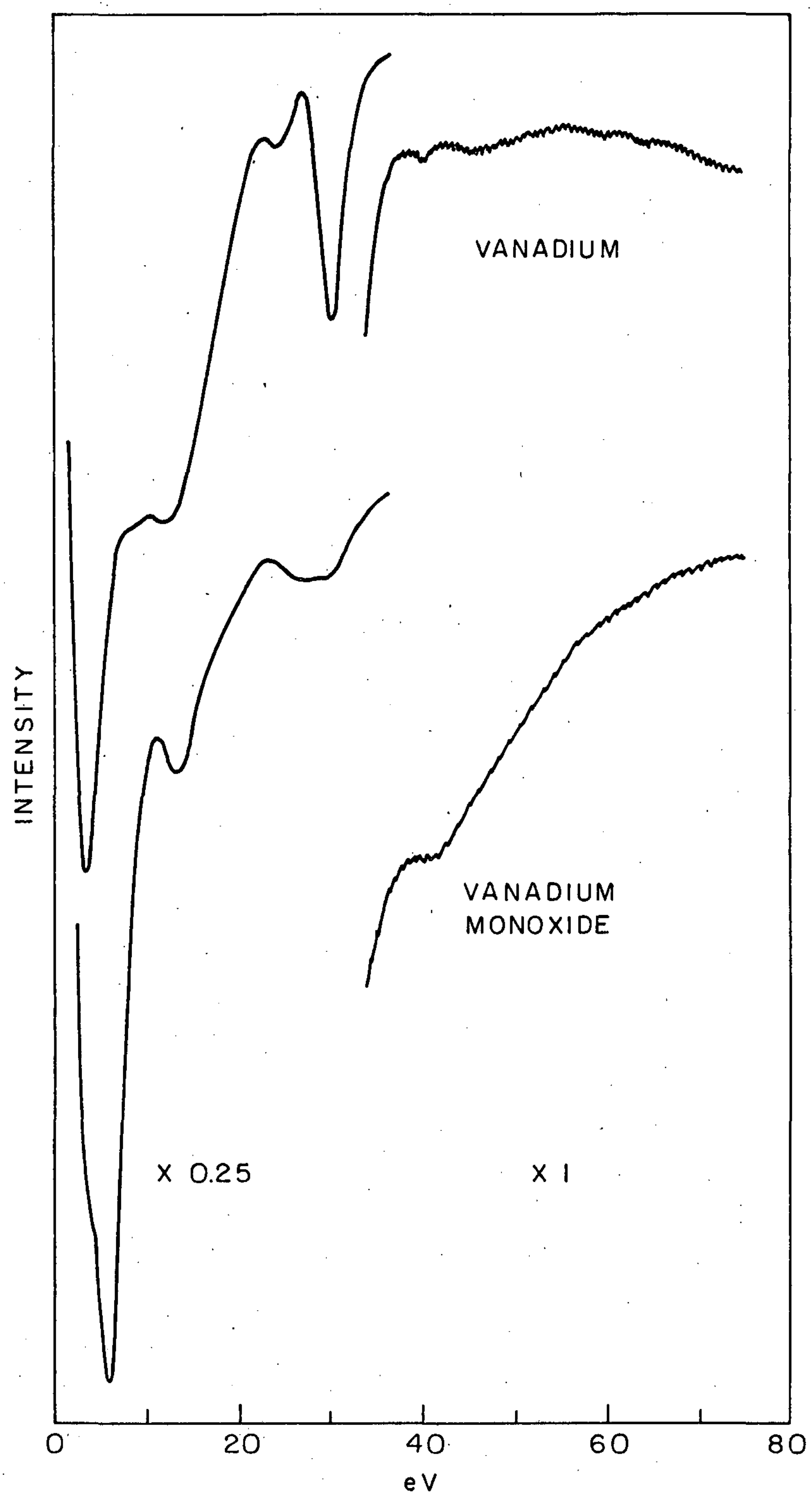

XBL 737-6483

Fig. III-12. The 0 eV to 75 eV region of the d^2I/dV^2 AES spectra of vanadium metal and of room temperature oxidized vanadium demonstrating the changes which occur upon oxidation.

strong energy variation of the transition probability existing for double valence band transitions. It has only been recently, however, that the influence of these effects has been pointed out by workers in the field of AES.[112] However because of their large intensity relative to that of the higher energy transitions and the often times large (≈ 15 eV) AES shifts observed, the majority of published AES shift data has focused on these peaks.[113-119]

The only Auger peak in this part of the vanadium spectrum which may be assigned with any degree of certainty is the one observed at 30.5 eV in the metal. Considering its energy, its amplitude, and its response to the adsorption of gases, it is almost assuredly a valence band transition of the type $M_{2,3}VV$. The low energy (3.7 eV) peak is also easily explained; it is not due to an Auger transition but rather is associated with the secondary electron cascade peak. The energy of the peak is changed by oxidation as one might easily have predicted from the short discussion of the cascade mechanism presented in Sec. I.A.3. In the figure, this peak is also seen to be doubled in the oxide. This phenomena arises from the fact that the sample was not fully oxidized within the detected volume: note that the $M_{2,3}VV$ Auger peak has not yet been completely eliminated (as it is in the fully oxidized sample) and also refer to Fig. I-20 to note the larger escape depth of the cascade peak electrons relative to that of 30 eV electrons. The 24.8 eV peak acted anomalously during different oxidation runs. At various times it appeared to 1) remain constant in amplitude throughout the experiment, 2) remain constant in amplitude until the $M_{2,3}VV$ peak had been eliminated whereupon it increased in intensity, and 3) grow in amplitude simultaneously with the decrease of the $M_{2,3}VV$ transition peak. This 24.8 eV peak occurs at the energy that would be predicted for the $M_1M_{2,3}V$ transition and energy considerations also suggest that its intensity may at least be partly due to a plasmon gain mechanism. In addition, since the peak lies just at the point where the d^2I/dV^2 curve seems to flatten out this may also be a factor in determining its behavior.

b. The $M_{2,3}VV$ transition and its oxidation behavior. The main reason for the study of this low energy spectrum, however, is not impaired by the uncertainty concerning the origin of most of the observed peaks since our interest lies in the one identifiable Auger transition. Since the $M_{2,3}VV$ transition is a double valence band transition any information gleaned from it would compliment that obtained from the inner shell and single valence band transitions. Spectra montoring this transition during a typical oxidation run are shown in Fig. III-13. As is readily perceivable from the figure, during this particular run the 24.8 eV peak was not appreciably affected during the extinction of the 30.5 eV $M_{2,3}VV$ peak and its intensity is enhanced only after a noticeably longer exposure to the oxygen gas. Such results as these strongly argue against the interpretation of Coad and Rivière who suggest that this 24.8 eV peak is the chemically shifted analog of the 30.5 eV clean metal peak. The shift in the position of the d^2I/dV^2 high energy minimum of this $M_{2,3}VV$ peak was then investigated and the dependence of the shift magnitude upon oxygen exposure is

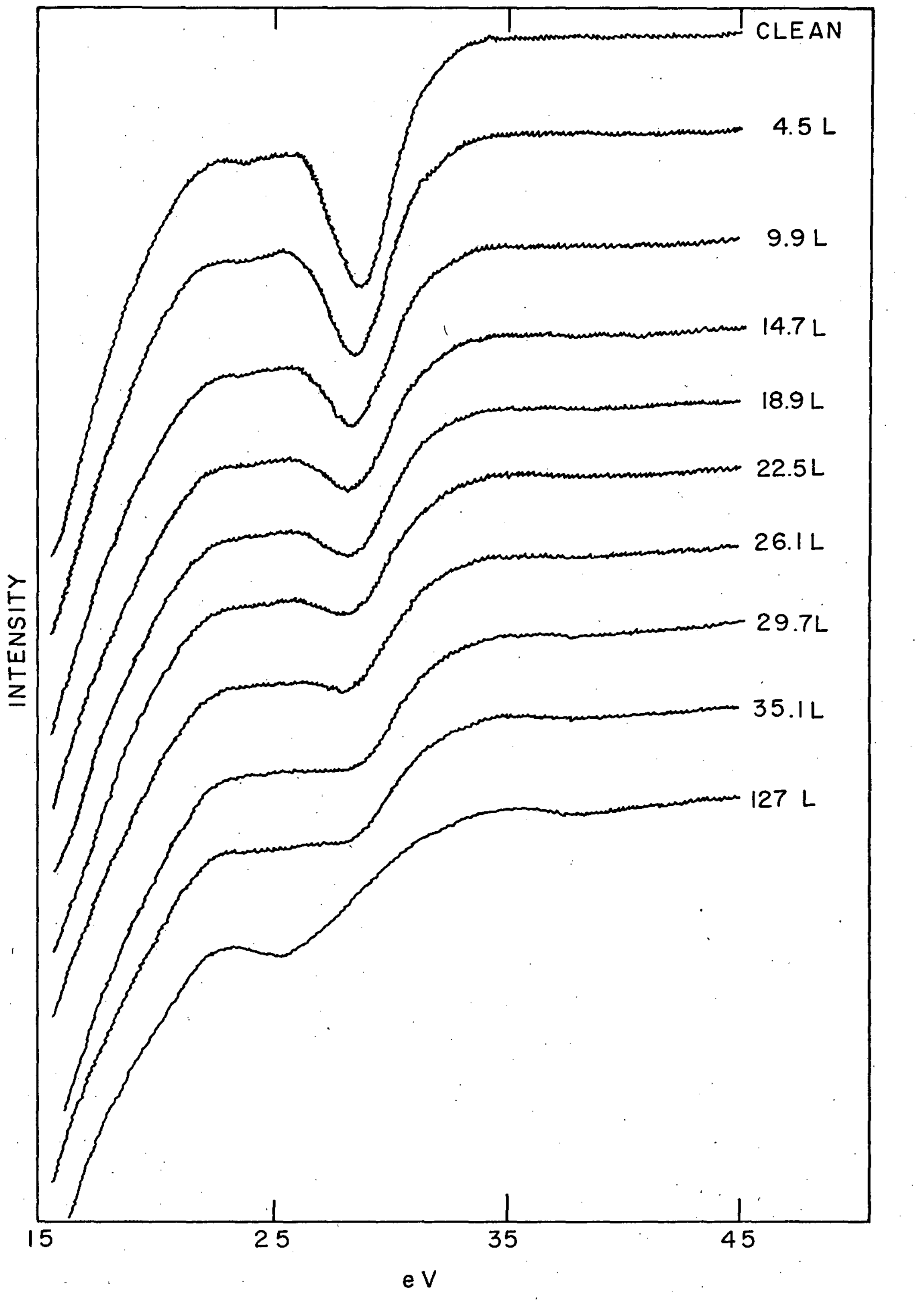

Fig. III-13. AES spectra taken in the vicinity of the vanadium $M_{2,3}VV$ transition showing the progressive changes which occur with increasing oxygen exposure.

shown in Fig. III-14. The dashed extension of the line is meant to indicate that the observed trend in the shift may continue beyond the last recorded point but no reliable value for the peak position was obtainable due to the reduced peak intensity and the consequent ill-definition of the peak high energy minimum. It is not believed that the slightly changing background slope in the vicinity of the peak is causing the observed shift, although it would tend to shift the observed transition energy in the proper direction, because 1) its contribution is negligible when the transition peak is still large during the initial few Langmuirs of exposure and 2) although somewhat different values of this slope were observed during different oxidation runs, Fig. III-14 show that the observed shifts clustered well around a constant value for the shift dependence upon the exposure. Because of the complexity of the processes involved here and the dearth of supplementary information on the valence band structure of VO, no attempt will be made to rationalize the shift observed here. It is of interest to note that the $M_{2,3}VV$ transition peak is entirely eliminated upon oxidation to VO. This fact suggests that either 1) there is a large unfilled density of states existing in the metal to which the transition is coupling and which is being destroyed upon oxidation or 2) the transition involves the two 4s electrons and the chemical combination localizes these electrons to such an extent that their spacial overlap is essentially eliminated.

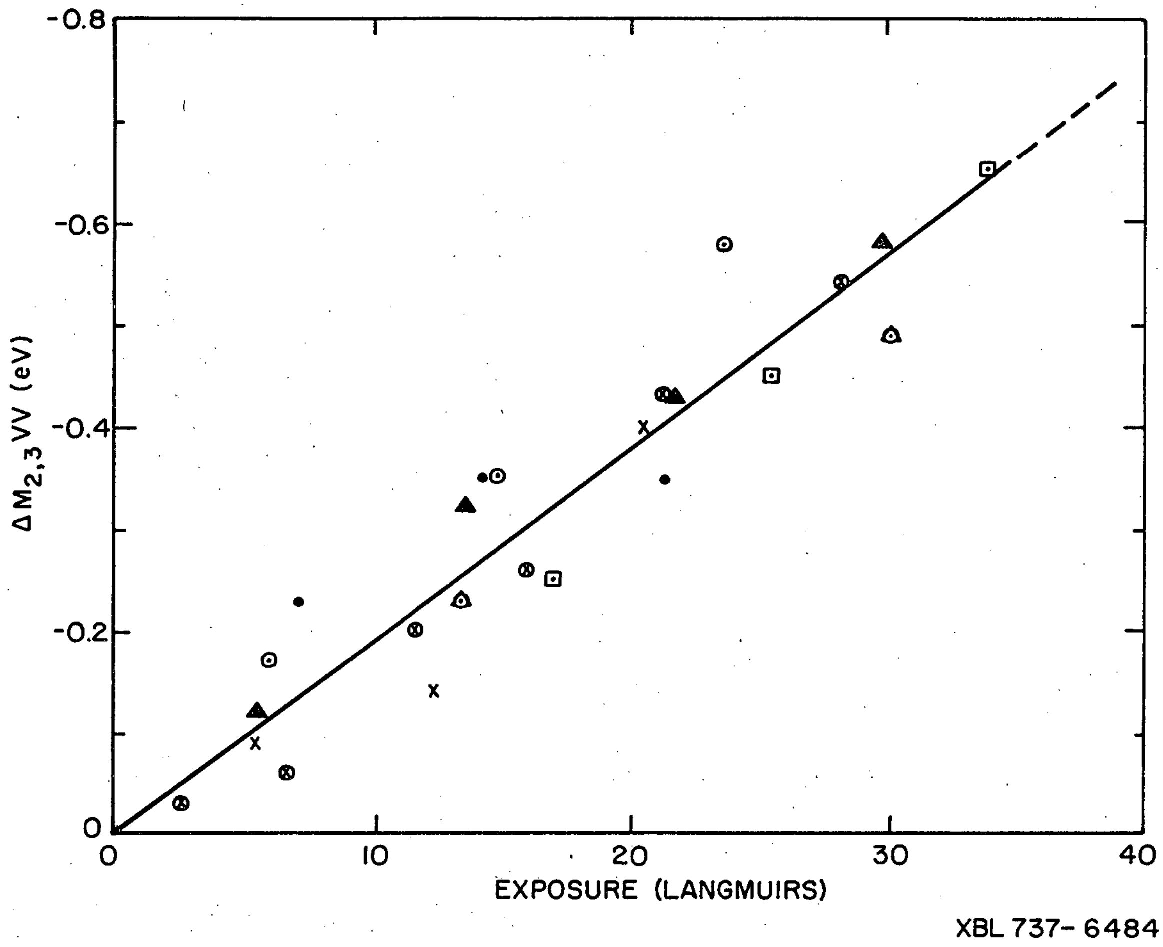

Fig. III-14. A graph showing the shift occurring in the high-energy minimum of the vanadium $M_{2,3}VV$ transition as a function of oxygen exposure.

ACKNOWLEDGEMENTS

As with many of the important things in life, my feelings upon writing this final portion of my thesis are of a bittersweet nature. There is no way that I can possibly express within a few words my feelings for all of the lovely people that I have encountered during my stay in the San Francisco Bay Area, but then hopefully I have been able to give to them during that period enough kindness, friendship, and love such that these words are not necessary. They will be written, however, because they should be and because it is a fact that the presence of these people will be sorely missed.

First of all, I wish to thank Professor Gabor Somorjai for having managed to put up with me for so many years and for his unflagging enthusiasm and concern for both myself and this research project. Very special thanks go to Helen Farrell who took me under her wing when I first joined the group, taught me the basics of research and kindness when I was lacking in both, and is now stuck with a lifelong friend whether she wants it or not. The long evenings and nights of that first year working with her and Richard Goodman will always be counted among the most rewarding of my stay in Berkeley. The height of my graditude to them is rivalled only by that for John and Wanda Gland, Richard and Jennifer and Claire Joyner, and Reed McFeely. The stimulating and informative discussions, technical and otherwise, and their ever-present friendship will always be remembered. Much of the same can also be said of Ray Kaplan, Steve and Sandy Bernasak, John Wasilczyk, Russ Palmeri, Swen Berglund, Al West, Marlo Martin (whose added assistance in introducing me to computer programming is greatly appreciated), Bernard Lang, Alan Morgan, Dan Howlett, and Ted French. A special affection is felt for the daily kindness and cheerfulness of the I.M.R.D. technical typing group: Shirley Ashley, Alice Ramirez (who also patiently suffered through this manuscript), Jean Wolslegel, Claudia Redwood, and before them Linda Leborgne, Jane Ball, and Pat Shand. For their technical assistance and personal kindness I am also indebted to all of the other first-rate members of the I.M.R.D. staff, particularly Lee Johnson, Julien Patenaude, Jim Severns (whose life was made miserable by myself and Varian electronics), Sandy Stewart, Del Peterson, Glen Baum, Patty Acuna, Mamie Brown, Walt Toutolmin, and Doug Kreitz. Emery Kozak is in a class by himself. The years were indeed fruitful ones. The latter ones were made even more so by the presence of Ann Bertrand who has touched me as deeply as one person may another. To her and to Emileah Beres (who probably more than anything else induced me to come to San Francisco) I can only offer my dearest thanks and my love.

In concluding, the author would like to thank Dr. Mario D. Banus of the M.I.T. Lincoln Laboratory for preparing and characterizing the VO solid-solution samples and to point out that this work was carried out under the auspices of the United States Atomic Energy Commission.

APPENDIX I.

An electron orbiting around the nucleus induces a magnetic field, the intensity and direction of which depend on the electron's velocity and orbital radius. There is also an inherent magnetic field associated with an electron, depending on the direction of its spin. The fields produced are commonly referred to as resulting from the orbital angular momentum $\vec{\ell}_i$ and the spin angular momentum, $\vec{s}_i$ of the electron, i. These individual electron spins and angular momenta are vector quantities and their sum gives the total electronic angular momentum, $\vec{j}_i = \vec{\ell}_i + \vec{s}_i$, for an isolated electron. For high atomic number elements, it has been found that the electronic interactions are well described by the sum over the individual $\vec{j}_i$'s to obtain the total atomic angular momentum $\vec{J}_{j-j} = \sum_i \vec{j}_i$. In this case, it is said that the electron-electron interaction obeys j-j coupling and the individual electrons are labelled according to the traditional X-ray spectroscopic notation as follows:

X-ray symbol	Electron energy state	Electron $\vec{\ell}$	Electron $\vec{j}$
K	1s	0	1/2
L_1	2s	0	1/2
L_2	2p	1	1/2
L_3	2p	1	3/2
M_1	3s	0	1/2
M_2	3p	1	1/2
M_3	3p	1	3/2
M_4	3d	2	3/2
M_5	3d	2	5/2
N_1	4s	0	1/2
⋮	⋮	⋮	⋮

Often, when the binding energies of two electron states are indistinguishable, the X-ray symbols are combined for brevity; e.g., M_4 and M_5 will become $M_{4,5}$. For low atomic number elements, however, the atom is better described if the individual orbital angular momenta are considered to interact together to produce a total orbital angular momentum, $\vec{L} = \sum_i \vec{\ell}_i$. In a like manner for the spin component, we obtain the total spin angular momentum, $\vec{S} = \sum_i \vec{s}_i$. These quantities may then couple together to form the total atomic angular momentum, $\vec{J}_{LS} = \vec{L} + \vec{S}$, in what is known as either the L-S or Russell-Saunders coupling scheme, where a given electron distribution is denoted by a term symbol of the form ${}^{(2\vec{S}+1)}L_{\vec{J}_{LS}}$.

APPENDIX II

This appendix contains the computer program which was used to reduce the data that was digitized and punched on paper tape by the Vidar DAS. A detailed discussion of the Vidar and the subroutine FRAMCON which was developed to transfer the paper tape data into the CDC6600 is presented elsewhere[58] and will not be discussed here. The program AUGERCS requires a total of six other input data cards in addition to the paper tape data. These input cards are read at the beginning of the program and the meaning of each entry is presented below, intertwined with a brief description of the program execution.

The program and its subroutines average together a NUMBER of experimental runs, each containing a maximum of NX data points. The voltage range to be analyzed is determined by specifying a starting voltage VZERO and a finishing voltage VSTOP. Data points outside this range are discarded. Data points within the range are placed into a number of storage bins for averaging. Any of the experimental runs may be deleted from the analysis by specifying the number of that run in the paper tape sequence within ISKIP(I). The width of each bin is DELTA and the number of bins is obviously determined by (VSTOP-VZERO)/DELTA. The data within each bin is averaged and the curve may be smoothed by specifying the number M of bins bordering each individual bin which are to be averaged together in the next step. The total number of bins averaged during this step is $2n+1$. A linear background slope compensation may be performed between the first and last points of the voltage range (SLOPCON) or for any stated slope

```
000210            GO TO 70
000211         90 CONTINUE
            C
            C     RUN DISCARD ROUTINE
            C
000214            NUMBER = INDEX
000215            INDEX = 0
000216            DO 110 J=1,NUMBER
000217            DO 100 I=1,NUMBER
000220            IF (J.EQ.ISKIP(I)) GO TO 110
000222        100 CONTINUE
000224            INDEX = INDEX + 1
000226            DO 105 K=1,NX
000236            X(K,INDEX) = X(K,J)
000237            Y(K,INDEX) = Y(K,J)
000240        105 CONTINUE
000241        110 CONTINUE
000244            NUMBER = INDEX
            C
            C     PRINT OUT RAW DATA
            C
000245            IF (PRINTRD.NE.8RRAW DATA) GO TO 145
000247            PRINT 820
000252            PRINT 830, NUMBER,NX
000262            N1 = 1
000263            N2 = 5
000264            IF (NUMBER.LE.5) N2=NUMBER
000270            GO TO 130
000271        120 CONTINUE
000271            N1 = N2 + 1
000273            N2 = N2 + 5
000274            IF (NUMBER.LE.N2) N2=NUMBER
000277        130 CONTINUE
000277            PRINT 840
000303            DO 140 I=1,NX
000305            PRINT 850, I,(X(I,J),Y(I,J),J=N1,N2)
000327        140 CONTINUE
000332            IF (N2.LT.NUMBER) GO TO 120
000334        145 CONTINUE
            C
            C     ASSIGN X-VALUES TO APPROPRIATE BIN NUMBERS N(I,J)
            C
000334            DO 180 J=1,NUMBER
000336            V1 = VZERO
000337            V2 = V1 + DELTA
000340            K = 1
000342            DO 170 I=1,NX
000343            A = X(I,J)
000346            IF (A.LT.V1) GO TO 170
000351        150 CONTINUE
000351            IF (A.LT.V2) GO TO 160
000354            K = K + 1
000355            V1 = V1 + DELTA
000357            V2 = V2 + DELTA
000360            GO TO 150
000361        160 CONTINUE
000361            N(I,J) = K
000365        170 CONTINUE
```

```
000370     180 CONTINUE
000372         DO 225 I=1,NX
000374         DO 225 J=1,NUMBER
000403         AVG(I,J) = 0.0
000404         NUM(I,J) = 0
000404     225 CONTINUE
         C
         C     CALCULATE AVERAGE VALUES WITHIN EACH RUN ... AVG(K,J)
         C
000410         KMAX = IFIX((VSTOP - VZERO)/DELTA)
000413         DO 230 J=1,NUMBER
000415         DO 230 I=1,NX
000416         K = N(I,J)
000421         IF (K.LE.0) GO TO 230
000430         AVG(K,J) = AVG(K,J) + Y(I,J)
000431         NUM(K,J) = NUM(K,J) + 1
000433     230 CONTINUE
000440         DO 250 J=1,NUMBER
000442         DO 250 K=1,KMAX
000443         IF (NUM(K,J).LE.0) GO TO 240
000447         AVG(K,J) = AVG(K,J) / NUM(K,J)
000453         GO TO 250
000453     240 CONTINUE
000453         AVG(K,J) = 0.0
000457     250 CONTINUE
         C
         C     CALCULATE TOTAL OF AVG(K,J) FOR ALL BINS ... TOTBIN(K)
         C
000464         DO 255 K=1,NX
000472         TOTBIN(K) = 0.0
000473         DBIN(K) = 0.0
000473     255 CONTINUE
000474         DO 258 K=1,KMAX
000475         DO 258 J=1,NUMBER
000476         IF (AVG(K,J).EQ.0.0.AND.K.GT.0.AND.K.LT.KMAX) AVG(K,J) =
              1(AVG(K+1,J) + AVG(K-1,J)) / 2.0
000523         TOTBIN(K) = TOTBIN(K) + AVG(K,J)
000530     258 CONTINUE
         C
         C     INTENSITY DELTA EXPANSION ROUTINE
         C
000534         M1=M+L+1 $ M2=KMAX-L-M
000537         IF (M.EQ.0) GO TO 275
000540         DO 265 K=1,KMAX
000545         TOTBINH(K) = TOTBIN(K)
000546         TOTBIN(K) = 0.0
000546     265 CONTINUE
000547         DO 270 K=M1,M2
000551         M3=K-M $ M4=K+M
000553         DO 270 I=M3,M4
000564         TOTBIN(K-L-M) = TOTBIN(K-L-M) + TOTBINH(I)
000566     270 CONTINUE
000571         GO TO 285
000572     275 CONTINUE
000572         DO 280 K=M1,M2
000601         TOTBIN(K-L) = TOTBIN(K)
000602     280 CONTINUE
000603     285 CONTINUE
```

```
000603          KMAX = KMAX - (2 * IFIX(GLM))
          C
          C     LINEAR SLOPE COMPENSATION ROUTINE
          C
000605          IF (SLOPCOM.NE.5RSLOPE) GO TO 315
000610          IF (SLOPNUM.NE.0.0) SLOPE=SLOPNUM
000612          IF (SLOPNUM.NE.0.0) GO TO 295
000613          SLOPE=(TOTBIN(KMAX)-TOTBIN(1))/(VSTOP-VZERO-DELTA*(1.0+(2.0*GLM)))
000623          SLOPNUM = SLOPE
000625      295 DO 310 K=1,KMAX
000627          IF (SLOPE) 300,310,305
000630      300 TOTBIN(K) = TOTBIN(K) + (DELTA*SLOPE*FLOAT(KMAX-K))
000635          GO TO 310
000636      305 TOTBIN(K) = TOTBIN(K) - (DELTA*SLOPE*FLOAT(K-1))
000643      310 CONTINUE
000646      315 CONTINUE
          C
          C     NORMALIZATION OF INTENSITY DATA
          C
000646          TOTMAX = TOTBIN(1)
000647          TOTMIN = TOTBIN(1)
000651          DO 320 K=2,KMAX
000656          TOTMAX = AMAX1(TOTBIN(K),TOTMAX)
000661          TOTMIN = AMIN1(TOTBIN(K),TOTMIN)
000663      320 CONTINUE
000664          DO 330 K=1,KMAX
000673          TOTBIN(K) = (TOTBIN(K)-TOTMIN) / (TOTMAX-TOTMIN)
000675      330 CONTINUE
          C
          C     CALCULATE THE DERIVATIVES OF THE INTENSITIES AND NORMALIZE
          C
000676          L1 = L + 1
000677          L2 = KMAX - L
000701          VL = FLOAT(L)
000702          DO 340 K=L1,L2
000715          KPLUS = K + L
000716          KMINUS = K - L
000717          DBIN(K) = (TOTBIN(KPLUS) - TOTBIN(KMINUS)) / (2.0*VL*DELTA)
000721      340 CONTINUE
000724          DBINMX = DBIN(L1)
000725          DBINMN = DBIN(L1)
000727          L1 = L1 + 1
000730          DO 350 K=L1,L2
000735          DBINMX = AMAX1(DBIN(K),DBINMX)
000740          DBINMN = AMIN1(DBIN(K),DBINMN)
000742      350 CONTINUE
000743          L1 = L1 - 1
000744          DO 360 K=L1,L2
000753          DBIN(K) = ((DBIN(K)-DBINMN) / (DBINMX-DBINMN))
000755      360 CONTINUE
          C
          C     PRINT OUT FINAL STATISTICS
          C
000760          VZERO = VZERO + (DELTA * GLM)
000761          VSTOP = VSTOP - (DELTA * GLM)
000763          VV(1) = VZERO + (DELTA * 0.5)
000765          PRINT 870, VZERO,VSTOP,DELTA
000776          IF (PUNCOPT.NE.5RPUNCH) GO TO 363
```

```
001000          PUNCH 950, IDNUM,VZERO,VSTOP,DELTAM,DERIVL,NUMBER,NX
001022      363 PRINT 880
001026          DO 370 K=1,KMAX
001030          PRINT 890, K,VV(K),TOTBIN(K),DBIN(K)
001043          IF (PUNCOPT.NE.5RPUNCH) GO TO 366
001045          PUNCH 960, K,VV(K),TOTBIN(K),DBIN(K)
001061      366 VV(K+1) = VV(K) + DELTA
001064      370 CONTINUE
001066          CALL GRAPH (1,KMAX,1,VV(1),TOTBIN(1),DUM)
001072          CALL GRAPH (1,KMAX,1,VV(1),DBIN(1),DUM)
          C
          C     CURVE FITTING ROUTINE
          C
001076          DO 400 I=1,2
001100          IF (RANGE(I).EQ.0.0) RANGE(I)=0.500
001103          IF (MIDPT(I).EQ.0.0) MIDPT(I)=0.500+(0.166*(I-1))
001112          IF ((ABS(0.500-MIDPT(I))+((RANGE(I)/2.0)-0.500)).GT.0.0) RANGE(I)
               1 = 2.0 * MIDPT(I)
001127          KSTART =(IFIX(FLOAT(KMAX) * (MIDPT(I)-(RANGE(I)/2.0)))) + 1
001133          KFINIS = KSTART + (INT(FLOAT(KMAX) * RANGE(I))) - 1
001136          KMAXCF = KFINIS - KSTART
001136          IF (I.EQ.2) GO TO 385
001141          DO 380 K=KSTART,KFINIS
001152          VVI(K-KSTART+1) = VV(K)
001153          TOTBIN(K-KSTART+1) = TOTBIN(K)
001154      380 CONTINUE
001155          VVIS = VVI(1) $ VVIF = VVI(KMAXCF+1)
001161          PRINT 980 $ CALL LSQPOL(VVI,TOTBIN,W,RESID,KMAXCF,SUM,1,A,B,8)
001176      381 DO 382 K=1,7
001205          AA(K) = CMPLX((K*B(K+1)),0.0)
001211      382 CONTINUE
001212          CALL ROOT (AA,7,R,1.0E-07)
001215          DO 384 K=1,6
001217          RI = AIMAG(R(K))
001222          RR = REAL(R(K))
001225          IF (RI.NE.0.0) GO TO 384
001226          IF (VZERO.LT.RR.AND.RR.LT.VSTOP) PRINT 985, RR
001242      384 CONTINUE
001244          GO TO 400
001245      385 CONTINUE
001245          DO 390 K=KSTART,KFINIS
001256          VV(K-KSTART+1) = VV(K)
001257          DBIN(K-KSTART+1) = DBIN(K)
001260      390 CONTINUE
001261          VVS = VV(1) $ VVF = VV(KMAXCF+1)
001265          PRINT 990 $ CALL LSQPOL(VV,DBIN,W,RESID,KMAXCF,SUM,1,A,B,8)
001302          GO TO 381
001303      400 CONTINUE
001305          PRINT 900, TOTMAX,TOTMIN,DBINMX,DBINMN,SLOPNUM
001323          PRINT 910, VVIS,VVIF,VVS,VVF
001337          PRINT 930, (ISKIP(I), I=1,40),NX,NUMBER,DERIVL,DELTAM,
               1VSTOP,VZERO,IDNUM
          C
001363      740 FORMAT (I4,1X,I3)
001363      750 FORMAT (2(R5,5X),R8,2X,F10.6)
001363      760 FORMAT (I3,2X,I3)
001363      770 FORMAT (4(F5.3,5X))
```

```
001363      780 FORMAT (40I2)
001363      790 FORMAT (3(F7.2,3X))
001363      800 FORMAT (2(A5,5X))
001363      820 FORMAT (1H1)
001363      830 FORMAT (///10X *PRINTOUT OF RAW DATA*I4,
               1*-EXPERIMENTAL RUNS WITH-* I4,*-DATA POINTS EACH.*)
001363      840 FORMAT (//3X*-I-* 5(3X*VOLTAGE---INTENSITY*3X)/)
001363      850 FORMAT (3X,I3,5(F10.2,F12.5,3X))
001363      870 FORMAT (1H1,10X*NORMALIZED INTENSITIES AND DERIVATIVES *
               1*OF INTENSITIES*///10X*VZERO IS-*F8.2, /10X*VSTOP IS-*F8.2, /
               210X*DELTA IS-*F8.2,//)
001363      880 FORMAT (/10X*-K-*7X*VOLTAGE*7X*INTENSITY*6X*DERIVATIVE*/)
001363      890 FORMAT (10X,I3,5X,F9.3,7X,F9.6,7X,F9.6)
001363      900 FORMAT (1H1, 10X *NORMALIZATION FACTORS* ///
               110X*TOTMAX IS-*F12.6,/10X*TOTMIN IS-*F12.6,/10X*DBINMX IS-*F12.6,/
               210X*DBINMN IS-*F12.6,/10X*SLOPE  IS-*F12.6)
001363      910 FORMAT (//// 11X*POLYNOMIAL CURVE FITTING INFORMATION* /// 10X
               1*THE INTENSITY CURVE HAS BEEN FITTED FROM   * F7.3 *  TO  * F7.3
               2*  VOLTS* / 10X*THE DERIVATIVE CURVE HAS BEEN FITTED FROM  * F7.3
               3*  TO  * F7.3 *  VOLTS* //)
001363      930 FORMAT (//10X*EXPERIMENTAL RUNS DELETED-*7X20I3,/43X20I3,/10X*DATA
               1 POINTS PER RUN-*I13, / 10X*NUMBER OF EXPERIMENTAL RUNS-*I5,
               2/10X*DERIVATIVE VOLTAGE WIDTH-*F8.2, /10X*INTENSITY VOLTAGE *
               3*WIDTH-*F9.2, /10X*FINISHING VOLTAGE OF RUN-*F8.2, /10X*STARTING*
               4* VOLTAGE OF RUN-* F9.2, /10X*ID. NUMBER OF EXP. DATA-*4X,A5)
001363      950 FORMAT (A5,4F7.2,I3,I4)
001363      960 FORMAT (I3,F9.3,2F9.6)
001363      980 FORMAT (1H1,10X*THE RESULT OF THE LEAST SQUARES FIT TO THE*
               1* INTENSITY CURVE IS*)
001363      985 FORMAT (//////////10X*THE MAXIMUM OF THE FITTED POLYNOMIAL IS AT*
               15X,F7.3,5X*VOLTS*)
001363      990 FORMAT (1H1,10X*THE RESULT OF THE LEAST SQUARES FIT TO THE *
               1*DERIVATIVE CURVE IS*)
001363          END


PROGRAM LENGTH INCLUDING I/O BUFFERS
015457

FUNCTION ASSIGNMENTS

STATEMENT ASSIGNMENTS
7       -  000176   80      -  000205   90      -  000212   110     -  000242   120     -  000272   130     -  000300
145     -  000335   150     -  000352   160     -  000362   170     -  000366   230     -  000434   240     -  000454
250     -  000460   275     -  000573   285     -  000604   295     -  000626   300     -  000631   305     -  000637
310     -  000644   315     -  000647   363     -  001023   366     -  001062   381     -  001177   384     -  001243
385     -  001246   400     -  001304   740     -  001426   750     -  001431   760     -  001435   770     -  001440
780     -  001443   790     -  001445   800     -  001450   820     -  001453   830     -  001455   840     -  001472
850     -  001500   870     -  001504   880     -  001524   890     -  001533   900     -  001540   910     -  001562
930     -  001611   950     -  001652   960     -  001655   980     -  001660   985     -  001672   990     -  001703

BLOCK NAMES AND LENGTHS

VARIABLE ASSIGNMENTS
A       -  064656   AA      -  065142   AVG     -  025377   B       -  065116   D       -  001757   DBIN    -  041157
DBINMN  -  065334   DBINMX  -  065333   DELTA   -  065275   DELTAM  -  065303   DERIVL  -  065302   DUM     -  065335
GLM     -  065301   HOLD1   -  065307   HOLD2   -  065310   I       -  065272   IDENT   -  062677   IDNUM   -  065277
```

```
INDEX   -  065306    ISKIP   -  062627    J       -  065304    JMAX    -  065300    K       -  065311    KFINIS  -  065337
KMAX    -  065316    KMAXCF  -  065340    KMINUS  -  065332    KPLUS   -  065331    KSTART  -  065336    L       -  065270
L1      -  065326    L2      -  065327    M       -  065271    MIDPT   -  062701    M1      -  065317    M2      -  065320
M3      -  065321    M4      -  065322    N       -  051017    NAME    -  065276    NGOOD   -  065305    NUM     -  001757
NUMBER  -  065266    NX      -  065265    N1      -  065312    N2      -  065313    PRINTRD -  065264    PUNCOPT -  065263
R       -  065212    RANGE   -  062703    RESID   -  063671    RI      -  065343    RR      -  065344    SLOPCOM -  065262
SLOPE   -  065323    SLOPNUM -  065267    SUM     -  064655    TOTBIN  -  043127    TOTBINH -  037207    TOTMAX  -  065324
TOTMIN  -  065325    VL      -  065330    VSTOP   -  065274    VV      -  045077    VVF     -  065346    VVI     -  051017
VVIF    -  065342    VVIS    -  065341    VVS     -  065345    VZERO   -  065273    V1      -  065314    V2      -  065315
W       -  062705    X       -  025377    Y       -  037207

START OF CONSTANTS-001366       TEMPS--001715     INDIRECTS-001745

ROUTINE COMPILES IN 046000
```

```
                     SUBROUTINE FRAMCON (NAME,NCHAN,D,IDENT,NGOOD,OUT)
                C
                C    THIS SUBROUTINE MAY BE USED TO CONVERT PAPER TAPE DATA FROM THE
                C    VIDAR DATA ACQUISITION UNIT.  IT CALLS SUBROUTINE PTGET,EDITS THE
                C    RETURNED RECORDS, AND CONVERTS THE INFORMATION IN EACH CHANNEL TO
                C    VOLTAGES THAT ARE RETURNED TO THE CALLING PROGRAM IN A TWO
                C    DIMENSIONAL MATRIX D.  THE CHANNEL IDENTIFICATION NUMBERS ARE
                C    RETURNED IN A VECTOR IDENT.
                C
000010               COMMON/PTCOM/LOOK,ER,EF,PECHO,UWCHO,EBCHO,ROCHO,PECHAR,UWCHAR,
                    1     EBCHAR,NC,LEADER,VAL(15),CHAR(15)
000010               INTEGER ER,EF,PECHO,UWCHO,EBCHO,ROCHO,PECHAR,UWCHAR,EBCHAR,
                    1     VAL,CHAR,FRAME(132),OUT
000010               DIMENSION D(NCHAN,1),IDENT(NCHAN)
000010               DATA PECHO,UWCHO,EBCHO,ROCHO,PECHAR,UWCHAR,EBCHAR,L5,L4,L3,L2,L1,
                    1        (VAL(I),CHAR(I),I=1,11)/
                    2        3,3,2,2,3333,4444,3777,100000,10000,1000,100,10,
                    3        100B,0,1B,1,2B,2,103B,3,4B,4,105B,5,106B,6,7B,7,10B,8,
                    4        111B,9,377B,377B/
000010               WRITE(2,108)
000013               IF(OUT.NE.1) GO TO 9
000020               WRITE(2,103)
000030          9    LOOK=377B
000031               ER=200B
000033               EF=200B
000033               NC=11
000034               LEADER=000B
000035               NF=12*NCHAN
000037               NGOOD=0
000040               NBAD=0
000040               ME=1
000041               LIM=NF+12
000043               ICOUNT=0
000044               ISIT=0
000045         11    CALL PTGET(NAME,FRAME,NFRAME,ME,LIM)
000050               IF(ME.EQ.2.AND.NFRAME.EQ.0) GO TO 11
000062               IF(ME.EQ.3.AND.NFRAME.EQ.0) GO TO 11
000070               ICOUNT=ICOUNT+1
000071               DO 12 I=1,NFRAME
000073               MYFRAM=FRAME(I)
000075               IF(MYFRAM.EQ.377B) GO TO 17
000077               IF(MYFRAM.GT.9) GO TO 2
000102         12    CONTINUE
000104               IF(NFRAME.NE.NF) GO TO 1
000106               NGOOD=NGOOD+1
000107               DO 6 J=1,NCHAN
000111               LOC=12*J-12
000113               IF(FRAME(LOC+1).NE.0) GO TO 3
000116               IF(FRAME(LOC+2).NE.0) GO TO 3
000120               ID=FRAME(LOC+3)
000122               IF(FRAME(LOC+4).EQ.1) GO TO 21
000125               IF(FRAME(LOC+4).NE.2) GO TO 4
000127         21    IF(FRAME(LOC+6).NE.0) GO TO 5
000131               VALU=FRAME(LOC+7)*L5+FRAME(LOC+8)*L4+FRAME(LOC+9)*L3
000142               VALU=VALU+FRAME(LOC+10)*L2+FRAME(LOC+11)*L1+FRAME(LOC+12)
000153               IEXP=FRAME(LOC+5)
000155               VALU=VALU/10.**IEXP
000161               IF(FRAME(LOC+4).EQ.2) VALU=-VALU
```

```
000166              ISIT=1
000167              IDENT(J)=ID
000171     6        D(J,NGOOD)=VALU
000177              GO TO (11,11,11,7,8) ME
000210     1        MD=1
000211              GO TO 14
000212     2        MD=2
000213              GO TO 14
000214     3        MD=3
000215              GO TO 15
000216     4        MD=4
000217              GO TO 15
000220     5        MD=5
000221              GO TO 15
000222     17       IF(NFRAME.EQ.1) 20,2
000226     20       IF(ISIT.EQ.0) 22,23
000231     22       NGOOD=NGOOD+1
000232              NBAD=NBAD-1
000234     23       NFRAME=NF
000235              MD=2
000236              ICOUNT=ICOUNT-1
000240     15       NGOOD=NGOOD-1
000242     14       NBAD=NBAD+1
000244              ISIT=0
000244              IF(OUT.NE.1) GO TO 16
000246              WRITE(2,101) ICOUNT,MD
000255              WRITE(2,102) (FRAME(I),I=1,NFRAME)
000273     16       GO TO (11,11,11,7,18) ME
000304     18       IF(NGOOD.EQ.0.AND.NFRAME.EQ.0.AND.(FRAME(1).AND.777777B).EQ.
                1       LOCF(FRAME(1)))  19,8
000323     19       WRITE(2,109)
000327              NBAD=0
000330              GO TO 13
000334     7        WRITE(2,104)
000340              GO TO 13
000344     8        WRITE(2,105)
000354     13       NTOT=NGOOD+NBAD
000356              WRITE(2,106) NTOT,NBAD
000365              IF(OUT.NE.1) GO TO 10
000372              WRITE(2,107)
000402     10       END FILE 2
000404              RETURN
           C
000405     101      FORMAT(1H0,4X,*RECORD NUMBER *,I4,* REJECTED FOR REASON *,I1)
000405     102      FORMAT(4X,12(1X,I4))
000405     103      FORMAT(1H ,*BELOW IS A DECIMAL COPY OF THE FRAME CONTENTS OF *
                1       *THE DELETED RECORDS*)
000405     104      FORMAT(1H0,*EXIT FROM FRAMCON DUE TO ENDFILE MARK ON PAPER TAPE*)
000405     105      FORMAT(1H0,*EXIT FROM FRAMCON DUE TO END OF PAPER TAPE COMMON*
                1       * FILE -- ENDFILE MARK MISSING ON TAPE*)
000405     106      FORMAT(1H0,*TOTAL NUMBER OF RECORDS READ = *,I6,/,1X,
                1       *NUMBER OF RECORDS REJECTED = *,I6,//)
000405     107      FORMAT(1H0,9X,*REASONS FOR REJECTION*,27X,*EXPLANATION OF FRAME *
                1       *CONTENTS*,///,
                2       10X,*1 -- INCORRECT RECORD LENGTH*,20X,
                3                      * 0-9 -- VALID CHARACTERS*,/
                4       10X,*2 -- ILLEGAL CHARACTER IN RECORD*,16X,
                5                      *3333 -- EVEN PARITY FRAME*,/
```

```
                 6      10X,*3 -- IMPROPER CHANNEL I.D. NUMBER*,15X,
                 7                *3777 -- ERROR SIGNAL FROM OPERATOR*,/
                 8      10X,*4 -- UNRECOGNIZED POLARITY SYMBOL*,15X,
                 9                *4444 -- UNWANTED CHARACTER IN FRAME*,/
                 1      10X,*5 -- SIXTH FRAME NOT BLANK*,22X,
                 2                *   9 -- SIGNALS VOLTAGE OVERLOAD IF IN FRAME 4*,/
                 3      58X,* 255 -- RECORD ELIMINATED BY DELETE BUTTON*)
000405    108    FORMAT(1H1)
000405    109    FORMAT(1H0,*PAPER TAPE COMMON FILE WAS NOT DEFINED BEFORE PROGRAM*
                 1      * EXECUTION -- EXIT FROM FRAMCON*)
          C
000405           END


SUBPROGRAM LENGTH
001113

FUNCTION ASSIGNMENTS

STATEMENT ASSIGNMENTS
1       -  000211    2       -  000213    3       -  000215    4       -  000217    5       -  000221    7       -  000335
8       -  000345    9       -  000031    10      -  000403    11      -  000046    13      -  000355    14      -  000243
15      -  000241    16      -  000274    17      -  000223    18      -  000305    19      -  000324    20      -  000227
21      -  000130    22      -  000232    23      -  000235    101     -  000420    102     -  000427    103     -  000432
104     -  000444    105     -  000454    106     -  000470    107     -  000504    108     -  000632    109     -  000634

BLOCK NAMES AND LENGTHS
PTCOM  -  000052

VARIABLE ASSIGNMENTS
CHAR    -  000033C01 EBCHAR  -  000011C01 EBCHO   -  000005C01 EF      -  000002C01 ER      -  000001C01 FRAME   -  000662
I       -  001102    ICOUNT  -  001077    ID      -  001106    IEXP    -  001110    ISIT    -  001100    J       -  001104
LEADER  -  000013C01 LIM     -  001076    LOC     -  001105    LOOK    -  000000C01 L1      -  001072    L2      -  001071
L3      -  001070    L4      -  001067    L5      -  001066    MD      -  001111    ME      -  001075    MYFRAM  -  001103
NBAD    -  001074    NC      -  000012C01 NF      -  001073    NFRAME  -  001101    NTOT    -  001112    PECHAR  -  000007C01
PECHO   -  000003C01 ROCHO   -  000006C01 UWCHAR  -  000010C01 UWCHO   -  000004C01 VAL     -  000014C01 VALU    -  001107

START OF CONSTANTS-000410        TEMPS--000650     INDIRECTS-000661

ROUTINE COMPILES IN 043100
```

```
                    SUBROUTINE PTGET (NAME,REC,NREC,ME,NLIM)
000007              INTEGER PECHO,PECHAR,EBCHO,EBCHAR,ROCHAR,VAL,CHAR
000007              INTEGER REC,BUF,SHIFT,FRAME,EF ,ER ,UWCHO,UWCHAR,ROCHO
000007              DIMENSION   REC(1),BUF( 513),IBUF(5)
000007              COMMON /PTCOM/ LOOK,ER,EF
                   1,PECHO, UWCHO, EBCHO, ROCHO
                   2,PECHAR,UWCHAR,EBCHAR,NC,LEADER,VAL(15),CHAR(15)
000007              IF(ME.NE.1) GO TO 3
000010              ROCHAR=LOOK.AND.377B
              C     INITIALIZE BUFFER
000012              IBUF(1)=NAME.AND.7777 7777 7777 0000 0000 B
000014              IBUF(2)=LOCF(BUF)
000015              IBUF(3)=IBUF(2)    $IBUF(4)=IBUF(2)
000020              IBUF(5)=IBUF(2)+513
000022              IBUF(1)=IBUF(1).OR. 568
000023              CALL XEQCIO(IBUF)
000025              CALL IOWAIT(IBUF)
000032              SHIFT=60
000033              NREC=0
000034              ISAME=0
000034              IF(ER.EQ.EF) ISAME=1
000040        11    ME=2
000041              RETURN
000042        3     NREC=0
000043              NR=0
000043        1     IF(NREC.EQ.NLIM) GO TO 11
000045              SHIFT=SHIFT-12
000046              IF(SHIFT.GE.0) GO TO 2
000050              SHIFT=48
000050              IBUF(4)=IBUF(4)+1
000052              IF(IBUF(4).EQ.IBUF(5)) IBUF(4)=IBUF(2)
000055        2     IF(IBUF(4).NE.IBUF(3))GO TO 6
000057              IF((IBUF(1).AND.30B).EQ.30B) GO TO 60
000061              IBUF(1)=IBUF(1).AND.7777 7777 7777 0000 0000B.OR.12B
000064              CALL XEQCIO(IBUF)
000065              CALL IOWAIT(IBUF)
000067              GO TO 2
000073        6     IWORD=IBUF(4)-IBUF(2)+1
000075              FRAME=NIGHT(BUF(IWORD),SHIFT).AND.7777B
000102              IF(FRAME.EQ.7777B) GO TO 1
000107              IF(FRAME.NE.3777B) GO TO 35
000110              IF(EBCHO.EQ.1) GO TO 1
000112              NREC=NREC+1
000113              REC(NREC)=EBCHAR
000115              GO TO 1
000115        35    FRAME=FRAME.AND.LOOK
000117              IF(FRAME.EQ.377B) GO TO 40
000120              IF(FRAME.EQ.LEADER) GO TO 1
000122              IF(FRAME.EQ.ROCHAR.AND.ROCHO.EQ.1) GO TO 1
000131              IF(PECHO.EQ.1) GO TO 40
000132              NBITS=NARITY(FRAME)
000134              IF(MOD(NBITS,2) .EQ.1) GO TO 40
000143              IF(PECHO.EQ.2) GO TO 1
000145              NREC=NREC+1
000145              REC(NREC)=PECHAR
000150              GO TO 1
000150        40    CONTINUE
000150              IF(NC.EQ.0) GO TO 120
```

```
000151          DO  100 I=1,NC
000153          IF(FRAME.EQ.VAL(I)) GO TO 101
000155    100   CONTINUE
000157    120   IF(FRAME.EQ.ER) GO TO 130
000161          IF(FRAME.EQ.EF) GO TO 125
000163          GO TO(175,165,170),UWCHO
000172    165   NREC=NREC+1
000173          REC(NREC)=FRAME
000176          GO TO 1
000176    170   NREC=NREC+1
000177          REC(NREC)=UWCHAR
000202    175   GO TO 1
000203    125   ME=4
000204          RETURN
000205    130   IF(NR.EQ.1) GO TO 125
000207          IF(ISAME.EQ.1) GO TO 140
000211    135   ME=3
000212          RETURN
000213    140   NR=1
000214          GO TO 1
000215    101   IF(NR.EQ.1) GO TO 110
000217    105   NREC=NREC+1
000220          REC(NREC)=CHAR(I)
000224          GO TO 1
000224    110   ME=3
000225          SHIFT=SHIFT+12
000226          IF(SHIFT.NE.60) RETURN
000231          SHIFT=0
000232          IBUF(4)=IBUF(4)-1
000234          RETURN
000234    60    ME=5
000235          RETURN
000236          END


SUBPROGRAM LENGTH
001302

FUNCTION ASSIGNMENTS

STATEMENT ASSIGNMENTS
1      - 000044   2      - 000056   3      - 000043   6      - 000074   11     - 000041   35     - 000116
40     - 000151   60     - 000235   101    - 000216   105    - 000220   110    - 000225   120    - 000160
125    - 000204   130    - 000206   135    - 000212   140    - 000214   165    - 000173   170    - 000177
175    - 000203

BLOCK NAMES AND LENGTHS
PTCOM  - 000052

VARIABLE ASSIGNMENTS
BUF    - 000265     CHAR   - 000033C01 EBCHAR - 000011C01 EBCHO  - 000005C01 EF     - 000002C01 ER     - 000001C01
FRAME  - 001267     I      - 001301    IBUF   - 001270    ISAME  - 001275    IWORD  - 001277    LEADER - 000013C01
LOOK   - 000000C01 NBITS  - 001300    NC     - 000012C01 NR     - 001276    PECHAR - 000007C01 PECHO  - 000003C01
ROCHAR - 000264     ROCHO  - 000006C01 SHIFT  - 001266    UWCHAR - 000010C01 UWCHO  - 000004C01 VAL    - 000014C01

START OF CONSTANTS-000241       TEMPS--000251     INDIRECTS-000261
```

```
[COMPASS] PARITY                                                                   08/18/72  [40] PAGENO.     1
                                                         IDENT PARITY
                                        000003     PROGRAM LENGTH

                                                   BLOCKS

                              000000    000003     PROGRAM*    LOCAL

                                                   ENTRY POINTS

                                         000001 NARITY

                                                         ENTRY NARITY
              000000  16012211243155000001               VFD 42/0HNARITY,18/1
              000001  00000000000000000000     NARITY    DATA 0
              000002  56110                              SA1 B1
                           47611                         CX6 X1
                                0200000001 +             JP NARITY
              000003                                     END

                                        020652      UNUSED STORAGE           8 STATEMENTS        1  SYMBOLS


    NARITY     0000001      PROGRAM*          000002
```

```
[COMPASS]     NIGHT                                                                08/18/72  [40] PAGENO.      1
                                                      IDENT      NIGHT
                          000004    PROGRAM LENGTH

                                    BLOCKS

                  000000    000004    PROGRAM*    LOCAL

                                    ENTRY POINTS

                           000001 NIGHT

                                                      ENTRY      NIGHT
     000000  16110710245555000002                     VFD        42/5HNIGHT,18/2
     000001  00000000000000000000    NIGHT            DATA       0
     000002  56110                                    SA1 B1
                  56220                               SA2 B2
                       63320                          SB3 X2
                            23631                     AX6 B3,X1
     000003  0200000001 +                             JP         NIGHT
     000004                                        END

                          020652     UNUSED STORAGE          10 STATEMENTS        1  SYMBOLS


   NIGHT      0000001     PROGRAM*        000003
```

```
                  SUBROUTINE GRAPH(K,M,N,X,Y,Z)
000010            DIMENSION X(1),Y(1),Z(1)
000010            COMMON/LOGSCL/SCALEL
000010            DATA SCALEL/1.0/
000010            DATA F,B,O,P,S/1H*,1H ,1H.,1H+,1HI/
000010            YMIN=Y(1) $ YMAX=Y(1) $ DO 1 I=1,M,N $ YMIN=AMIN1(Y(I),YMIN)
000017          1 YMAX=AMAX1(Y(I),YMAX) $ IF(K.EQ.1.OR.K.EQ.3)GOTO3
000033            DO 2 I=1,M,N $ YMIN=AMIN1(Z(I),YMIN)
000040          2 YMAX=AMAX1(Z(I),YMAX)
000045          3 IF(K.LT.3)GOTO4 $ YMAX=AMAX1(YMAX,1.0E-100)
000053            SCALE=YMAX/SCALEL          $ YMIN=AMAX1(YMIN,SCALE)
000057          4 IF(YMAX.EQ.YMIN)YMAX=YMAX+1. $ IF(K.GE.3)A=ALOG10(YMAX/YMIN)
000072            YDIF=YMAX-YMIN $ MM=M-N+1 $ GOTO(5,6,7,8)K
000111          5 WRITE(3,1001) $ WRITE(3,1007)(J,J=1,9) $ GO TO 9
000135          6 WRITE(3,1002) $ WRITE(3,1007)(J,J=1,9) $ GO TO 9
000161          7 WRITE(3,1003) $ WRITE(3,1008) $ GO TO 9
000200          8 WRITE(3,1004) $ WRITE(3,1008) $ GO TO 9
000217          9 WRITE(3,1005)(S,J=1,101) $ DO 1000 I=1,MM,N $ GOTO(12,11,14,13)K
000244         11 IP=2.+100.*(((Z(I)-YMIN)/YDIF)+0.005)
000253         12 IO=2.+100.*(((Y(I)-YMIN)/YDIF)+0.005)  $ GO TO 15
000263         13 A1=AMAX1(Z(I),YMIN) $ IP=2.+100.*ALOG10(A1/YMIN)/A
000303         14 A2=AMAX1(Y(I),YMIN) $ IO=2.+100.*ALOG10(A2/YMIN)/A
000323         15 IF(K.EQ.1.OR.K.EQ.3)GOTO160
000332            IF(IO.GT.IP+1)GOTO110 $ IF(IO.LT.IP-1)GOTO120
000337            IF(IO.GT.IP)GOTO130 $ IF(IO.LT.IP)GOTO140 $ GOTO150
000343        100 I1=IO-1 $ I2=103-IO
000347            WRITE(3,1006)X(I),(B,J=1,I1),F,(B,J=1,I2),Y(I) $ GOTO1000
000407        110 I1=IP-1 $ I2=IO-IP-1 $ I3=103-IO $ WRITE(3,1006)X(I),
                 1(B,J=1,I1),P,(B,J=1,I2),O,(B,J=1,I3),Y(I),Z(I) $ GOTO1000
000472        120 I1=IO-1 $ I2=IP-IO-1 $ I3=103-IP $ WRITE(3,1006)X(I),
                 1(B,J=1,I1),O,(B,J=1,I2),P,(B,J=1,I3),Y(I),Z(I) $ GOTO1000
000555        130 I1=IP-1 $ I2=103-IO $ WRITE(3,1006)X(I),(B,J=1,I1),P,O,
                 1(B,J=1,I2),Y(I),Z(I) $ GOTO1000
000632        140 I1=IO-1 $ I2=103-IP $ WRITE(3,1006)X(I),(B,J=1,I1),O,P,
                 1(B,J=1,I2),Y(I),Z(I) $ GOTO1000
000707        150 I1=IP-1 $ I2=103-IP $ WRITE(3,1006)X(I),(B,J=1,I1),F,
                 1(B,J=1,I2),Y(I),Z(I) $ GOTO1000
000761        160 I1=IO-1 $ I2=103-IO
000765            WRITE(3,1006)X(I),(B,J=1,I1),O,(B,J=1,I2),Y(I)
001025       1000 CONTINUE $ WRITE(3,1005)(S,J=1,101) $ WRITE(3,1008) $ RETURN
001050       1001 FORMAT (6H1*OVF*4X*X*3X*LINEAR SCALE*96X*Y*)
001050       1002 FORMAT (6H1*OVF*4X*X*3X*LINEAR SCALE*54X,50H. = Y         + = Z
                 1  * = Y AND Z          Y          Z)
001050       1003 FORMAT (6H1*OVF*4X*X*3X*LOGARITHMIC SCALE*91X*Y*)
001050       1004 FORMAT (6H1*OVF*4X*X*3X*LOGARITHMIC SCALE*49X,50H. = Y         + = Z
                 1        * = Y AND Z          Y       Z)
001050       1005 FORMAT (14X,101A1)
001050       1006 FORMAT (1X,F10.3,2H  ,103A1,2F7.3)
001050       1007 FORMAT (/14X,10(1H0,9X),1H1, /14X,10(1H.,9X),1H., /14X,1H0,
                 19(9X,I1),9X,1H0, /14X,10(1H0,9X),1H0,/)
001050       1008 FORMAT (/14X,1HI,10(9X,1HI),/)
001050            END


SUBPROGRAM LENGTH
0 1210
```

```
FUNCTION ASSIGNMENTS

STATEMENT ASSIGNMENTS
3       - 000046   4      - 000060   5      - 000112   6      - 000136   7      - 000162   8      - 000201
9       - 000220   11     - 000245   12     - 000254   13     - 000264   14     - 000304   15     - 000324
100     - 000344   110    - 000410   120    - 000473   130    - 000556   140    - 000633   150    - 000710
160     - 000762   1000   - 001026   1001   - 001062   1002   - 001067   1003   - 001101   1004   - 001107
1005    - 001122   1006   - 001125   1007   - 001131   1008   - 001144

BLOCK NAMES AND LENGTHS
LOGSCL -  000001

VARIABLE ASSIGNMENTS
A       - 001175   A1     - 001203   A2     - 001204   B      - 001165   F      - 001164   I      - 001173
IO      - 001202   IP     - 001201   I1     - 001205   I2     - 001206   I3     - 001207   J      - 001200
MM      - 001177   O      - 001166   P      - 001167   S      - 001170   SCALE  - 001174   SCALEL - 000000C01
YDIF    - 001176   YMAX   - 001172   YMIN   - 001171

START OF CONSTANTS-001053        TEMPS--001150     INDIRECTS-001162

ROUTINE COMPILES IN 043700
```

```
                FORTRAN IV SUBROUTINE LSQPOL(X,Y,W,RESID,N,SUM,L,A,B,M)             ANE20603
          C                                                                         ANE20602
          C     LEAST SQUARE POLYNOMIAL FIT                                         ANE20601
          C                                                                         ANE20604
000014          DIMENSION X(500),Y(500,1),RESID(500,1),A(20,8),B(20,8),C(500,8),
               X          SUM(1), W(500)
000014          COMMON /LSP/ C
          C                                                                         ANE20608
000014       10 DO 20 I=1,N                                                         ANE20609
000022       20 C(I,1)=1.0                                                          ANE20610
000027       30 DO 50 J=2,M                                                         ANE20611
000031       40 DO 50 I=1,N                                                         ANE20612
000041       50 C(I,J)=C(I,J-1)*X(I)                                                ANE20613
000052       60 DO 100 I=1,M                                                        ANE20614
000054       70 DO 100 J=1,M                                                        ANE20615
000056       80 A(I,J)=0.0                                                          ANE20616
000063       90 DO 100 K=1,N                                                        ANE20617
000100      100 A(I,J)=A(I,J)+C(K,I)*C(K,J)*W(K)                                    ANE20618
000114      105 DO 150 J=1,L                                                        ANE20619
000116      110 DO 150 I=1,M                                                        ANE20620
000120      120 B(I,J)=0.0                                                          ANE20621
000125      130 DO 150 K=1,N                                                        ANE20622
000142      150 B(I,J)=B(I,J)+C(K,I)*Y(K,J)*W(K)                                    ANE20623
000160     170  CALL MATINV (A,M,B,L,DETERM)
000171      180 DO 205 J=1,L                                                        ANE20625
000173      185 SUM(J)=0.0                                                          ANE20626
000175      192 DO 195 K=1,M                                                        ANE20627
000205      195 C(K,1)=B(K,J)                                                       ANE20628
000213      198 DO 205 I=1,N                                                        ANE20629
000215      200 RESID(I,J)=POLYE1(X(I),M,C(1,1))-Y(I,J)
000237      205 SUM(J)=SUM(J)+RESID(I,J)**2*W(I)                                    ANE20631
000251      210 RETURN                                                              ANE20632
000252     220  END
          C     MATRIX INVERSION WITH ACCOMPANYING SOLUTION OF LINEAR EQUATIONS    ANF40201
          C                                                                         F4020002


SUBPROGRAM LENGTH
000304

FUNCTION ASSIGNMENTS

STATEMENT ASSIGNMENTS
10      -  000015   30      -  000030   40      -  000032   60      -  000053   70      -  000055   80      -  000057
90      -  000064   105     -  000115   110     -  000117   120     -  000121   130     -  000126   170     -  000161
180     -  000172   185     -  000174   192     -  000176   198     -  000214   200     -  000216   210     -  000252

BLOCK NAMES AND LENGTHS
LSP     -  007640

VARIABLE ASSIGNMENTS
A       -  000001   B       -  000002   C       -  000000C01 DETERM -  000303   I       -  000300   J       -  000301
K       -  000302   L       -  000000   M       -  000003

START OF CONSTANTS-000255       TEMPS--000257     INDIRECTS-000265

ROUTINE COMPILES IN 041400
```

```
                FORTRAN IV SUBROUTINE MATINV(A,N,B,M,DETERM)                     F4020003
          C                                                                      F4020004
000007          DIMENSION IPIVOT(20), A(20,20), B(20,1), INDEX(20,2), PIVOT(20)  F4020005
000007          COMMON /LSP/ PIVOT,IPIVOT,INDEX
000007          EQUIVALENCE (IROW,JROW), (ICOLUM,JCOLUM), (AMAX, T, SWAP)        F4020007
          C                                                                      F4020008
          C     INITIALIZATION                                                   F4020009
          C                                                                      F4020010
000007       10 DETERM=1.0                                                       F4020011
000010       15 DO 20 J=1,N                                                      F4020012
000015       20 IPIVOT(J)=0                                                      F4020013
000022       30 DO 550 I=1,N                                                     F4020014
          C                                                                      F4020015
          C     SEARCH FOR PIVOT ELEMENT                                         F4020016
          C                                                                      F4020017
000024       40 AMAX=0.0                                                         F4020018
000025       45 DO 105 J=1,N                                                     F4020019
000027       50 IF (IPIVOT(J)-1) 60, 105, 60                                     F4020020
000032       60 DO 100 K=1,N                                                     F4020021
000034       70 IF (IPIVOT(K)-1) 80, 100, 740                                    F4020022
000037       80 IF (ABS(AMAX)-ABS(A(J,K))) 85, 100, 100
000046       85 IROW=J                                                           F4020024
000050       90 ICOLUM=K                                                         F4020025
000052       95 AMAX=A(J,K)                                                      F4020026
000056      100 CONTINUE                                                         F4020027
000061      105 CONTINUE                                                         F4020028
000064          IF(AMAX) 110,800,110                                             F402REV.
000065      110 IPIVOT(ICOLUM)=IPIVOT(ICOLUM)+1                                  F4020029
          C                                                                      F4020030
          C     INTERCHANGE ROWS TO PUT PIVOT ELEMENT ON DIAGONAL                F4020031
          C                                                                      F4020032
000070      130 IF (IROW-ICOLUM) 140, 260, 140                                   F4020033
000072      140 DETERM=-DETERM                                                   F4020034
000073      150 DO 200 L=1,N                                                     F4020035
000075      160 SWAP=A(IROW,L)                                                   F4020036
000101      170 A(IROW,L)=A(ICOLUM,L)                                            F4020037
000107      200 A(ICOLUM,L)=SWAP                                                 F4020038
000113      205 IF(M) 260, 260, 210                                              F4020039
000115      210 DO 250 L=1, M                                                    F4020040
000117      220 SWAP=B(IROW,L)                                                   F4020041
000123      230 B(IROW,L)=B(ICOLUM,L)                                            F4020042
000131      250 B(ICOLUM,L)=SWAP                                                 F4020043
000135      260 INDEX(I,1)=IROW                                                  F4020044
000137      270 INDEX(I,2)=ICOLUM                                                F4020045
000141      310 PIVOT(I)=A(ICOLUM,ICOLUM)                                        F4020046
000146      320 DETERM=DETERM*PIVOT(I)                                           F4020047
          C                                                                      F4020048
          C     DIVIDE PIVOT ROW BY PIVOT ELEMENT                                F4020049
          C                                                                      F4020050
000150      330 A(ICOLUM,ICOLUM)=1.0                                             F4020051
000154      340 DO 350 L=1,N                                                     F4020052
000170      350 A(ICOLUM,L)=A(ICOLUM,L)/PIVOT(I)                                 F4020053
000175      355 IF(M) 380, 380, 360                                              F4020054
000177      360 DO 370 L=1,M                                                     F4020055
000212      370 B(ICOLUM,L)=B(ICOLUM,L)/PIVOT(I)                                 F4020056
          C                                                                      F4020057
          C     REDUCE NON-PIVOT ROWS                                            F4020058
          C                                                                      F4020059
```

```
000217      380 DO 550 L1=1,N                                                   F4020060
000221      390 IF(L1-ICOLUM) 400, 550, 400                                     F4020061
000223      400 T=A(L1,ICOLUM)                                                  F4020062
000227      420 A(L1,ICOLUM)=0.0                                                F4020063
000233      430 DO 450 L=1,N                                                    F4020064
000245      450 A(L1,L)=A(L1,L)-A(ICOLUM,L)*T                                   F4020065
000253      455 IF(M) 550, 550, 460                                             F4020066
000255      460 DO 500 L=1,M                                                    F4020067
000266      500 B(L1,L)=B(L1,L)-B(ICOLUM,L)*T                                   F4020068
000274      550 CONTINUE                                                        F4020069
          C                                                                     F4020070
          C     INTERCHANGE COLUMNS                                             F4020071
          C                                                                     F4020072
000301      600 DO 710 I=1,N                                                    F4020073
000303      610 L=N+1-I                                                         F4020074
000306      620 IF (INDEX(L,1)-INDEX(L,2)) 630, 710, 630                        F4020075
000311      630 JROW=INDEX(L,1)                                                 F4020076
000313      640 JCOLUM=INDEX(L,2)                                               F4020077
000315      650 DO 705 K=1,N                                                    F4020078
000317      660 SWAP=A(K,JROW)                                                  F4020079
000323      670 A(K,JROW)=A(K,JCOLUM)                                           F4020080
000332      700 A(K,JCOLUM)=SWAP                                                F4020081
000337      705 CONTINUE                                                        F4020082
000341      710 CONTINUE                                                        F4020083
000344      740 RETURN                                                          F4020084
000345      800 DETERM = 0.                                                     F402REV.
000346          RETURN                                                          F402REV.
000346          END


SUBPROGRAM LENGTH
000376

FUNCTION ASSIGNMENTS

STATEMENT ASSIGNMENTS
10     -  000010   15     -  000011   30     -  000023   40     -  000025   45     -  000026   50     -  000030
60     -  000033   70     -  000035   80     -  000040   85     -  000047   90     -  000051   95     -  000053
100    -  000057   105    -  000062   110    -  000066   130    -  000071   140    -  000073   150    -  000074
160    -  000076   170    -  000102   205    -  000114   210    -  000116   220    -  000120   230    -  000124
260    -  000136   270    -  000140   310    -  000142   320    -  000147   330    -  000151   340    -  000155
355    -  000176   360    -  000200   380    -  000220   390    -  000222   400    -  000224   420    -  000230
430    -  000234   455    -  000254   460    -  000256   550    -  000275   600    -  000302   610    -  000304
620    -  000307   630    -  000312   640    -  000314   650    -  000316   660    -  000320   670    -  000324
700    -  000333   710    -  000342   740    -  000345   800    -  000346

BLOCK NAMES AND LENGTHS
LSP    -  000120

VARIABLE ASSIGNMENTS
AMAX   -  000370   I      -  000372   ICOLUM -  000367   INDEX  -  000050C01 IPIVOT -  000024C01 IROW   -  000366
J      -  000371   JCOLUM -  000367   JROW   -  000366   K      -  000373   L      -  000374   L1     -  000375
PIVOT  -  000000C01 SWAP  -  000370   T      -  000370

START OF CONSTANTS-000351      TEMPS--000353      INDIRECTS-000361

ROUTINE COMPILES IN 042100
```

```
                FORTRAN IV FUNCTION POLYE1(X,M,C)
          C X=THE VALUE AT WHICH THE POLYNOMIAL IS TO BE EVALUATED
          C M=THE NUMBER OF COEFFICIENTS
          C C IS THE ARRAY OF COEFFICIENTS
000005          DIMENSION C(500) $S=C(M)  $N=M-1  $DO 1 I=1,N  $K=M-1  $S=S*X+C(K)
000016        1 CONTINUE  $POLYE1=S  $RETURN  $END


SUBPROGRAM LENGTH
000036

FUNCTION ASSIGNMENTS

STATEMENT ASSIGNMENTS

BLOCK NAMES AND LENGTHS

VARIABLE ASSIGNMENTS
I       - 000034    K       - 000035    N       - 000033    POLYE1 - 000031    S       - 000032

START OF CONSTANTS-000025       TEMPS--000026    INDIRECTS-000030

ROUTINE COMPILES IN 041000
```

```
                 SUBROUTINE ROOT (A,N,R,ERROR)
000006           COMPLEX A(1), R(1)
000006           COMPLEX X,Y,POLY,DPOLY,SAVE1,SAVE2
000006           ERR=ERROR
000006           IF(ERROR.LT.1.E-09) ERR=1.E-09
000012           X=0.0
000014           NM1=N-1

000015           DO 5 M=1,NM1
000017           K=N-M+1
000021           DO 2 I=1,400
             C  CALCULATE THE VALUE OF THE POLYNOMIAL (POLY), AND ITS DERIVATIVE (DPOLY).
000022           POLY=0.0
000023           DPOLY=0.0
000025           DO 1 L=1,K
000032           DPOLY=DPOLY*X+POLY
000042           POLY=POLY*X+A(K-L+1)
000053         1 CONTINUE
000054           IF(CABS(DPOLY).EQ.0.0) X=X+0.123456789
000067           IF(CABS(DPOLY).EQ.0.0) GO TO 2
             C  NEWTON≠S METHOD.
000075           Y=X-POLY/DPOLY
000106           IF(CABS(Y-X).LT.ERR) GO TO 4
000121           X=Y
             C  IF STUCK TRY A JOG IN COMPLEX PLANE (E.G. THIS IS NECESSARY TO FIND
             C   A COMPLEX ROOT OF A REAL POLYNOMIAL).
000124           IF(I.EQ.200)    X=X+(.1234,.5678)
000132         2 CONTINUE

000134           PRINT 99,M
000142        99 FORMAT (X*----------- WARNING, SUBROUTINE ROOT CAN NOT FIND THE *I5
                $ *-TH ROOT OR BEYOND. -----------*)
000145           DO 3 I=M,NM1
000155           R(I)=CMPLX(17770000000000000000B,17770000000000000000B)
000157         3 CONTINUE
000160           RETURN

000163         4 R(M)=Y
             C  SYNTHETIC DIVISION.
000167           SAVE1=A(K)
000171           SAVE2=A(K-1)
000174           A(K)=0.0
000176           DO 5 I=2,K
000203           A(K-I+1)=A(K-I+2)*R(M)+SAVE1
000220           SAVE1=SAVE2
000222           SAVE2=A(K-I)
000226         5 CONTINUE
000234           RETURN
000235           END


SUBPROGRAM LENGTH
0:0326

FUNCTION ASSIGNMENTS

STATEMENT ASSIGNMENTS
```

```
2       - 000133   4       - 000162   99      - 000246
BLOCK NAMES AND LENGTHS

VARIABLE ASSIGNMENTS
DPOLY  - 000312   ERR     - 000320   I       - 000324   K       - 000323   L       - 000325   M       - 000322
NM1    - 000321   POLY    - 000310   SAVE1   - 000314   SAVE2   - 000316   X       - 000304   Y       - 000306

START OF CONSTANTS-000240      TEMPS--000262    INDIRECTS-000274

ROUTINE COMPILES IN 041400
```

APPENDIX III.

The generalized Taylor series formula is

$$f(x+h) = f(x) + h\,\frac{df}{dx} + \frac{h^2}{2!}\,\frac{d^2f}{dx^2} + \frac{h^3}{3!}\,\frac{d^3f}{dx^3} + \ldots$$

where h is the perturbation on x of which f is some function. The situation where the current, I, is expanded as a function of a dc voltage (V_o) with ac modulation ($k \sin \omega t$) superimposed upon it follows:

$$I(V_o + k \sin \omega t) = I(V_o) + k \sin \omega t\,\frac{dI}{dV_0} + \frac{k^2 \sin^2 \omega t}{2!}\,\frac{d^2I}{dV_0^2}$$

$$+ \frac{k^3 \sin^3 \omega t}{3!}\,\frac{d^3I}{dV_0^3} + \frac{k^4 \sin^4 \omega t}{4!}\,\frac{d^4I}{dV_0^4}$$

$$+ \frac{k^5 \sin^5 \omega t}{5!}\,\frac{d^5I}{dV_0^5} + \frac{k^6 \sin^6 \omega t}{6!}\,\frac{d^6I}{dV_0^6} + \ldots$$

$$= I(V_o) + k \sin \omega t\,\frac{dI}{dV_0} + \frac{k^2}{2!} + \left(\frac{1-\cos 2\omega t}{2}\right)\frac{d^2I}{dV_0^2}$$

$$+ \frac{k^3}{3!}\left(\frac{3\ \sin\omega t + \sin 3\omega t}{4}\right)\frac{d^3I}{dV_0^3}$$

$$+ \frac{k^4}{4!}\left(\frac{3/2-2\cos 2\omega t + 1/2\cos 4\omega t}{4}\right)\frac{d^4I}{dV_0^4}$$

$$+_{-} \frac{k^5}{5!}\left(\frac{10\sin\omega t-5\sin 3\omega t+\sin 5\omega t}{16}\right)\frac{d^5I}{dV_0^5}$$

$$+ \frac{k^6}{6!} \left(\frac{5/2 - 15/4\cos 2\omega t + 3/2\cos 4\omega t - 1/4\cos 6\omega t}{8}\right) \frac{d^6 I}{dV_0^6}$$

$$+ \ \ldots$$

$$= I(V_0) + \left[\frac{k^2}{4} \frac{d^2 I}{dV_0^2} + \frac{k^4}{64} \frac{d^4 I}{dV_0^4} + \frac{k^6}{2304} \frac{d^6 I}{dV_0^6} + \ldots\right]$$

$$+ \left[k \frac{dI}{dV_0} + \frac{k^3}{8} \frac{d^3 I}{dV_0^3} + \frac{k^5}{192} \frac{d^5 I}{dV_0^5} + \ldots\right] \sin\omega t$$

$$- \left[\frac{k^2}{4} \frac{d^2 I}{dV_0^2} + \frac{k^4}{48} \frac{d^4 I}{dV_0^4} + \frac{k^6}{1536} \frac{d^6 I}{dV_0^6} + \ldots\right] \cos 2\omega t$$

$$- \left[\frac{k^3}{24} \frac{d^3 I}{dV_0^3} + \frac{k^5}{384} \frac{d^5 I}{dV_0^5} + \ldots\right] \sin 3\omega t$$

$$= I(V_0) + A_0 + A_1 \sin\omega t - A_2 \cos 2\omega t - A_3 \sin 3\omega t + \ldots$$

The following trigonometric relations have been used above:

$$\sin^2\omega t = \frac{1}{2}(1-\cos 2\omega t)$$

$$\sin^3\omega t = \frac{1}{4}(3\sin\omega t-\sin 3\omega t)$$

$$\sin^4\omega t = (\sin^2\omega t)^2 = \frac{1}{4}\left(\frac{3}{2} - 2\cos 2\omega t + \frac{1}{2}\cos 4\omega t\right)$$

$$\sin^5\omega t = \frac{1}{16}(19\sin\omega t-5\sin 3\omega t+\sin 5\omega t)$$

$$\sin^6\omega t = (\sin^2\omega t)^3 = \frac{1}{8}\left(\frac{5}{2} - \frac{15}{4}\cos 2\omega t + \frac{3}{2}\cos 4\omega t - \frac{1}{4}\cos 6\omega t\right)$$

APPENDIX IV.

A. The Gaussian Distribution Function

The form of the Gaussian distribution function and its subsequent five derivatives are:

$$I_G^{i} \equiv I_G^{i}(V) = i \left(\frac{1}{\sqrt{2\pi}\,\sigma}\right) \exp\left(\frac{-V^2}{2\sigma^2}\right)$$

$$I_G^{ii} = \left(\frac{-V}{\sigma^2}\right) I_G^{i}$$

$$I_G^{iii} = \left(\frac{-1}{\sigma^2} + \frac{V^2}{\sigma^4}\right) I_G^{i}$$

$$I_G^{iv} = \left(\frac{3V}{\sigma^4} - \frac{V^3}{\sigma^6}\right) I_G^{i}$$

$$I_G^{v} = \left(\frac{3}{\sigma^4} - \frac{6V^2}{\sigma^6} + \frac{V^4}{\sigma^8}\right) I_G^{i}$$

$$I_G^{vi} = \left(\frac{-15V}{\sigma^6} + \frac{10V^3}{\sigma^8} - \frac{V^5}{\sigma^{10}}\right) I_G^{i}$$

The point(s) at which the Gaussian distribution exhibits its maximum (positive or negative) slope will occur where the value of the derivative of the distribution, I_G^{ii}, passes through a (positive or negative) maximum. Since the derivative of I_G^{ii} must equal zero at these points, the maximum slope points of the Gaussian distribution are easily calculable.

$$I_G^{iii} = \left(\frac{-1}{\sigma^2} + \frac{V^2}{\sigma^4}\right) I_G^i = 0$$

$$\therefore \left(\frac{-1}{\sigma^2} + \frac{V^2}{\sigma^4}\right) = 0$$

$$V^2 = \sigma^4 \left(\frac{1}{\sigma^2}\right) = \sigma^2$$

$$V = \pm \sigma$$

For the Gaussian distribution, the deviations from proportionality as defined in Eqs. (II-6) and (II-7) in the text, are:

$$\Delta A_1 = \frac{\left[kI_G^i + \frac{k^3}{8}\left(\frac{-1}{\sigma^2} + \frac{V^2}{\sigma^4}\right) I_G^i + \frac{k^5}{192}\left(\frac{3}{\sigma^4} - \frac{6V^2}{\sigma^6} + \frac{V^4}{\sigma^8}\right) I_G^i\right] - kI_G^i}{kI_G^i}$$

$$= -\left[\frac{1}{8} - \frac{V^2}{8\sigma^2} - \left(\frac{1}{64} - \frac{V^2}{32\,\sigma^2} + \frac{V^4}{192\,\sigma^4}\right)\left(\frac{k}{\sigma}\right)^2\right]\left(\frac{k}{\sigma}\right)^2$$

$$\Delta A_2 = \frac{\left\{-\left[\frac{k^2}{4}\left(\frac{-V}{\sigma^2}\right) I_G^i + \frac{k^4}{48}\left(\frac{3V}{\sigma^4} - \frac{V^3}{\sigma^6}\right) I_G^i + \frac{k^6}{1536}\left(\frac{-15V}{\sigma^6} + \frac{10V^3}{\sigma^8} - \frac{V^5}{\sigma^{10}}\right) I_G^i\right] + \frac{k^2}{4}\left(\frac{-V}{\sigma^2}\right) I_G^i\right\}}{-\frac{k^2}{4}\left(\frac{-V}{\sigma^2}\right) I_G^i}$$

$$= -\left[\frac{1}{4} - \frac{V^2}{12\,\sigma^2} - \left(\frac{15}{384} - \frac{10V^2}{384\,\sigma^2} + \frac{V^4}{384\,\sigma^4}\right)\left(\frac{k}{\sigma}\right)^2\right]\left(\frac{k}{\sigma}\right)^2$$

When evaluated at the peak maximum (V=0) and at the point of maximum slope (V=σ), these equations reduce to the following forms:

$$\Delta A_1(V{=}0) \quad = \quad -\left[\frac{1}{8} - \frac{1}{64}\left(\frac{k}{\sigma}\right)^2\right]\left(\frac{k}{\sigma}\right)^2$$

$$\Delta A_1(V{=}\sigma) \quad = \quad -\left[\frac{1}{96}\left(\frac{k}{\sigma}\right)^4\right]$$

$$\Delta A_2(V{=}0) \quad = \quad 0$$

by peak symmetry considerations or by invoking l'Hôpital's Rule in the evaluation of ΔA_2 (noting that the denominator in the above equation for ΔA_2 is zero when V=0).

$$\Delta A_2(V{=}\sigma) = -\left[\frac{1}{6} - \frac{1}{64}\left(\frac{k}{\sigma}\right)^2\right]\left(\frac{k}{\sigma}\right)^2$$

B. The Lorentzian Distribution Function

The corresponding expressions for the Lorentzian distribution function are:

$$I_L^i \equiv I_L^i(V) = i\left(\frac{1}{\pi}\right)\left(\frac{\Gamma/2}{V^2 + (\Gamma/2)^2}\right)$$

$$I_L^{ii} = \frac{-2\pi V}{(\Gamma/2)}\left(I_L^i\right)^2$$

$$I_L^{iii} = \frac{-2\pi}{(\Gamma/2)}\left(I_L^i\right)^2 + \frac{8\pi^2 V^2}{(\Gamma/2)^2}\left(I_L^i\right)^3$$

$$I_L^{iv} = \frac{24\pi^2 V}{(\Gamma/2)^2}\left(I_L^i\right)^3 - \frac{48\pi^3 V^3}{(\Gamma/2)^3}\left(I_L^i\right)^4$$

$$I_L^{v} = \frac{24\pi^2}{(\Gamma/2)^2}\left(I_L^i\right)^3 - \frac{288\pi^3 V^2}{(\Gamma/2)^3}\left(I_L^i\right)^4 + \frac{384\pi^4 V^4}{(\Gamma/2)^4}\left(I_L^i\right)^5$$

$$I_L^{vi} = \frac{-720\pi^3 V}{(\Gamma/2)^3}\left(I_L^i\right)^4 + \frac{3840\pi^4 V^3}{(\Gamma/2)^4}\left(I_L^i\right)^5 - \frac{3840\pi^5 V^5}{(\Gamma/2)^5}\left(I_L^i\right)^6$$

The maximum slope points are:

$$I_L^{iii} = \left[\frac{-2\pi}{(\Gamma/2)}\left(I_L^i\right)^2 + \frac{8\pi^2 V^2}{(\Gamma/2)^2}\left(I_L^i\right)^3\right] = 0$$

$$\therefore \quad \left[-1 + \frac{4\pi V^2}{(\Gamma/2)}\left(I_L^i\right)\right] = \left[-1 + \frac{4V^2}{V^2+(\Gamma/2)^2}\right] = 0$$

$$V^2 = \frac{1}{4}\left[V^2+(\Gamma/2)^2\right] = \frac{4}{3}\,\frac{(\Gamma/2)^2}{4}$$

$$V = \pm\frac{(\Gamma/2)}{\sqrt{3}} = \pm\ 0.5775\ (\Gamma/2)$$

The deviations from proportionality are:

$$\Delta A_1 = -\left[\frac{1}{4} - \frac{V^2}{B} - \left(\frac{1}{8} - \frac{3V^2}{2B} + \frac{2V^4}{B^2}\right)\left(\frac{k^2}{B}\right)\right]\left(\frac{k^2}{B}\right)$$

where

$$B = [V^2 + (\Gamma/2)^2]$$

$$\Delta A_2 \quad = - \left[1 - \frac{2V^2}{B} - \left(\frac{15}{16} - \frac{5V^2}{B} + \frac{5V^4}{B^2}\right) \left(\frac{k^2}{B}\right)\right]\left(\frac{k^2}{B}\right)$$

The evaluation of these deviations at V=0, σ leads to the expressions:

$$\Delta A_1(V=0) \quad = \quad - \quad \left[\frac{1}{4} - \frac{1}{8} \left(\frac{k}{(\Gamma/2)}\right)^2\right] \left(\frac{k}{(\Gamma/2)}\right)^2$$

$$= \quad - \quad \left[\frac{c^2}{4} - \frac{c^4}{8} \left(\frac{k}{\sigma}\right)^2\right] \left(\frac{k}{\sigma}\right)^2$$

where

$$\sigma = c(\Gamma/2) \quad = \quad 0.5775 \ (\Gamma/2)$$

$$\Delta A_1(V=\sigma) \quad = - \left[\frac{1}{4C} - \frac{1}{C^2} - \left(\frac{1}{8C^2} - \frac{3}{2C^3} + \frac{2}{C^4}\right) \left(\frac{k}{\sigma}\right)^2\right]\left(\frac{k}{\sigma}\right)^2$$

where

$$C \quad = \quad (1 + 1/c^2)$$

$$\Delta A_2(V=0) = 0$$

$$\Delta A_2(V=\sigma) = - \left[\frac{1}{C} - \frac{2}{C^2} - \left(\frac{15}{16C^2} - \frac{5}{C^3} + \frac{5}{C^4}\right)\left(\frac{k}{\sigma}\right)^2\right] \left(\frac{k}{\sigma}\right)^2$$

APPENDIX V

If the fairly linear portions of the sides of a Gaussian curve are extented to the base of the peak, it has been found[120] that the base width, BW, so defined bears the following relationship to the full width at half height, FWHH, and the standard deviation, σ, of the curve:

$$\begin{aligned} BW &= 1.76\ \mathrm{FWHH} \\ &= 4.14\ \sigma \end{aligned}$$

If one allows for the increase in the base width due to the peak-to-peak magnitude of the modulation voltage, 2k, and the instrumental linewidth of the instrument at the Auger peak energy, eV_{Auger}, the corrected base width is

$$BW_{corr} = BW - 2k - 1.76\ [0.30 + (0.00248)V_{Auger}]\ .$$

The corrected full width at half height, FWHH_{corr}, is then obtained by dividing BW_{corr} by 1.76.

REFERENCES

1. G. A. Somorjai, in Principles of Surface Chemistry, (Prentice-Hall Inc., New Jersey, 1972).
2. G. F. Amelio and E. J. Scheibner, Surf. Sci. 11, 242 (1968).
3. C. J. Davisson and L. H. Germer, Phys. Rev. 30, 705 (1927).
4. P. J. Estrup and E. G. McRae, Surf. Sci. 25, 1 (1971).
5. G. A. Somorjai and H. H. Farrell, in Advances in Chemical Physics, Ed. I. Prigogine and S. A. Rice (John Wiley and Sons, Inc., New York, 1971) Vol. XX, p. 215.
6. E. A. Wood, J. Appl. Phys., 35, 1306 (1964).
7. P. J. Estrup, in Modern Diffraction and Imaging Techniques in Material Science, Ed. S. Amelinckx et al. (North-Holland Publishing Co., Amsterdam, 1970) p. 377.
8. C. Kittel, in Introduction to Solid State Physics (John Wiley and Sons, Inc., New York, 1966).
9. D. Bohm and D. Pines, Phys. Rev. 92, 609 (1953).
10. E. A. Stern and R. A. Ferrell, Phys. Rev. 120, 130 (1960).
11. R. H. Ritchie, Phys. Rev. 106, 874 (1957).
12. A. Ia. Viatskin, Soviet Phys. - Tech. Phys. 3, 2038, 2252 (1958).
13. A. J. Dekker, in Solid State Physics (Academic Press, New York, 1958) Vol. 6.
14. P. A. Wolff, Phys. Rev. 95, 56 (1954).
15. H. Stolz, Annalen der Physik 3, 197 (1959).
16. A. I. Guba, Soviet Phys. - Solid State 4, 1197 (1965).

17. G. F. Amelio and E. J. Scheibner, in The Structure and Chemistry of Solid Surfaces, Ed. G. A. Somorjai (Wiley, New York, 1969) p. 11-1.

18. P. Auger, J. Phys. Radium 6, 205 (1925).

19. I. Bergström and R. D. Hill, Arkiv Fysik 8, 21 (1954).

20. T. A. Clarke, et al., J. Chem. Soc. (A), 1156 (1971).

21. K. Siegbahn, et al., in ESCA: Atomic, Molecular, and Solid State Structure Studied by Means of Electron Spectroscopy (Almquist and Wiksalls Boktryckeri AB, Uppsala, Sweden, 1967).

22. I. Bergström and C. Nordling, in Alpha-, Beta-, and Gamma-Ray Spectroscopy, Ed. K. Siegbahn (North-Holland Publishing Co., Amsterdam, 1965), Vol. 2, p. 1523.

23. T. W. Haas, J. T. Grant, and G. J. Dooley, Phys. Rev. B1, 1449 (1970).

24. H. A. Bethe, Ann. Phys. 5, 325 (1930).

25. M. Gryzinski, Phys. Rev. 138, A336 (1965).

26. W. Bambynek, et al., Rev. Mod. Phys. 44, 716 (1972).

27. M. A. Listengarten, Bull. Acad. Sci. U.S.S.R. Phys. Ser. U.S.A. 26, 182 (1962).

28. G. Wenzel, Z. Phys. 43, 524 (1927).

29. E. H. S. Burhop, J. Phys. Radium 16, 625 (1955).

30. H. L. Hagedoorn and A. H. Wapstra, Nucl. Phys. 15, 146 (1960).

31. M. P. Seah, Surf. Sci. 32, 703 (1972).

32. P. W. Palmberg and T. N. Rhodin, J. Appl. Phys. 39, 2425 (1968).

33. S. M. Sze, et al., Solid State Electronics 7, 509 (1964).

34. E. R. Jones, et al., Phys. Rev. 151, 476 (1966).

35. J. C. Rivière, in Solid State Surface Science, Ed. M. Green (Dekker, New York, 1969) Vol. 1.

36. Y. Baer, et al., Solid State Communications 8, 1479 (1970).

37. H. Kanter, Phys. Rev. B1, 522 (1970).

38. W. F. Krolikowski and W. E. Spicer, Phys. Rev. B1, 478 (1970).

39. K. Jacobi, Surf. Sci. 26, 54 (1971).

40. J. W. T. Ridgeway and D. Haneman, Surf. Sci. 24, 451 (1971).

41. J. W. T. Ridgeway and D. Haneman, Surf. Sci. 26, 683 (1971).

42. R. G. Steinhardt, et al., in International Conference on Electron Spectroscopy, Ed. D. A. Shirley (North-Holland Publishing Co., Amsterdam-London, 1972) p. 557.

43. D. Eastman, 1972 Physical Electronics Conference, Albuquerque

44. L. L. Levenson, et al., J. Vac. Sci. and Tech. 9, 608 (1972).

45. M. L. Tarng and G. K. Wehner, 1972 Physical Electronics Conference, Albuquerque.

46. F. Meyer and J. J. Vrakking, Surf. Sci. 33, 271 (1972).

47. M. Perdereau, Surf. Sci. 24, 239 (1971).

48. J. H. Pollard, Surf. Sci. 20, 269 (1970).

49. P. W. Palmberg, Appl. Phys. Letters 13, 183 (1968).

50. L. A. Harris, Surf. Sci. 15, 77 (1969).

51. C. C. Chang, Surf. Sci. 25, 53 (1971).

52. H. E. Bishop and J. C. Rivière, AERE Report R5834 (1968) and J. Appl. Phys. 40, 1740 (1969).

53. N. J. Taylor, Rev. Sci. Instrum. 40, 792 (1969).

54. T. E. Gallon, J. Phys. D: Appl. Phys. 5, 822 (1972).

55. R. L. Gerlach and A. R. DuCharme, Surf. Sci. 32, 329 (1972).

56. G. A. Somorjai and F. J. Szalkowski, in Advances in High Temperature Chemistry, Ed. L. Eyring (Academic Press, New York, 1971) Vol. 4, p. 137.

57. W. M. Mularie and W. T. Peria, Surf. Sci. 26, 125 (1971).

58. L. A. West, LBL-107 (Ph.D. thesis, 1971).

59. W. E. Spicer and C. N. Berglund, Rev. Sci. Instrum. 35, 1665 (1964).

60. L. B. Leder and J. A. Simpson, Rev. Sci. Instrum. 29, 571 (1958).

61. L. A. Harris, J. Appl. Phys. 39, 1419 (1968).

62. G. Liebmann, Phil. Mag. 39, 281 (1947).

63. D. A. Huchital and J. D. Rigden, in International Conference on Electron Spectroscopy, Ed. D. A. Shirley (North-Holland Publishing Co., Amsterdam,-London, 1972) p. 79.

64. K. R. Spangenberg, in Vacuum Tubes (McGraw-Hill Book Co., New York, 1948).

65. K. Ulmer and B. Zimmermann, Z. Physik 182, 194 (1964).

66. J. A. Simpson and C. E. Kuyatt, J. Appl. Phys. 37, 3805 (1966).

67. T. W. Haas, A. G. Jackson, and M. P. Hooker, J. Chem. Phys. 46, 3025 (1967).

68. R. Kaplan, UCRL Report # 19661 (1970).

69. M. Hansen, in Constitution of Binary Alloys, First Supplement, Ed. R. P. Elliot (McGraw-Hill, New York, 1965).

70. R. L. Park and H. H. Madden, Surf. Sci. 11, 188 (1968).

71. F. A. Cotton and G. Wilkinson, in Advanced Inorganic Chemistry (Interscience Pub. Co., New York, 1962), 2nd edition, p. 523.

72. L. Fiermans and J. Vennik, Surf. Sci. 24, 541 (1971).

73. K. K. Vijai and P. F. Packman, J. Chem. Phys. 50, 1343 (1969).

74. G. W. Simmons and E. J. Scheibner, J. Appl. Phys. 43, 693 (1972).

75. L. Fiermans and J. Vennik, Phys. Stat. Sol. 41, 621 (1970).

76. J. L. Robins and J. B. Swan, Proc. Phys. Soc. (London) 76, 857 (1960).

77. J. L. Robins, Ph.D. Thesis, U. of Western Australia (1961).

78. P. E. Best, Proc. Phys. Soc. (London) 80, 1308 (1962).

79. L. Fiermans and J. Vennik, Surf. Sci. 35, 42 (1973).

80. E. A. Bakulin, et.al., Soviet Phys.-Solid State 11, 549 (1969).

81. O. Klemperer and J. P. G. Shepherd, Advan. Phys. 12, 355 (1963).

82. L. F. Mattheiss, Phys. Rev. 134, A970 (1964).

83. J. B. Goodenough, in Progress in Solid State Chemistry, Ed. H. Reiss (Pergamon Press Ltd, Oxford, 1971), vol. 5, p. 145.

84. J. M. Honig, et.al., Phys. Rev. B6, 1323 (1972).

85. D. W. Fischer, J. Appl. Phys. 40, 4151 (1969).

86. D. E. Eastman, Solid State Commun. 7, 1697 (1969).

87. T. W. Haas, J. T. Grant, and G. J. Dooley, Phys. Rev. B1, 1449 (1970).

88. J. P. Coad and J. C. Rivière, Phys. Stat. Sol. 7, 571 (1971).

89. J. P. Coad, Phys. Letters 37A, 437 (1971).

90. Analysis performed by the American Spectrographic Lab. Inc., San Francisco.

91. R. J. H. Clarke, in The Chemistry of Titanium and Vanadium (Elsevier Pub. Co., Amsterdam, 1968).

92. J. C. Phillips, Rev. Mod. Phys. 42, 317 (1970).

93. J. A. Van Vechten, Phys. Rev. 182, 891 (1969).

94. S. H. Wemple and M. DiDomenico, Phys. Rev. B3, 1338 (1971).

95. R. W. Shaw, Phys. Rev. Letters 25, 818 (1971).

96. B. F. Levine, Phys. Rev., B7, 2591 (1973).

97. Because of the difficulties in ascribing valencies to the vanadium and silicon atoms in this intermetallic compound, its ionicity was determined using the method of Shaw after determining his proportionality constant (C^2) from the calculated PV ionicity for VC and the calculated $\bar{E}_d^2$ value obtained following the method prescribed in his paper.

98. G. Herzberg, in Atomic Structure and Atomic Spectra (Dover Pub., New York, 1944).

99. L. Ramquist, et.al., J. Phys. Chem. Solids, 30, 1835 (1969).

100. L. Hedin and G. Johansson, J. Phys. B2, 1336 (1969).

101. D. A. Shirley, Chem. Phys. Letters 16, 220 (1972).

102. D. A. Shirley, LBL Report # 1207 (1973).

103. W. N. Asaad and E. H. S. Burhop, Proc. Phys. Soc. 71, 369 (1958).

104. L. Fiermans and J. Vennik, Surf. Sci. 18, 317 (1969).

105. T. W. Haas and J. T. Grant, Physics Letters 30A, 272 (1969).

106. F. J. Szalkowski and G. A. Somorjai, J. Chem. Phys. 56, 6097 (1972).

107. W. W. Beeman and H. Friedman, Phys. Rev. 56, 392 (1939).

108. W. S. Williams, Science 152, 34 (1966).

109. T. Katsura and M. Hasegawa, Bull. Chem. Soc. of Japan 40, 561 (1967).

110. T. Hurlen, Acta Chemica Scandinavica 13, 365 (1959).

111. International Conference on Electron Spectroscopy, Ed. D. A. Shirley (North-Holland Pub. Co., Amsterdam-London, 1972), Chapter IV.

112. C. J. Powell, Phys. Rev. Letters 30, 1179 (1973).

113. T. W. Haas and J. T. Grant, Appl. Phys. Letters 16, 172 (1970).

114. C. C. Chang, Surf. Sci. 23, 283 (1970).

115. J. T. Grant and T. W. Haas, Surf. Sci. 23, 347 (1970).

116. R. J. Fortner and R. G. Musket, Surf. Sci. 28, 339 (1971).

117. M. Salmerón and A. M. Baró, Surf. Sci. 29, 300 (1972).

118. G. C. Allen and R. K. Wild, Chem. Phys. Letters 15, 279 (1972).

119. M. Saleman and E. B. Patterson, Surf. Sci. 35, 75 (1973).

120. P. R. Bevington, in Data Reduction and Error Analysis for the Physical Sciences (McGraw-Hill, New York, 1969).

LEGAL NOTICE

TECHNICAL INFORMATION DIVISION
LAWRENCE BERKELEY LABORATORY
UNIVERSITY OF CALIFORNIA
BERKELEY, CALIFORNIA 94720